EXPERIMENTAL STUDY OF THE DEVELOPMENT FLOW REGION ON STEPPED CHUTES

by Rafael Eduardo Murillo - Muñoz

A thesis submitted to the Faculty of Graduate Studies in partial fulfillment of the requirements for the degree of

Doctor of Philosophy

Department of Civil Engineering
University of Manitoba
Winnipeg, Manitoba, Canada

February, 2006

Abstract

The development flow region of stepped chutes was studied experimentally. Three configuration of chute bed slopes $3.5H : 1V$, $5H : 1V$ and $10H : 1V$, were used to study the flow characteristics. Each model had five horizontal steps and with constant step height of 15 cm. Constant temperature anemometry was used to investigate the velocity field characteristics as well as local void fraction. Pressure transducers were used to examine the pressure distribution. The conditions of aerated and non-aerated cavity were studied.

It was found that the temperature anemometry is a valuable tool in the study of water flow problems due to its good spatial and temporal resolution. It is recommended that the constant overheat ratio procedure should be used in dealing with non-isothermal water flows.

Flow conditions along the development flow region were found to be quite complex with abrupt changes between steps depending whether or not the flow jet has disintegrated. The flow on this region does not resemble a drop structure and after the first step, the step cavity condition does not affect the flow parameters.

Pressure distribution was also found to be complex. It was found that there are no conclusive pressure profiles either on the step treads nor on step risers. No correlation was observed with the values of pool depth.

The instantaneous characteristics of the velocity field along the jet of a drop structure were also studied. It was concluded that the cavity condition does not affect the velocity field of the sliding jet. The shear stress layer at the jet/pool interface was quantified.

Acknowledgments

Table of contents

List of figures

List of Tables

List of symbols

A_o [-]   regression coefficient

A_1 [-]   regression coefficient

A_2 [-]   regression coefficient

d_1 [m]   water depth immediately after the jet impact

E [V]   anemometer output voltage

E_A [V]   output voltage at T_A

E_{ref} [V]   output voltage at T_{ref}

Fr [-]   Froude number

Gr [-]   Grashof number

g [m/s^2]   acceleration due to gravity

h [m]   step height

j [-]   index

k [-]   index, total number of points on the liquid phase

L [m]   step length

L_i [m]   distance along the step tread measured from the step riser

N [-]   total number of steps, total number calibration values

Nu [-]   Nusselt number

n [-]   exponent, number of points on the liquid phase

P [Pa]   pressure

Q [m^3/s]   flow discharge

R_E	[-]	Reynolds number
R_o	[ohms]	sensor cold resistance
R_s	[ohms]	sensor operating resistance
s	[m]	chord size
T	[s]	total time
T_A	[°C]	water temperature
T_{ref}	[°C]	reference temperature
T_s	[°C]	sensor temperature
T_{setup}	[°C]	sensor temperature at setup
Tu	[-]	turbulence intensity
t_{AB}	[s]	time interval between point A and B
U	[m/s]	flow velocity
U_{avg}	[m/s]	depth average flow velocity
U_c	[m/s]	calculated flow velocity
U_m	[m/s]	measured flow velocity
u	[m/s]	instantaneous water velocity values,
u^2	[m²/s²]	normal stress
We	[-]	Weber number
y	[m]	water depth
y_c	[m]	critical water depth
y_{jet}	[m]	thickness of the water jet

y_p	[m]	water depth behind the overfalling jet
y_T	[m]	total water depth
$y*$	[m]	distance along the step riser measured upwards from the tread
α	[-]	void fraction
γ	[N/m^3]	specific weight of water
ε	[-]	squared error
θ	[degrees]	chute slope
Θ	[-]	overheat ratio
ϕ	[m]	pipe diameter

<div style="text-align: right">

Chapter 1 *Introduction*

</div>

The hydraulics of stepped spillways is a field that has evolved in the last 25 years in direct connection with new construction techniques and new materials. Nevertheless, it has been in the last decade that three possible flow regimes on a stepped spillway have been clearly identified: the nappe, the transition, and the skimming flow regimes. Each one of these regimes has different hydraulic properties and characteristics not yet well understood, which makes the subject challenging for hydraulic engineers. In addition, stepped spillways have proved to be an economic alternative for many dams and its environmental benefits have just begun to be explored.

1.1 Stepped chutes and cascades

For the last few decades, stepped spillways have become a popular method for handling flood releases. The key characteristic of them is the configuration of the chute, which is made with a series of steps from near the crest to the toe. These steps increase

significantly the rate of energy dissipation taking place along the spillway face and reduce the size and the cost of the downstream stilling basin.

Stepped chutes have been used for centuries. Applications can be found in the ancient dams in the Khosr River (Iraq), in the Roman Empire, and in the Inca Empire among other cultures. Chanson (1995a, 1995b, 1998, 2000, 2001c) presented an interesting recompilation on the history of stepped spillways and cascades.

The recent popularity of stepped spillways is based on the development of new construction materials, e.g., roller compacted concrete (RCC) and gabions among others. The construction of a stepped spillway is compatible with RCC placement methods and slip-forming techniques. Also stepped spillways are the most common type of spillways used for gabion dams. Soviet engineers developed the concept of an overflow earthen dam. In this type of structure, the spillway consists of a revetment of precast concrete blocks with steps, which lays on a filter and erosion protection layer.

Stepped spillways are also utilized in water treatment plans. As an example, five artificial cascades were designed along a waterway system to help the re-oxygenation of the polluted canal (Macaitis, 1990; Robison, 1994). Stepped chutes and cascades have also been used with aesthetic purposes. Examples can be found in the aqueducts of the Roman Empire, in the Renaissance palaces of France, and in the modern Hong Kong architecture among other places. Chanson (1998, 2001b) discussed this application in detail.

Over the past decade, several dams have been built with overflow-stepped spillway around the world: Clywedog dam (U.K.), La Grande 2 (Canada), Monksville dam (U.S.A.), and Zaaihoek dam (South Africa) are a few examples.

1.2 Hydraulics expertise

In spite of the fact that examples of stepped chutes and cascades are present in many ancient civilizations, there are not many references about them. Perhaps, the oldest modern reference about stepped spillways is Wegmann (1907), who described the design of the New Croton Dam, U.S.A. The next known references are given by Poggi (1949, 1956) and Horner (1969). Later on, Essery and Horner (1978) did a significant study to quantify the energy dissipation and to describe the nappe and skimming flow regimes.

With the introduction of RCC dams during the 1980's, stepped chutes regained popularity and its literature revitalized (Young, 1982; Sorensen, 1985; Houston and Richardson, 1988). Since then, many researchers (Diez-Cascon et al., 1991; Chanson, 1993, Chamani, 1997; Boes, 1999; among many others) have investigated the hydraulic characteristics of such chutes; investigations that eventually led to the first international workshop of stepped spillways held in Switzerland in March 2000 (Minor and Hager, 2000). All these efforts have shown that stepped chute flows can be divided into three regimes: nappe flow for low discharges, transition flow for intermediate discharges, and skimming flow for large discharges.

Of the three flow regimes, the skimming flow has captured the attention of most of the studies. Research on the transition and nappe flow regimes is scarce. Descriptions of the transition flow regime can be found in Ohtsu and Yasuda (1997), Chanson (2001a, b), Chanson and Toombes (2001, 2004) as well as De Marinis et al. (2001). On the other hand, Horner (1969), Essery and Horner (1978), Peyras et al. (1991, 1992) as well as Chanson (1995a, 2001c) amongst others described some aspects of the nappe flow

regime. Chanson (1999a) used the drop structure's concept to study the flow in the nappe flow regime and Chanson and Toombes (1998a, b) reported experiments with supercritical flow on a single step.   Pinhero and Fael (2000) studied the energy dissipation process and more recently Aigner (2001) utilized sharp-crested weirs to create a nappe flow regime in pooled steps. Finally, El-Kamash et al. (2005) studied the bubble characteristics in the two phase flow of the nappe flow regime. A brief description of the three regimes follows.

1.2.1 Flow regimes in a stepped chute

As mentioned before, stepped chutes can present three flow regimes: nappe, transition and skimming. In the nappe flow regime each step always has a falling nappe, and an air pocket can be observed in the step cavity (Figure 1.1a), i.e., the step cavity is fully aerated. In the transition flow (Figure 1.1b) air pockets are formed in some steps, and recirculating vortices are formed in the other steps. This regime is characterized by strong hydrodynamic fluctuations (Ohtsu and Yasuda, 1997) and nappe stagnation on each horizontal face associated with a downstream spray (Chanson, 2001c).

Finally, in the skimming flow regime the air pocket is filled with water and recirculating vortices are always presented at each step (Figure 1.1c). In this regime the water flows over a pseudo bottom formed by the vortices and huge amounts of air are entrained, therefore it is considered to be two-phase flow. Clear boundaries between the three regimes have not been established yet.   Rajaratnam (1990), Chamani and Rajaratnam (1999), Yasuda and Ohtsu (1999), Minor and Boes (2001), Chanson and Toombes (2004) as well as Ohtsu et al. (2004) have proposed expressions for the

boundary between transition and skimming flow regimes. Similarly, a few expressions for the boundary between nappe and transition flow regimes have been proposed; these will be discussed in §1.3. As an example of the available criteria, Figure 1.2 presents the boundaries for the three regimes as defined by Yasuda and Ohtsu (1999). In this figure h is the step height, L is the step length and y_c is the critical water depth.

1.3 Nappe flow regime

Chanson (2001c) defines the nappe flow regime as a succession of free falling nappes and jet impacts from one step onto the next one when the step cavity is fully aerated. This regime occurs at low discharges and it is characterized by the free falling nappe at the upstream end of each step, an air cavity, and a pool of recirculating water. The geometry of the step can be horizontal, inclined (upward or downward) or pooled (Figure 1.3). In the following paragraphs the state-of-the-art on the nappe flow regime is summarized.

1.3.1 Onset conditions

The required hydraulic conditions to establish the nappe flow regime in a stepped chute have not been clarified yet. Using experimental data available in the literature, Rajaratnam (1990) proposed that values of $y_c/h > 0.80$ will produce skimming flow in the range $0.421 \leq h/L \leq 0.842$ leaving the nappe flow regime when $y_c/h \leq 0.80$. Stephenson (1991), using the experience of South Africa dams, suggested that the most suitable conditions for nappe flow situations are

$$\tan\theta = \frac{h}{L} < \frac{1}{5}, \tag{1.1}$$

and

$$\frac{y_c}{h} < \frac{1}{3}. \tag{1.2}$$

Neither author considered transition flow regime.

Yasuda and Ohtsu (1999) considered the minimum step height required to form the nappe flow. They expressed the boundary between nappe and transition flows as

$$\frac{h}{y_c} = 1.4\left(1.4 - \tan\theta\right)^{-0.26}. \tag{1.3}$$

Chanson and Toombes (2004) proposed that the same boundary is given by

$$\frac{y_c}{h} = 0.9174 - 0.381\frac{h}{L}, \tag{1.4}$$

for the range $0 \le h/L \le 1.7$. All of the above expressions were developed for horizontal steps and they are presented in Figure 1.4. This figure indicates that Stephenson (1991) gives the more conservative criterion while Rajaratnam (1990) is the least conservative. Yasuda and Ohtsu (1999) fairly agree with Chanson and Toombes (2004) on the boundary between the nappe and transition flow regimes.

1.3.2 Nappe flow sub-regimes

In the case of chutes with horizontal steps, Horner (1969) as well as Essery and Horner (1978) described two types of nappe flow: the isolated nappe flow and the nappe interference flow.   In the former, the nappe wholly strikes the tread of the step immediately below and it occurs at low discharges. In the latter, the nappe overshoots

the tread section of the step and collides with the jet leaving this step. In both cases, the water flow is supercritical along the entire cascade.

On the other hand, Chanson (2001c) suggested the existence of three nappe flow sub-regimes: a) nappe flow with fully developed hydraulic jump (sub-regime NA1), b) nappe flow with partially developed hydraulic jump (sub-regime NA2) and, c) nappe flow without hydraulic jump (sub-regime NA3). Figure 1.5 gives a representation of each sub-regime.

In the sub-regime NA1, the flow is critical at the step edge, supercritical in the free falling nappe up to the hydraulic jump, and subcritical downstream of the jump and up to the edge. On the other hand, in the NA2 sub-regime the hydraulic jump interferes with the downstream step edge, and in sub-regime NA3 the flow is supercritical at any position (Chanson, 2001c). Chanson (1994) determined that sub-regime NA2 occurs for values of y_c/h smaller than a critical value given by

$$\frac{y_c}{h} < 0.0916 \left(\frac{h}{L}\right)^{-1.276},\tag{1.5}$$

in the range $0.2 \le h/L \le 6$.

1.3.3 Flow development characteristics

Horner (1969) mentioned that as the flow enters a chute with a given step geometry the stream accelerates and becomes fragmented on the initial reach of the structure. He described this zone of the cascade as the transitory zone. Furthermore, Horner pointed out that on steps lower down an equilibrium state is reached and flow geometry is the same at each step. He referred to this section as the uniform flow.

Essery and Horner (1978) added to the uniform flow description that the flow geometry is the same at each step but the depth varies across each one. Finally, Horner concluded that the only flow not behaving in the manner outlined above are subcritical nappe flows on inclined step cascades, which will be introduced in §1.6.

The length of the transitory zone is influenced by discharge per unit of width, overall slope, step shape and step size, geometry of the spillway crest and the presence of piers and gates (Horner, 1969). On the other hand, the most striking features of the uniform flow are high velocities and fragmentation of the nappe (Horner, 1969).

In contrast to the above, Chanson (2001c) described two regions in nappe flows without hydraulic jump (NA3 sub-regime): the flow establishment region and the gradually varied flow region. The flow establishment region occurs on the first few steps and it is characterized by three dimensional flow patterns, e.g., shock waves, and sidewall standing waves (Chanson, 2001c). In the gradually varied flow region the flow patterns are nearly identical from one step to another and a significant amount of air is entrained.

1.4 Transition flow regime

The transition flow regime is an intermediate stage between the nappe and the skimming flow regimes. It appears at medium flows and it does not present the succession of free jets observed in nappe flow nor the quasi-smooth free surface of skimming flow. Nappe stagnation on each step and significant downstream spray are the main characteristics of this flow regime.

1.4.1 Onset conditions

As discussed in §1.3, the onset conditions for nappe flow regime are not well defined yet. Hence, the conditions for the transition flow regime have not been established as well. Similarly, the boundary between the transition and the skimming flow is still under study as it will discussed in §1.5.

1.4.2 Transition flow sub-regimes

Two sub-regimes in transition flow have been cited by Chanson and Toombes (2004). The authors mentioned a lower range of transition flows with a longitudinal flow pattern characterized by an irregular alternance of small to large air cavities downstream of the inception point of the free surface aeration. They designated these ranges of flow as the first sub-regime. On the other hand, the second sub-regime corresponded to the upper range of transition flow rates in which the longitudinal flow pattern is characterized by an irregular alternance of air cavities (small to medium) and filled cavities.

1.4.3 Flow development characteristics

The flow development characteristics on the transition flow are not clear yet. Chanson (2001a) indicated that on flat slopes the flow in the development region is very chaotic and it is characterized by significant changes in flow properties from one step to the next one. The author mentioned that downstream, the flow becomes gradually varied with slow variations of the flow properties from step to step, along with significant longitudinal variations on each step. At the upstream end of the step, the flow is

characterized by a pool of recirculating water, stagnation and significant spray and water deflection immediately downstream.

On a steep slope, Chanson (2001c) indicated that the upstream flow is smooth and transparent. In the first few steps, the free surface is undular in phase with the stepped geometry and some aeration in the step corners is observed immediately upstream of the inception point (Chanson, 2001c). Downstream of this point, significant splashing is observed.

1.5 Skimming flow regime

There is general agreement that the skimming flow regime appears once the step cavity is filled with water and it cushions the flow. Thus, the external edges of the steps form a pseudo-bottom over which the flow passes and stable recirculating vortices develop between steps (Figure 1.1c). These vortices are maintained through the transmission of shear stress from the fluid flowing past the edges of the steps and they are believed to be responsible for the large energy dissipation that characterizes this regime.

For a stepped spillway with the skimming flow regime, the free surface of the flow is smooth in the early steps and no air entrainment occurs in this region. This zone occurs near the crest and it is distinguished by the presence of clear water. Next to the boundary however, turbulence is generated. When the outer edge of the turbulent boundary layer reaches the free surface, air entrainment at the free surface occurs. The point where this phenomenon occurs is known as the point of inception. Downstream of this point, a layer containing a mixture of both air and water extends gradually through

the fluid producing a region of gradually varied flow. Far downstream, the flow becomes uniform and this reach is defined as the uniform equilibrium flow region.

1.5.1 Onset conditions

For small discharges and flat slopes, the water flows as a succession of waterfalls (i.e., nappe flow regime). A small increase in discharge or slope might induce the formation of transition flow regime and, if the discharge or the slope is further increased, the skimming flow regime will develop. The onset of skimming flow is a function of the discharge, the step height, and step length.

Several authors have studied the onset of the skimming flow regime. Rajaratnam (1990) proposed that skimming flow appears once $y_c / h > 0.8$. Chanson (1996) defined the "onset of skimming flow" by the disappearance of the cavity beneath the free falling nappes, and hence, the water flowing as a quasi-homogeneous stream. According to Chamani and Rajaratnam (1999), the expression proposed by Chanson (1996) predicts much larger values of y_c / h, especially for h/L greater than about 1.0. Furthermore, they mentioned that during their experiments it was noted that, at the onset of skimming flow the air pockets under the jet did not disappear. Thus, although the flow skims over the steps, the recirculating flow did not fill the pockets under the jet. They argued that this observation is contrary to the underlying assumption of Chanson (1996). Therefore, Chamani and Rajaratnam (1999) proposed a different criterion based on visual observations and assuming that the jet is parallel to the slope of the stepped spillway. Their criterion is

$$\frac{h}{L} = \sqrt{0.89\left[\left(\frac{y_c}{h}\right)^{-1} - \left(\frac{y_c}{h}\right)^{-0.34} + 1.5\right] - 1}\,. \tag{1.6}$$

According to Chamani and Rajaratnam (1999), prediction of Equation (1.6) is generally good for h/L greater than about 1.0, which is applicable for steeply sloped stepped spillways. Furthermore, they suggested that the inner side of the jet just hits the edge of the steps when

$$\frac{h}{L} = 0.405\left(\frac{y_c}{h}\right)^{-0.62}. \tag{1.7}$$

Moreover, James et al. (1999) indicated that skimming flow appears once y_c/h is larger than

$$\frac{y_c}{h} = 0.541\left(\frac{h}{L}\right)^{-1.07}, \tag{1.8}$$

for $h/L < 0.84$. Yasuda and Ohtsu (1999) give the step height for the formation of the skimming flow as

$$\frac{h}{y_c} = 1.16\left(\tan\theta\right)^{0.165}, \tag{1.9}$$

in the region $0.1 \leq \tan\theta \leq 1.43$, $0 \leq h/y_c \leq 1.4$, $5 \leq H_{dam}/y_c \leq 80$. Boes, cited by Boes and Minor (2000), indicated that skimming flow sets in for ratios larger than

$$\frac{y_c}{h} = 0.91 - 0.14\tan\theta. \tag{1.10}$$

A general agreement on the boundary between the transition and the skimming flow has not been yet achieved. Yet, the best practice is to choose the criterion that best fits the specific designing conditions.

1.5.2 Skimming flow sub-regimes

Chanson (2001c) distinguished three skimming flow sub-regimes depending on the slope of the spillway. On flat slopes, the author mentioned the wake-step interference and the wake-wake interference sub-regimes. The first sub-regime is characterized by the fact that the wake does not cover completely the step tread and a three-dimensional unstable recirculation is present in it. On the other hand, the main characteristic of the second sub-regime is that the length of the wake and step tread is approximately the same, therefore there is some interference between one step and the next one. Finally, on steep slopes, Chanson (2001c) mentioned the recirculating cavity flow sub-regime. In this sub-regime, the recirculating flow appears asymmetrical with most vorticity activity occurring in the downstream part of the cavity.

1.5.3 Flow development characteristics

On a stepped chute, the flow can be subdivided into so-called clear water and white water regions. Starting from the crest to the inception point, a clear water region may be observed, whereas the white water region develops in the downstream portion with the characteristic two-phase air-water flow. The critical depth mainly governs the clear water region, while the uniform aerated flow depth has a significant effect on the white water region.

The flow in the clear water region always has a drawdown curve due to the transition from sub- to supercritical flow on the spillway crest. In contrast, the air-water mixture flow always has a backwater curve due to the entrainment of air and the resulting

flow bulking. Therefore, for a very long stepped spillway of constant slope, there exist three characteristic flow depths:

a) the critical depth at the spillway crest,

b) the inception depth (a local minimum), and

c) the uniform aerated depth (asymptotic maximum).

The transitions between these three characteristics flow depths are the drawdown and the backwater curves. Hager and Boes (2000) presented expression for both curves.

1.6 Stepped chutes with inclined steps

Stepped chutes and cascades with inclined steps have not been studied in detail. Horner (1969), Essery and Horner (1978), Peyras et al. (1991, 1992), Chanson (2001c) discussed some experimental results with inclined steps. Horner (1969) concluded that flow behavior on inclined steps falls into two categories: that in which the approach flow to each drop is subcritical, and that in which it is supercritical. He also observed a transition category in which both states of flow occurred.

The subcritical category was observed by Horner (1969) at relative low discharges and it was characterized by subcritical pools on all the step surfaces (Horner, 1969). The flow leaving the steps passed from the subcritical flow state through critical depth and into the supercritical nappes. Further downstream, the flow changes from supercritical to subcritical by means of a hydraulic jump. According to Horner, little or no fragmentation of the nappe occurs with flows of the subcritical category and the uniform zone may be considered to extend over the whole of the cascade. On the other

hand, the transitory category is characterized by supercritical flow in the transitory zone and subcritical flow in the uniform zone (Horner, 1969).

In the supercritical category flow behavior is similar to that on a cascade of horizontal steps (Horner, 1969). That is, conditions are everywhere supercritical and the flow passes through a transitory zone before equilibrium is established in a uniform zone. At any discharge, the number of steps on an inclined step cascade over which the transition zone forms is less than the number on a horizontal step cascade with the same overall slope and step size (Essery and Horner, 1978).

Horner (1969) also considered the influence of nappe ventilation on the flow conditions. In the case of flow in the subcritical category his investigation revealed that the effect of aeration on flow behavior of a cascade was similar to the influence at a single drop. That is to say on a cascade with no air vents the pressure beneath the nappes became sub-atmospheric. With flows in the supercritical category, however, Horner concluded that there was no marked difference between the uniform zone flow patterns created on cascades with and without ventilation. Horner pointed out that the reason for this was the highly fragmented nature of the stream after the first few steps, and the consequent provision of an adequate supply of air through the nappes.

Finally, Peyras et al. (1991, 1992) observed an NA1 sub-regime on an upward inclined step and pooled step chutes at low discharges only. They applied Rand's (1955) expressions and concluded that these expressions can be used on inclined steps as preliminary computations. Peyras et al. performed their experiments on stepped gabion weirs.

1.7 Objectives of the study

This research project on stepped spillways pursues the goal of characterizing the development flow region of such structures. In order to achieve this goal, the following objectives have been defined:

a) To determine a proper procedure to use constant temperature anemometry in water flows;

b) to adequately describe the velocity field in the development flow region of stepped chutes;

c) to characterize the pressure distribution in the development flow region; and

d) to study the instantaneous characteristics of the velocity field in the jet of a drop structure.

1.8 Structure of the report

This report is divided into seven chapters in order to present clearly the findings of the research. Chapter 1 summarizes the state of the art on the development flow region as well as the objectives of the study. Chapter 2 describes the apparatus and instrumentation used in the project whilst Chapter 3 deals with the use of constant temperature anemometry in water flows. Chapter 4 presents the research findings regarding void fraction and velocity measurements and Chapter 5 introduces the pressure measurements as well as its analysis. In Chapter 6, observations regarding the drop structure are given and finally, Chapter 7 discusses the conclusions of the research and delineates future research work.
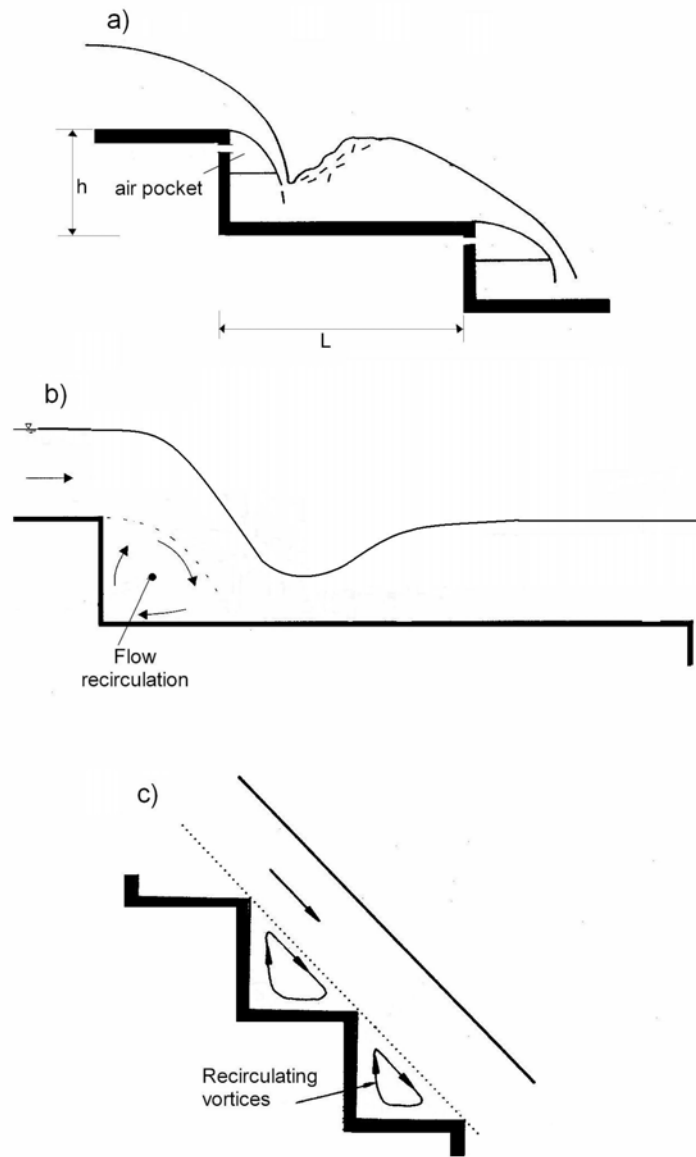
Figure 1.1 Flow regimes on stepped spillways. a) Nappe

flow regime. b) Transition flow regime. c)

Skimming flow regime.
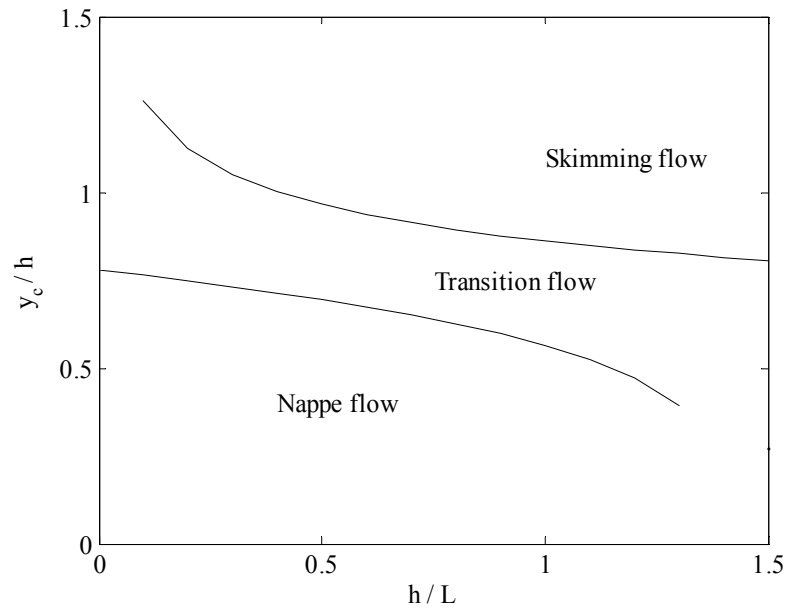
Figure 1.2 Flow regimes criterion according to Yasuda

and Ohtsu (1999).
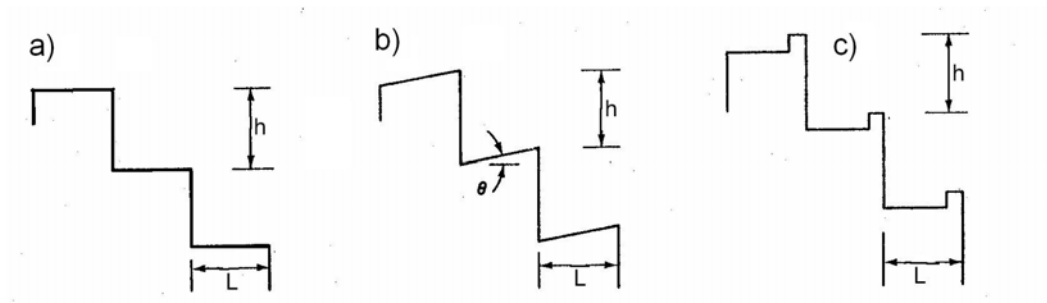
Figure 1.3 Different step types: a) horizontal step, b) upward steps, c) pooled steps.
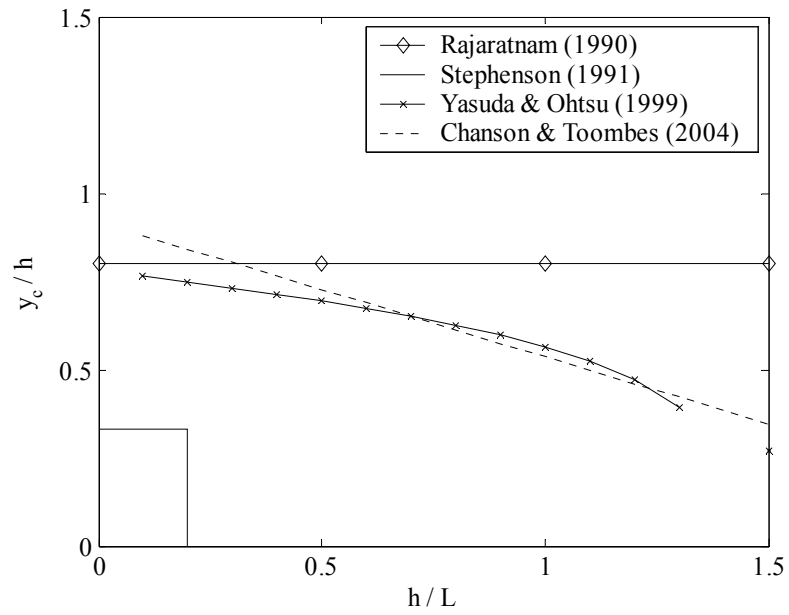
Figure 1.4 Nappe flow regime criteria.
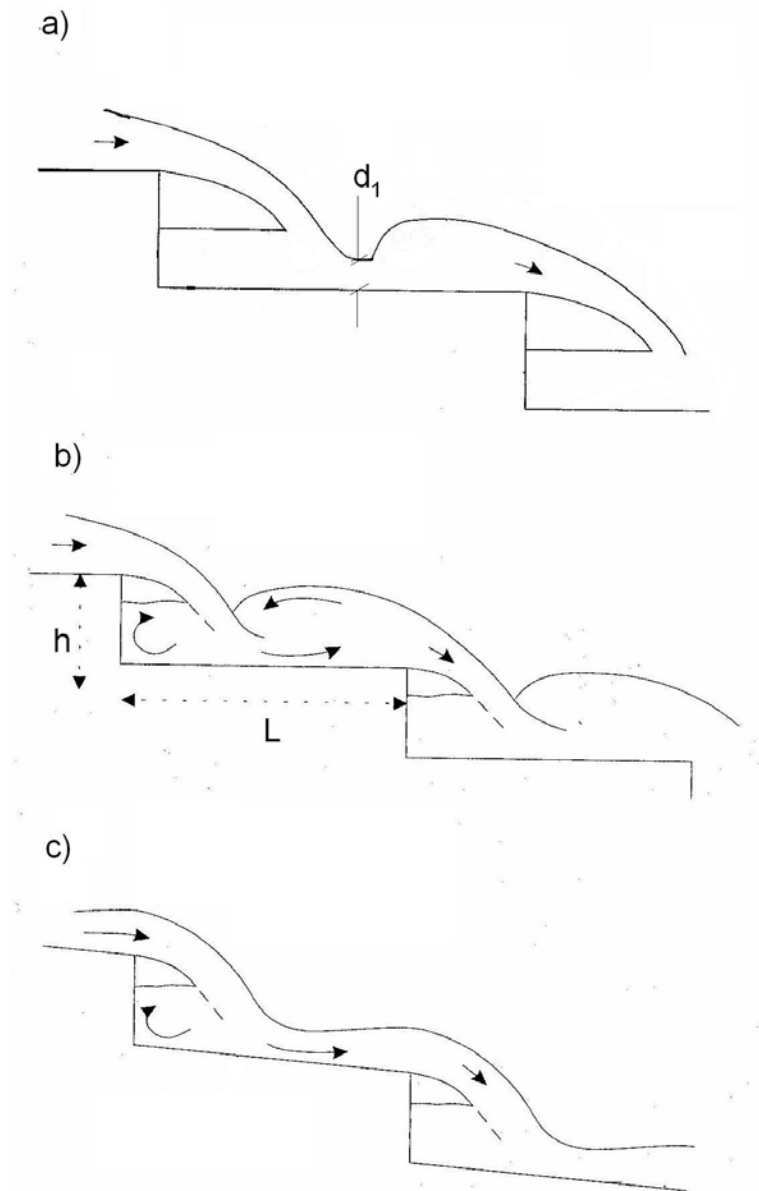
Figure 1.5 Nappe flow sub-regimes according to Chanson (2001e). a) Nappe flow with fully developed hydraulic jump (sub-regime NA1). b) Nappe flow with partially-developed hydraulic jump (sub-regime NA2). c) Nappe flow without hydraulic jump (sub-regime NA3).

_____
Chapter 2   *Experimental setting*

2.1 Introduction

This chapter presents the characteristics of the models used during the experimental work of this study. It also describes the instrumentation and data acquisition systems employed throughout the project. Descriptions of the calibration procedures and modeling conditions are also included as well as theoretical considerations about constant temperature anemometry. Factors affecting such a technique as well as its use in two phase flow measurements is also described.

2.2 Model description

Three models of a stepped chute were built at the Hydraulics Research & Testing Facility (HRTF), University of Manitoba. The models were made of High Density Overlay (HDO) plywood and they consist of three sections: a forebay, an approach channel and the stepped chute (Figures 2.1). The forebay was a box of $1.22 \times 2.44 \times 1.22$ m^3 where perturbations, produced by the discharge of pressure flow

from the supply line, were dissipated. The approach channel was 7.32 m in length, with a rectangular cross section $\left(0.412 \times 0.610 \text{ m}^2\right)$ and a horizontal slope. Due to space limitations at the time of construction, the channel intake had an angle of 45° with respect to the head tank as well as a 45° left turn 3.66 m downstream of the intake. Honeycombs made of PVC pipe $\left(\phi = 7.5 \text{ cm}\right)$ 30 cm in length were used in order to ensure the correct flow distribution. At the stepped chute section three different slopes were used: $3.5H : 1V$, $5H : 1V$, $10H : 1V$; all of them with five steps. To provide air into each step cavity a small tube ($\phi = 8.7$ mm) was installed on the right sidewall while the left sidewall was made of Plexiglas in order to observe the flow pattern. Figure 2.2 shows the models and the overall layout of the experimental arrangement.

The design of the models presented constrains in terms of minimum discharge, minimum water depth as well as maximum discharge. The minimum discharge used depended on the restriction of minimum water depth. In modeling spillways, the USBR (1953) recommends a minimum water depth of 3 cm. This value prevents surface tension problems as well as allows the instruments to operate safely. The water depth d_1 immediately after the jet impact is the limiting depth, which depends on both the discharge and the step high. Hence, a combination of minimum discharge and step high was determined such that $d_1 > 3$ cm. Table 2.1 presents the results of the selection process for the three slopes used in the project, in this table it is assumed that y_c occurs at the step brink. To simplify the construction of the models, the same step height was selected for the three models. As Table 2.1 indicates, the step height was 15 cm and y_c was 7 cm for a minimum y_c/h ratio of 0.47.

The maximum discharge is the other restriction and it is defined by the boundary between nappe and transition flow regime. In designing the models, the boundary proposed by Chanson and Toombes (2004) was adopted and it is given in Equation (1.4). According to this expression the maximum discharge and its flow characteristics are indicated in Table 2.1.

Table 2.1 Hydraulic parameters for minimum and maximum flow.

			Minimum flow			Maximum flow		
Slope	h/L $(-)$	h (cm)	y_c (cm)	y_c/h $(-)$	Q (m^3/s)	y_c (cm)	y_c/h $(-)$	Q (m^3/s)
$3.5H:1V$	0.29	15.0	7.0	0.47	0.024	12.1	0.809	0.055
$5H:1V$	0.20	15.0	7.0	0.47	0.024	12.6	0.841	0.058
$10H:1V$	0.10	15.0	7.0	0.47	0.024	13.2	0.879	0.062

2.3 Instrumentation and data acquisition

In order to measure the different hydraulic parameters three systems were used during the project. These systems are the data acquisition, pressure measurement, and velocity measurement systems. Both, the pressure and velocity measurement systems connect to the data acquisition, which controls the actual gathering of data. A description of these three systems follows.

2.3.1 Data acquisition system

This systems consists of a data acquisition card (PCI-MIO-16E-4) and a shielded connector block (SBC-68), both manufactured by National Instruments. It also includes a personal computer as well as the software package LabVIEW™ used to control the gathering of data.

The PCI-MIO-16E-4 card has a resolution of 12 bits and a data logging speed that varies from 250 ks (multi-channel) up to 500 ks (single–channel). In addition, it has 8 differential input channels (16 single-ended) with variable voltage range (software selectable). The SCB-68 is a shielded board with 68 screw terminals for easy connection to National Instruments 68-pin products. To these screw terminals the pressure and velocity measurement systems were connected using a differential scheme to reduce noise pick up.

As mentioned before, LabVIEW™ (v 6.1) was used to control the data acquisition and settings of the PCI card. An appropriate virtual instrument was developed to control channel voltage range, scan frequency, total number of points to acquire as well as buffer characteristics. The software and PCI card were installed on a Pentium-II, 400 MHz personal computer with 256 MB ram and 20GB SCSI hard disk.

2.3.2 Pressure measurement system

The pressure measurement system consists of four DP45 differential pressure transducers and one multi-channel carrier demodulator, both elements manufactured by Validyne Engineering. The set of transducers consists of two DP45-28 and two DP45-26. The DP45-28 transducers have a pressure range capability of ±56 cm of water column

whilst the DP45-26 sensors have a range of ± 35 cm. All four transducers have a frequency response greater than 600 Hz. The multi-channel carrier demodulator (CD280) is a four-channel unit that includes power supply, carrier oscillator as well as zero and span adjustments for each channel. The power supply provides regulated 5 VAC, 5 kHz carrier power to the transducers and then demodulates and amplifies the input signal to a ± 10 VDC full-scale output. This DC output was fed to the data acquisition card via a differential connection. The carrier has a frequency response greater than 1000 Hz and a zero control of ± 10 mV .

2.3.3 Velocity measurements

In dealing with air-water flows classical velocity measurement probes (e.g., pointer gauge, Pitot tube, LDA and ADV velocimeters) are affected by air bubbles and can produce inaccurate readings. In such a type of flow the use of intrusive phase detection probes is therefore preferred, notably optical and conductivity/resistivity probes. Intrusive probes are designed to pierce bubbles and droplets. The principle behind the optical probe is the change in optical index between the two phases. The principle behind the conductivity, or electrical probe, is the difference in electrical resistivity between air and water. An especial type of resistivity probe is the hot-film probe. Its operation relies on the variation of the electrical resistance of the sensor material with the cooling effect of the air-water flow. The hot-film probe allows the correct determination of the water velocity characteristics as well as the air content of the flow and therefore it was selected for this study.

The hot-film probe was controlled using a constant temperature anemometer (CTA). The anemometer is a DISA 55M system, which consists of a power pack (55M05), a main unit (55M01) and a standard bridge (55M10). The power pack contains circuits to rectify and smooth out the AC line voltage, as well as voltage limiting and short-circuit protection circuits. The main unit contains all circuits required for operating the anemometer whilst the standard bridge compensates for the cable impedance and provides two output connections. A brief theoretical description of the use of CTA is given in §2.6. Overall, the system has a maximum output frequency of 30 kHz when used on liquids and an output noise of ± 0.2 mV.

Several types hot-film probes are available on the market. Nevertheless, conical hot-film probes are preferred in water flows since they are less sensitive to contamination. Hence, a conical hot-film probe (55R42) manufactured by Dantec Dynamics was used with the anemometer; this probe is heavy coated as required for liquid applications. The manufacture indicates an applicable velocity range of 0.01 to 25 m/s and a maximum frequency response of 20 kHz.

2.3.4 Other equipment

In addition to the above systems, it was necessary to use the water distribution system available at the HRTF facility. This system consists of a storage tank, two water pumps (60 HP and 75 HP) that feed a constant head tank up to a maximum of 0.5 m^3/s. From this tank four pipelines $(\phi = 60 \text{ cm})$ distribute the water to different areas of the facility, each of this lines have a 1:50 butterfly valve for precise control of the discharge. The system is completed by a 7.5 m^3 volumetric tank for discharge measurement.

In addition, a MSR magmeter (Magnum Standard) was installed on the supply line in order to measure the flow in real time. A LabVIEW™ virtual instrument was developed to communicate with the flowmeter via the RS232 computer port. The MSR magmeter was calibrated in situ via the volumetric tank. Water temperature was monitored using a digital platinum resistance thermometer (Guildline, model 9540) with a resolution of $0.01°C$. Finally, point gauges $(\pm 0.02 \text{ cm})$ were used to measure water depths and levels as necessary.

2.4 Instrument calibration

The calibration procedure of the pressure transducers is discussed in this section. Similarly, the necessary equipment to calibrate the constant temperature anemometer is described in detail.

2.4.1 Pressure transducers

The pressure transducers were calibrated using a stilling well. This simple device consists of a 62.5 cm Plexiglas tube equipped with a pressure port and point gauge, each transducer was attached to the pressure port for individual calibration. The calibration procedure consists of five steps as follows:

A. Reading of zero offset on the point gauge.

B. Adjustment of the zero in the carrier demodulator.

C. Fill up the stilling well and adjustment of the demodulator's span.

D. Empty the well and readjustment of the demodulator's zero.

E. Readings of data at different water levels.

The zero and span on each carrier demodulator channel were adjusted using a digital multimeter (HP-34401A; ±0.001 mV). The data from the transducers was acquired through the data acquisition card. Using the collected data, individual plots (Figure 2.3) were prepared and according with the tendency shown, a linear regression between average voltage output (E) and water pressure (P) in centimeters was fit to the data. Correlation coefficients larger than 0.999 were obtained in all calibrations.

2.4.2 Constant temperature anemometer

The anemometer was calibrated using a water tunnel with a jet submerging into a reservoir in front of the jet (Figure 2.4). The water tunnel was made of Plexiglas and in it the water was circulated through a rotameter into a stagnation section. At this section a low-turbulence plug flow formed to enter the exit nozzle. The stagnation section was made of a 33 cm piece of Plexiglas tube $(\phi = 7.5 \text{ cm})$ whilst the nozzle was a hose barb to MIP adaptor $(2.54 \text{ cm} \times 0.64 \text{ cm})$ with an internal diameter of 4.72 mm. The rotameter was a model GT-8-1306 with tube size R8M-127-4-F-BR-1/2-35G5, produced by Brooks Instruments. This arrangement provided a range of velocities from 0.15 m/s to 5.40 m/s. The velocity was adjusted manually by means of a ball valve. Water was supplied to the tunnel directly from the 60 cm supply pipeline through a clear hose $(\phi = 2.54 \text{ cm})$ attached at the available admission valve.

The nozzle water jet was calibrated using the volumetric method. In such a procedure a graduate cylinder was used to record the volume of water, this cylinder had a maximum capacity of 1000 ml and a graduation of 10 ml. Using this device and an electronic stop watch, the 130 mm rotameter' scale was calibrated against the indirect

velocity measurements. Once the rotameter was calibrated the water tunnel was ready to be used with the constant temperature anemometer. To perform the static and dynamic calibrations of the CTA system the procedure described in its instruction manual (DISA, 1977) was followed.

2.5 Modeling conditions

As mentioned before, the upstream boundary of the models was given by the horizontal approach channel; therefore, the approaching fully rough flow defines an H2 profile in the vicinity of the stepped chute model (see Figure 2.5). The other upstream boundary condition was given by the discharge; Table 2.2 indicates the range of discharges for each flow regime according to the slope chute. On the other hand, the downstream boundary condition was given by the fifth step; this brings the water from the stepped chute to a rectangular channel $\left(1.02 \times 0.61 \, \text{m}^2\right)$ with a nearly horizontal slope that conveyed the water to the recirculation tank. The flow in this channel did not affect the hydraulic conditions in the chute models.

It is also opportune to mention the testing conditions in terms of the Reynolds $\left(R_E\right)$, Froude $\left(Fr\right)$ and Weber $\left(We\right)$ numbers. The Reynolds number during the tests oscillated in the range of $63000 \leq R_E \leq 400000$ while the Froude numbers varied from $2.5 \leq Fr \leq 5.8$. The Weber numbers were in the range of $49 \leq We \leq 126$. These values were calculated at the downstream end of the first step. Appendix A indicates the flow conditions for each one of the runs.

Table 2.2 Modeling conditions on the stepped chutes. Regime flow defined according to Chanson and Toombes (2004). Discharge in m^3/s.

Regime	Model slope		
	$3.5H:1V$	$5H:1V$	$10H:1V$
Nappe flow	$y_c/h < 0.809$ $Q < 0.0545$	$y_c/h < 0.841$ $Q < 0.0578$	$y_c/h < 0.879$ $Q < 0.0618$
Transition flow	$0.809 \leq y_c/h \leq 1.143$	$0.841 \leq y_c/h \leq 1.204$	$0.879 \leq y_c/h \leq 1.294$
Skimming flow	$y_c/h > 1.143$ $Q > 0.0916$	$y_c/h > 1.204$ $Q > 0.0991$	$y_c/h > 1.294$ $Q > 0.1103$

Finally, stepped chutes are usually built using step heights of 30, 60, 90 and 120 cm; being 60 and 90 cm the most common choice for RCC dams. The three models used in the study had a step height of 15 cm and therefore they are related to prototype conditions by scales of 1:2, 1:4, 1:6 and 1:8, respectively. Boes (2000) recommended that a minimum scale of about 1:10 to 1:15 should be used in modeling stepped chutes in order to minimize scale effects. Hence, the models used in this study are of sufficient size to overcome the effects of viscous and surface tension forces introduce by the use of the Froude similarity law.

2.6 Constant temperature anemometry

Constant temperature anemometry is based on the detection of the cooling effects of fluid motion on a small heated sensor. The heat transfer is expressed by a particular law that must be determined for each probe. In a non-isothermal water flow, this law is significantly affected by the change in the physical properties of the water due to the temperature drift as well as by the variation in overheat ratio due to the modification of the temperature difference between the sensor and the water. Two procedures can be used to minimize the influence of temperature drift: the constant overheat ratio and the constant sensor temperature procedure.

The use of CTA in liquids is also affected by electrolysis, cracking of the sensor quartz coating, presence of ions in the water, contamination and bubble formation on the probe (Brunn, 1996). Electrolysis and cracking of the sensor quartz coating are strictly related since the former is prevented by the latter. Cracking on the other hand, is usually the result of a large potential drop between the water surrounding the probe and the film element, this problem is resolved by connecting the CTA ground reference to the water. The presence of ions is particularly important for multi-sensor probes where the conductivity of the water can cause considerable cross-talk between sensors. The use of de-ionized water and de-ionizer units is recommended to prevent ion effects. This type of water is also recommended to prevent probe contamination in conjunction with the use of bypass filtration units and algae inhibitors. Finally, the formation of bubbles on the probe surface can be prevented by using a low overheat ratio. Rasmussen (1967) concluded that the use of an overheat ratio smaller than 10% minimizes the possibility of bubble formation.

2.6.1 Two-phase flow measurements using CTA

The development of instrumentation for two-phase flow is of the utmost importance to back up theoretical investigations in many fields. Technically sound measurement techniques provide information on the local structure of two-phase flows characterized by the flow pattern, the specific area and the bubble diameter probability function. Constant temperature anemometry has provided two-phase flow measurements for more that 30 years; it exploits the large difference in heat transfer from the sensor to the liquid and gas to discriminate the signal between the two phases. For a sufficient long observation, the fraction of time the probe detects the gas can be interpreted as the local void fraction.

In order to discriminate the hot-film signal into the gas and liquid phases, the dynamic response of the anemometer output to the passage of a gas bubble across the sensor needs to be well understood. As the bubble front approaches the probe the signal output increases because the liquid in front of the bubble is moving with a greater velocity than the average liquid velocity (Figure 2.6). The signal continues to increase until the probe pierces the bubble (point A), and this is accompanied by a small overshoot. The signal then shows a steep drop due to the evaporation of the liquid film on the sensor surface. When the rear of the bubble arrives at the probe (point B), the rapid covering of the probe with the liquid results in a steep rise in the signal output, this is the result of the dynamic meniscus effect between the sensor and the liquid. This effect also produces an overshot that is marked in Figure 2.2 as point C. The region immediately following this point (up to point D) will also not represent a true continuous phase (Farrar et al., 1995).

Farrar and Bruun (1989) presented a complete description of the interaction between bubbles and hot-film probes. Following the above description, for a continuous phase evaluations the signal between A and D of each bubble must be eliminated. On the other hand, the two events, A and B, correspond to the bubble front and the back contacting the sensor, and need to be clearly identified to localize the bubble passage.

Several examples of bubble detection techniques can be found in the literature. In general most of the techniques are variants of one (or combinations or both) of two basic methods: the amplitude threshold method and the slope threshold method. In the amplitude threshold method the raw anemometer signal is compared with a threshold value. Any data points in the signal which lie below the voltage threshold are considered to belong to the gas phase, and those points which are above the threshold voltage are assumed to represent the continuous phase velocity. This method is easy to implement and it is very effective in detecting a large proportion of the bubble in the signal. However, some partial hits or very small bubbles may not be detected and more important, it does not identify any of the important points A, B, C or D. On the other hand, the slope threshold method uses the first derivative of the signal $\partial E/\partial t$ and it compares its value with one or more threshold levels. This method takes advantage of the fact that the arrival of the front and rear of the bubble is associated with a sign change in the time derivative of the signal. Similar criterion is used to detect the position of points C and D.

2.6.2 Bubble detection method

The analysis of the CTA output signal requires the separation of the two flow phases. In order to do so it is necessary to detect the bubbles by locating the points A, B, C and D of each individual bubble. The detection technique employed in this study is based on the methodology describe by Farrar et al. (1995). This methodology combines the amplitude and the slope threshold methods and it takes into account the possibility of water film breakage spike events. The amplitude threshold method is only used to detect the presence of a bubble according to a preset threshold value while the slope threshold method is used to determine the actual location of points A, B, C and D. The detection method initiates by locating the point where the signal goes below the amplitude threshold (Figure 2.7a), at this point it is considered that the sensor is in a bubble and a two stage search is initiated. In the first stage the procedure looks backwards on the signal and it compares the slope of the first derivative with a small negative slope threshold to determine the location of point A (Figure 2.7b). Once point A is located, the second stage looks forward for the point where the signal goes above the amplitude threshold. At this point two new subroutines look for points B and C by comparing again the first derivative of the signal with corresponding slope thresholds. Finally, a similar procedure is used to locate point D. A more detail description of the methodology can be found in Farrar et al. (1995).

2.6.3 Signal analysis

The CTA signal analysis initiates with the identification and consequent separation of the continuous and gas phases, this is carried out using the technique

described in the previous section. Once the phases have been separated relevant information can be obtained. In the continuous phase the signal output from the hot-film anemometers is related to the local fluid velocity by the heat transfer law. From there, the mean flow velocity (U), the normal stress (u^2) and turbulence intensity (Tu) can easily be evaluated. These values are given by

$$U = \frac{1}{n}\sum_{j=1}^{k} u_j \,, \tag{2.1}$$

$$u^2 = \frac{1}{n-1}\sum_{j=1}^{k}\left(u_j - U\right)^2 \,, \tag{2.2}$$

and

$$Tu = \frac{\sqrt{u^2}}{U} \,, \tag{2.3}$$

where u_j represent instantaneous water velocity values and k is the total number of points on the liquid phase. In the case of the gas phase, the local void fraction (α) is defined as

$$\alpha = \frac{\sum t_{AB}}{T} \,, \tag{2.4}$$

where t_{AB} is the time between points A and B (see Figure 2.6) and T is the total time of the signal record (including both continuous and gas phase). Furthermore, the bubble chord size is calculated as

$$s = U t_{AB} . \tag{2.5}$$

Equation (2.2) assumes that the probe pierces through the center of each bubble, which might not be always the case.
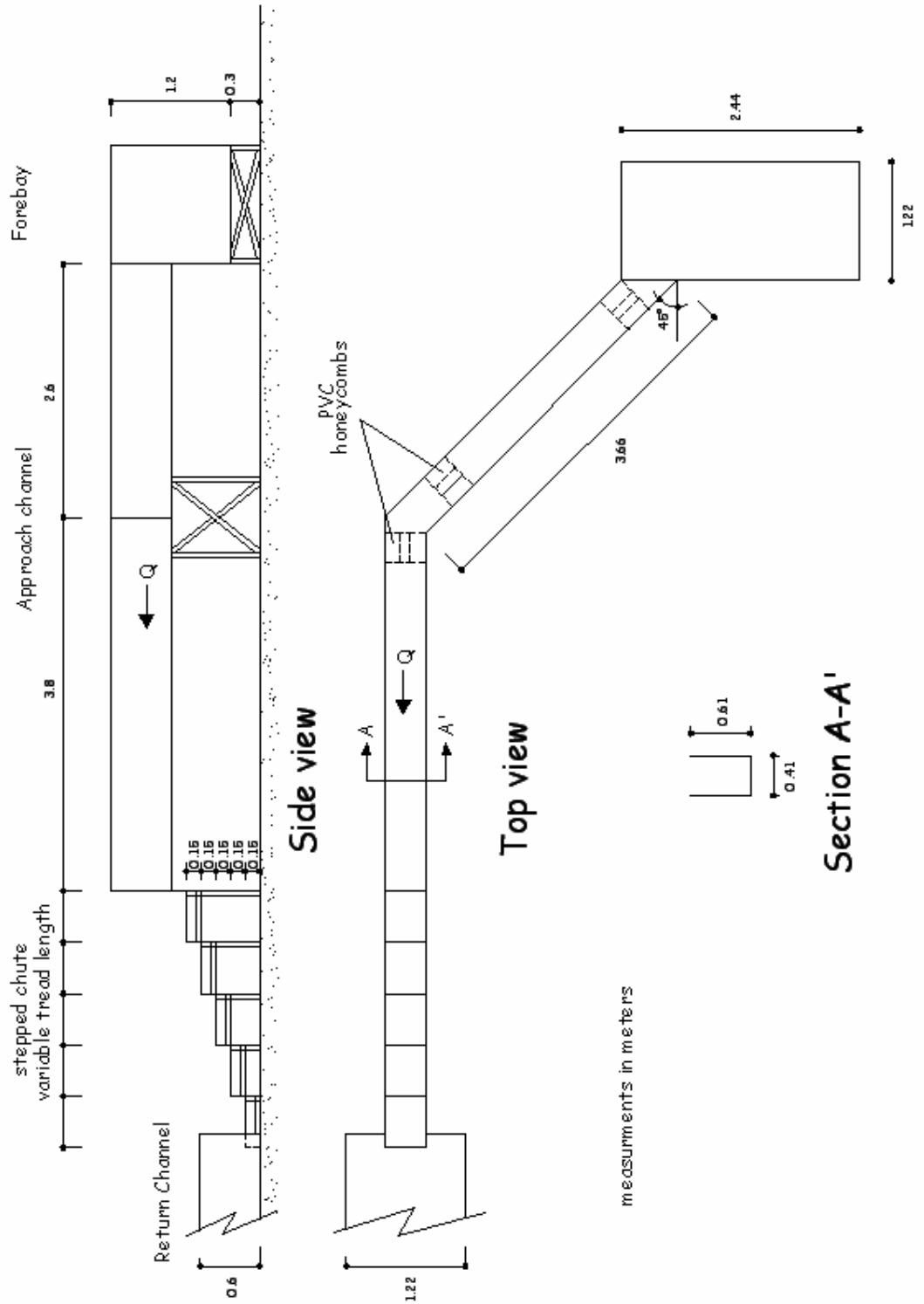
Figure 2.1 General layout of the models.
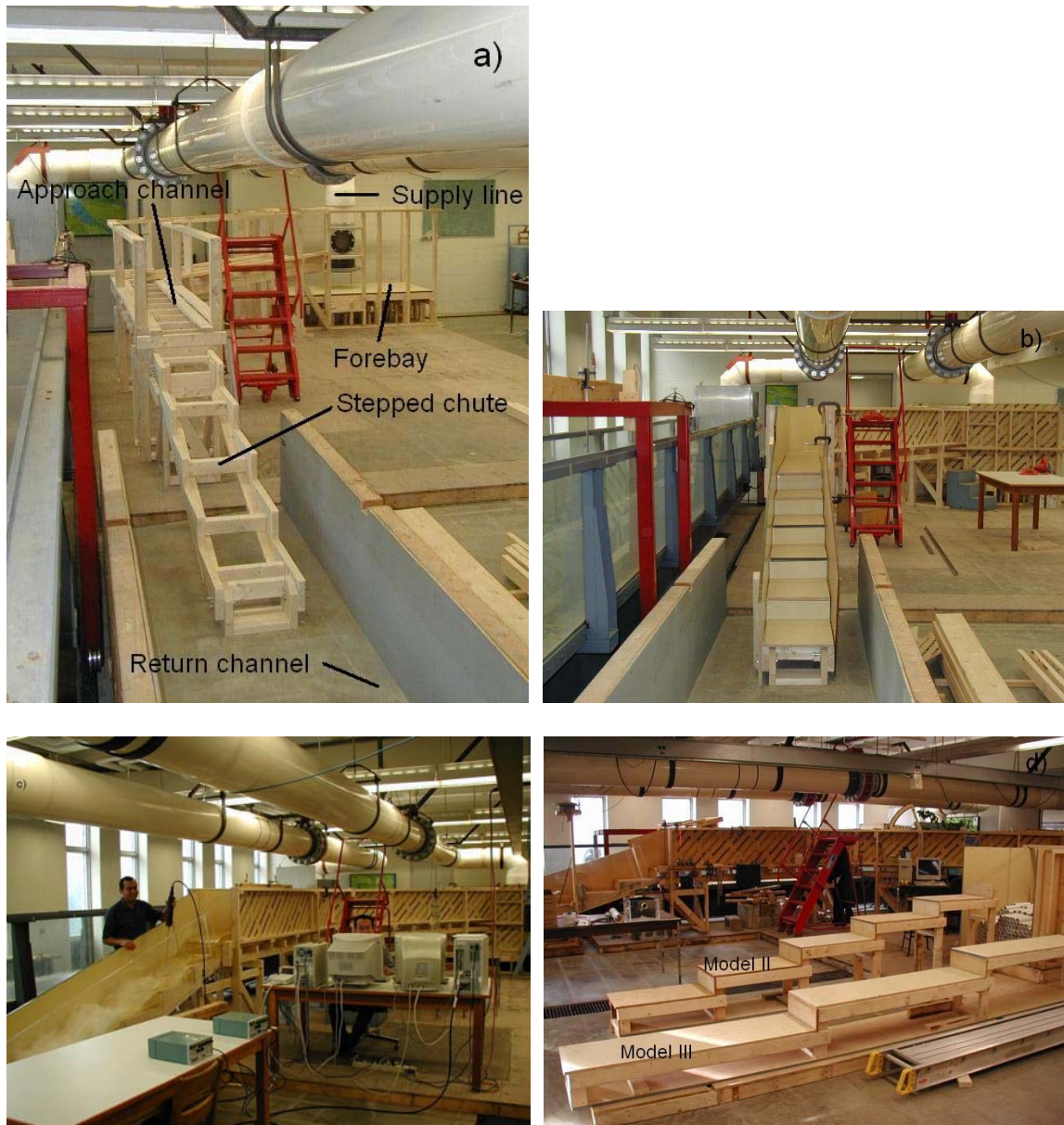
Figure 2.2 General overview of the models. a) Model I during construction. b) Final layout of Model I. c) Model I during initial tests. d) Overview of the three models.
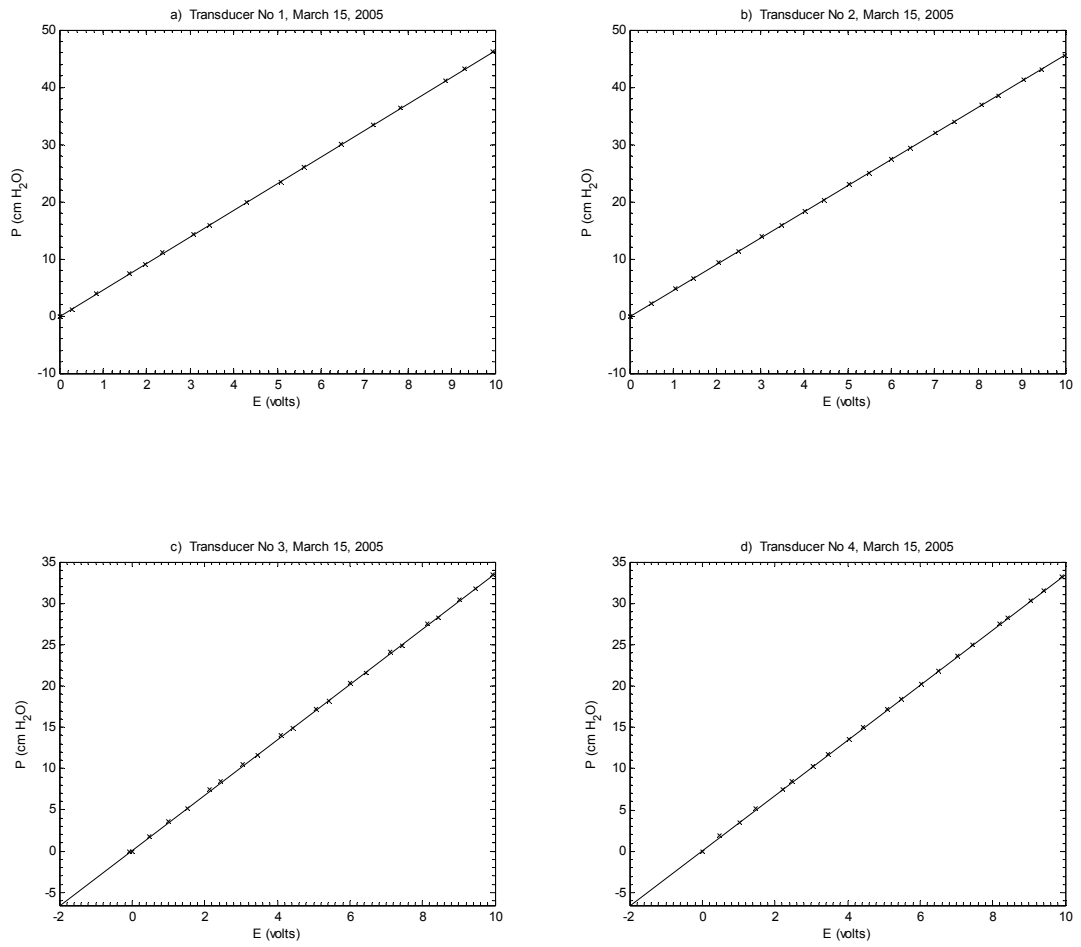
Figure 2.3 Linear response of the pressure transducers.

Calibration of March 15, 2005.
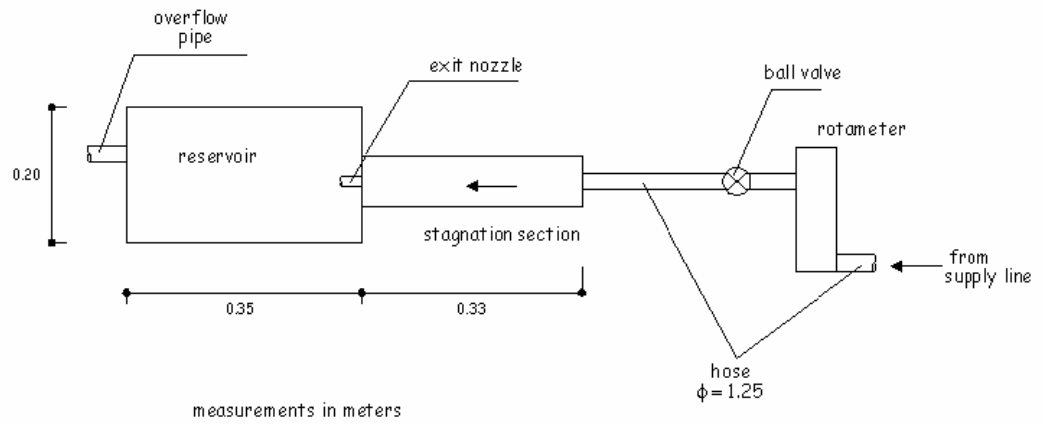
Figure 2.4 Schematic diagram of the water tunnel.
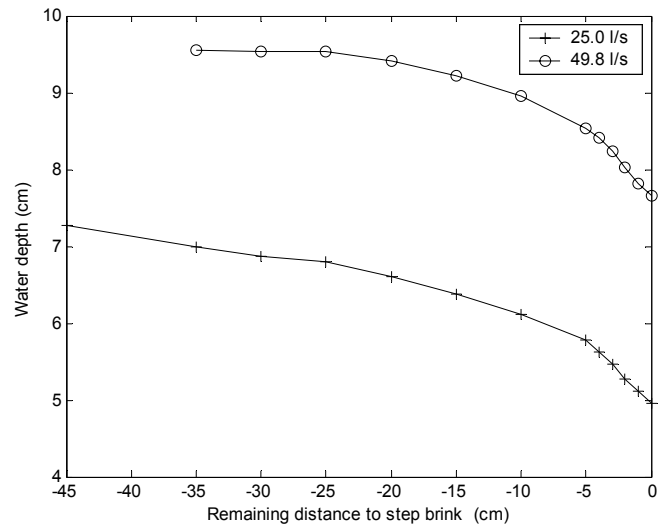
Figure 2.5 Measured H2 profiles on the approach channel.
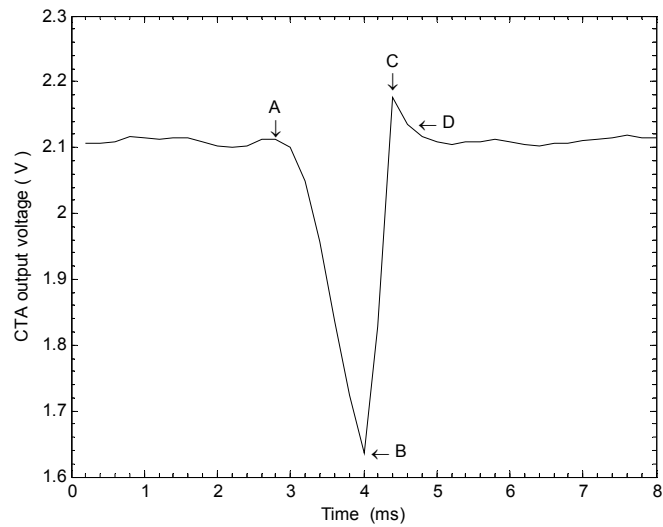
Figure 2.6 Schematic representation of a signal from a

hot-film probe immersed in a liquid bubbly with gas

bubbles.
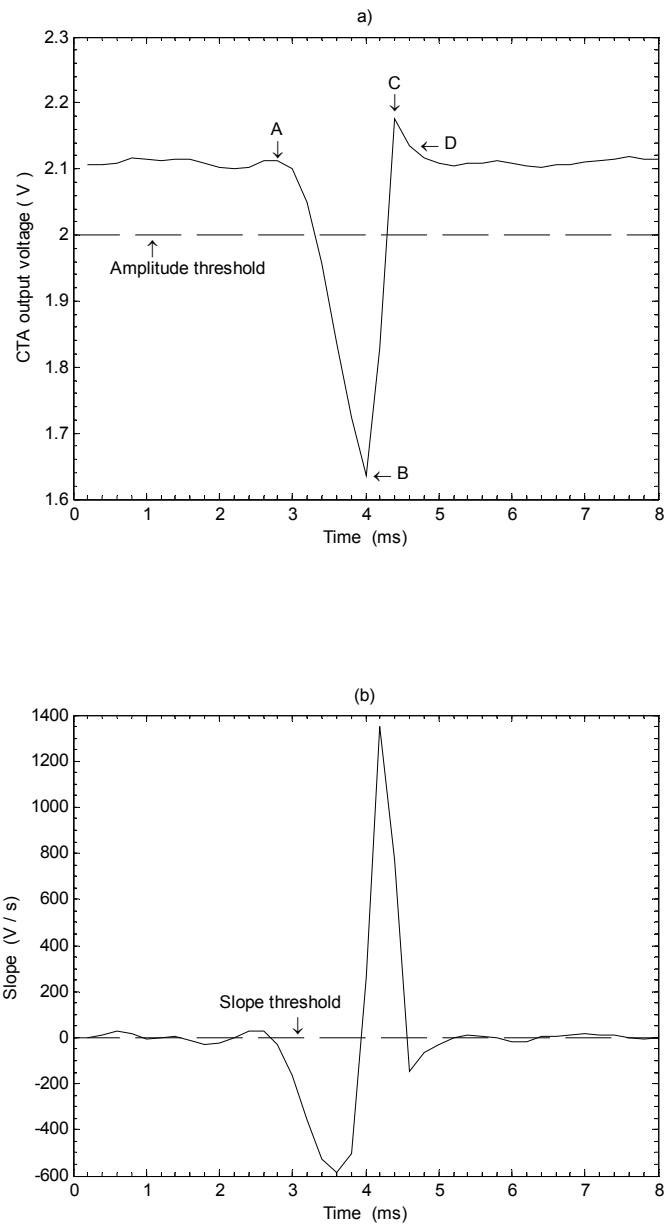
Figure 2.7 Schema of bubble detection method. a)

Amplitude threshold. b) slope threshold.

Chapter 3   *Constant temperature anemometry*

compensation

3.1 Introduction

The procedures to compensate a constant temperature anemometer are described in this chapter. Initially the two available procedures are introduced and later the development of the heat transfer law is given. Finally, the effects of natural convection are briefly discussed.

3.2 Temperature compensation

Temperature compensation is a procedure necessary when dealing with CTA measurements in non-isothermal flows. Two procedures can be employed to compensate for temperature drift: the constant sensor temperature and the constant overheat ratio procedure.

The two procedures differ significantly; the former requires several calibrations at different water temperatures and operating resistances as well as constant monitoring of the water temperature. The latter on the other hand, the constant overheat ratio procedure, requires fewer calibrations (usually at the beginning and the end of the experiment) but more frequent adjustments during the experimental runs.

3.3 Constant sensor temperature procedure

As the name suggests, in this procedure the temperature of the sensor is kept constant and the anemometer output voltages are corrected before any heat transfer law is sought. The sensor operating temperature (T_s) is kept constant by fixing the decade resistance at the time of setup, and it remains unaltered during calibration and data acquisition. In water flows, the expression of Morrow and Kline, cited by Stenhouse and Stoy (1974), can be used to correct CTA output voltages. Morrow and Kline's correction is given by

$$E_{ref} = \frac{T_S - T_{ref}}{T_S - T_A} E_A,$$
(3.1)

where E_{ref} and E_A are the anemometer output voltages at a reference temperature T_{ref} and water temperature T_A; Morrow and Kline used 22°C as the reference temperature. Stenhouse and Stoy (1974) found Equation (3.1) to be quite accurate for water temperatures ranging from 15°C to 28°C for the sensor temperature (44.5°C) that they used during their tests. However, in the 16 tests carried out using the constant sensor temperature procedure Equation (3.1) did not work adequately. In fact, a close inspection of Figure 3.1 suggests that the temperature correction should depend on the flow velocity

U since the calibration curves become closer to a logarithmic function as U decreases. Figure 3.2 presents the variation of the Nusselt number Nu with overheat ratio Θ expressed in terms of temperature as follows

$$\Theta = \frac{T_S - T_A}{T_{setup}},$$ (3.2)

where T_{setup} is the water temperature at the time that the CTA system was setup. To compute Nu, the physical properties of the water were evaluated at film temperature, i.e., the arithmetic average between T_S and T_A. Figure 3.2 indicates that for a given value of flow velocity, a linear relationship between Nu and Θ exists. A result that is supported by the fact that a linear relationship was also observed between the sensor cold resistance R_o and T_A (see Figure 3.3). Once the linear dependence of Nu with Θ was established, a heat transfer law or calibration curve for any other water temperature can be interpolated in order to transform the CTA output voltages. Figure 3.4 compares the results of using this approach with calibration test G13. As shown, values of flow velocity agree within reasonable limits. Furthermore, an analysis of the 'G' tests indicate that for a given CTA setup, calibration curves should be obtained within the expected water temperature range in order to allow proper interpolation. However, the same tests also suggest that if the water temperature varies more than $0.5°C$ from its value at the time of setup, the anemometer output signal deteriorates rapidly.

3.4 Constant overheat ratio procedure

In this procedure the overheat ratio is kept constant by manually or automatically adjusting the anemometer resistance (Lekakis, 1996; Jørgensen, 2002). In doing so, the

anemometer "sees" an isothermal flow since the excess temperature remains unaltered, i.e., the difference between sensor operating temperature T_S and the ambient (water) temperature T_A is unaltered. This procedure assumes that T_A remains nearly constant during each data acquisition. Figure 3.5 is a schematic representation of the manual adjustment of overheat ratio. Initially, the variation of the sensor cold resistance (R_o) with T_A should be determined, subsequently, the sensor operating resistance (R_S) is computed for the selected overheat ratio and the expected water temperature range. Next, T_A is measured and the value of the CTA decade resistance is adjusted to match the value of R_S at T_A and the selected overheat ratio. Finally, the anemometer output voltage is acquired.

As an example, Figure 3.6 presents two calibration curves of a conical hot-film probe obtained by manually adjusting the decade resistance of the CTA system. The difference between output voltages were smaller than 4% which speaks for the goodness of the procedure. Automatic overheat adjustment would minimize temperature effects even further.

3.4.1 Heat transfer law

To obtain the heat transfer law from curves like those in Figure 3.6 an analytical calibration function relating E and U for a single sensor is needed. This calibration function can take several forms. Wu and Bose (1993) suggested an extended power law of the form

$$E^2 = \sum_{j=0}^{k} A_j U^{jn} ,$$ (3.3)

where A_j and n are experimental constants. King's law is a specific case of Equation (3.3) corresponding to $k = 1$; the cases of $k = 2$ and $k = 3$ were also studied herein . It has also been suggested (Bruun et al., 1988) the following variation of the extended power law

$$E^2 = A_0 + A_1 U^n + A_2 U .$$ (3.4)

A third-order polynomial expression in terms of E^2 has also been used (Bruun et al., 1988; Lekakis, 1996) as well as a fourth-order polynomial in terms of E (Lekakis, 1996; Bruun, 1996; Jørgensen, 2002). Finally, Bruun et al. (1988) recommended the use of cubic spline interpolation to fit the CTA raw data. The suitability of these functions to accommodate the response of the conical hot-film probe was analyzed using Matlab™. Values of the experimental constants and polynomial coefficients were obtained by the least-squares fitting technique provided by Matlab™, the spline routine of this software was also used in the analysis. To compare the goodness of fit the sum of squared error was applied to the difference in flow velocite,i.e.,

$$\varepsilon = \sum_{j=1}^{N} \left(U_m - U_c \right)^2 ,$$ (3.5)

where U_m and U_c are the measured and calculated flow velocity, respectively, and N is the number of measured calibration values.

All the analytical functions, with the exception of $k = 3$ in Equation (3.3), followed the trend dictated by the cloud of (E, U) points. Nevertheless, the spline, the fourth order polynomial in terms of E, as well as the extended power law (Eq. (3.4))

produce the smallest cumulative error (see Table 3.1). In fact, the cubic spline interpolation produced a zero cumulative error, although this is not a surprising find since the technique uses the provided (E, U) values as knots. However, the spline interpolation presented small wiggles which do not correspond to the probe response and prevents a smooth fit through the velocity range. In addition, the spline interpolation did not represent well the probe response at velocities smaller than 0.15 m/s (see Figure 3.7). A similar problem was observed in the fourth order polynomial in terms of E, although it did produce a smooth response over the velocity range. The extended power law however, produced a good probe response while keeping a small error in the least-squares fitting procedure. The downside of Equation (3.4) is there is no obvious solution for U, however, using Newton-Raphson its value can be obtained as

$$U_{j+1} = U_j - \frac{A_0 + A_1 U^n + A_2 U - E^2}{n A_1 U^{n-1} + A_2},$$
(3.6)

which can be programmed in a few lines of code. Alternatively, a look-up table technique will solve this inconvenience.

Table 3.1 Sum of the squared error for the 12 tests.

Analytical function	Cumulative ε
$E^2 = A_0 + A_1 U^n$	0.482
$E^2 = A_0 + A_1 U^n + A_2 U^{2n}$	0.523
$E^2 = A_0 + A_1 U^n + A_2 U^{2n} + A_3 U^{3n}$	3309
$E^2 = A_0 + A_1 U^n + A_2 U$	0.158
$U = A_0 + A_1\left(E^2\right) + A_2\left(E^2\right)^2 + A_3\left(E^2\right)^3$	0.274
$U = A_0 + A_1 E + A_2 E^2 + A_3 E^3 + A_4 E^4$	0.150
Cubic spline interpolation	0

3.4.2 Sensitivity analysis

Since the overheat ratio was kept constant using a manual procedure, it was necessary to estimate the effect of a possible overcompensation or an undercompensation of the film probe. Figure 3.8 shows the effect of a unit variation of the decade resistance on a calibration curve. As the figure indicates an overcompensation produces larger voltages whilst an undercompensation produces smaller voltages for a given flow velocity. Hence, overcompensation would produce larger velocity flows with the possibility of extrapolation of the calibration curve whereas undercompensation would produce smaller velocities. Table 3.2 presents the error in output voltage as well as in flow velocity estimation due to an over or an under compensation. As the table shows,

both conditions produce significant error and therefore compensation is a critical issue when it is carried out manually.

Table 3.2 Variation of the CTA output voltage with a unit
change in decade resistance.

	Error in E		Error in U	
U	Minus one	Plus one	Minus one	Plus one
(m/s)	(%)	(%)	(%)	(%)
0	-4.3	3.0	0	0
0.19	-6.2	4.6	-49	132
0.59	-6.4	5.5	-62	69
0.94	-6.5	5.8	-53	89
2.42	-6.9	6.6	-49	90
3.9	-7.1	6.9	-50	-550
5.5	-7.5	7.0	-51	-609

3.5 Buoyancy effects

Buoyancy effects occur at low velocities when convection currents form because of the buoyancy of the heated fluid surrounding the sensor. Thus, the sensor losses heat by convection even in still air and this free convection flow tends to mask any low-velocity forced convection cooling. Collins and Williams (1959) concluded that buoyancy effects are small provided

$$R_E = Gr^{1/3}, \tag{3.7}$$

where R_E and Gr are the Reynolds and Grashof numbers, respectively. Dantec Dynamics (2003) indicates that natural convection overrules the forced convection when R_E is smaller than twice $Gr^{1/3}$, i.e., a safety factor of two in Equation (3.7). Figure 3.9 presents the case of a typical conical hot-film probe operated at a constant overheat ratio of 10% in a water flow. As shown in the figure, the probe would safely operate in the forced convection zone at water flow velocities as low as 0.5 cm/s. Dantec Dynamics (2005) indicates that conical probes have influence from natural convection up to approximately 0.1 m/s in air flows, no indication is given for water flows.

3.6 Final comments

It has been found that the three problems attributed to the use of CTA in water flows measurements can be overcome by an appropriate selection of the overheat ratio and a careful use of the proper temperature compensation technique.

Temperature drift may be compensated adequately by using the constant sensor temperature procedure as long as the water temperature variations are smaller than $0.5°C$. The compensation is performed by applying a temperature correction to the raw data. This correction not only depends on the overheat ratio but also on the flow velocity. In the present case, a linear correction in terms of the Nusselt number and the actual overheat ratio Θ was obtained for each fixed value of flow velocity. In addition, heat transfer laws for the expected water temperature range should be obtained for each CTA setup condition, i.e., for each fixed value of R_s.

On the other hand, compensation of temperature drift by means of the constant overheat ratio procedure produces good results and does not require numerous calibrations. Hence, in water flows this procedure should be preferred over the constant sensor temperature one. In the present study, manual compensation produced good results and minimized the effects of temperature change and, it is expected that a fully automatic process would produce even better results. From the analytical functions tested, the use of an extend power law in form of Equation (3.4) produced a good and smooth representation of the conical hot-film probe response. A fourth order polynomial in terms of E does produce satisfactory results although there is the risk of strong deviations in the lower range of flow velocities. Cubic spline interpolation also has this weakness with the additional presence of small wiggles. The use of a larger number of calibration points may enhance the performance of these two analytical functions.

Finally, probe contamination, can be easily overcome by performing frequent calibrations. In addition, the conical hot-film probe employed herein was used for more than 300 hours with no appreciable contamination effects, this is in spite of the fact that no special measurements were taken to prevent such effects; these results are encouraging when considering the use of the hot-film anemometry technique in experimental procedures where large water flows are involved. Furthermore, buoyancy effects are likely to occur only at extremely low velocities, which where not present in these data.
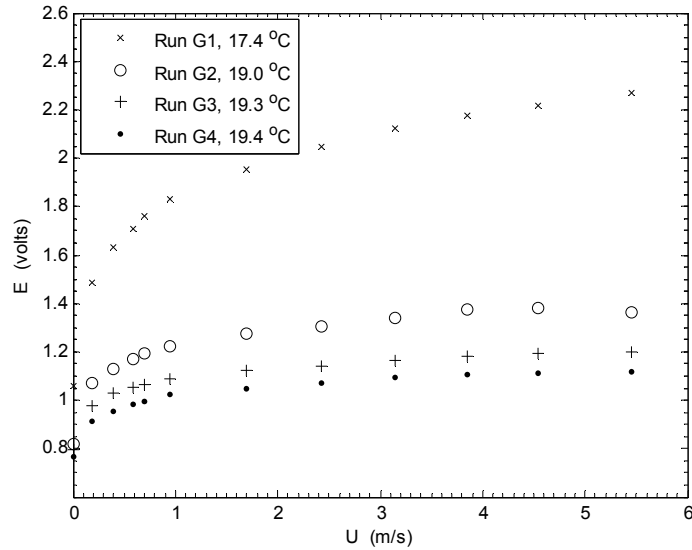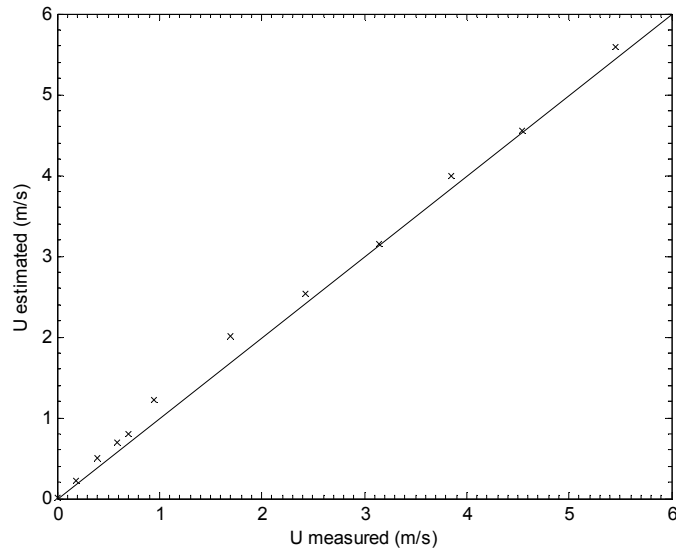
Figure 3.1 Calibration curves of a conical probe using the

constant sensor temperature procedure. Overheat

ratio $= 10\%$, $T_{setup} = 18.5°C$, $R_S = 15.53$ ohms.
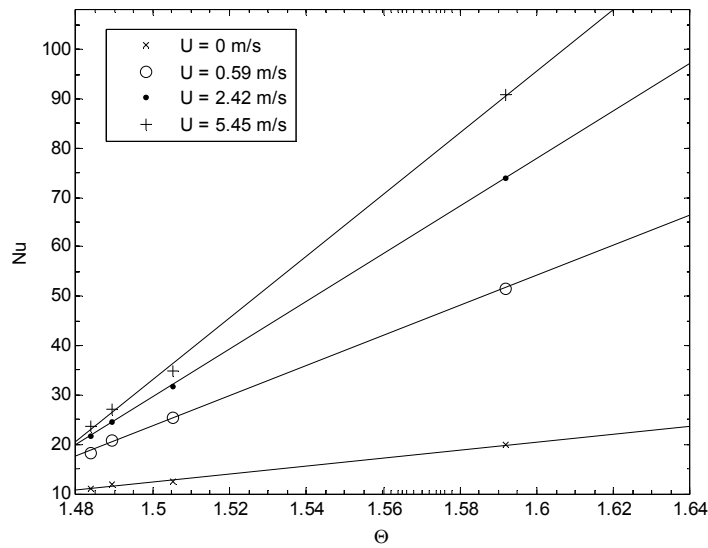
Figure 3.2 Variation of Nu with actual overheat ratio Θ.
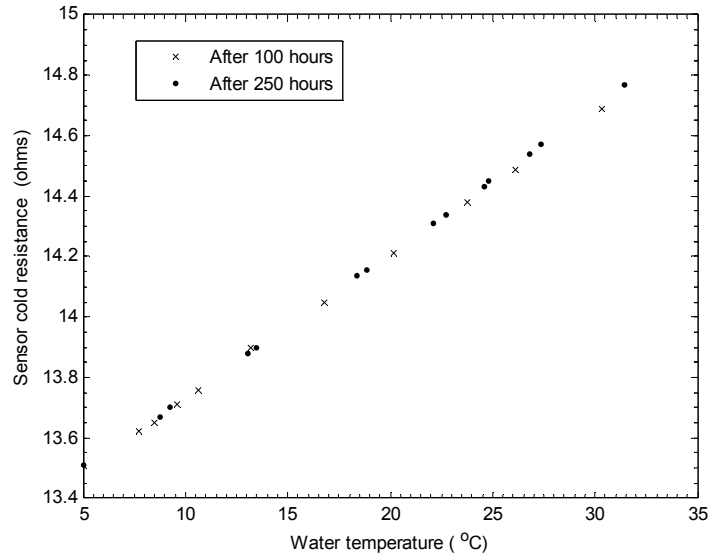
Figure 3.3 Variation of the conical probe cool resistance

with temperature.

Figure 3.4 Comparison of flow velocity, test G13.
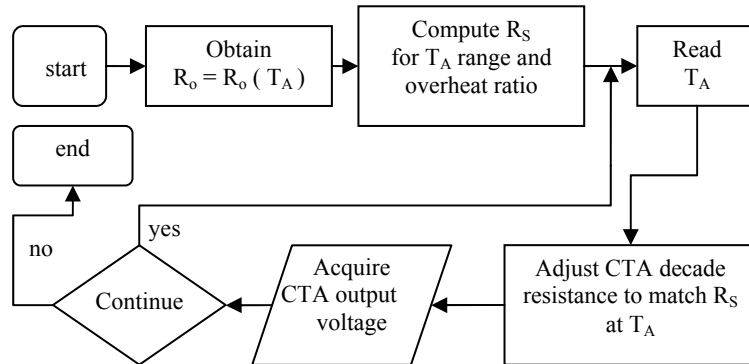
Figure 3.5 Schematic diagram of the manual adjustment of

the overheat ratio.
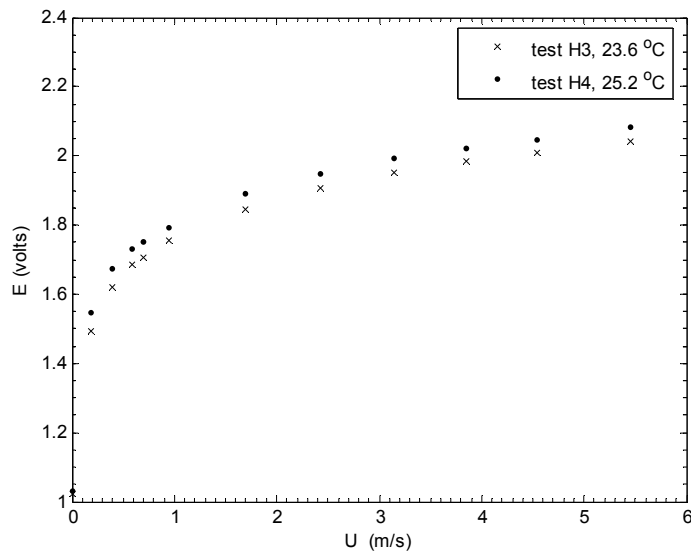
Figure 3.6 Example of test results using the constant

overheat ratio technique.
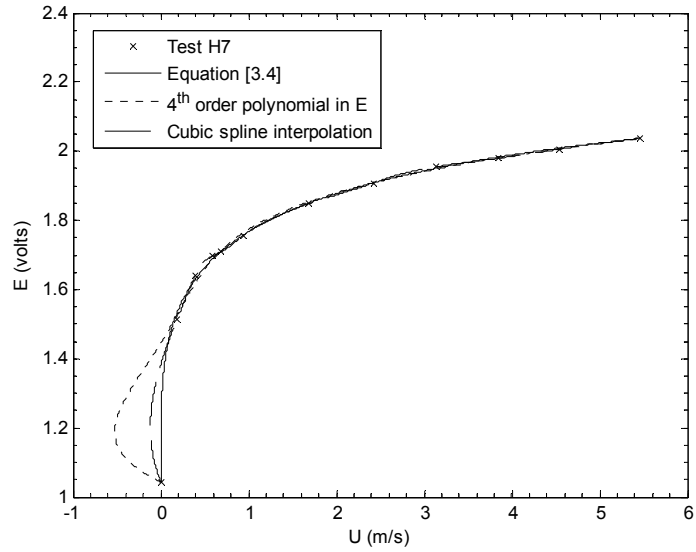
Figure 3.7 Fitting results of analytical functions, test H7.
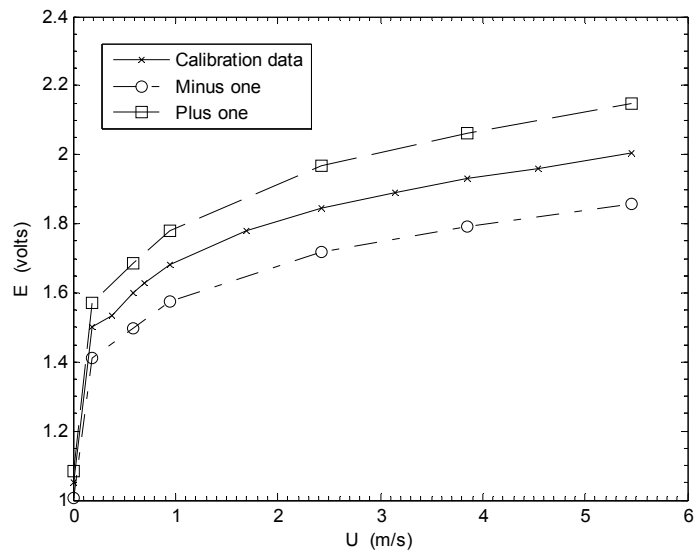
Figure 3.8 Variation of the CTA output with changes in

decade resistance.
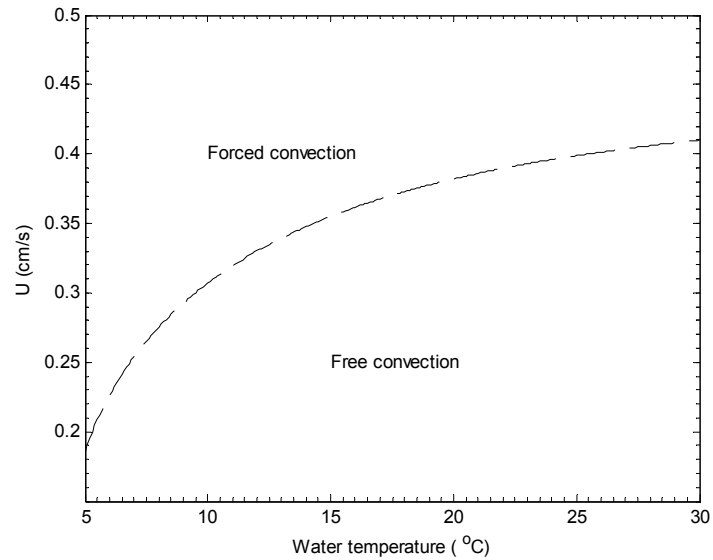
Figure 3.9 Region of forced and free convection flow for a

typical conical hot-film probe operated with the

constant overheat ratio technique. Overheat ratio

set at 10%.

_____

Chapter 4   *Velocity and local void fraction*

observations

_____

4.1 Introduction

This chapter presents the results obtained with the constant temperature anemometer. Initially, it discusses the procedure to separate the gas and liquid phases as well as the manipulation of the CTA raw data. Later on, the experimental conditions are described, flow descriptions are given, and velocity observations are presented. Finally, local void fraction and chord length are discussed.

4.2 Phase detection

As explained in §2.6 the phase detection technique employed in this study is based on the methodology described by Farrar et al. (1995). This methodology combines the amplitude and the slope threshold methods to distinguish between the gas and continuous phases. The key element of this methodology is the proper selection of the threshold value for the amplitude and the slope.

_____

Delhaye (1968) pointed out that the probability density function corresponding to a very large sample of hot-film data have a bimodal shape (See Figure 4.1a), consisting of two peaks separated by a lower level plateau region. In a bubbly two-phase flow the modal peak at large voltages corresponds to the fluctuations associated with the continuous phase turbulence whilst the other modal peak reflects the bubble passage, this is located on the range of low voltage values of the hot-film signal.

Several approaches were attempted to separate the two phases. Initially, the hot-film signal was considered a mixture of two normal distributions, one for each phase. Under this assumption a maximum likelihood estimation algorithm (Agna and Ibrahim, 1984) was employed to determine the statistical parameters (mean and standard deviation) of the two individual distributions. Using these parameters, the amplitude threshold value was selected from the voltage/velocity Gaussian distribution as the value with probability of occurrence of 5%. However, inspection of the sample histogram indicated that the voltage/velocity sub-sample tends to be negatively skew and therefore the sub-sample mean value was smaller than the mode value. Hence, the computed threshold value was often too small and inside the gas phase, especially if the spread of the continuous phase was large. As a consequence of this small threshold value the parameters of both phases were computed incorrectly.

Another approach consisted in dividing the anemometer signal into two sub-samples using the average between the two extreme values of the signal record. Then, the continuous phase sub-sample was checked for normality using Lilliefors' test (Lilliefors, 1967) and, if the Gaussian distribution was confirmed, the standard deviation was calculated, otherwise, the standard deviation was assumed to be equal to the

interquartile range (IQR). Finally, using these two parameters the threshold value was selected as the mode minus twice the standard deviation. This would correspond approximately to a probability of 5% in a normal distribution. This procedure corrected the location since it explicitly uses the mode but once again, the obtained threshold values were small due to the large spread of some samples. So, a new approach was sought.

The new approach consisted of taking a sub-sample of the signal values larger than a prefix voltage in the plateau region of probability density function. Then, the mode of the sub-sample was obtained and the empirical cumulative density function between the minimum value and the mode was calculated. Finally the autocorrelation values of the empirical cumulative density function were calculated and the threshold value was selected at the point were the autocorrelation was zero (see Figure 4.1b). The selection of this point is based on the idea that if the CTA output voltage is in the plateau region the relative frequency of each bin shown in Figure 4.1a is similar, hence, the increments of the empirical cumulative density function are nearly constant and so the autocorrelation is close to one. As the voltage gets into the continuous phase, the relative frequencies become larger and the increments on the cumulative density function do so as well; at this moment the autocorrelation begins to decrease and it goes to zero where the increment given by the relative frequency is completely dissimilar (or independent) from the previous one.

The above approaches were also used to select the threshold value for the slope method. Nevertheless, close inspection of the time series of CTA output voltages (Fig. 4.2a) and its corresponding slope plots (Fig. 4.2b) suggested that the proper selection of

the bubble characteristic points were obtained by setting the threshold value at zero, i.e., when the slope signal changes its sign.

4.3 Voltage correction

The possibility of inducing errors by overcompensation or under-compensation was introduced in §3.4. Therefore, it was necessary to develop a procedure to correct this issue; this was done using the information of the sensitivity analysis presented in the previous chapter. Figure 4.3a presents the relationships between the corrected CTA output voltages and an overcompensated or undercompensated signal. The relationships are linear, which simplified greatly the analysis. Figure 4.3b presents of am example of a velocity profile with an error induced by overcompensation. As seen in the figure, the top 3 points show a step in velocity and are clearly different from the trend. Inspection of the water temperature and CTA decade resistance records indicated that different settings were used for these three points than for the previous eight, i.e., at point 9th the decade resistance was manually readjusted. Using the linear relationships from Figure 4.3a, the raw voltage values of the time series for these three points were corrected and the correct velocity profile was obtained. This procedure was followed in all cases that present an error by over/under compensation.

4.4 Experimental conditions

As mentioned in §2.3 a constant temperature anemometer equipped with a conical hot-film probe was used to record the flow velocities. Data acquisition was carried out at

a frequency of 5000 Hz for 180 second duration. The precision of the data acquisition card was set to ±1.22 mV and the water temperature was collected manually using a digital platinum resistance thermometer (Guildline, model 9540) with a resolution of $0.01°C$. Measurements were obtained in the width centerline and vertical positioning was manually controlled using a point gauge with a precision of ±0.02 cm.

Measurements on Model I $(3.5H:1V)$ were carried out using the constant sensor temperature procedure discussed in §3.3. This procedure is quite sensitive to water temperature fluctuations and unfortunately, temperature drift compromised the quality of the time series. Hence, it was decided not to include the CTA data of Model I in this study. On the other hand, measurements on Models II and III ($5H:1V$ and $10H:1V$, respectively) were taken using the constant overheat ratio procedure presented in §3.4.

4.5 Flow description

The flow conditions on the models varied greatly. The effect of providing air into the step cavity only had effects on nappe flow regime and they were limited to the first step. Figure 4.4 and 4.5 shows the first two steps of Models II and III, respectively. As seen in these figures provision of air on the first step did have an effect on the flow geometry. If air was provided into the step cavity the formation of the air pocket was possible (Figures 4.4a and 4.5a) and the flow resembled a drop structure. Nevertheless if air was not provided, the jet was depleted towards the step riser (see Figures 4.4b and 4.5b), there was no air pocket and the jet struck at a stepper angle. In either case however, no flow disturbance was observed downstream of the jet impact and clear water prevailed along the step. On the contrary, whether air was provided or not into the step cavity of the

second step did not produced appreciable difference on the flow geometry (see Figures 4.4c-d and 4.5c-d). Furthermore, air was observed in the jet and inside the recirculating pool while significant flow disturbance was observed at the jet impact. It is also worth mentioning that supercritical flow was always observed along the steps during all the tests carried out.

On nappe flow regime the flow characteristics change in downstream direction. As mentioned before, the geometry on the first step depends on whether air was provided or not into the step cavity. On Models II and III the jet remain supercritical along this step and no air was observed in the main stream although small bubbles were observed at the interface between the jet and the air pocket (see Figures 4.6a and 4.7a). On the second step, the air pocket was always observed suggesting that the jet was sufficiently broken at this drop to allow air into the cavity. The recirculating pools still resembled the one from a drop structure. At the jet impact, there was considerable turbulence as well as air entrainment (Figures 4.6b and 4.7b). From this point onwards Models II and III behaved differently. On Model II, the flow adopted a white water condition due to the presence of air and flow disturbances were carried in downstream direction; the proximity of next drop did not give enough length to the jet to reorganize and become once again a coherent jet. Hence, the jet became more turbulent as the flow moved in downstream direction. On the contrary, on Model III the length of the step tread provides sufficient space for the flow to dissipate the disturbances, release the air bubbles and act as a single jet once again at the next drop. The third step on model II was characterized by a complete two phase flow situation and disintegration of the jet (Figure 4.6c). The recirculating pool was shallow and elongate with significant oscillation of the water

surface. On Model III, more air entrainment and turbulence was observed at the jet impact than at the previous step (Figure 4.7c), the subsequent turbulence dissipation and air release took also longer than at step 2. Nevertheless close to the brink, the flow showed some bubbles but the flow was generally calm. As in the case of Model II, the recirculating pool was shallow and elongate when compared to the drop structure. Finally, at step 4 the flow on model II was more chaotic than in the previous step with a jet completely disintegrated in a two phase flow situation (Figure 4.6d). In Model III, the flow is similar than in the previous step but more air bubbles were observed close to the brink (Figure 4.7d).

Figure 4.8 and 4.9 show the transition flow regime. Model II (Figure 4.8) presented a clear water flow on step 1 with the water surface in phase with the step geometry. Nevertheless, the water surface had little oscillations; the step cavity was full of water with no air bubbles and a vortex formed inside it. On step 2 the jet began to entrain air, bubbles were observed inside the recirculating pool and along the jet. Within the recirculating pool, the bubbles concentrated towards the jet. Downstream of the jet impact the jet began to break and significant amount of splash developed. Notably, this regime presented significant amount of spray; drops were detected to reach 4 to $5h$ above the chute invert on average, although, some drops were observed at 7 to $8h$. On step 3 significant amount of air was observed as well as a small air pocket. The flow was a mixture of air and water and the jet was completely broken. At step 4, the air pocket was bigger with large oscillations on the water surface of the recirculating pool. On Model III (Figure 4.9), the first step also had clear water with no air cavity or air bubbles. As in Model II, little oscillations on the water surface were also observed but the water

surface remained in phase with the step geometry. On step 2, the jet began to disintegrate after hitting the tread and most of the air entrainment occurred at this point. The step cavity was full of water although a small air pocket randomly formed. Figure 4.10 depicts the formation of air pocket. Initially, the step cavity had little bubbles along the boundary between the jet and the recirculating pool (Figure 4.10a). The subsequent photos (Figures 4.10b-c) show the entrainment of air at this boundary which will eventually produce a small air pocket (not shown) and then, the air was carried away (Figures 4.10d-e) leaving the step cavity in a clear water conditions. Downstream of the jet impact the water surface was irregular and the flow carried pocket of bubble, probably released from the step cavity. Moreover, step 3 also presented the random formation of the air cavity, the flow carried significant amount of air and the jet was clearly broken and marked by considerable deformation of the water surface. At the step 4, there was a permanent air cavity, the flow was a air-water mixture and highly fragmentated.

The skimming flow regime on model II presented a water surface in phase with the step geometry, clear water flow and step cavities completely filled with water (see Figure 4.11). On the third step some bubbles were observed inside the recirculating pool while at step 4 bubbles were also observed in the jet. Small oscillations of the water surface were also observed in steps 3 and 4, which gave a white water appearance when looking from the top. Vortices were presented inside the step cavities. Model III also presented a clear water flow in phase with the chute geometry in the first two steps (Figure 4.12). Beyond this step surface oscillation became important and a three dimensional feature began to develop. This feature corresponded to shock waves which can be observed in Figure 4.13. Model II did also present such feature but the breaking

process of the jet masked these waves and prevented its development. As the flow progressed downstream on Model III, the shock waves became bigger and they brought air into the upper part of the flow as seen in Figures 4.12c and 4.12d. Furthermore, inside the step cavity of steps 3 and 4, that is, the steps affected by shock waves, a three-dimensional ascendant spiral flow was observed in the zone close to the step riser. This flow was directed towards the step riser on the bottom part and then towards the sides of the chute with an upward direction that gave the spiral movement. The formation of these spiral vortices is probably due to the action of the shock waves.

4.6 Velocity observations

Measured velocity profiles at the step brinks are presented in Figures 4.14 to 4.19. Appendices B and C give profiles at other locations for Models II and III, respectively. Profiles of velocity gradient, turbulence intensity and normal stress are also given in those appendices. For these profiles the water depth (y) was measured with respect to the step tread and y_T is the total water depth. The velocity is represented by U, and U_{avg} corresponds to the depth flow average velocity.

Figures 4.14 and 4.15 present the nappe flow velocity profiles on Models II and III, respectively. As the figures show, there is no appreciable difference between the aerated and non-aerated condition. The profiles on step 1 present a logarithmic distribution as in open channel flow, which progressively disappears as the water moves downstream, especially at large discharges as in Figure 4.15. Between models, the

velocity profiles at the brinks are similar (Figure 4.16 and 4.17) before the jets break up, once this occurs, there is no defined velocity distribution as the flow losses its coherence.

Figures 4.18 and 4.19 present the velocity profiles for transition and skimming flow. There is general agreement between models and the profile follow a logarithmic distribution on those steps with clear water.

4.7 Local void fraction observations

It is well known that air bubbles not only modify the flow characteristics but also the downstream water quality. Specifically, high levels of turbulence and large air-water interface area enhance the transfer of atmospheric and volatile gases between air and water. Knowledge about the variables involve in this transfer mechanism is indispensable in the design of water treatment systems and preservation of aquatic habitat, since it is often observed saturation of dissolved oxygen and nitrogen downstream of hydraulic structures carrying air-water flows. In this regard, turbulence levels were already presented in the previous section while quantification of the interface area requires the knowledge of three basic parameters: local void fraction, bubble count rate and bubble chord length.

Local void fractions at the step brinks are presented in Figures 4.20 to 4.25. Several other locations are given in Appendices B and C. According to the observations, specifically, the local void fraction is not affected by the conditions of the step cavity, Figures 4.20 and 4.21 indicated that similar results were recorded for an aerated and non-aerated step cavity. Furthermore, similar results were also obtained between models. The air concentration seems to have a "C" shape, that is, larger values were observed at

the bottom and top while minimum values in the middle of the water column. The observations also indicate that air concentration in the development flow region remains below 0.6.

The chord length of a bubble is the length of the straight line connecting the two points where the tip of the conical probe pierces the bubble whilst bubble count rate is the number of bubble impacting the probe tip. Chord length distributions as well as bubble count rates are shown in Appendices B and C. The results indicate that within a step, larger chord lengths are obtained along the step tread than at the brink, specifically, immediately after the sliding jet hits the step tread. Furthermore, the trend of the chord length is to increase in downstream direction (from brink to brink) and results indicated that it stays smaller than about 12 mm. At the step brink, larger chord sizes were recorded on Model II than on Model III, likely due to the fact that the tread on the former is halve the size of the latter giving time for large bubbles to reach the surface.
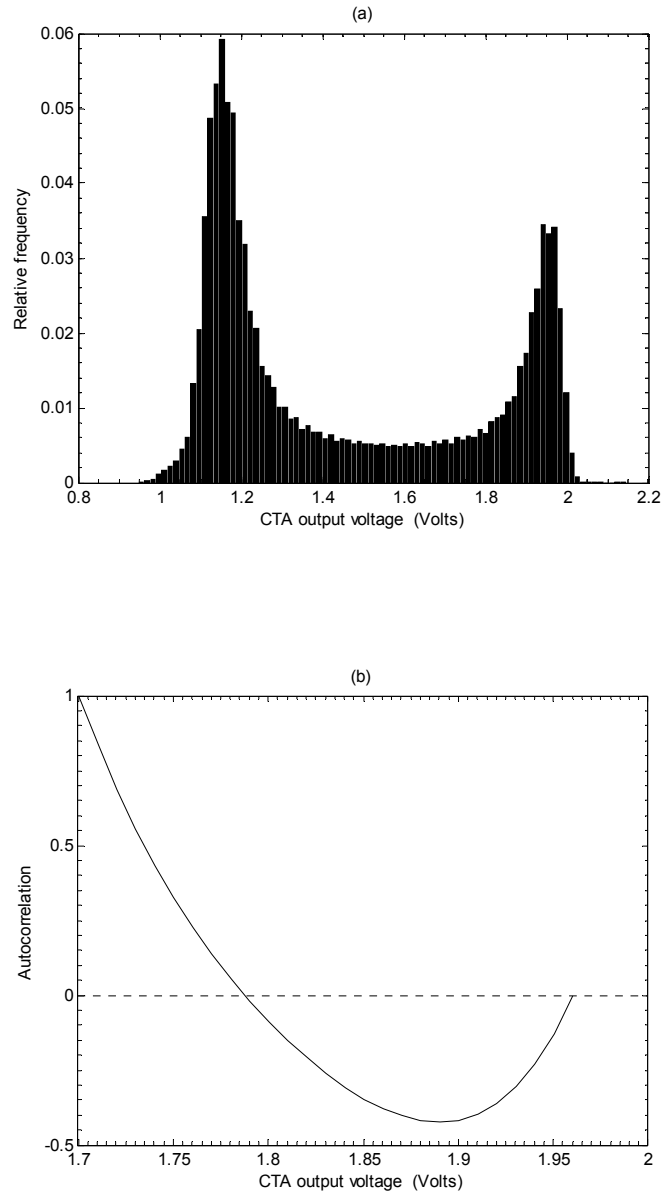
Figure 4.1 Selection of voltage threshold. a) histogram of

CTA output voltage b) autocorrelation plot.
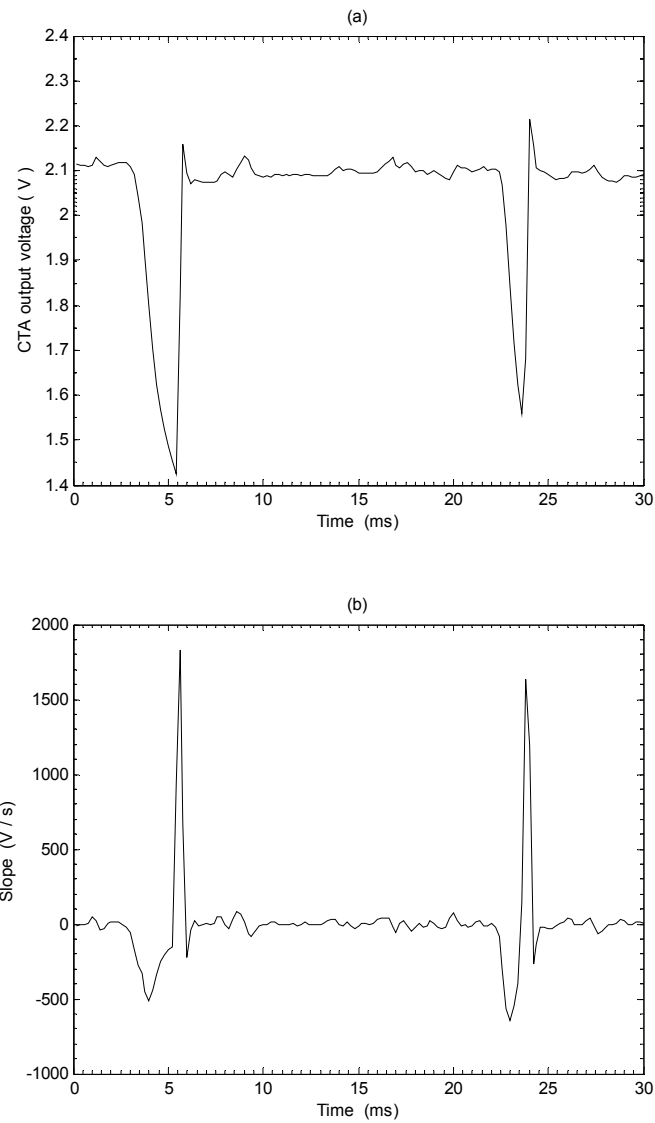
Figure 4.2 Selection of slope threshold. a) typical time

series of CTA output voltage b) slope of the CTA

output signal.
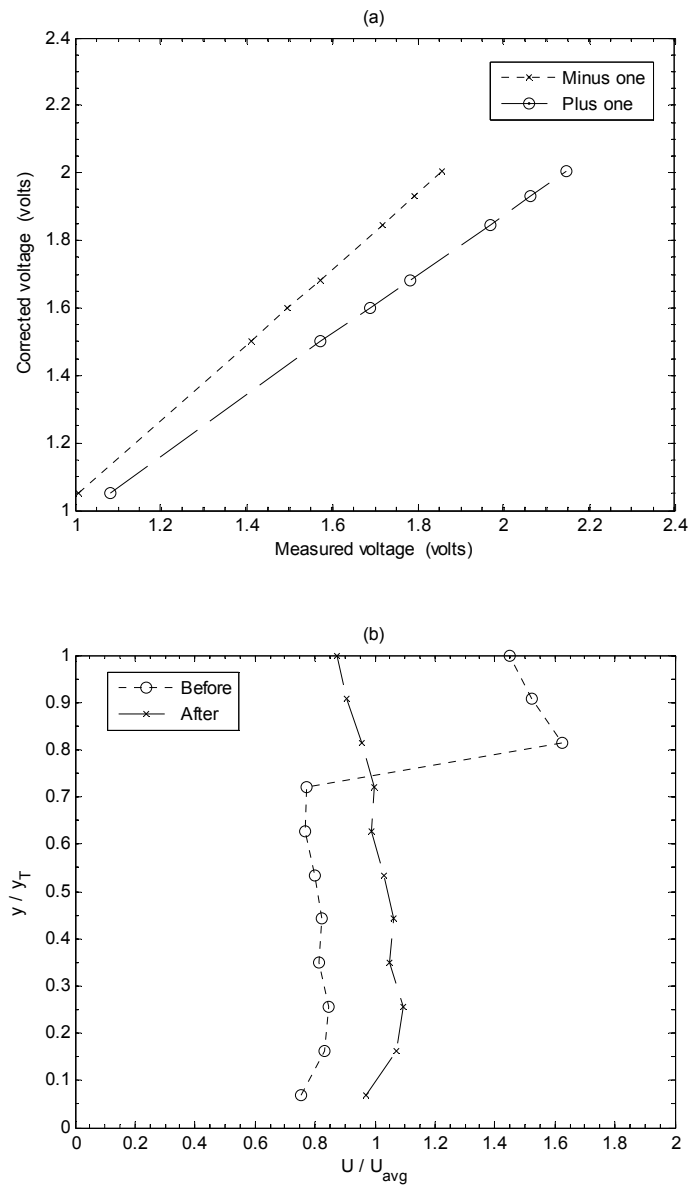
Figure 4.3 Correction of voltages. a) relationship between

corrected voltage and under-compensated (minus

one) and over-compensate signal (plus one) b)

velocity profile before and after correction.

a)

b)

c)

d)
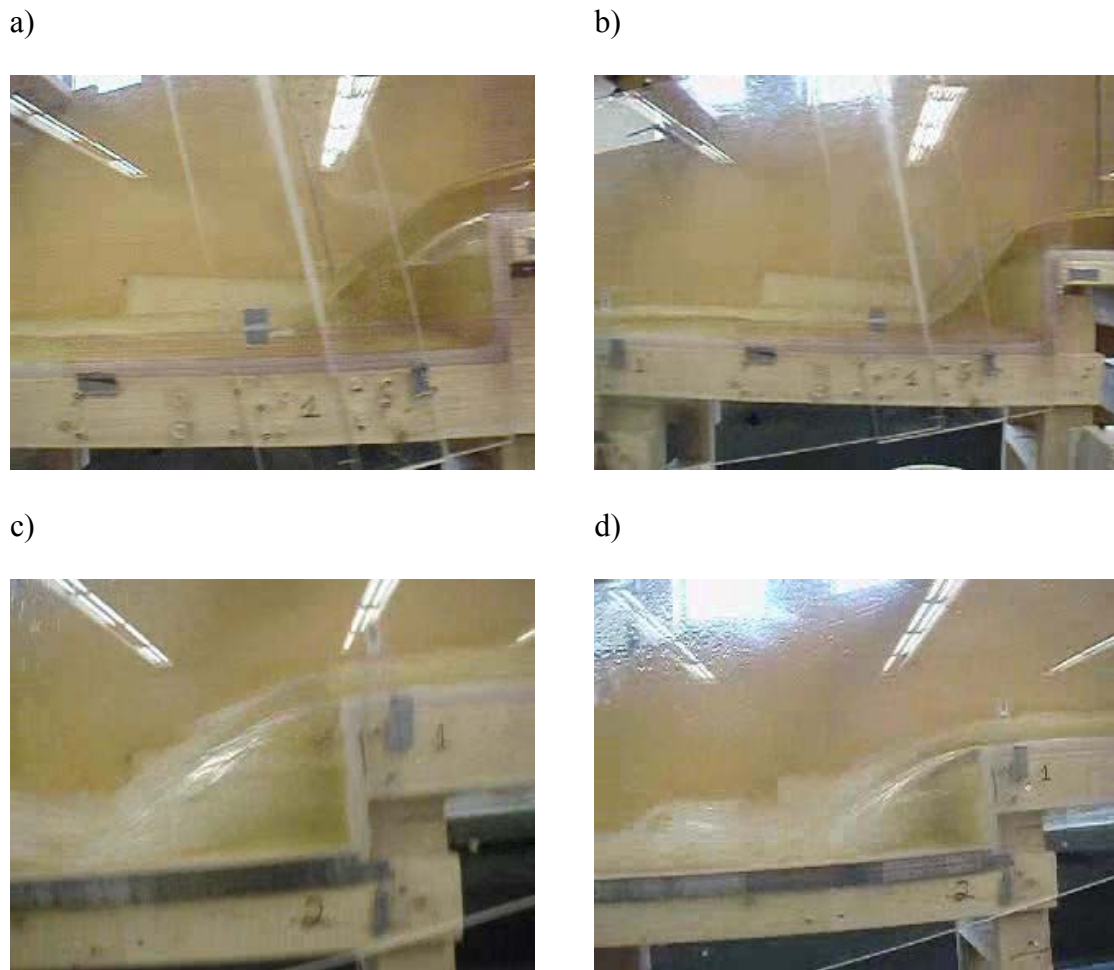
Figure 4.4 Step cavity conditions on Model II. a) step 1,

aerated. b) step 1, non-aerated. c) step 2, aerated. d)

step 2, non-aerated.

a)

b)

c)

d)
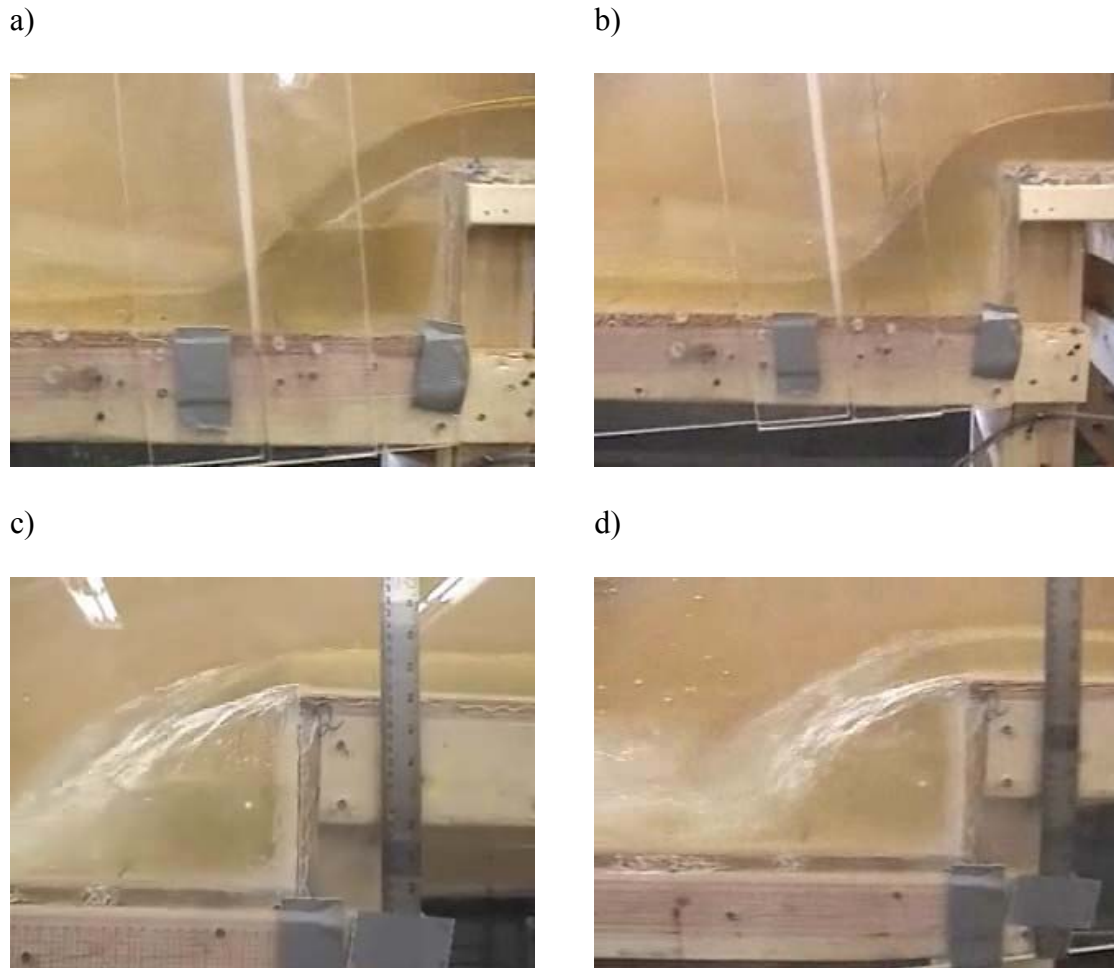
Figure 4.5 Step cavity conditions on Model III. a) step 1, aerated. b) step 1, non-aerated. c) step 2, aerated. d) step 2, non-aerated.

a)

b)

c)

d)
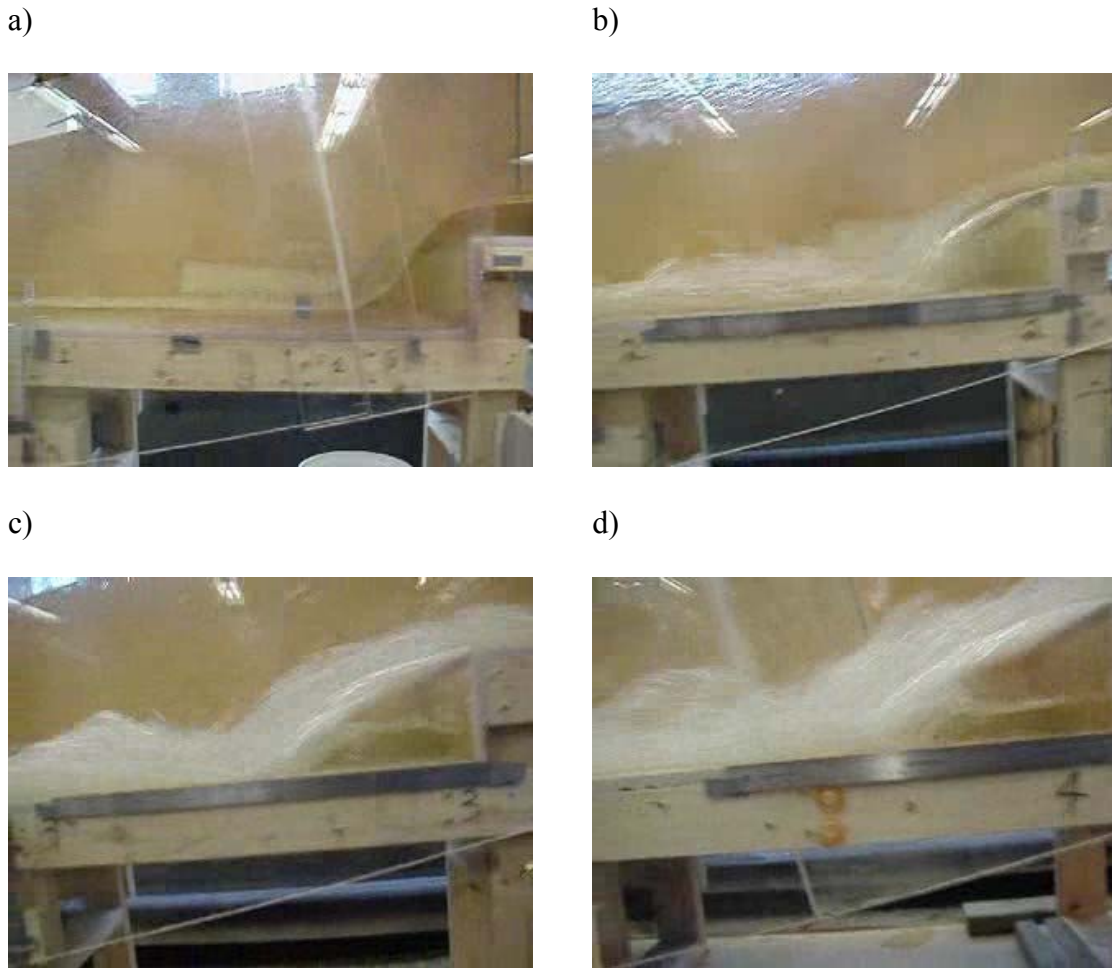
Figure 4.6 Nappe flow regime on Model II. Non-aerated step cavity, $y_c/h = 0.51$. a) step 1. b) step 2. c) step 3. d) step 4.
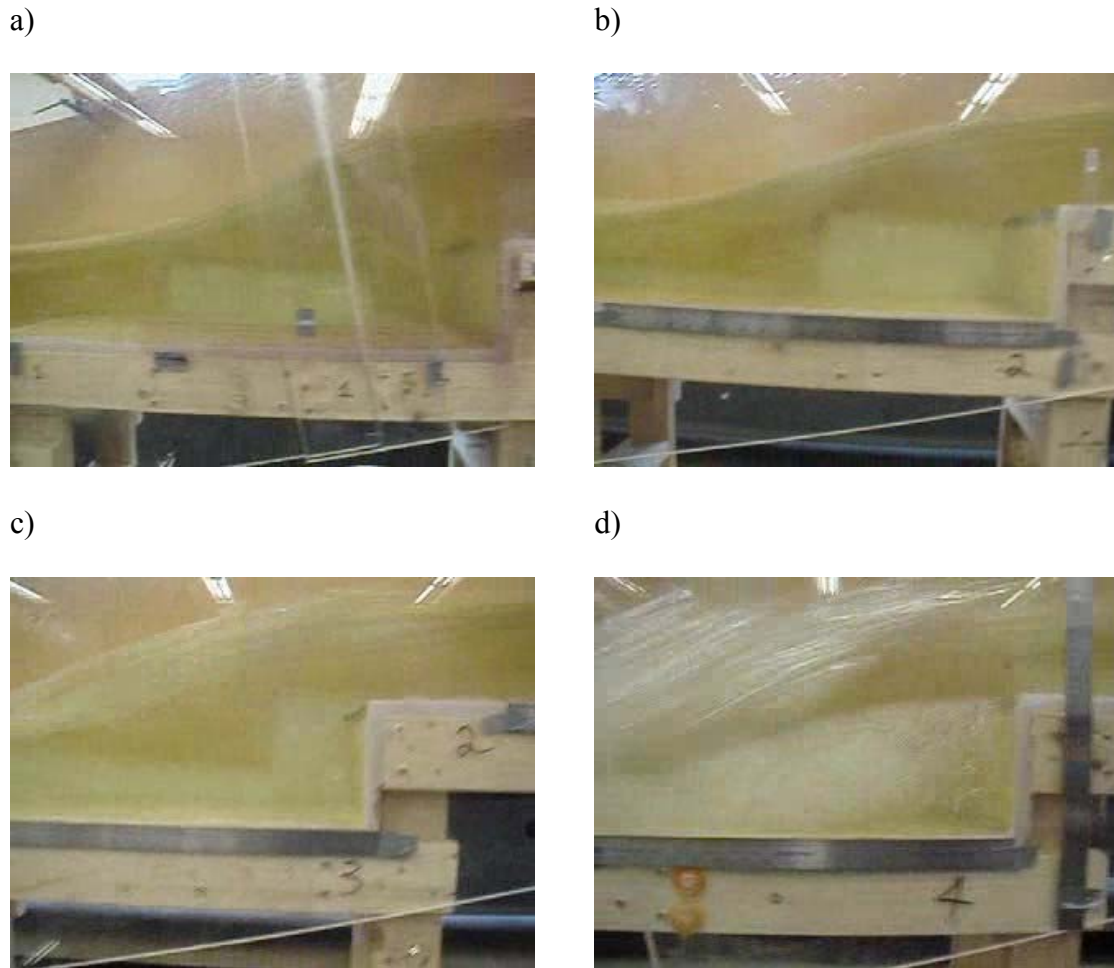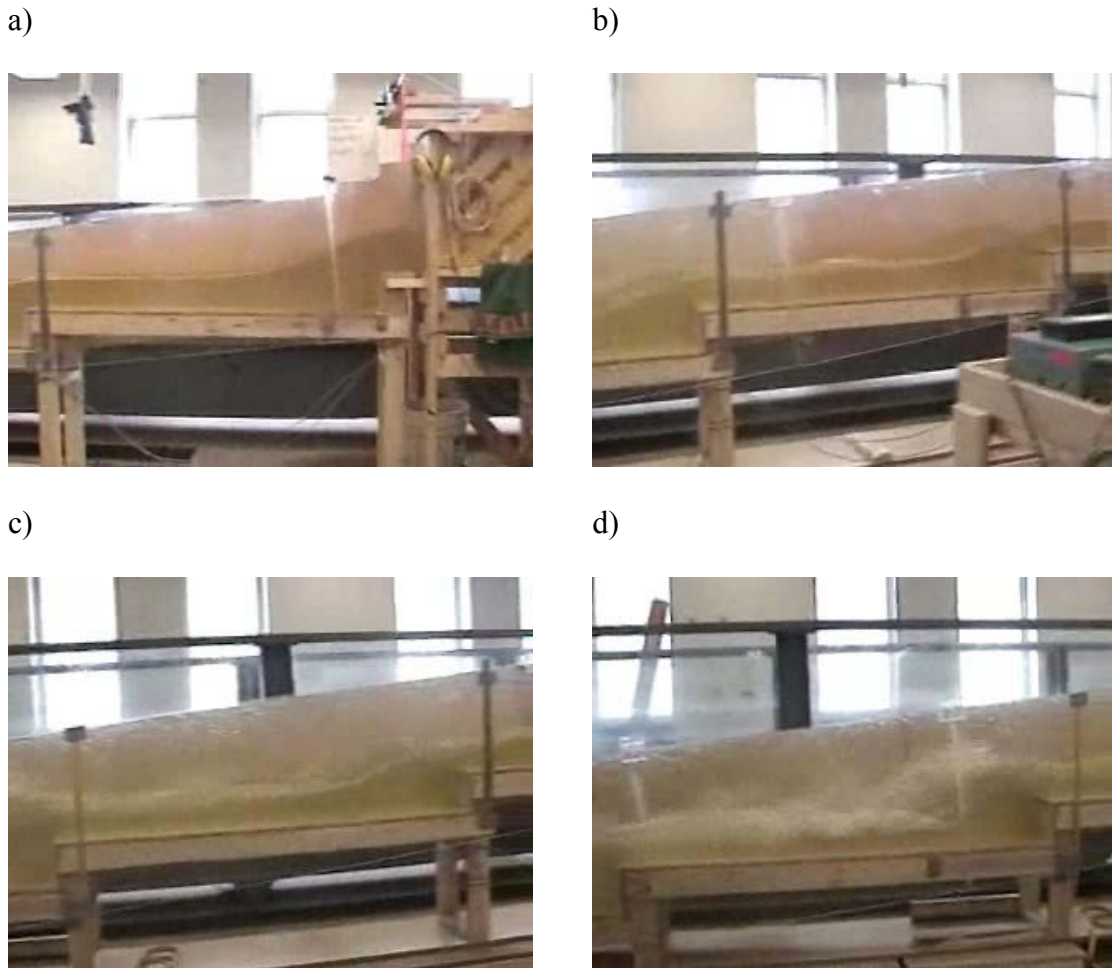
a)

b)

c)

d)
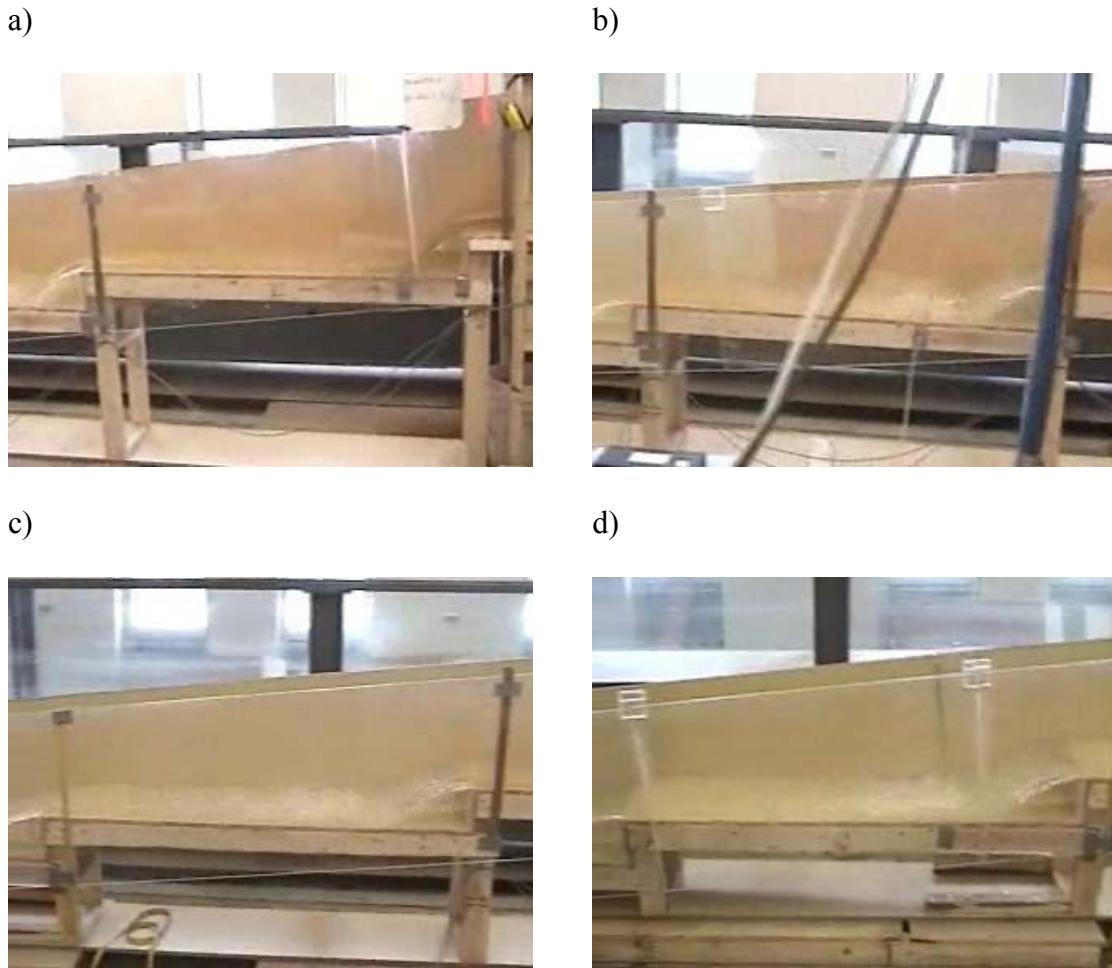
Figure 4.7 Nappe flow regime on Model III. Aerated step

cavity, $y_c/h = 0.49$. a) step 1. b) step 2. c) step 3. d)

step 4.

a)

b)

c)

d)
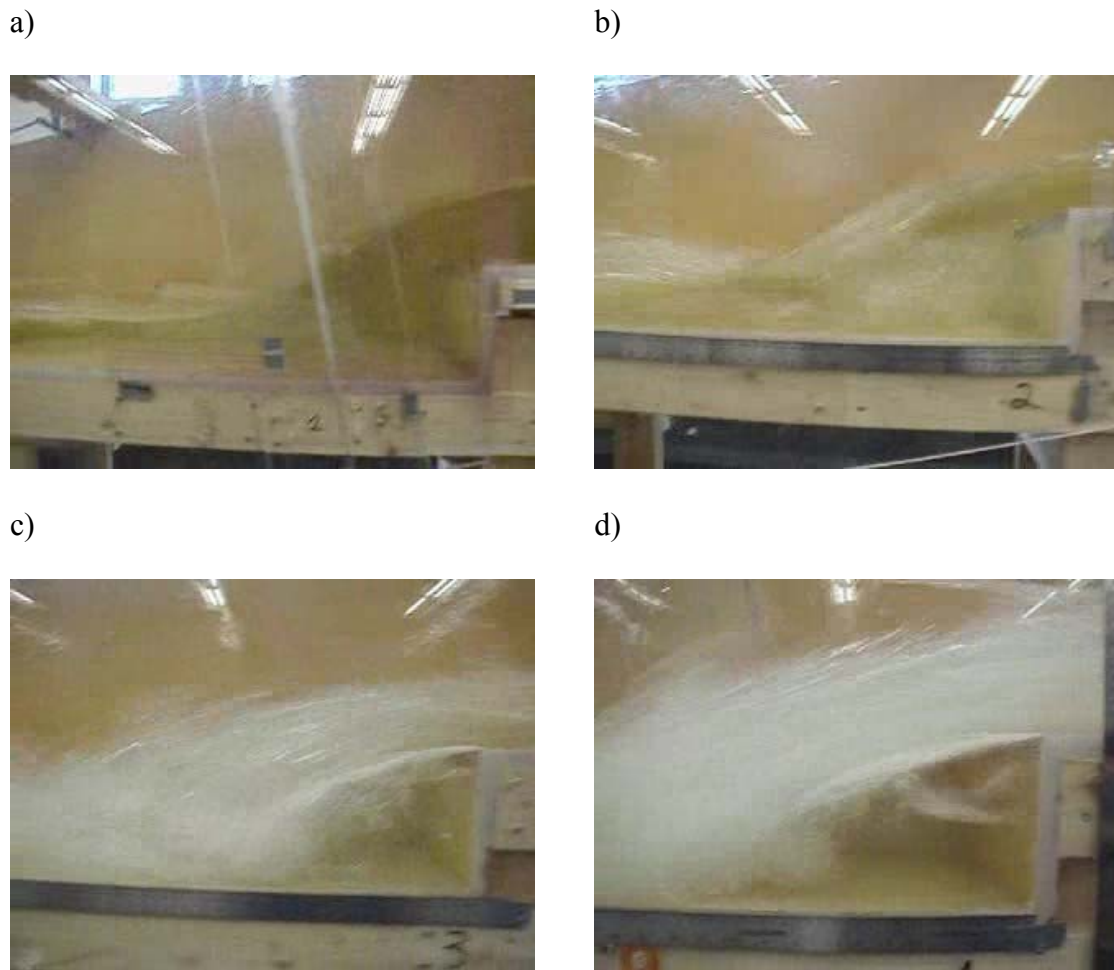
Figure 4.8 Transition flow regime on Model II. Non-

aerated step cavity, $y_c/h = 1.01$. a) step 1. b) step 2.

c) step 3. d) step 4.

a)

b)

c)

d)
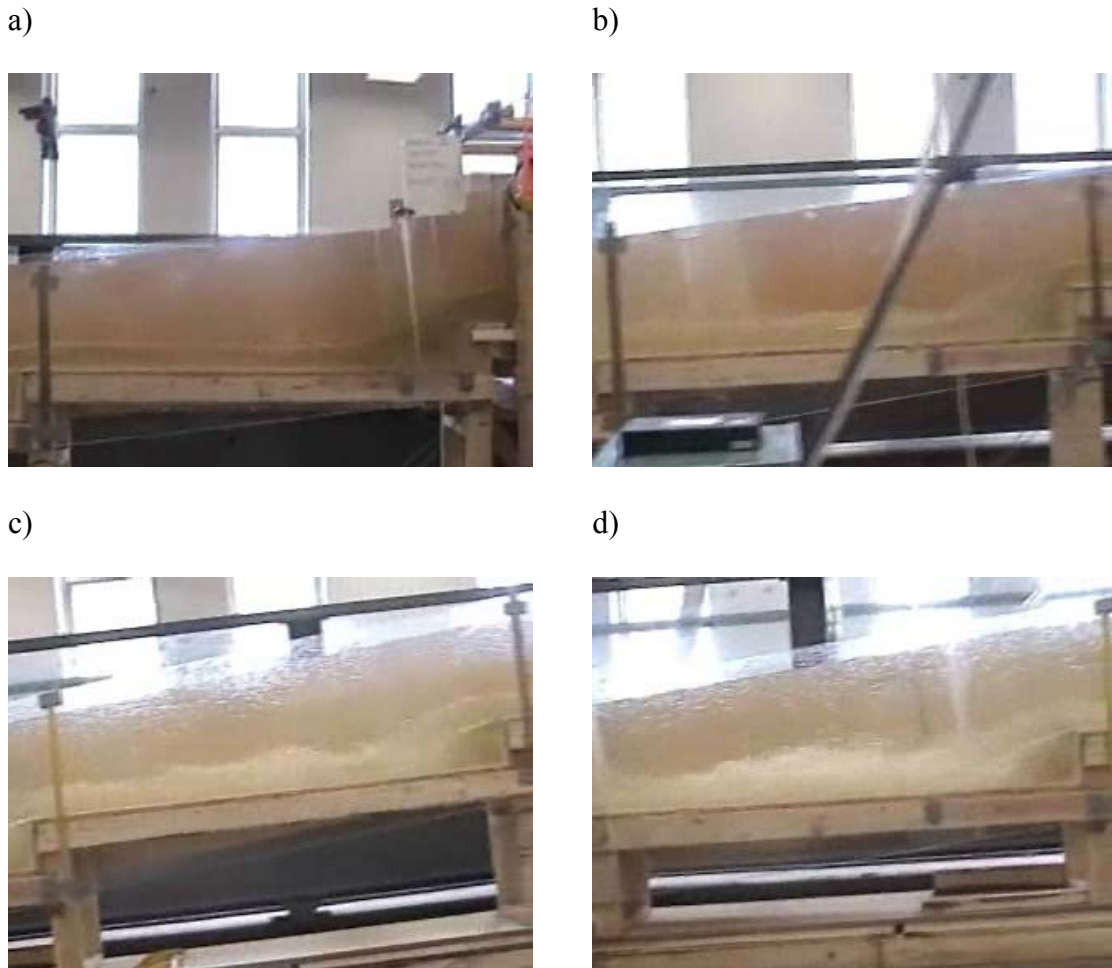
Figure 4.9 Transition flow regime on Model III. Aerated

step cavity, $y_c/h = 1.09$. a) step 1. b) step 2. c) step

3. d) step 4.

a)

b)

c)

d)

e)
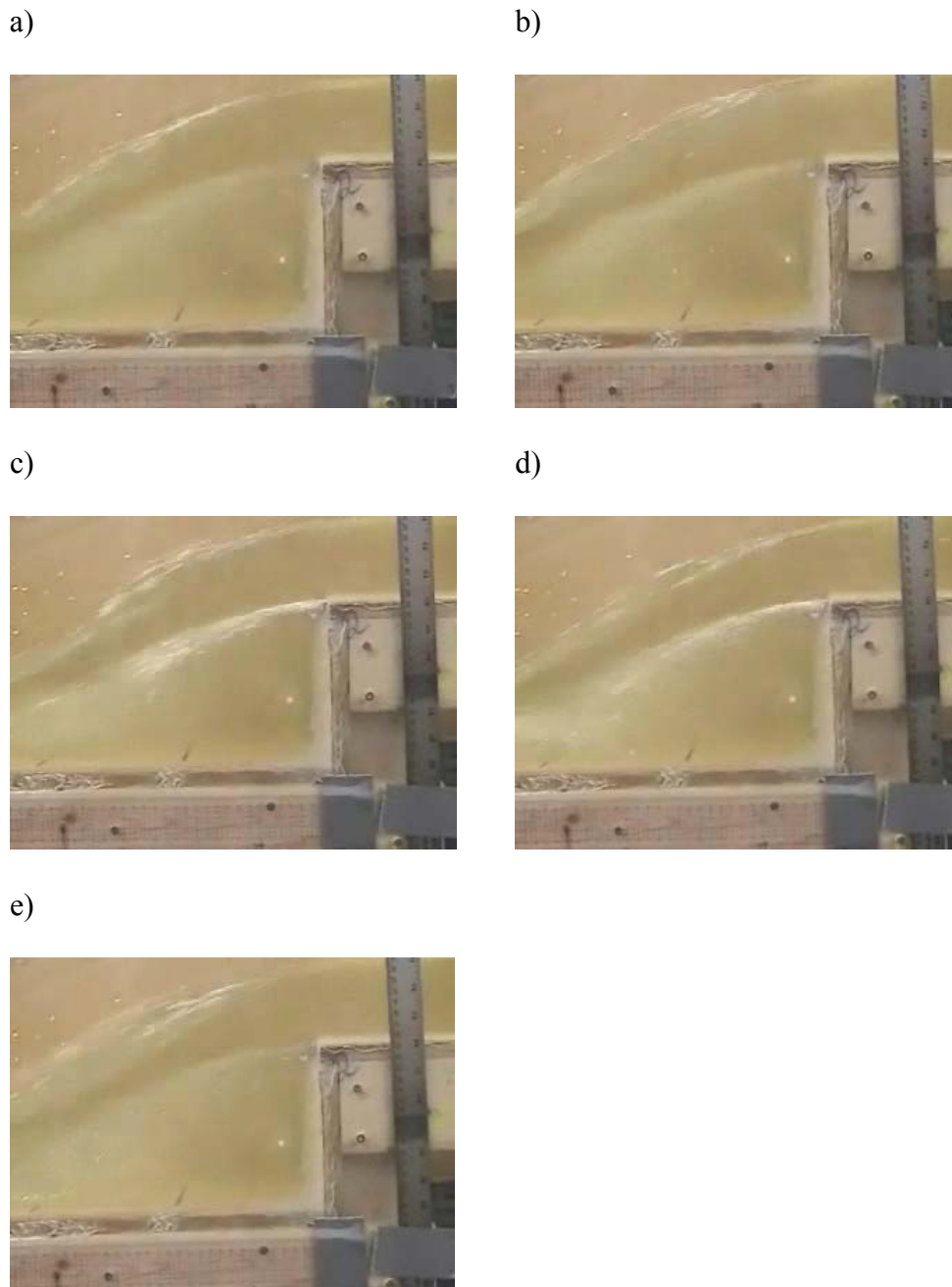
Figure 4.10 Entrainment of air into the step cavity. Model

III, $y_c/h = 1.09$, step 2. Imagines approximately

every 0.4 s.

a)

b)

c)

d)

Figure 4.11 Skimming flow regime on Model II. Non-

aerated step cavity, $y_c/h = 1.66$. a) step 1. b) step 2.

c) step 3. d) step 4.

a)

b)

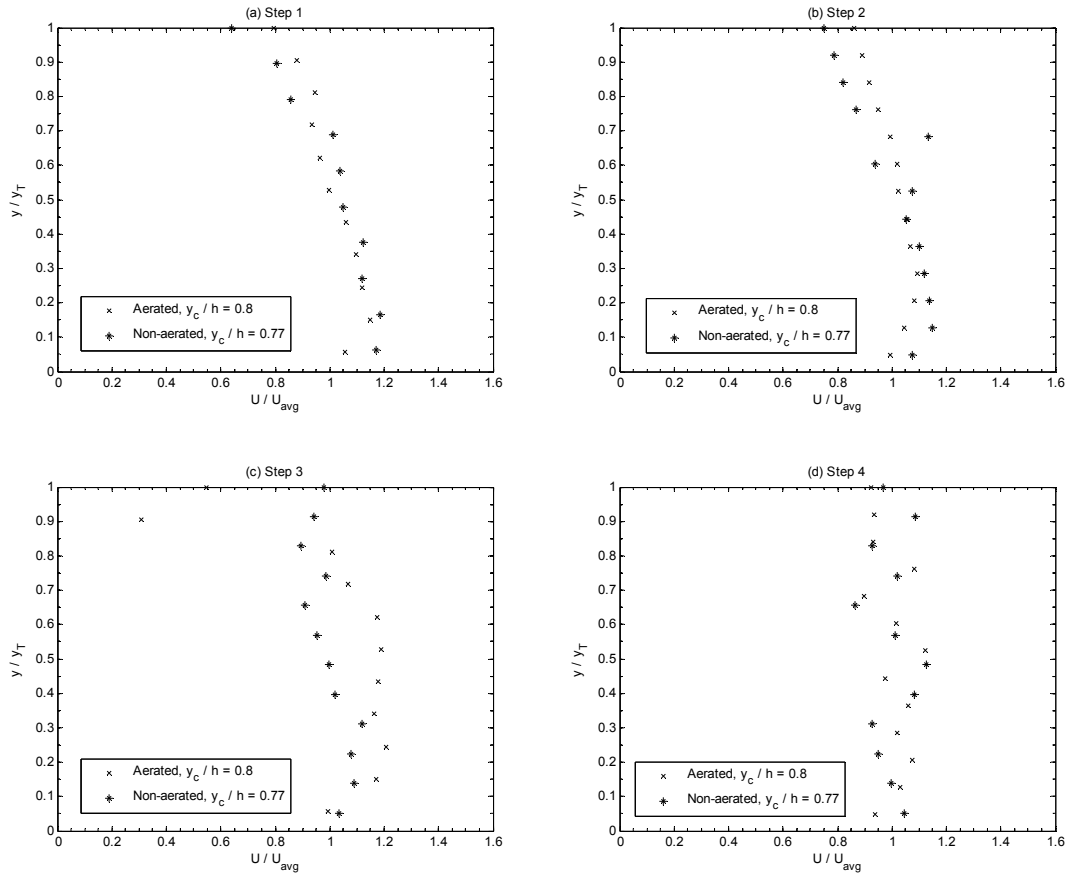c)

d)

Figure 4.12 Skimming flow regime on Model III. Aerated

step cavity, $y_c/h = 1.66$. a) step 1. b) step 2. c) step

3. d) step 4.

a)

b)

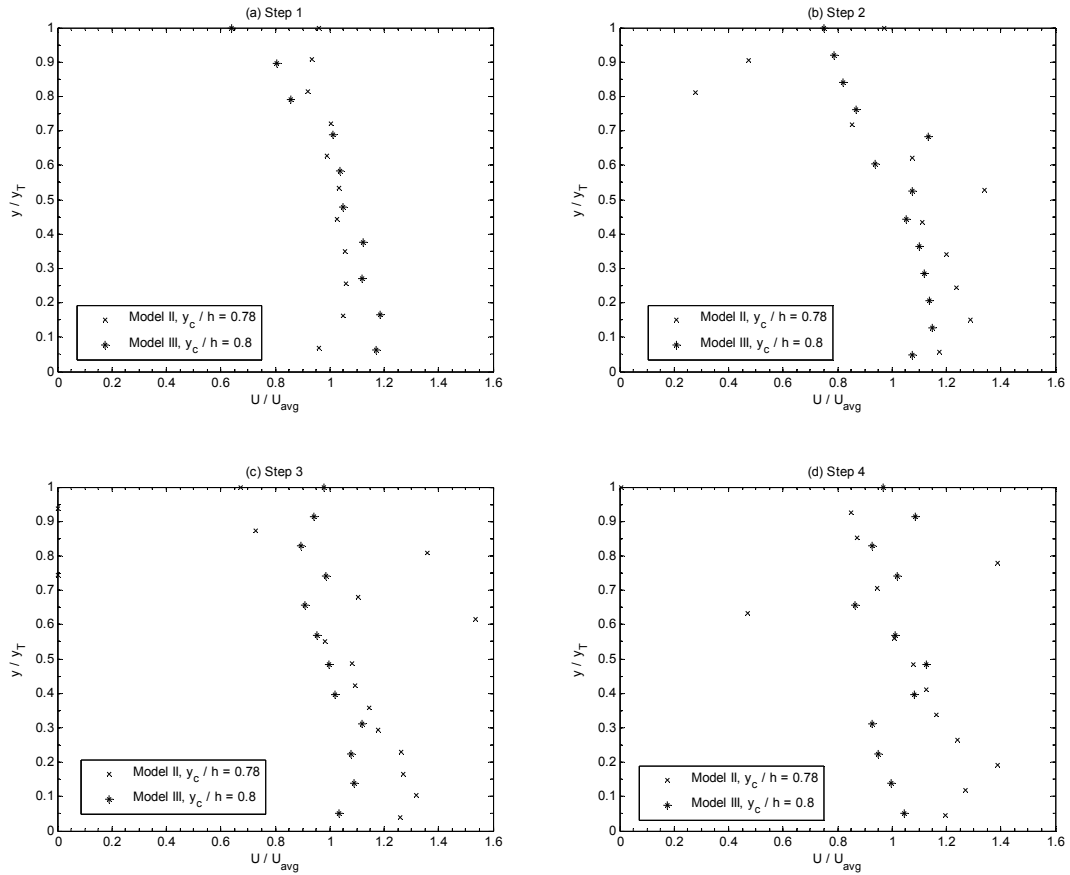**Figure 4.13** Shock waves at skimming flow regime. a)
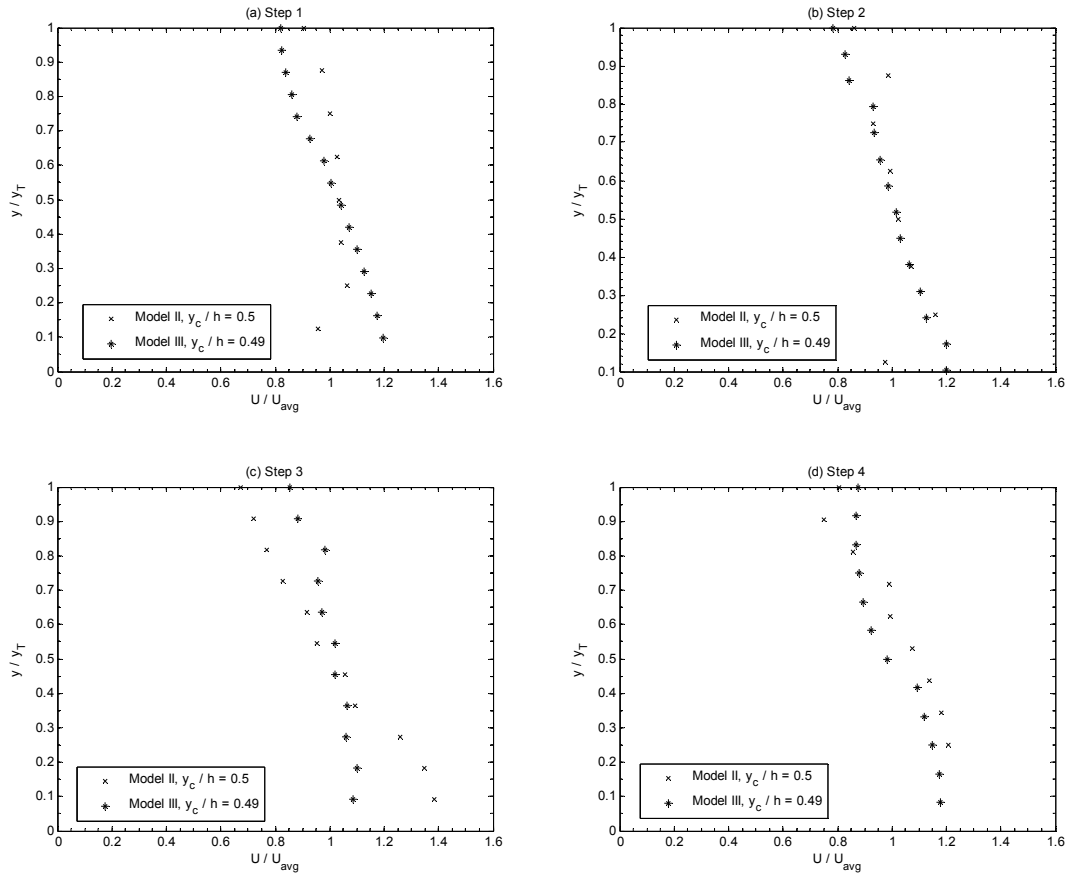
Model II. b) Model III.
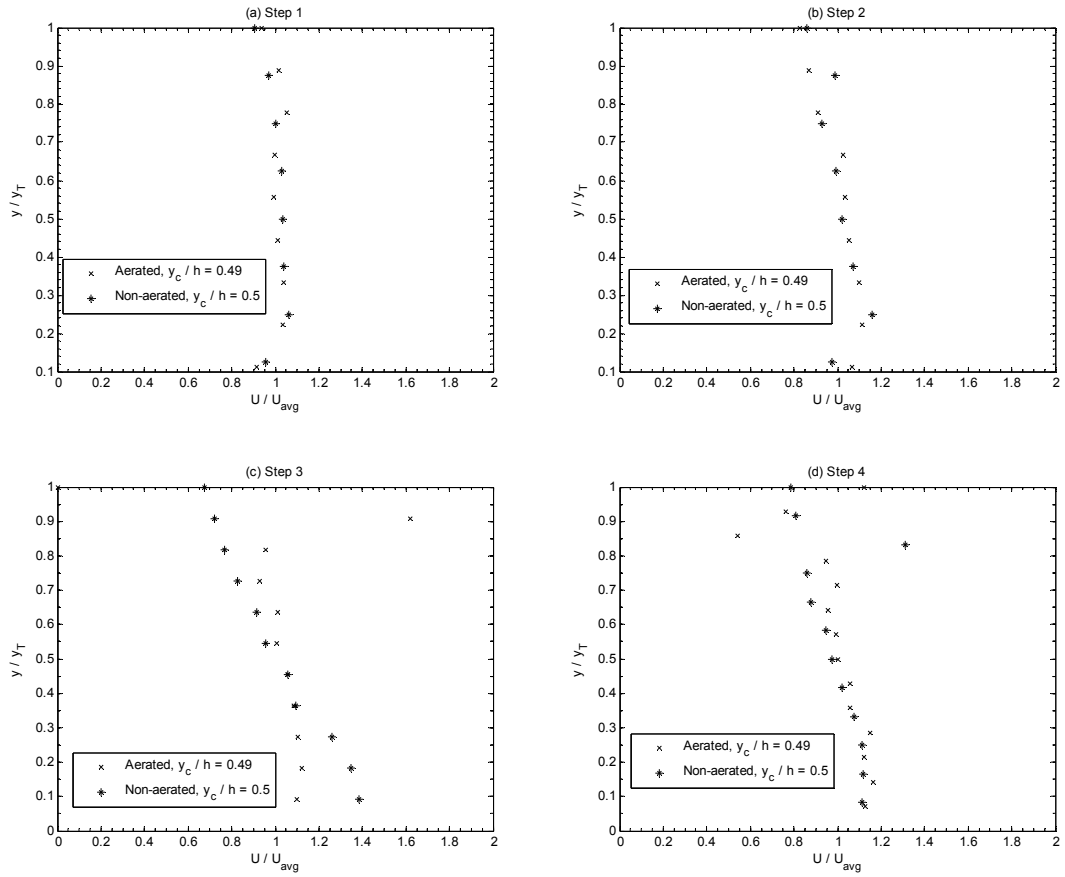
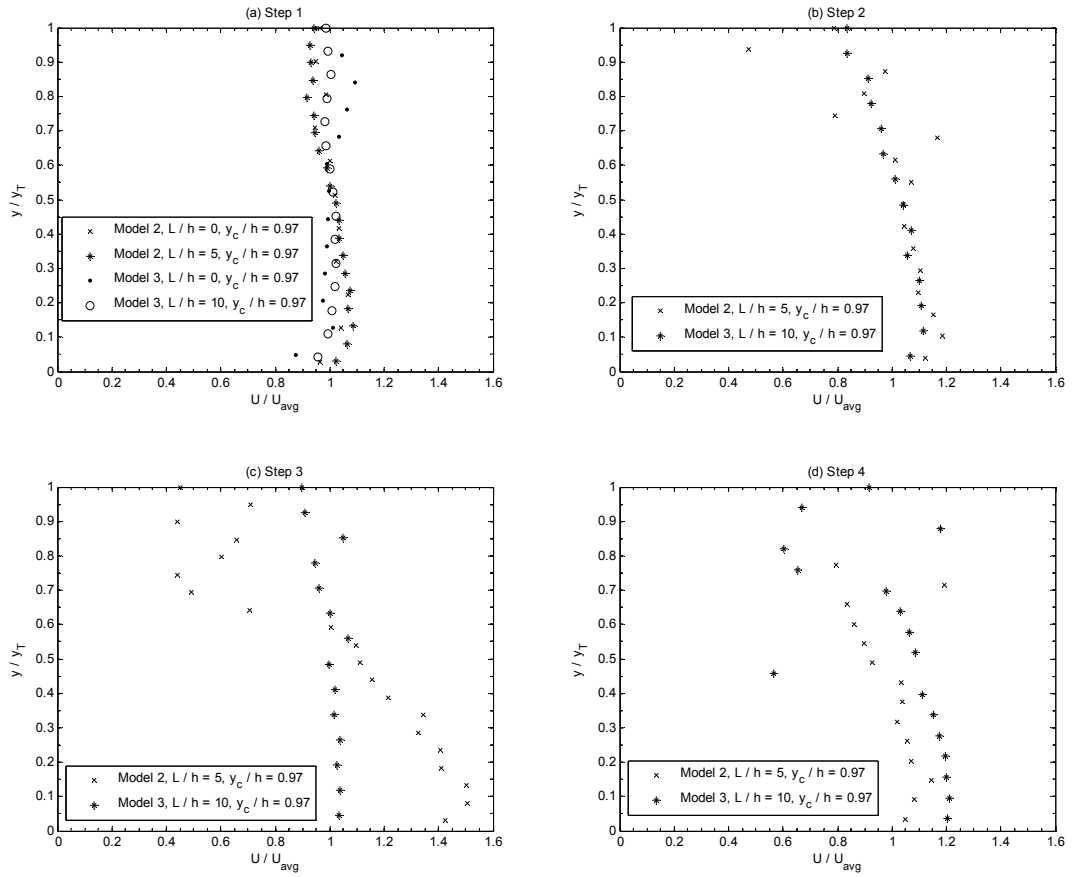**Figure 4.14** Velocity profiles at step brink, $L/h = 5$. Model II.

Figure 4.15 Velocity profiles at step brink, $L/h = 10$. Model III.

Figure 4.16 Comparison of velocity profiles with aerated flows at step

brinks. Model II at $L/h = 5$, Model III at $L/h = 10$.

Figure 4.17 Comparison of velocity profiles with non-aerated flows at step brinks. Model II at $L/h = 5$, Model III at $L/h = 10$.

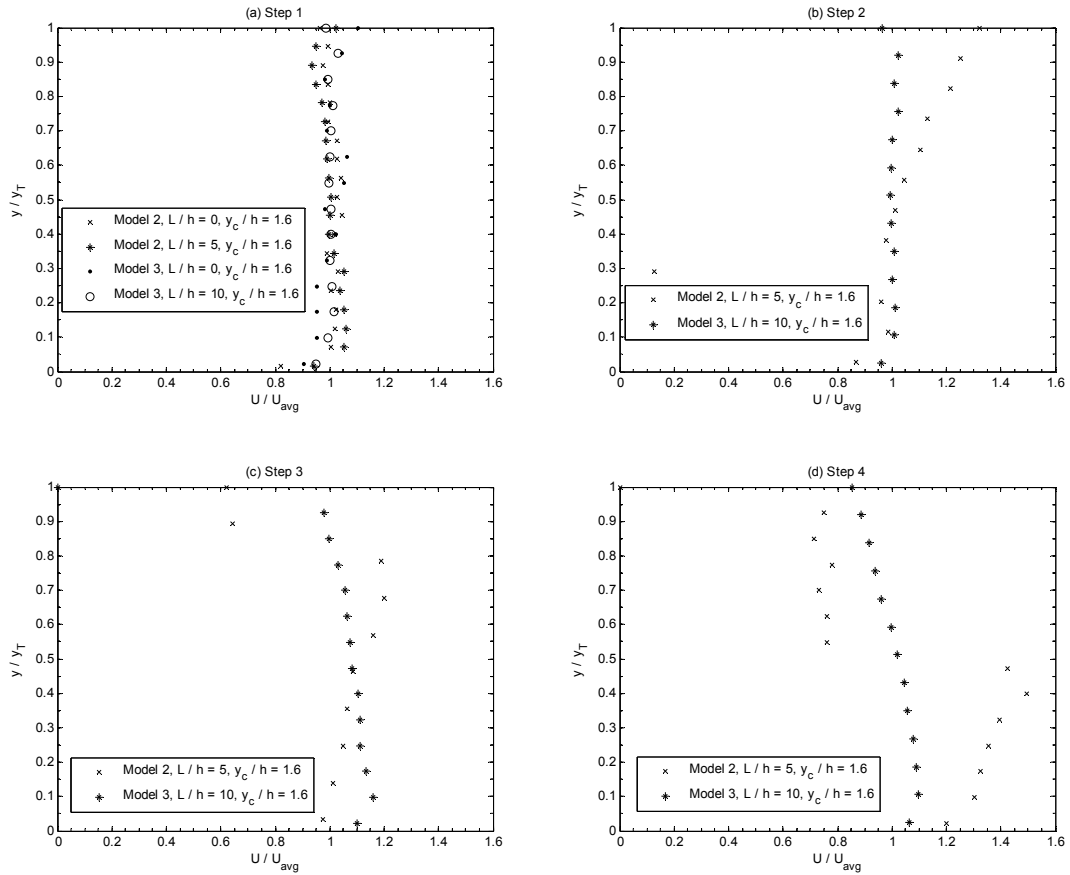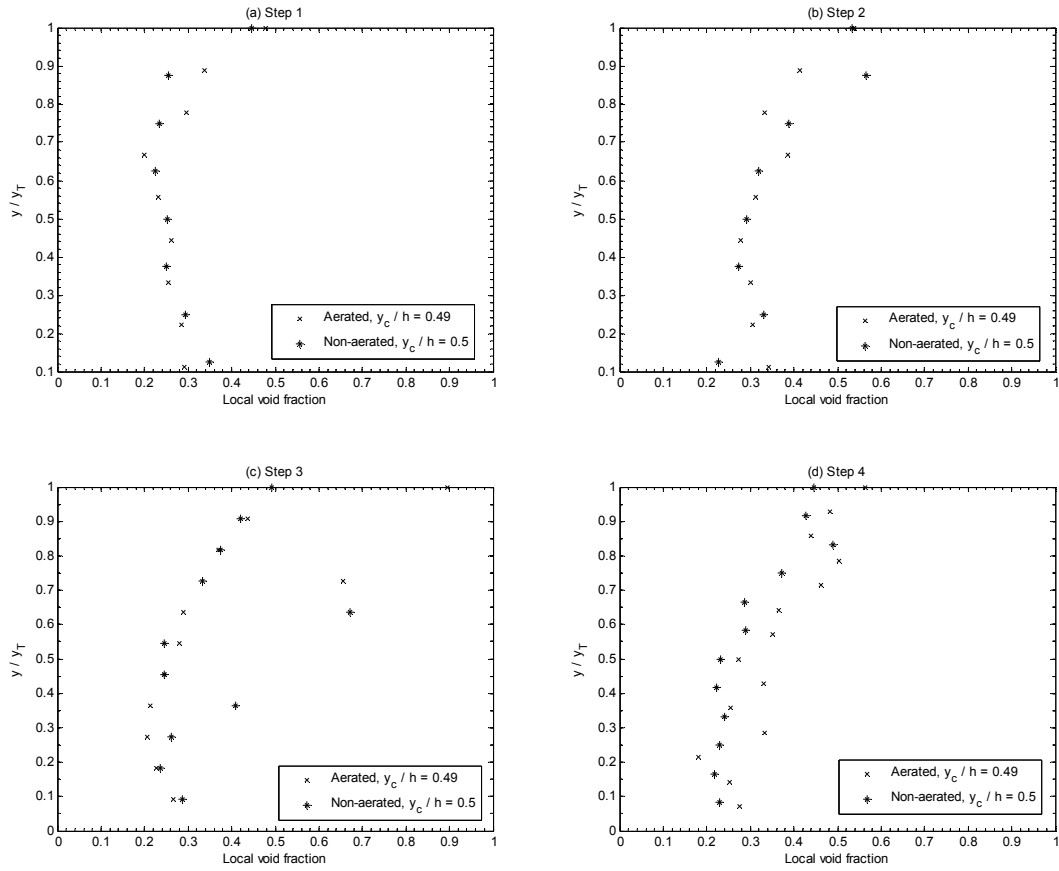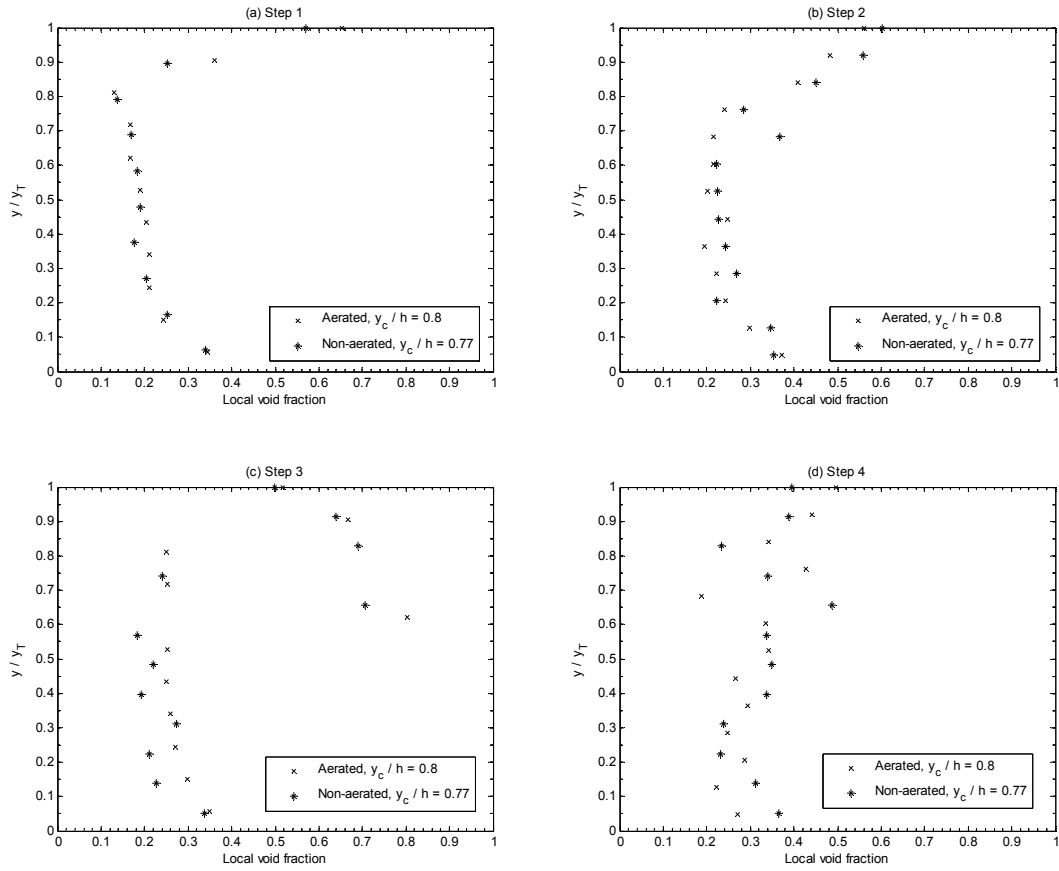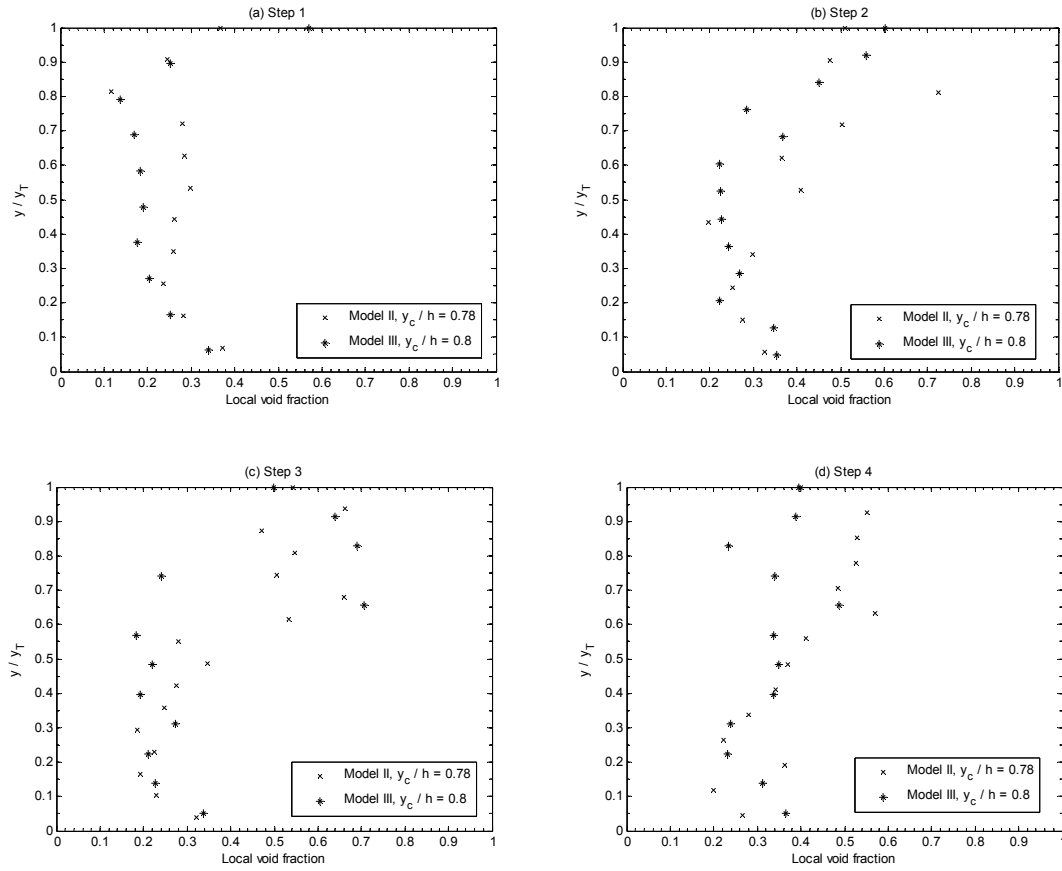**Figure 4.18** Velocity profiles at transition flow regime.

Figure 4.19 Velocity profile at skimming flow regime.

Figure 4.20 Local void fraction profiles at step brink, $L/h = 5$. Model II.

Figure 4.21 Local void fraction profiles at step brink, $L/h = 10$. Model III.

Figure 4.22 Comparison of local void fraction profiles with aerated flows

at step brinks. Model II at $L/h = 5$, Model III at $L/h = 10$.
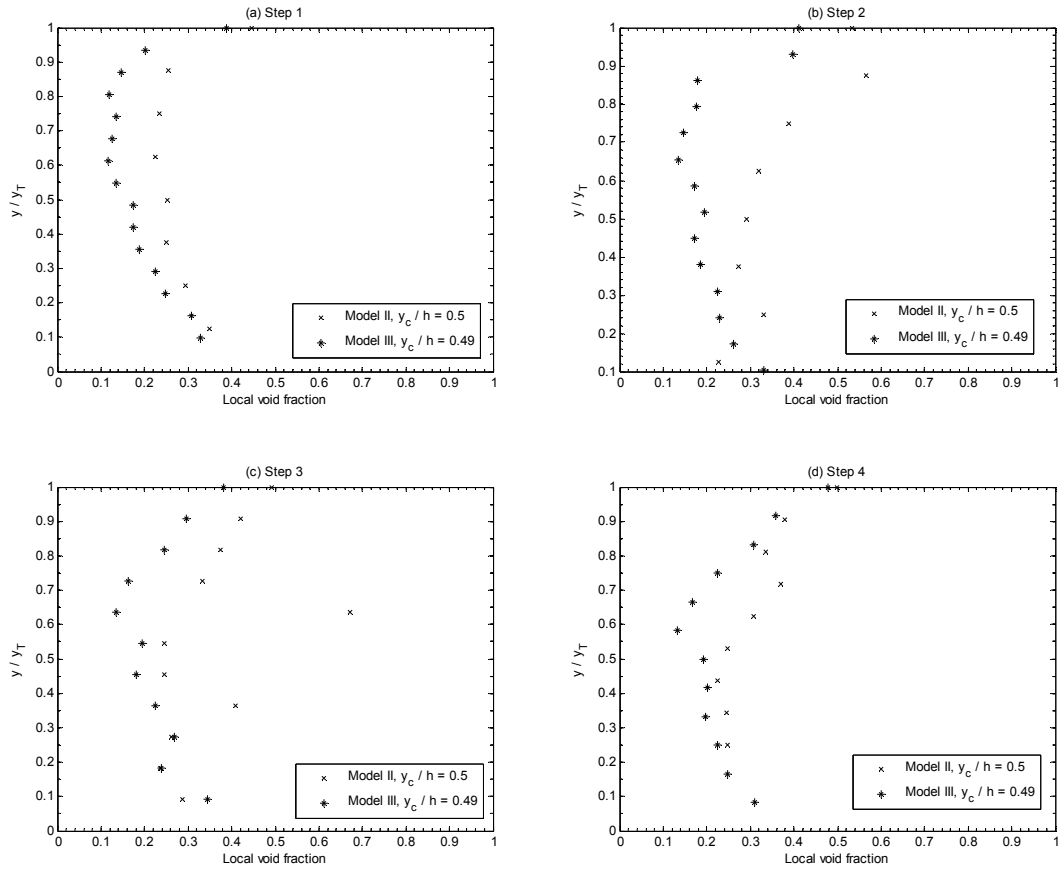
Figure 4.23 Comparison of local void fraction profiles with non-aerated
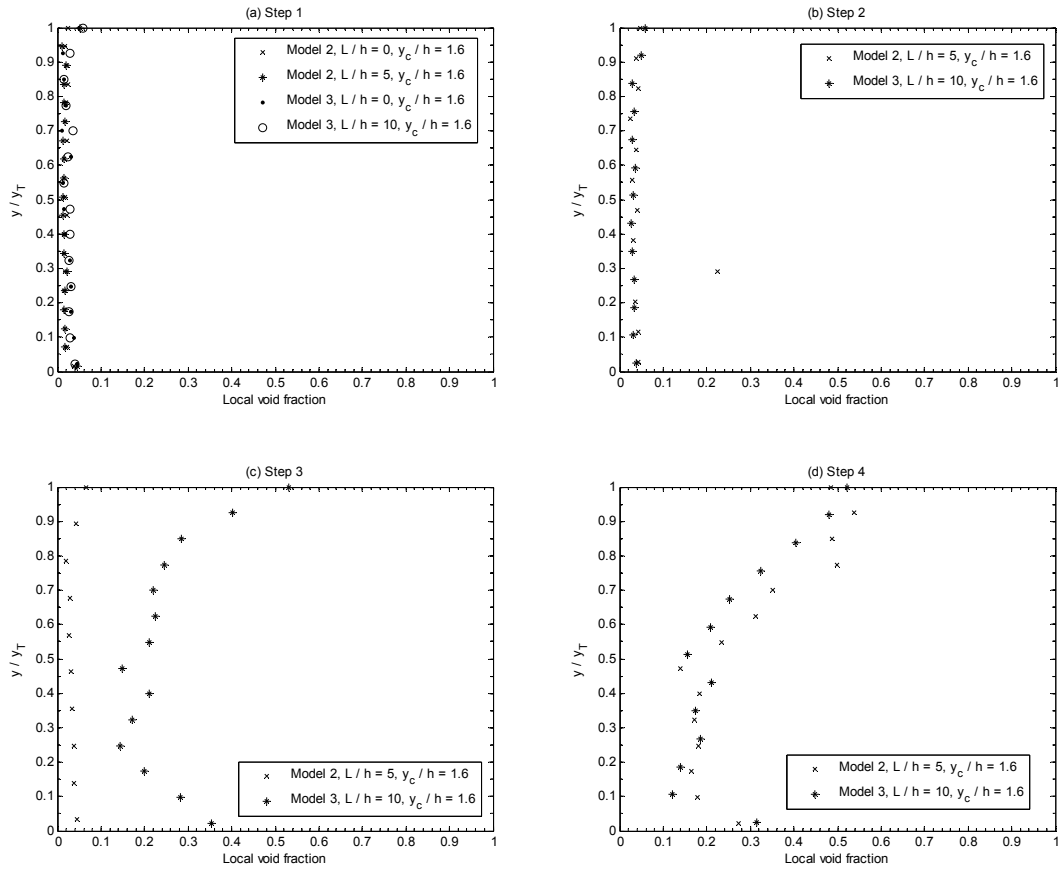
flows at step brinks. Model II at $L/h = 5$, Model III at $L/h = 10$.
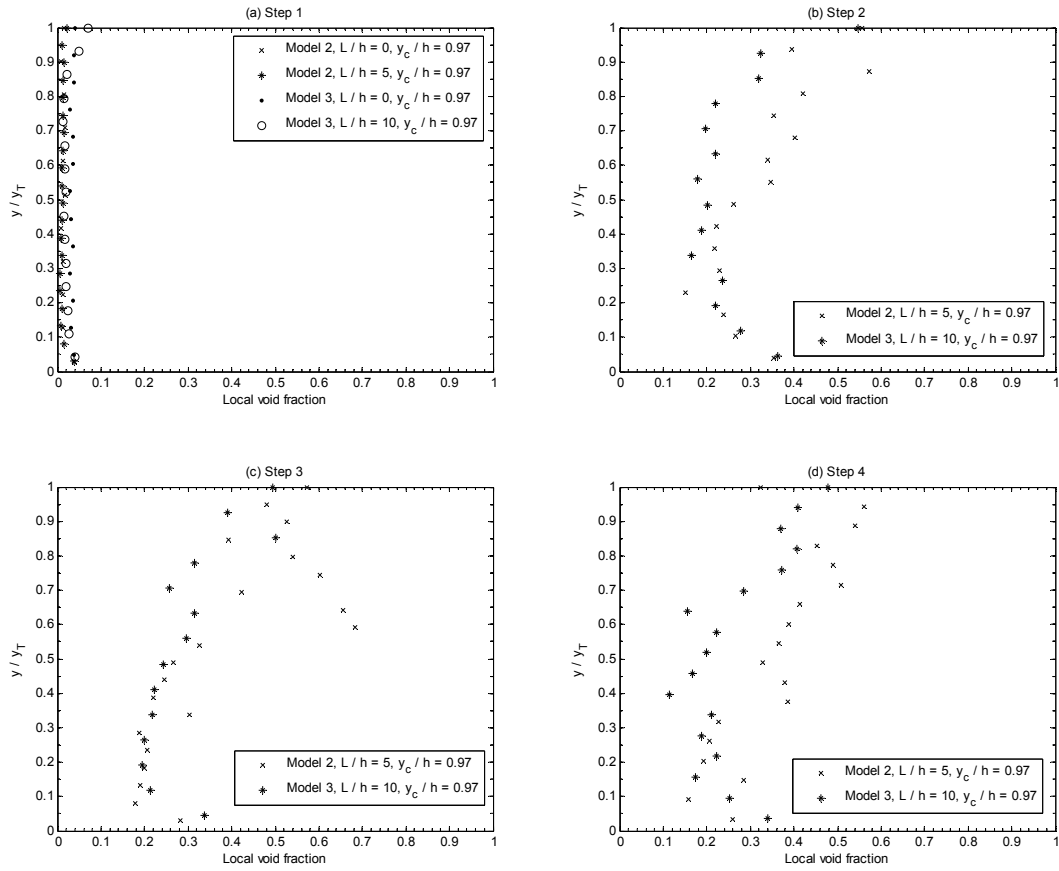
Figure 4.24 Local void fraction profiles at transition flow regime.

Figure 4.25 Local void fraction profile at skimming flow regime.

_____

Chapter 5   *Pressure observations*

_____

5.1 Introduction

The results of the pressure observation carried out on the three studied models are presented in this chapter. Initially, observations regarding the filling up process of the step cavity are presented. Later the measurements and the results on the step tread and on the step riser are given. Following this, observations and comments regarding the recirculating pool are presented.

5.2 Step cavity observations

The step cavity corresponds to the area enclosed by the lower nappe of the water jet and the two faces of a step. Within the step cavity two sections are distinguished: the recirculating pool and the air pocket. The recirculating pool is formed by the water that gets diverted towards the step riser when the water jet strikes the step tread. The air pocket is the volume of air entrapped by the water jet, the recirculating pool and the step;

this pocket can be aerated or non-aerated depending on whether or not aeration is provided.

The water level in the recirculating pool increases as the discharge increases and therefore the air pocket slowly vanishes. The air pocket can also vanish if aeration is not provided, in this case, the air is entrained into the flow and the water jet deflects towards the step riser as the air pocket diminishes. Figure 5.1 presents the limit discharge – expressed as y_c/h, where the air pocket disappears on the four initial steps of the three models studied. This figure indicates that at step 1 the condition of the step cavity affects significantly the values at which the air pocket disappears. In contrast, at steps 2, 3 and 4, there is no significant difference between the aerated and non-aerated condition for the chute slopes studied. This is an indication that after the first step, the water nappe is sufficiently broken to allow air into the cavity.

The value of y_c/h at which step cavities become filled with water seems to have a dependency on the chute slope. Figure 5.2 presents such an effect for a constant step height of 15 cm. In the case of aerated flows (Figure 5.2a), step 1 presents a linear trend, i.e., as the slope increases so does the value of y_c/h at which the step becomes full of water. In contrast, steps 2, 3 and 4 present a concave trend, where the maximum values of y_c/h were observed at a chute slope of $5H:1V$ $(\theta = 11.3°)$, i.e., the filling up process of the step cavity was slower at this slope. Furthermore, the tendency of these steps as the slope decreases in the rising limb of the curve $(\theta < 11.3°)$ is to converge towards the value of step 1, which suggests that the step tread would be long enough so there would be no interference between steps and each step would eventually behave independently.

In the decreasing limb $(\theta > 11.3°)$, however, there is no clear tendency and this disparity is likely to be caused by the deflection of the water jet or perhaps the by the water jet overshooting the step, although this situation was not observed.

In the case of non-aerated step cavities (Figure 5.2b), the first step became filled with water at a minimum discharge since the air pocket was depleted by the entrainment of air into the flow, therefore, this step is not shown in Figure 5.2b. Step 2 on the other hand, shows a convex tendency with a minimum value of y_c/h at $5H:1V$, while Steps 3 and 4 a concave trend. Once again, at slopes smaller than $\theta = 11.3°$ the steps tend to converge whereas at larger slopes the tendency is not clear. Finally, it is worth mentioning that on the three slopes analyzed in this study the four steps did not become filled with water at the same value, but rather in a progressive order, which is an indication that the preceding upstream flow conditions significantly affected the behavior of each step.

5.3 Pressure observations on step treads

Several pressure measurements were carried out on the initial four steps of each model. On Model I, seven pressure ports were installed along the each step tread and measurements were carried out with aeration provided into the step cavity. On Models II and III, eight ports were installed and measurements were taken for aerated and non-aerated step cavities. Table 5.1 shows the location L_i/h of the pressure ports where L_i is the horizontal distance from the step riser.

Table 5.1 Location of pressure ports on step treads.

Model slope	Pressure port location (L_i/h)
$3.5H : 1V$	0.18, 0.35, 0.70, 1.05, 1.40, 2.45, 3.15
$5H : 1V$	0.25, 0.50, 1.00, 1.50, 2.00, 2.75, 3.75, 4.75
$10H : 1V$	0.50, 1.00, 1.50, 2.00, 3.00, 4.00, 5.50, 9.50

As mentioned before, pressure measurements along the step tread were carried out for the conditions of an aerated and non-aerated step cavity. Measurements were taken at a frequency of 200 Hz during 50 seconds and the data acquisition card was set to a precision of ±4.88 mV. Figures 5.3 to 5.5 show a selection of results for the three models. Measurements indicated that the condition of the step cavity does not affect significantly the pressure profile downstream of the jet impact. Upstream of the jet impact, at the recirculating pool, there was however, a slight variation of the pressure levels where the non-aerated condition produced slightly larges values. These larger values are due to the lower pressure conditions which tend to increase the water depths within the recirculating pool. Similar results were observed on Models II and III.

On the other hand, a comparison between the steps of a given model (Figures 5.6 to 5.8) yielded a diversity of results. In the case of Model I $(3.5H : 1V)$ the data indicated that there is no similarity of the pressure profile between the steps of the model, i.e., each step presented a different pressure profile. Model II $(5H : 1V)$ showed that at low and intermediate discharges the pressure profiles on each step were different as well. However, at large discharges the recorded measurements suggested a similar pressure

profile at steps 2, 3 and 4 but not at step 1. In the case of Model III $\left(10H:1V\right)$, the measured pressure profiles were similar on all four steps. This might indicate that in the range of chute slope $\left(5.7° \leq \theta \leq 11.3°\right)$ there is a change in the hydraulic behavior of a stepped spillway, which is reflected by a similar pressure distribution along the step tread. This effect is initially felt at approximately $\theta = 11.3°$ when large discharges are flowing but it is completely dominant at a slope $\left(\theta\right)$ of about $5.7°$.

Finally, a comparison of the results for a given step for each of the different models is shown in Figures 5.9 to 5.12. On step 1, the three models presented a similar pressure profile at low flows but this similitude disappeared at intermediate and large discharges. Conversely, the resemblance on step 2 is stronger at large flows than at low discharges, which is opposite to the behavior observed for step 1. Steps 3 and 4 however, presented similar pressure profiles for all three models. Therefore it seems, that there is no conclusive typical pressure profile between the models, where each model seems to behave in a characteristic way with some similarities but not sufficient to determine a unique pressure profile. There is nevertheless, a pattern profile on the step treads, which moves in the downstream direction on the step tread as the discharge increases. This pattern of pressure profile initiates with intermediate pressure values at the recirculating pool, the values then start to increases as L_i approaches the point of jet impact, where the pressure level reaches a maximum. Once L_i passes the jet impact point, the pressure level starts to decrease until a plateau level is reached, which holds until the step brink. The magnitude of pressure on the plateau is lower than it is in the recirculating pool. The

location of the jet impact point varies with the step and slope characteristics and it was observed to be in the range of $1.5 \leq h \leq 3$.

5.4 Pressure measurements on step risers

As in the case of the step tread, measurements on the step risers were carried out with and without aeration in the step cavity. Similarly to the step treads, the sampling rate on the data acquisition was 200 Hz and it lasted for 50 seconds. Pressure ports were located at several points along the height of the steps as table 5.2 shows, where $y*$ is the upward distance from the step tread.

Measurements within a model displayed a similar pressure profile for the aerated and non-aerated condition (Figures 5.13 to 5.15) and larger pressure were observed at larger flows. On Model I, the data indicate that the profile was not linear but rather has a saw shape. This shape is more accentuated with the non-aerated condition, where slightly smaller pressures were recorded on some of the ports. Similarly to Model I, the measurements on Model II also defined a saw shape, indistinctively of the condition of the step cavity. For Model III, the profiles were similar for both aerated and non-aerated measurements but in contrast to Model I and II, the shape of the profile is more linear (but not hydrostatic), that is, the saw pattern is substantially less noticeable, with the exception of step 3. This change in pressure profile reinforces the idea that between slopes of 5.6° to 11.3° there is a change in the hydraulic behavior of a stepped chute, for both the aerated and non-aerated condition.

Table 5.2 Location of pressure ports on the step risers.

	Step 1 $(y*/h)$	Step 2 $(y*/h)$
Model I	0.06, 0.16, 0.32, 0.48, 0.64, 0.80, 0.96	0.06, 0.16, 0.33, 0.49, 0.66, 0.82, 0.94
Model II	0.10, 0.19, 0.30, 0.39, 0.49, 0.59, 0.68, 0.78	0.09, 0.20, 0.30, 0.39, 0.49, 0.59, 0.69, 0.79
Model III	0.10, 0.20, 0.30, 0.39, 0.49, 0.59, 0.69, 0.79	0.11, 0.21, 0.30, 0.40, 0.49, 0.59, 0.69, 0.78
	Step 3 $(y*/h)$	Step 4 $(y*/h)$
Model I	0.06, 0.16, 0.33, 0.49, 0.65, 0.82, 0.95	0.06, 0.16, 0.33, 0.49, 0.66, 0.82, 0.94
Model II	0.10, 0.20, 0.30, 0.40, 0.50, 0.60, 0.70, 0.79	0.10, 0.20, 0.30, 0.40, 0.50, 0.59, 0.69, 0.79
Model III	0.11, 0.21, 0.30, 0.40, 0.50, 0.60, 0.70, 0.80	0.10, 0.20, 0.29, 0.39, 0.48, 0.58, 0.67, 0.77

In spite of the similitude between the aerated and non-aerated condition within a given model, the pressure profiles on each step are not similar. In Model I for example (see Figure 5.16), the four steps presented the saw shape but with different magnitudes of pressure. Furthermore, at intermediate flows, steps 1, 3 and 4 presented a more uniform shape while step 2 retained the saw form. For the case of larger discharges, steps 1 and 2 again showed the saw shape while steps 3 and 4 a uniform profile.

Model II (Figure 5.17) on the other hand, presented similar saw profiles on the four steps for all flow conditions. Interestingly, step 1 gave the largest pressure values while step 4 the smallest; steps 2 and 3 presented intermediate pressure values in a

descended fashion. Measurements on Model III (Figure 5.18) indicated a more similar and uniform profile on all steps and flow conditions; nevertheless, there were still some signs of the saw shape especially on step 3.

Finally, a comparison of the results of a given step (Figure 5.19 to 5.22) shows no correlation between the observed pressure magnitudes.

The observed saw profile was not expected and it was initially thought to be an instrumentation or numerical error. Nevertheless, after extensive revisions of the post processing procedures numerical error was discarded as a source of this observed pressure variation. Instrumentation error was discarded as the source of the observed pressure variation by the fact that vertical profiles on the steps were obtained for a variety of situations as well as the fact that tests on the pressure transducer were carried out before and after the runs on each step were completed. A more detailed study of the pressure profile should bring light into the theoretical justification of the observed saw profile.

5.5 Pools depths observations

Pool depths correspond to the water level on the recirculating pool area which were measured with respect to the step tread. Figure 5.23 shows the observed pool depth y_p for different discharges on the four steps of all three models for the aerated step cavity condition. This figure assumes that the average water levels on the pool are equal to the observed pressure levels on ports 1 to 3 on Model I and, ports 1 and 2 on Models II and III. It would be expected that a correlation should be presented in at least step 1,

since it is the step that resembles a drop structure. Nevertheless, no such correlation was distinguished on step 1, or on steps 2, 3 or 4.

When the air pocket was presented it was also observed that the recirculating pool became shallower and elongated in downstream direction; a fact that was more evident at the smallest slope tested but it was also noticeable at $\theta = 11.3°$. The water level on the pool fluctuated intensively, which might have had an influence on the observed saw shape of the riser pressure profile. These fluctuations were more intensive at the steeper slope and it was also observed that on average, the water level was slightly inclined towards the point of jet impact, i.e., larger water depths on the riser zone and lower depths close to the jet impact.

Finally, when the step cavity became full of water two symmetric spiral vortices were observed in the vicinity of the step riser, these vortices had a flow direction towards the sides of the models in the area closest to the riser and in the ascending flow direction.
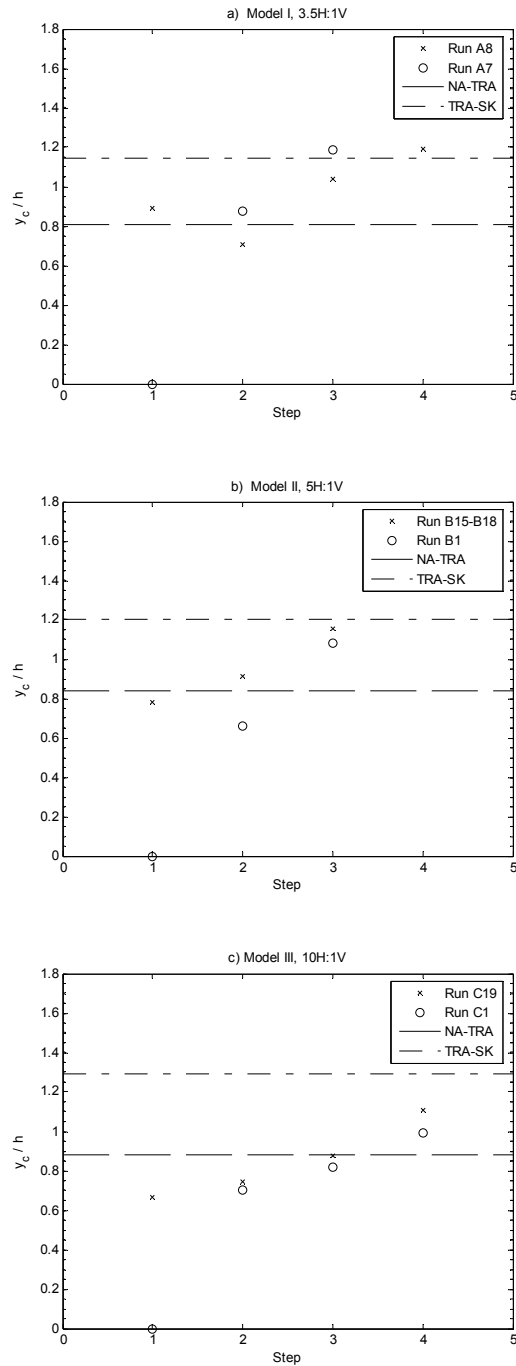
Figure 5.1 Observed points where the air pocket vanishes.

Aerated condition: runs A8, B15-B18 and C1. Non-

aerated condition: runs A7, B1 and C1.
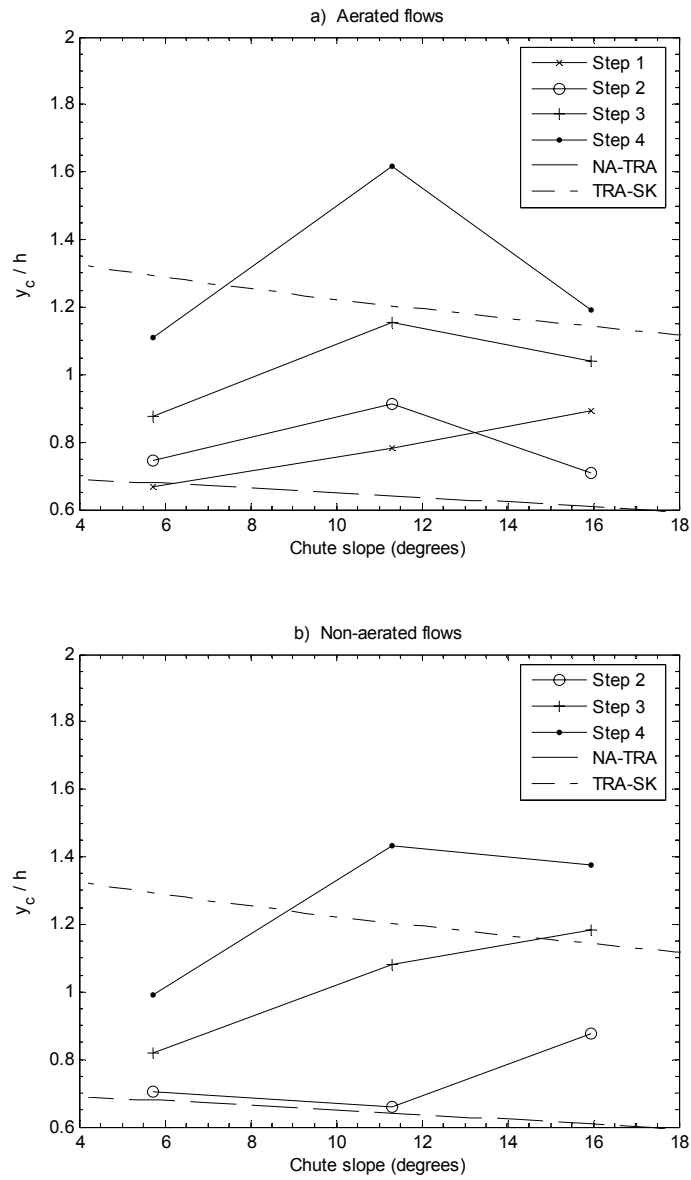
Figure 5.2 Slope effect on the presence of the air pocket.
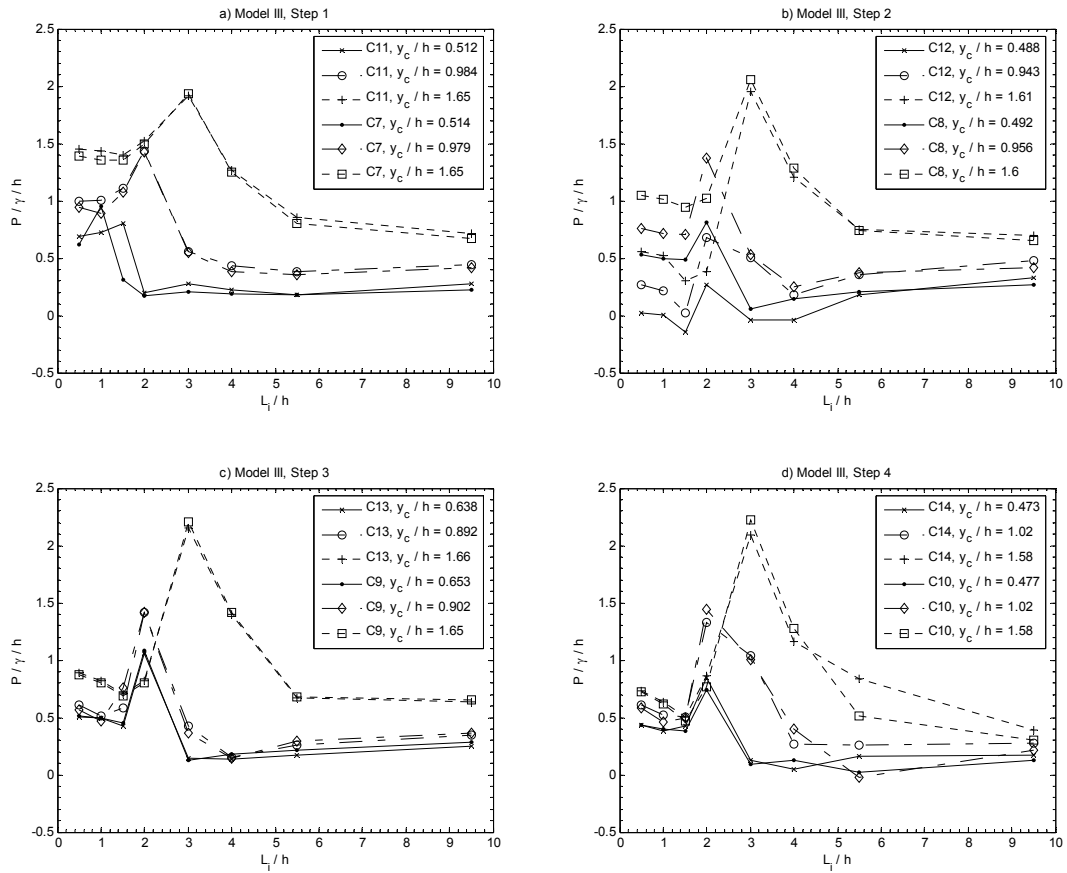
Constant step height of 15 cm.
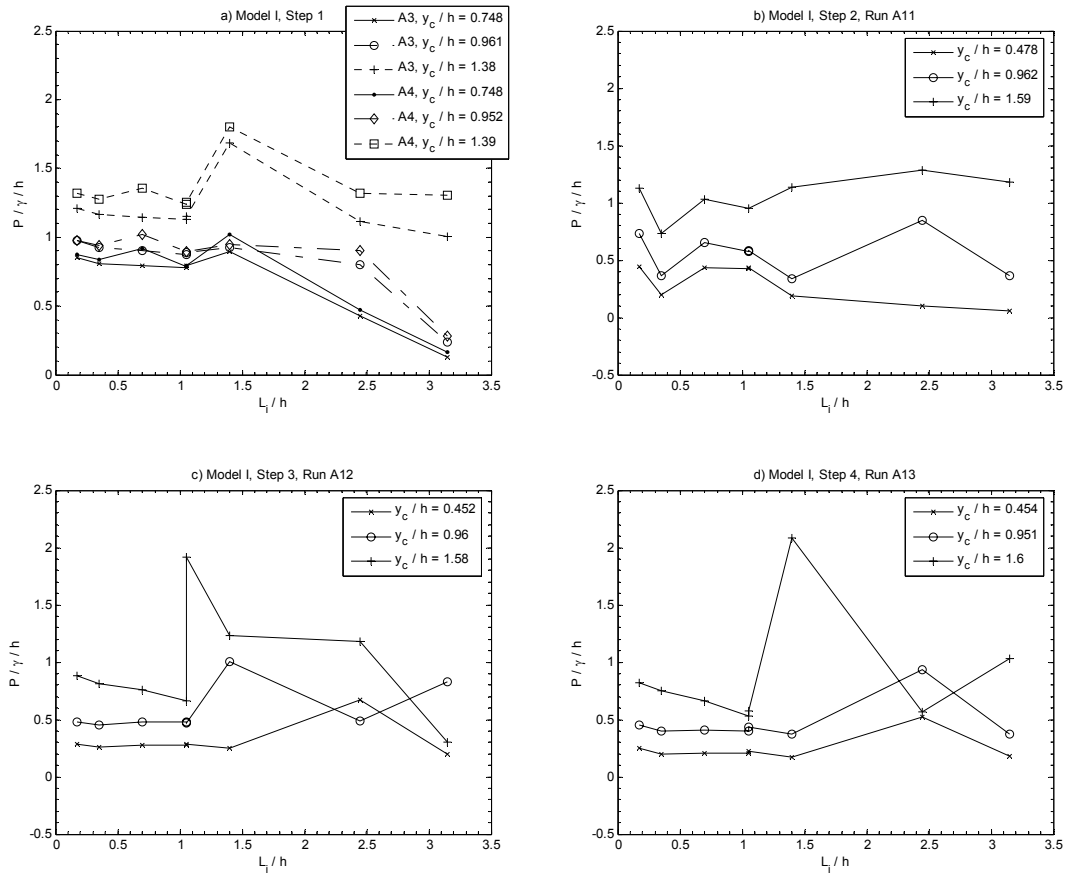
Figure 5.3 Observed average pressure along Step 1 on Model I. Aerated

condition: run A3, A11 to A13; non-aerated: run A4.
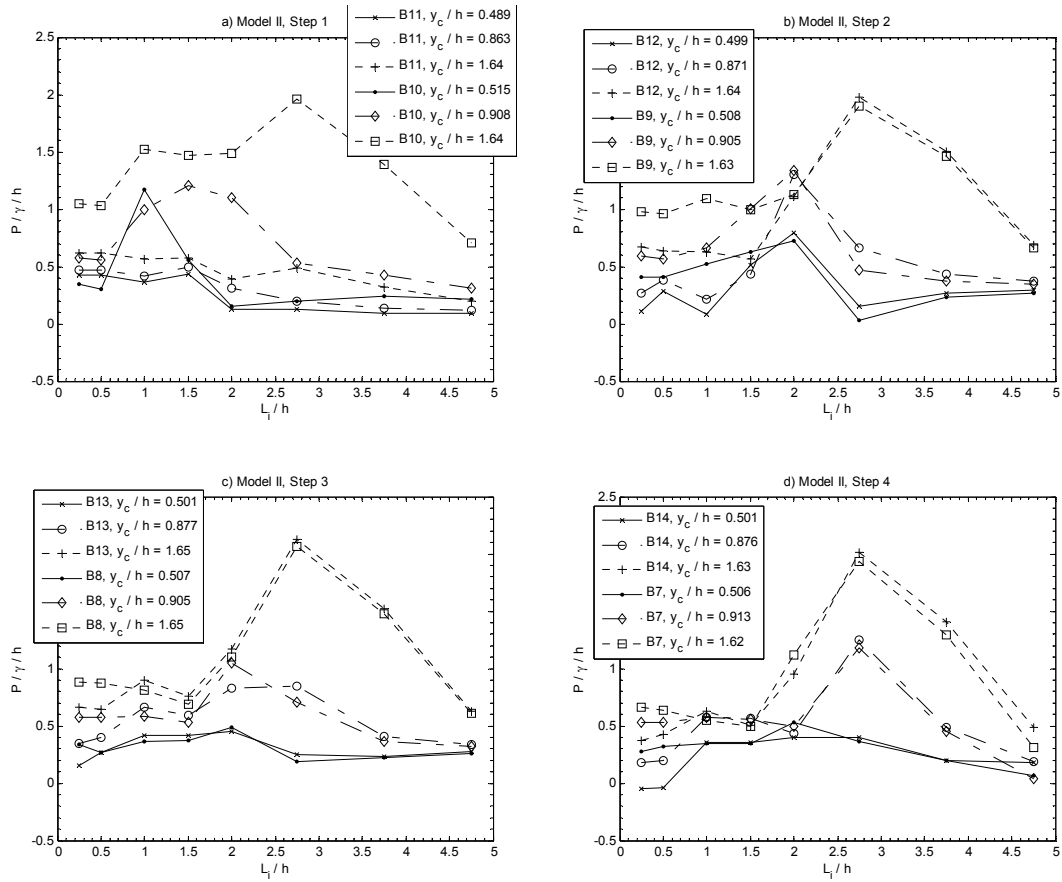
**Figure 5.4** Measured average pressure on step treads on Model II.

Aerated condition: run B11 to B14; non-aerated condition: runs

B7 to B10.

Figure 5.5 Measured average pressure on step treads on Model III.

Aerated condition: run C11 to C14; non-aerated condition: runs

C7 to C10.

a) Nappe flow regime

b) Transition flow regime

c) Skimming flow regime
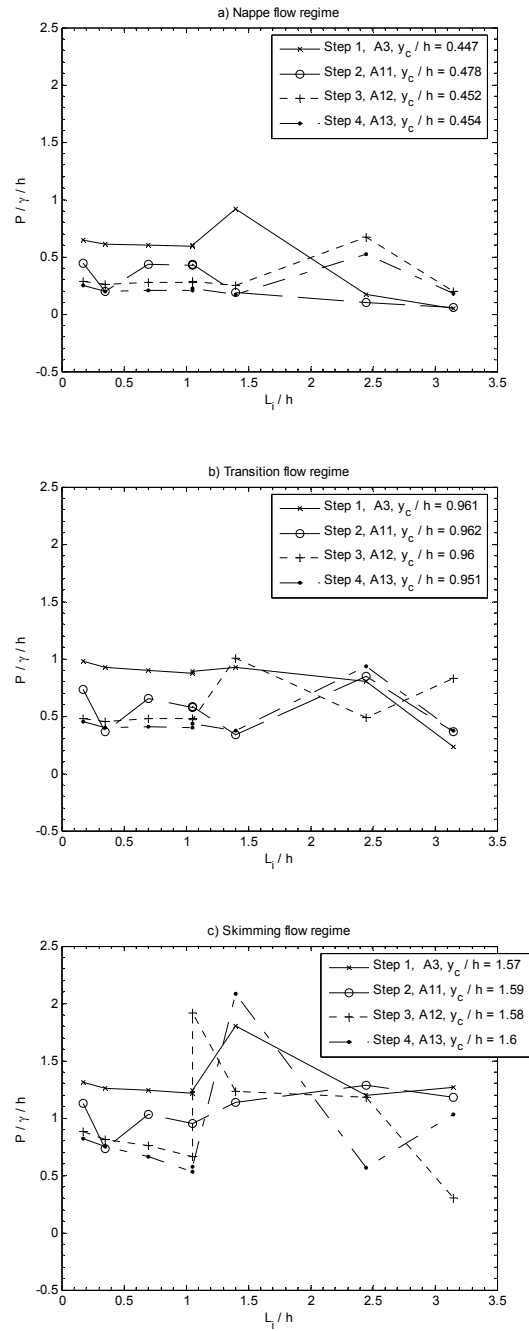
Figure 5.6 Recorded pressure on the treads of Model I,

aerated flow condition.
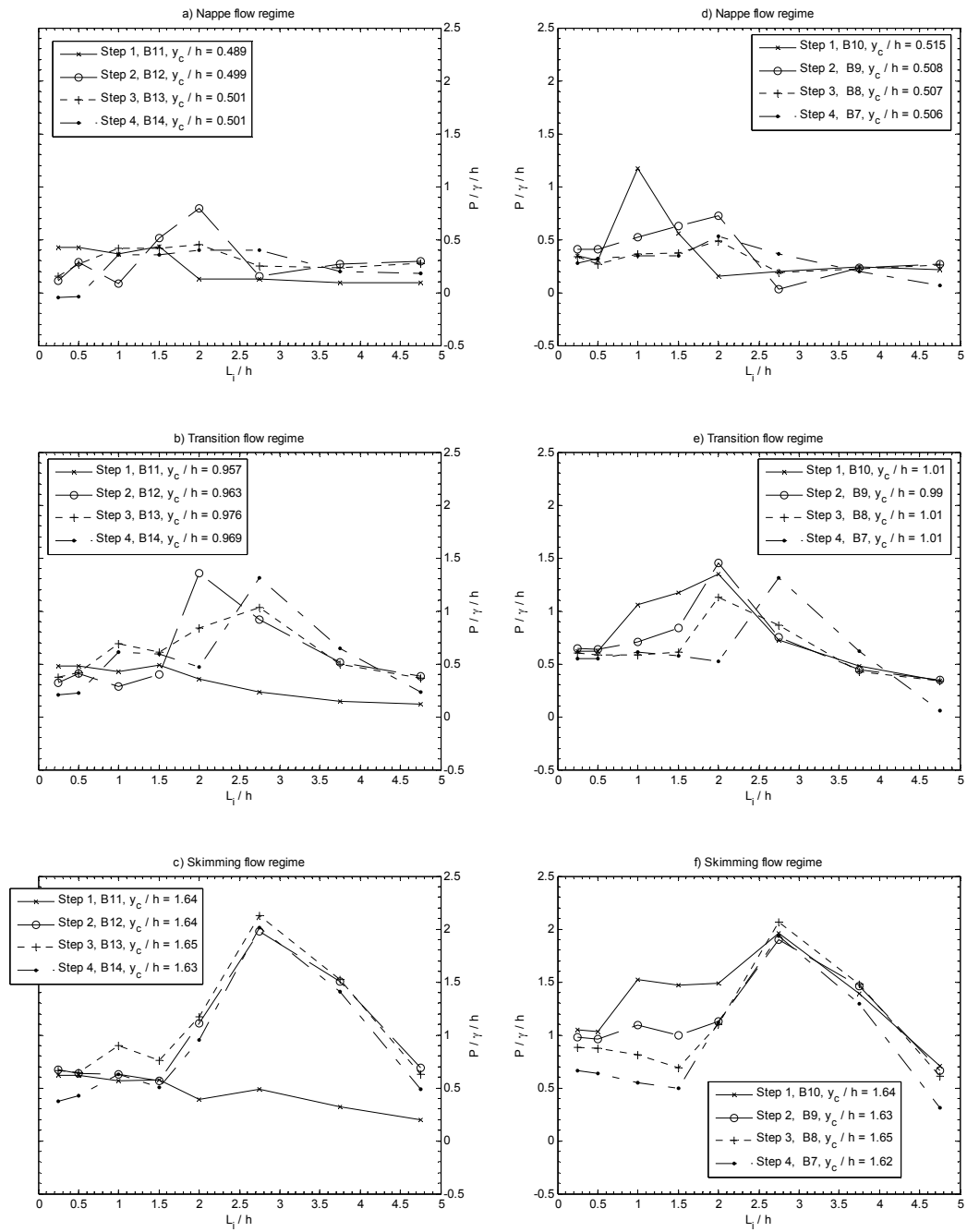
Figure 5.7 Average pressure on the treads of Model II. Aerated cavity:
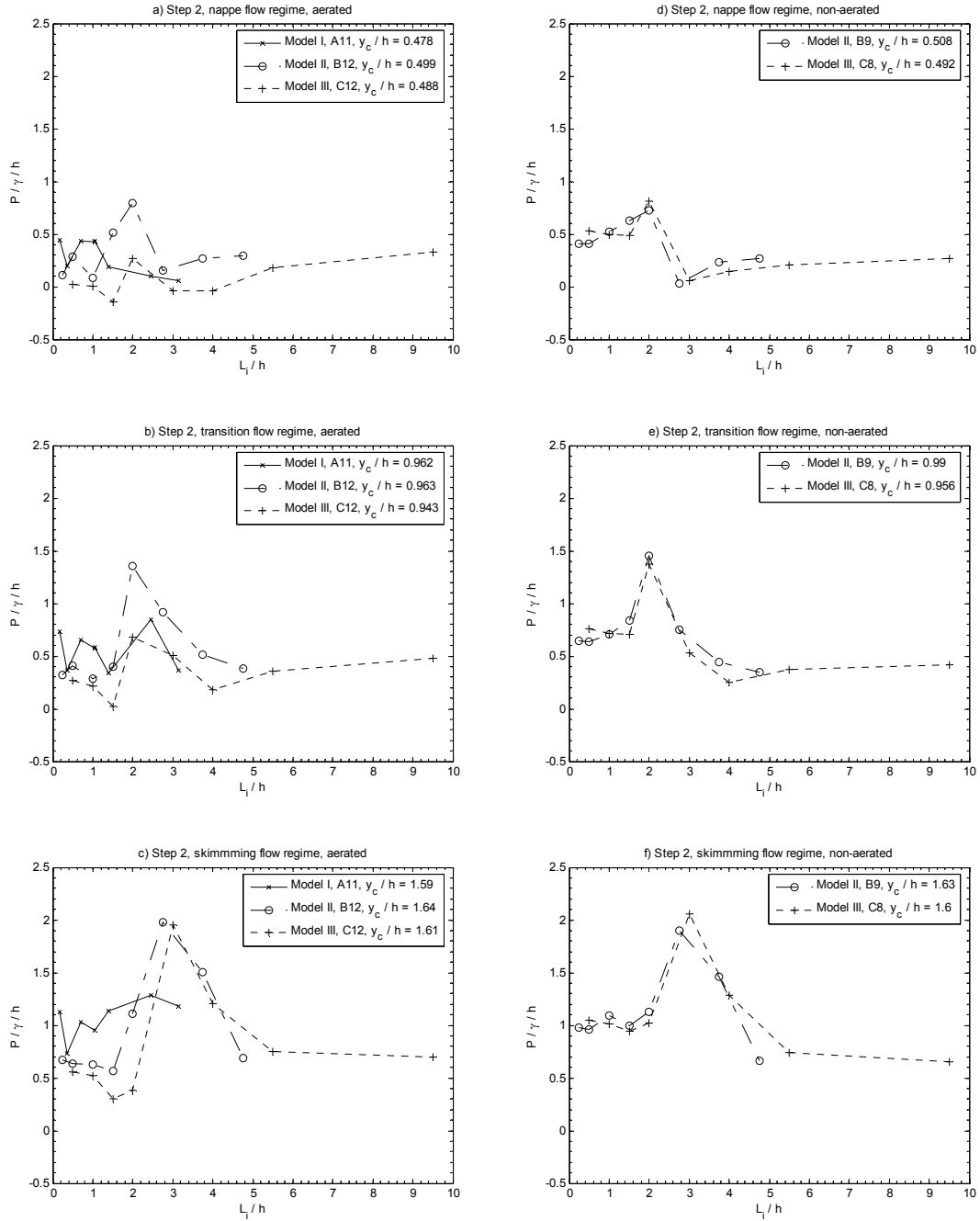
figures a to c; Non-aerated cavities: figures d to f.
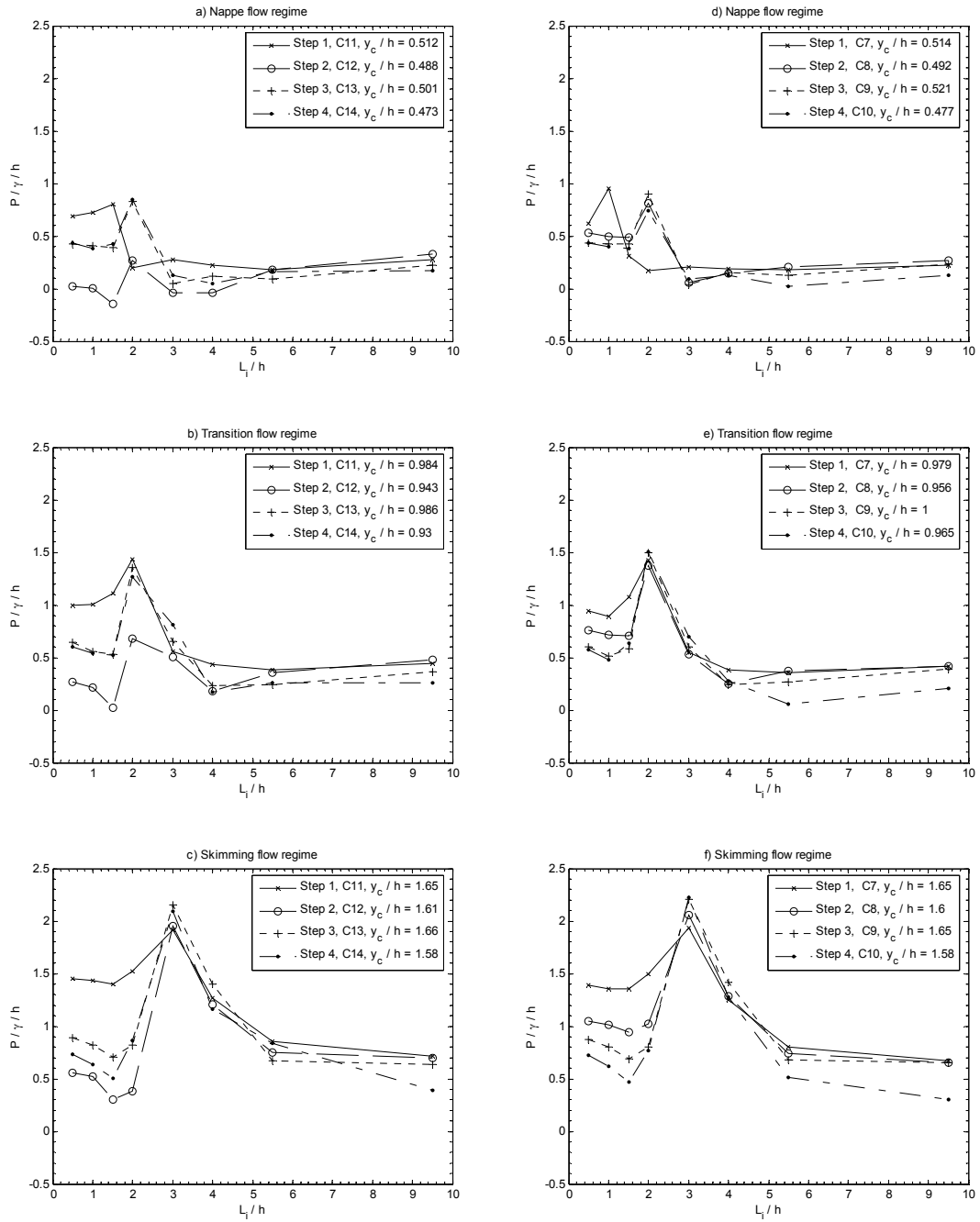
Figure 5.8 Average pressure on the treads of Model III. Aerated cavity:

figures a to c; Non-aerated cavities: figures d to f.
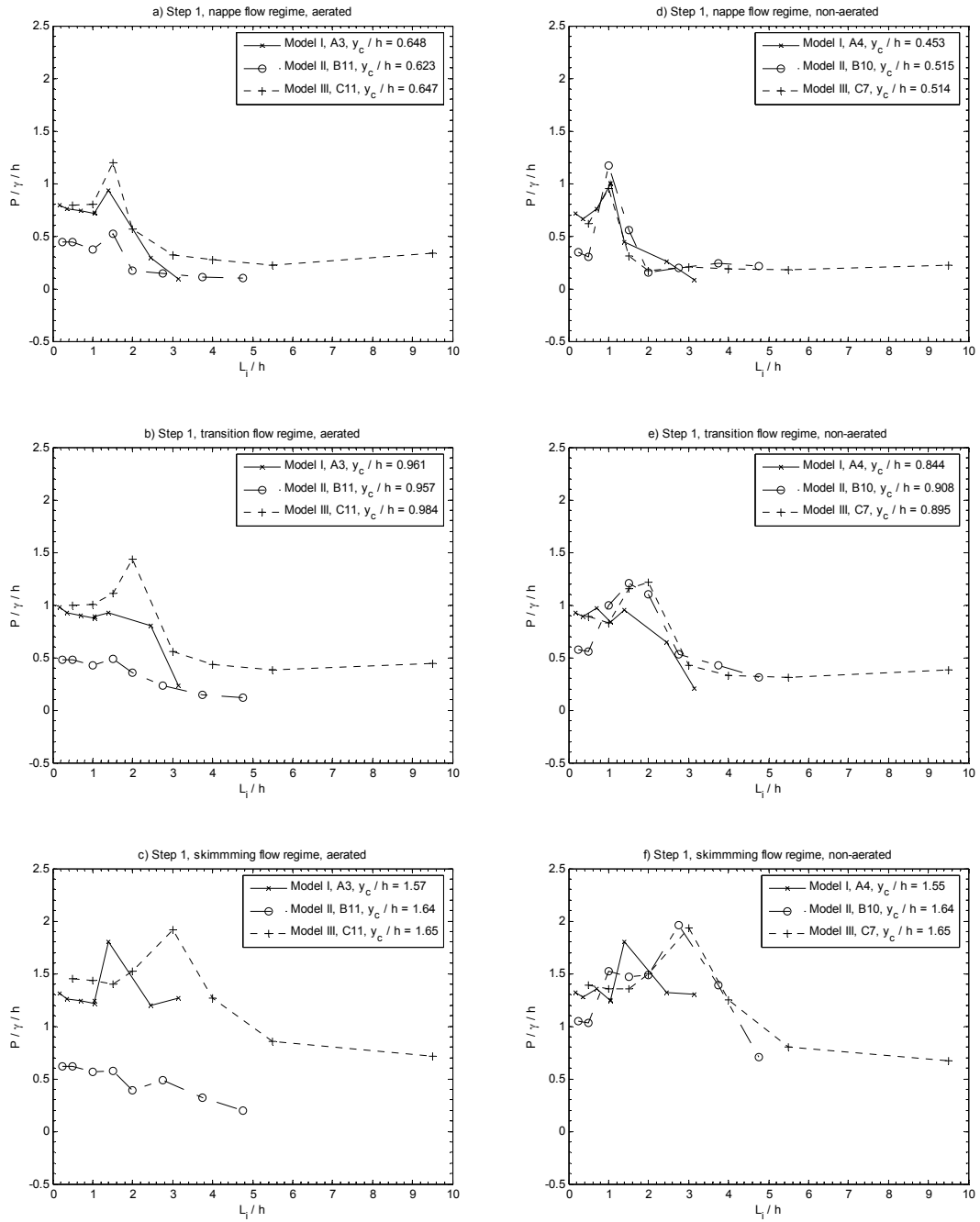
Figure 5.9 Average pressure on the tread of step 1.

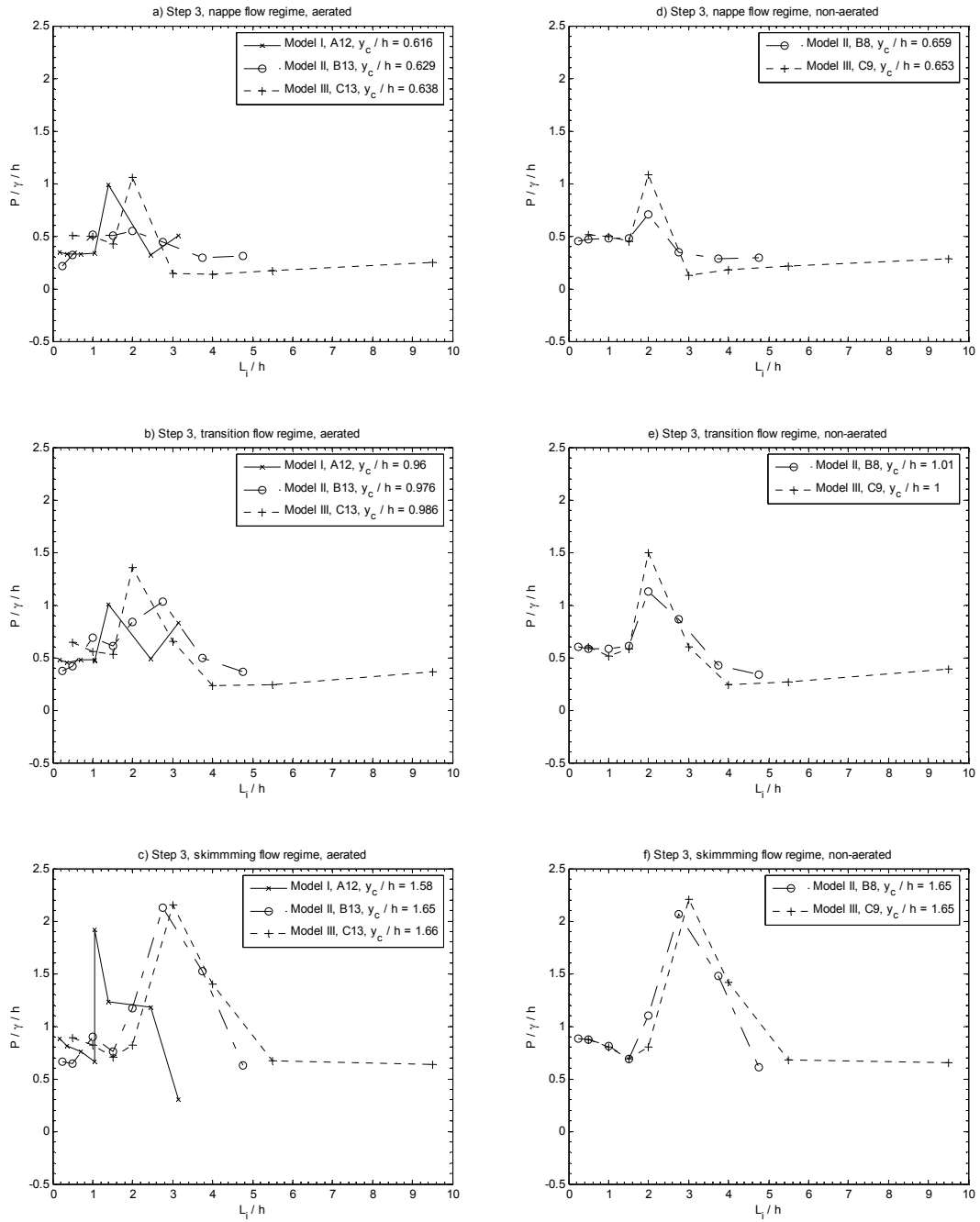**Figure 5.10** Average pressure on the tread of step 2.

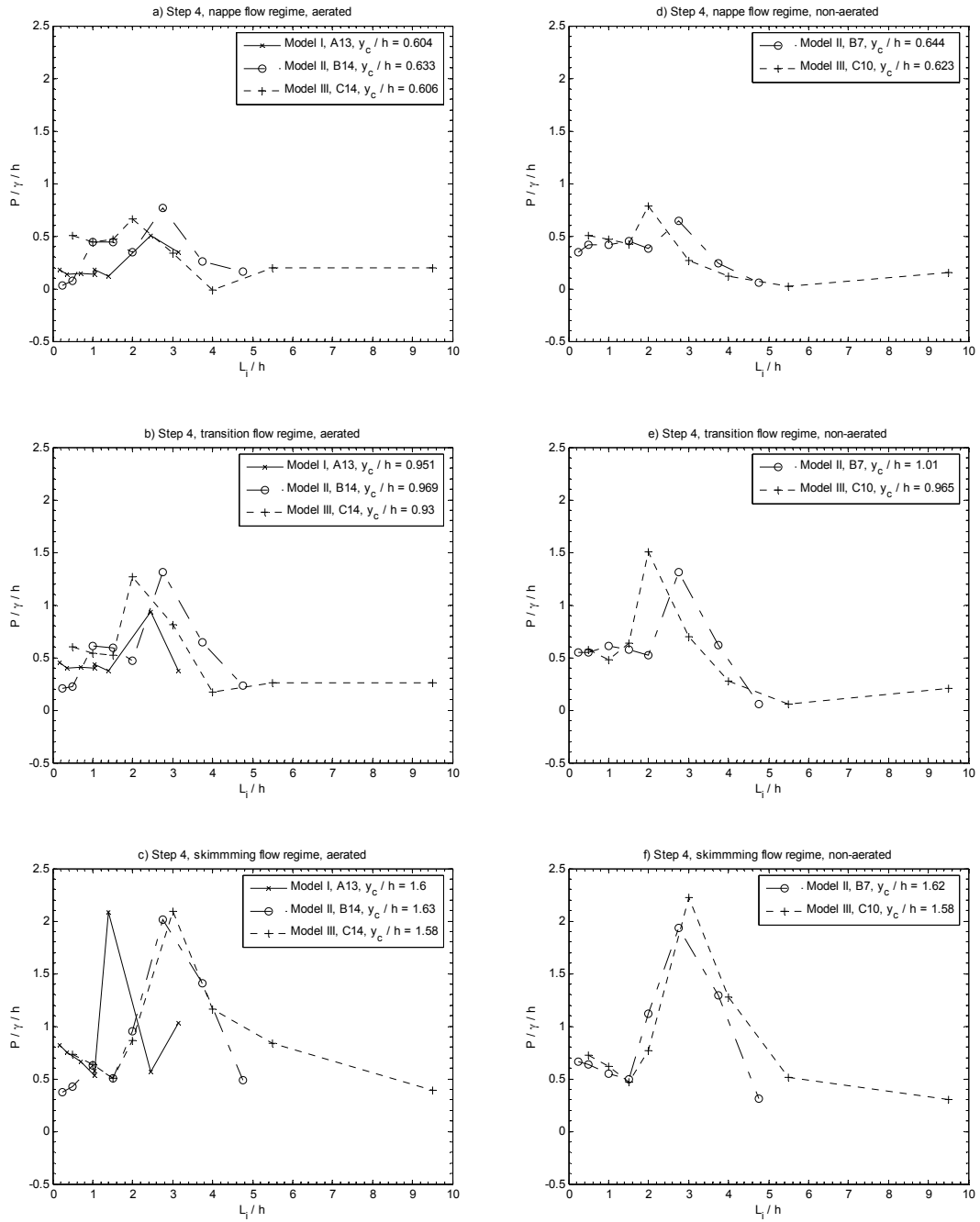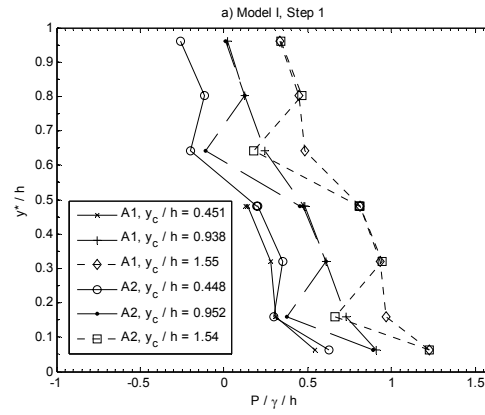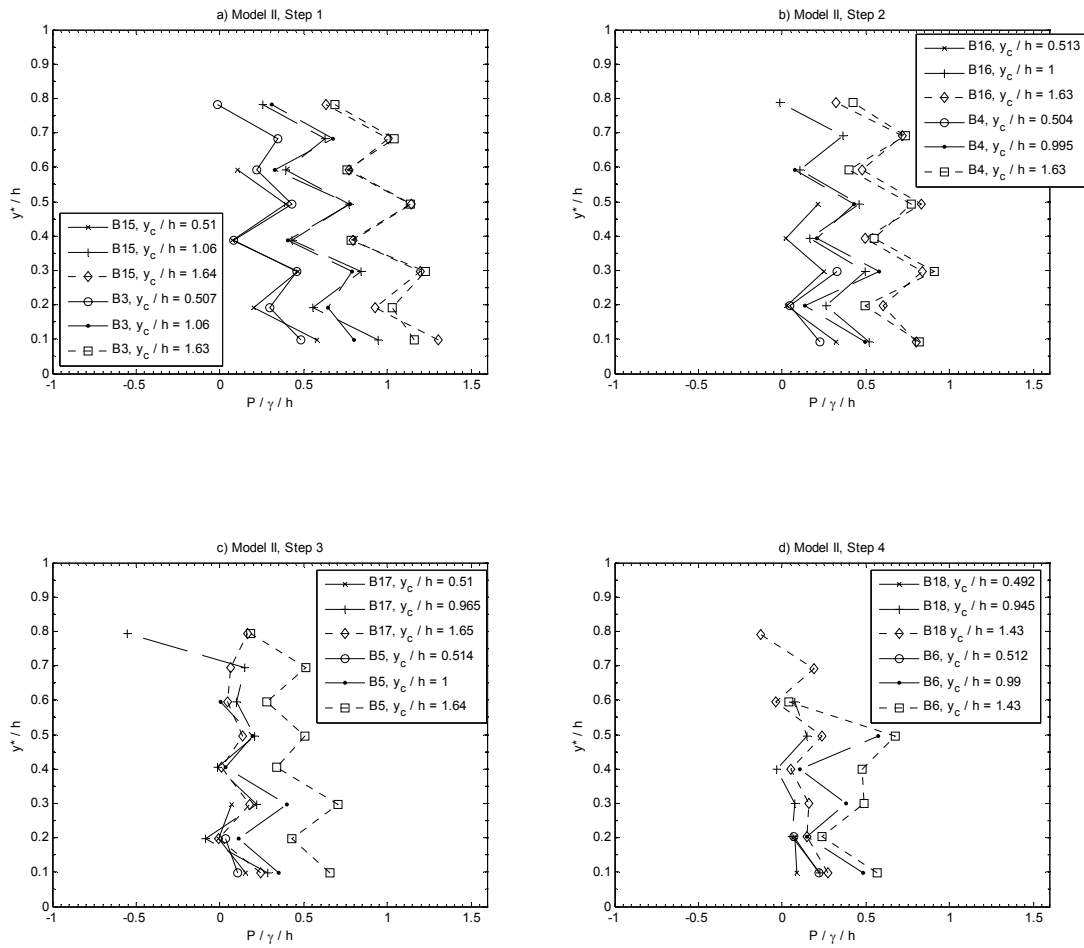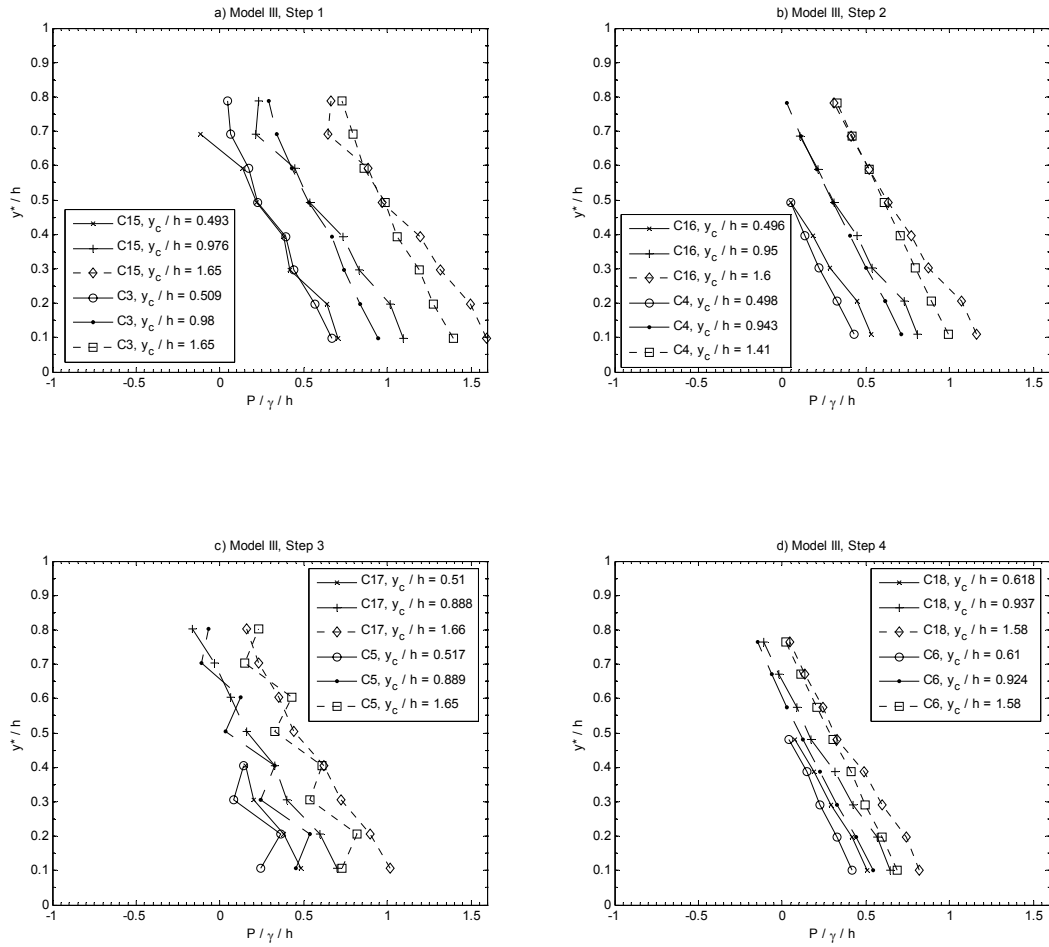**Figure 5.11** Average pressure on the tread of step 3.

Figure 5.12 Average pressure on the tread of step 4.

a) Model I, Step 1

Figure 5.13 Average pressures on the riser of step 1,

Model I. Aerated step cavity: run A1; non aerated

step cavity: run A2.

Figure 5.14 Average pressures on risers of Model II. Aerated step cavity:

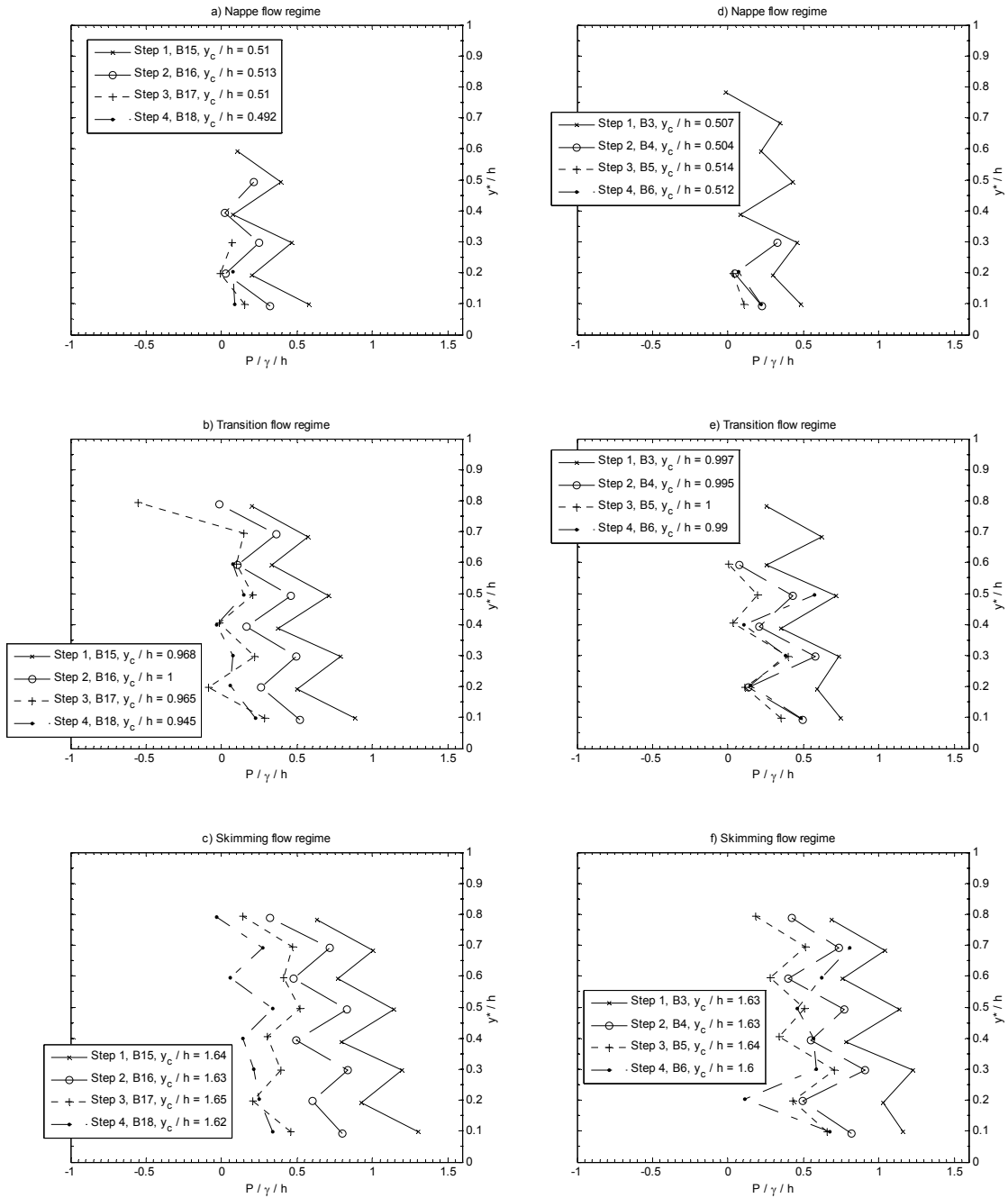runs B15-B18; non aerated step cavity: runs B3-B6.

Figure 5.15 Average pressures on risers of Model III. Aerated step

cavity: runs C15-C18; non aerated step cavity: runs C3-C6.
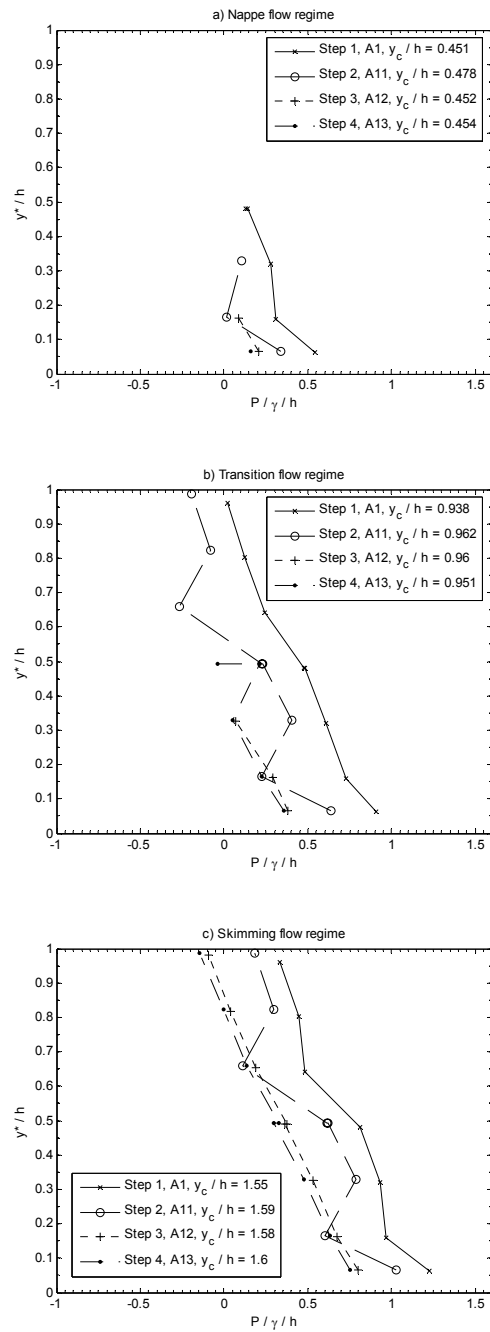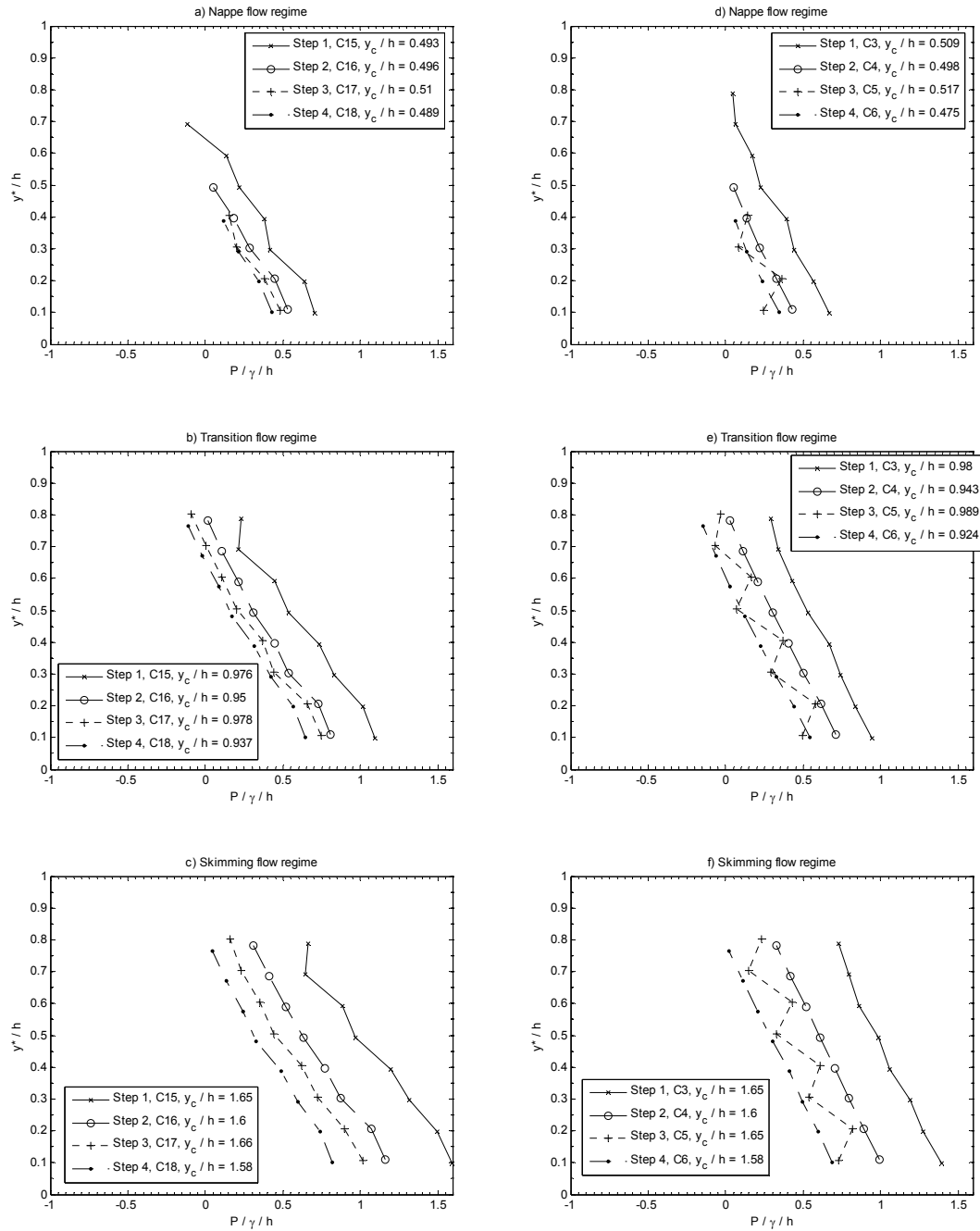
Figure 5.16 Average pressure on the risers of Model I.

Condition of the step cavity: aerated.

Figure 5.17 Average pressure on the risers of Model II. Aerated step

cavity: figures a to c; non-aerated step cavity: figures d to f.

Figure 5.18 Average pressure on the risers of Model III. Aerated step

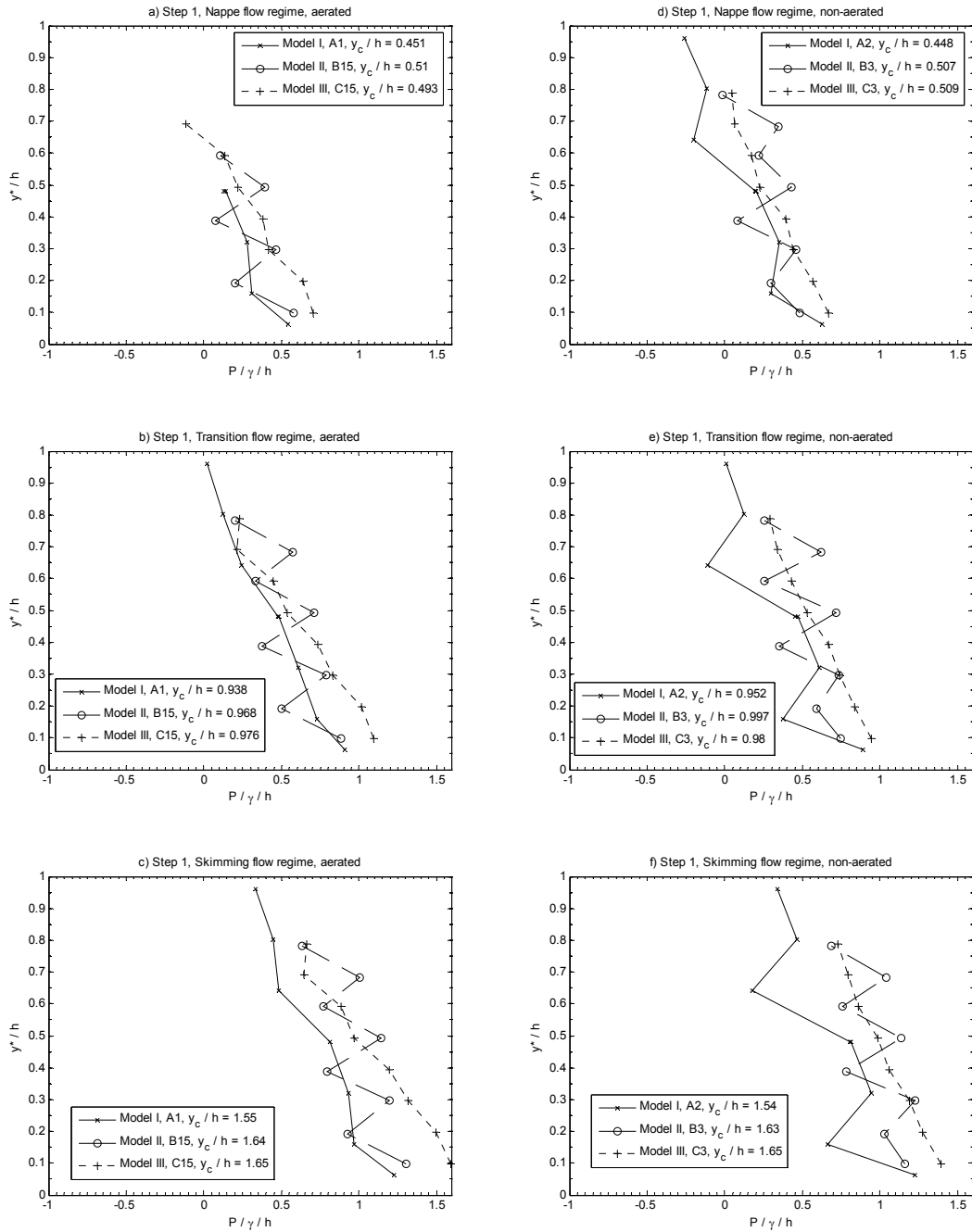cavity: figures a to c; non-aerated step cavity: figures d to f.

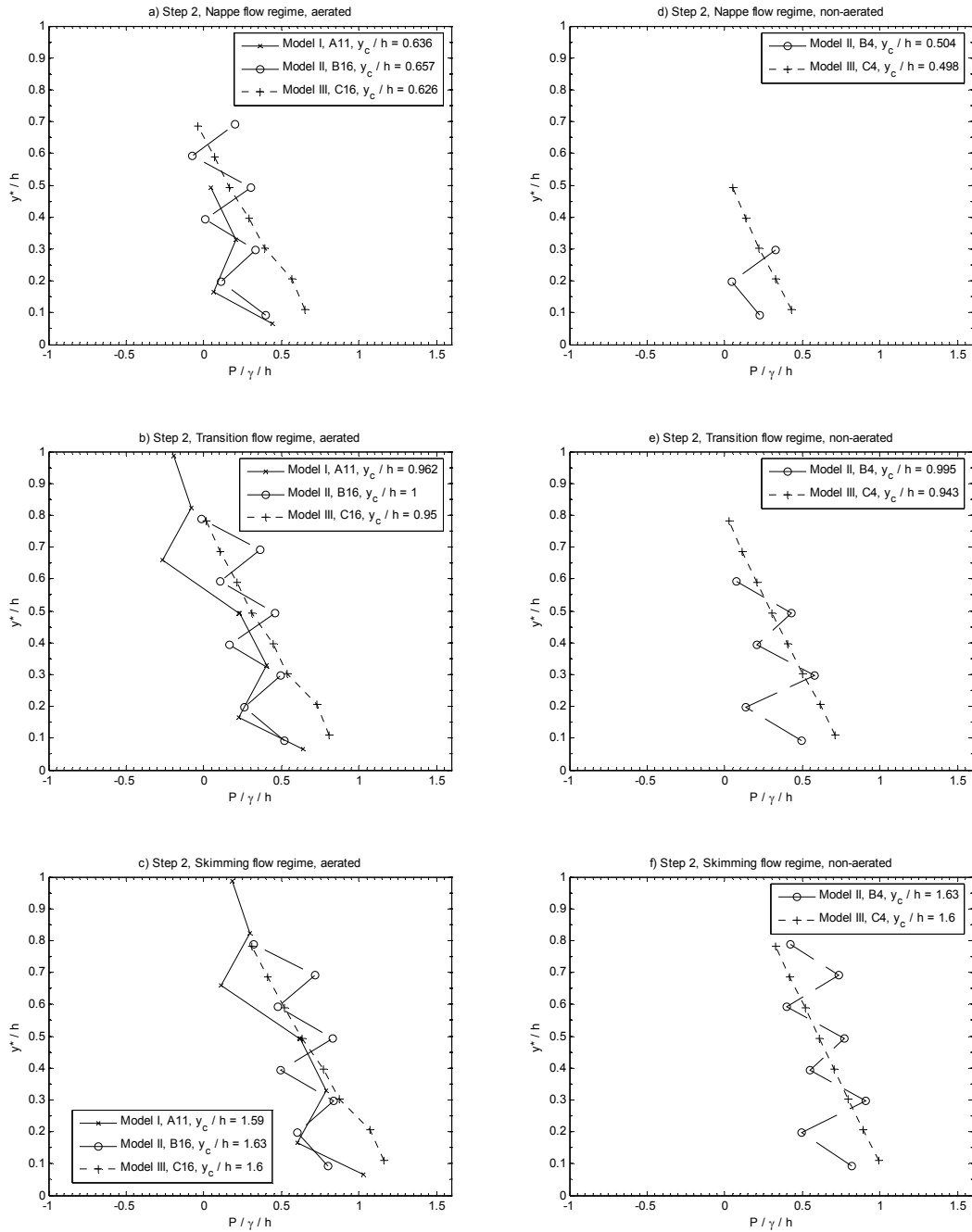**Figure 5.19** Average pressure on the riser of step 1.

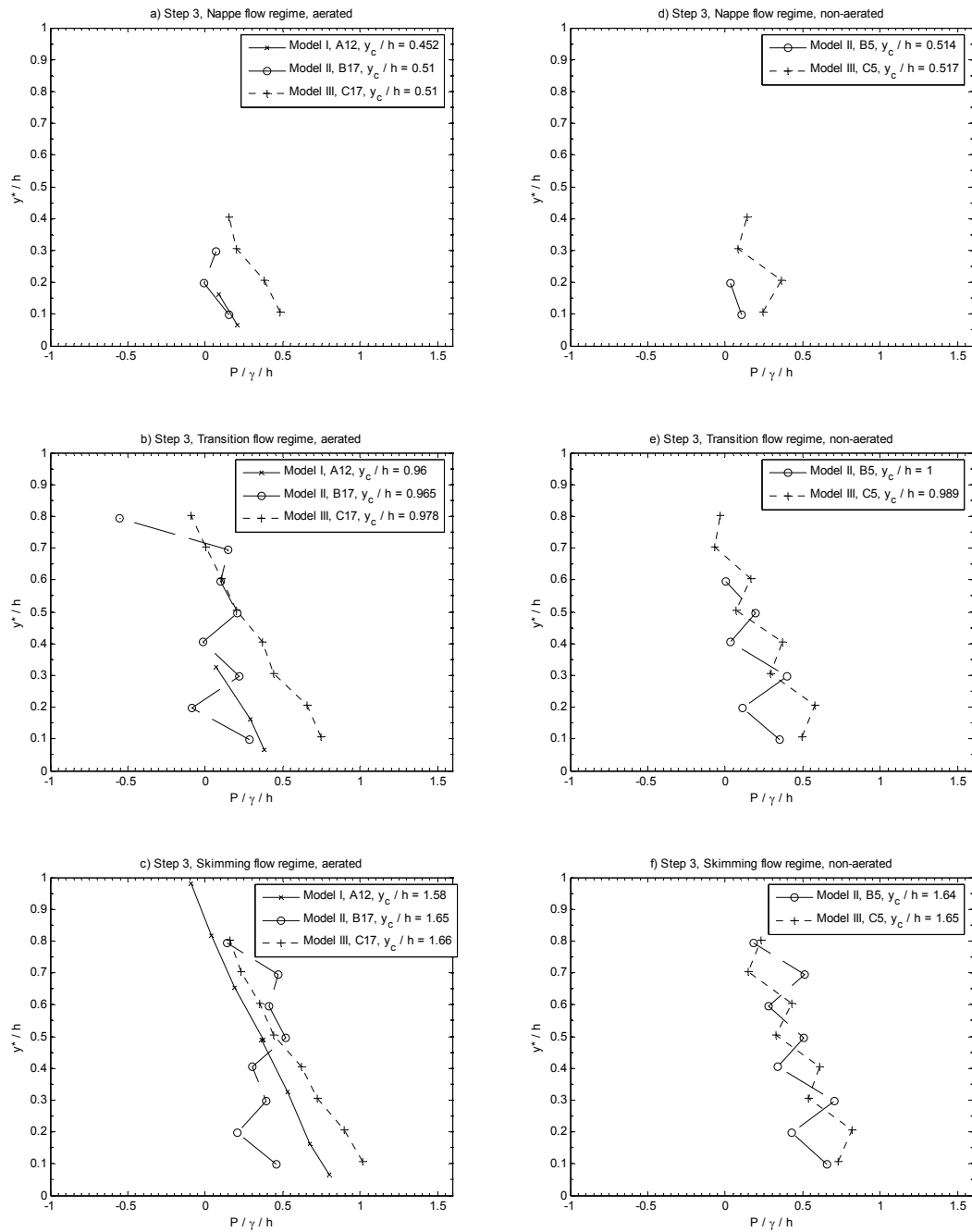**Figure 5.20** Average pressure on the riser of step 2.

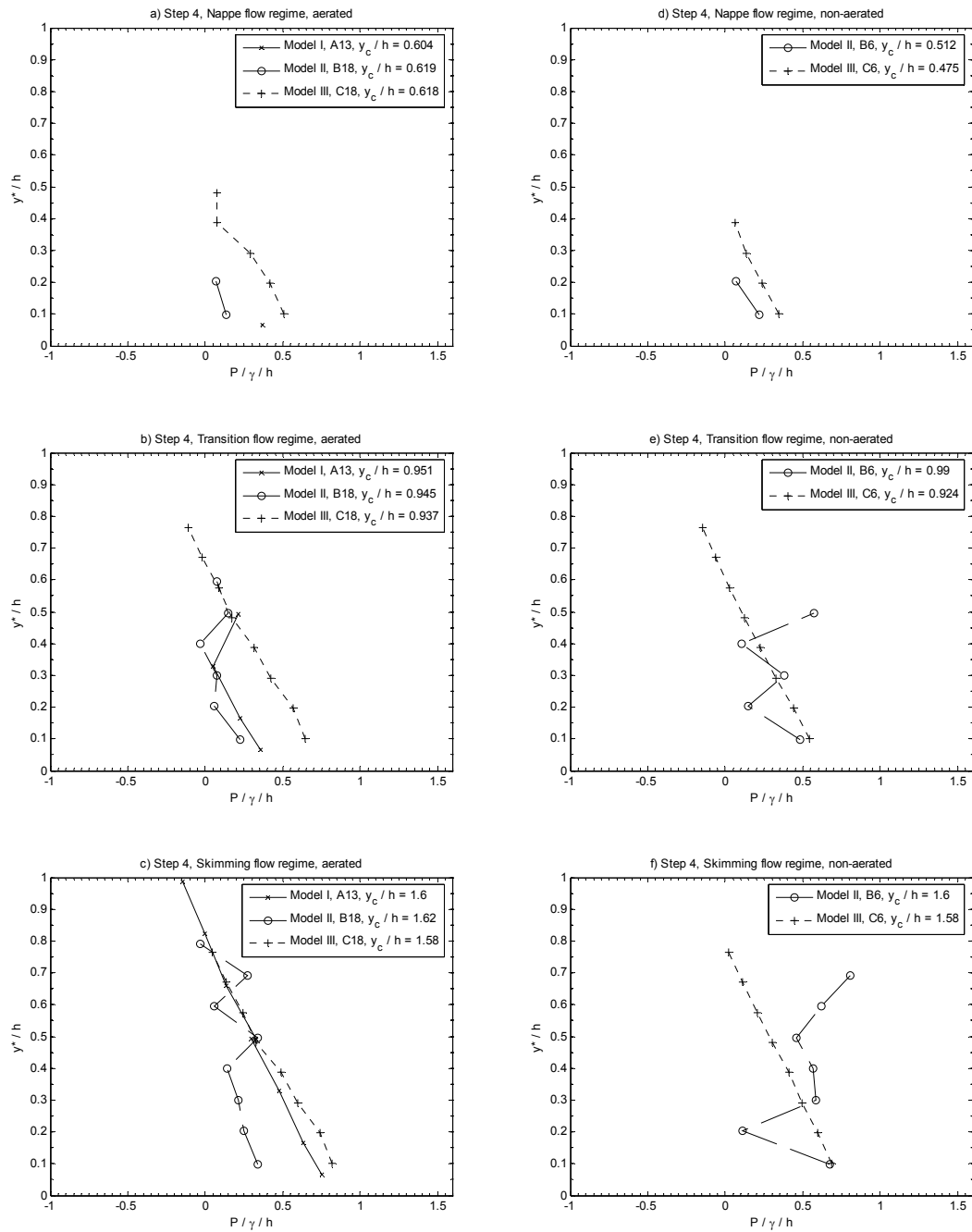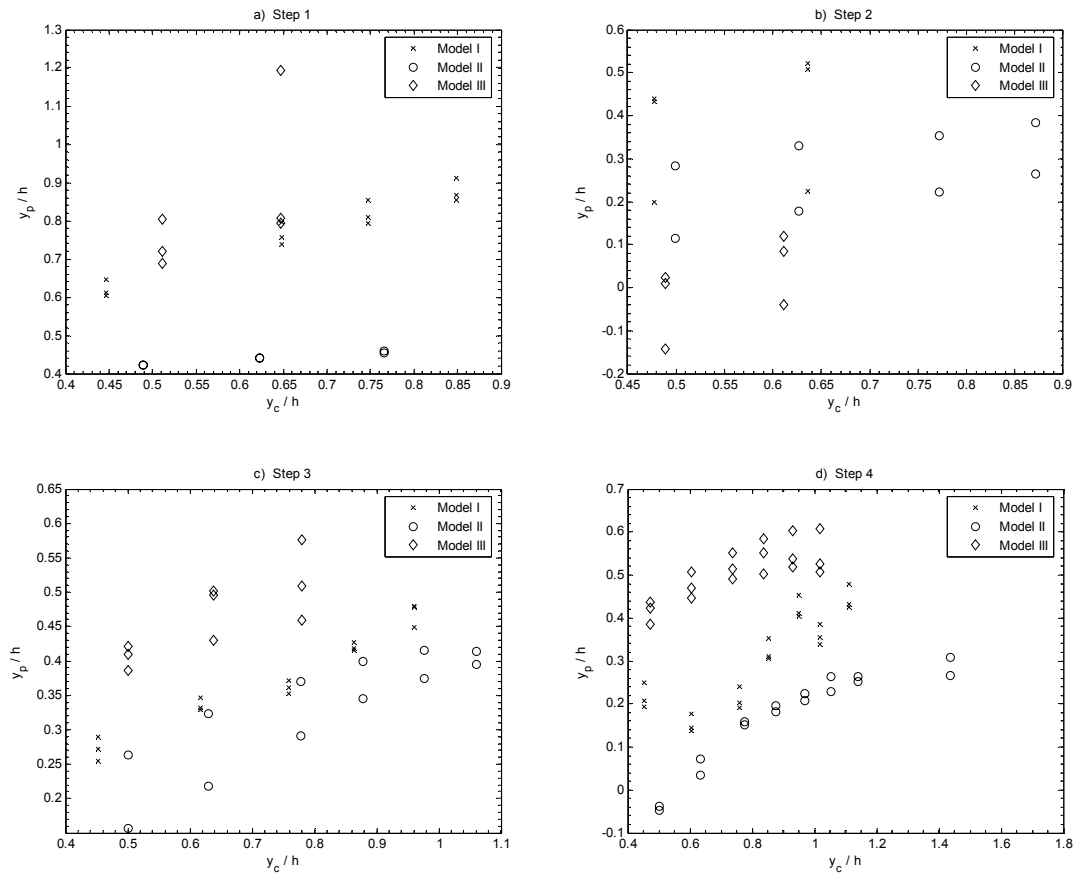**Figure 5.21** Average pressure on the riser of step 3.

Figure 5.22 Average pressure on the riser of step 4.

Figure 5.23 Correlation between water pool levels and discharge.

Condition of the step cavity: aerated.

_____

Chapter 6   Drop structure observations

_____

6.1 Introduction

Observations on a drop structure are presented in this chapter. These observations were taken on the first step of Model II. Initially, the location and conditions of the measurements are introduced then profiles of velocity and its gradient, turbulence intensity and normal stress, and finally local void fraction as well as chord length values are given.

6.2 Profile locations

Taking advantage of the geometric similarity between a drop structure and the first step of a stepped chute, profile measurements were carried out on Model II in order to study such a structure. The flow on a fully aerated drop structure can be divided into the free falling jet, the recirculating pool, the air cavity and the sliding jet, which is the section of the jet that is in contact with the recirculating pool (Figure 6.1). Several profiles were taken on the width centerline along the free falling and sliding jet using the

conical hot-film probe and the technique described in Chapter 4. The probe was carefully positioned parallel to the streamlines in order to fulfill the one-dimensional condition of the probe. The cases of an aerated cavity as well as of a fully depleted jet (non-aerated) were considered.

6.3 Velocity measurements

Velocity profiles on the midsection of the sliding jet are given in Figure 6.2. In this figure the ordinates were normalized using the jet thickness $\left(y_{jet} \right)$, which was considered to be the depth of maximum velocity gradient. The case of the aerated flow is presented in Figure 6.2a. Two discharges are shown in this figure and as can be seen, the velocity profiles agree fairly well. The case of the fully depleted jet is presented in Figure 6.2b and once again, the agreement is quite good. Furthermore, Figures 6.2c and 6.2d present the comparisons between the aerated and non-aerated conditions. These two figures indicate that at large discharges the profiles are alike while at small discharges the aerated condition has a slightly sharper transition form the jet area to the pool area as well as an almost vertical distribution.

The observations of the velocity profiles suggest an influence of the recirculating pool on the sliding jet. At small discharges the length of the sliding jet is smaller (large air cavity) and therefore there is less contact and possibility of energy dissipation at the interface between both areas. Hence, at small discharges the profiles would differ since there is a slim possibility of interaction while at large discharges the larger interface length benefits the interaction. The difference corresponds to the sharper transition and an

almost vertical distribution as mentioned before. In the case of a fully depleted jet, the length is maximized and consequently, the velocity profiles would agree as observed.

Figure 6.3 shows the velocity gradient at the midsection of the sliding jet. As in the case of velocity, the gradients of the aerated and non-aerated conditions agree as well. This figure suggests that maximum values of shear stress are located at the jet/pool interface, but then decrease rapidly in both directions and are almost negligible about 40% of the distance from this interface.

Turbulence intensity profiles are presented in Figure 6.4. Similarly, Figure 6.4a and 6.4b present the aerated and non-aerated cases, respectively. Comparison between these two cases is given in Figures 6.4c and 6.4d; the profiles are similar in shape. Small turbulence levels $(Tu < 10\%)$ were measured in the jet area and as the measurements approach the pool section, the values of Tu increase to a maximum of about 55% for the smallest discharge and 50% for the largest discharge. Once inside the recirculating pool, the turbulence intensity decreases slightly. In addition to the aforementioned profiles, Figure 6.5 gives the normal stress profiles. As in the case of the previous variables, the profiles agree in shape for both cases: aerated and fully depleted jet. Minimum values were recorded near the surface and deep inside the recirculating pool. Maximum values of u^2 were measured at the transition between the jet and the pool.

The measurements of turbulence intensity and normal stress suggest a coherent flow profile on the sliding jet area with well define streamlines and small energy dissipation within. On the other hand, the recirculating pool area has a more chaotic flow structure with energy dissipation taking place due to the high levels of turbulence intensity. Nevertheless, the majority of the energy dissipation is estimated to occur along

the interface between the sliding jet and the pool, where the maximum values of turbulence, shear and normal stress were measured. The measurements also suggest a continuous transfer of momentum and energy from the sliding jet towards the pool. In fact, the observed distribution of normal stress (Fig. 6.5) indicates that the transformation into kinetic energy initiates at about $y/y_{jet} = 0.8$, where the larger increments in Tu begin. The maximum transfer of kinetic energy seems to occur at the interface between the jet and the pool and decays rapidly towards the center of the pool, most likely due to the dissipation by viscous forces.

Figure 6.6 presents the velocity profiles along the trajectory of the flow. The approach flow to the brink was subcritical and velocity profiles at this location are given in Figure 6.6a. The profiles at this section are not uniform and they present larger velocities closer to the bottom. Rajaratnam and Muralidhar (1968) as well as Chamani (1993) measured similar profiles. Measured velocity gradient, turbulence intensity levels as well as normal stress presented negligible values at this location (see Figures 6.7 to 6.9). Figure 6.6b gives the velocity distribution in the midsection of the free falling jet and in this figure, y_{jet}, corresponds to the actual thickness of the jet. This profile was taken at a tilt angle of 41° and it is quite distinctive from the one at the brink. The velocity field has redistributed and resembles a plug flow, although it has a small "S" shape where the velocities on the top half of have increased considerable with respect to those values at the brink, possible due to the gravitational effect, whereas at the lower nappe they have increased slightly in accordance with new boundary conditions, i.e., air. The measured profile agrees in general terms with the ones given by Chamani (1993) but unfortunately, the level of detail presented by Chamani was not enough to allow an

adequate comparison. Similar to the brink section, values of velocity gradient, turbulence intensity and normal stress were negligible.

Velocity profiles in the sliding jet are given in Figure 6.5c. This figure presents profiles at the intersection line and at the midsection of the sliding jet; they were taken at tilt angles of $45°$ $(y_c/h = 0.489)$ and $40°$ $(y_c/h = 0.779)$. The velocity profile at the intersection line presents a more accentuated "S" shape with still larger velocity values on the bottom section of the jet. Given the shape of the profile, it seems that the gravitational effect together with the two air boundaries has its maximum influence at the section. No effect of the recirculating pool is felt yet at this location. The transition of the profile towards the pool is sharp and the values of velocity inside the pool get close to zero quickly, this indicates the possibility of a stagnation zone in the vicinity of the intersection between the free falling jet and the pool. On the other hand, the profiles at the midsection of the sliding jet showed the interaction effects of the recirculating pool. Lower velocities were measured on the bottom section of the jet while larger ones were measured at the top, resembling a uniform velocity profile. This re-arrangement of the velocity profile is likely to be caused by the strong interaction between the recirculating pool and the jet. Moreover, this interaction developed velocities in the recirculating pool and therefore there is a profile inside the pool, in which the decrease in velocity is less abrupt. Chamani (1993) and Lin et al. (2002) measured similar profiles in the midsection of a sliding jet. Magnitudes and profiles of velocity gradient, turbulence intensity and normal stress were similar in both, intersection line and midsection, (Figure 6.7 to 6.9).

Finally, the velocity field at the toe of the sliding jet is giving in Figure 6.6d. The shape is fairly uniform and they are in agreement with the profiles reported by

Bakhmeteff and Feodoroff (1943). Measured turbulence intensities were smaller than 12% while normal stress values were smaller than 0.03; in both cases, the maximum values occurred close to the bottom. Downstream of this location the flow was always supercritical.

6.4 Local void fraction and chord lengths

Similar to velocity, the local void fraction was measured at the brink, as a free falling jet, a sliding jet, and at the toe. Nevertheless, small values were measured at all sections. Figure 6.10 shows the variation of the void fraction profile with depth. Two things are noticeable form this figure. Firstly, the distribution of the local void fraction has a similar shape for both discharges and secondly, larger void fractions were detected inside the reciculating pool area where turbulence intensity levels where also larger.

Chord lengths distributions at the intersection line and at the midsection of the sliding jet are presented in Figure 6.11. Inspection of this figure suggests that more bubbles were detected in the intersection line than at the midsection. Furthermore, chord sizes at the intersection line are smaller than at the midsection.
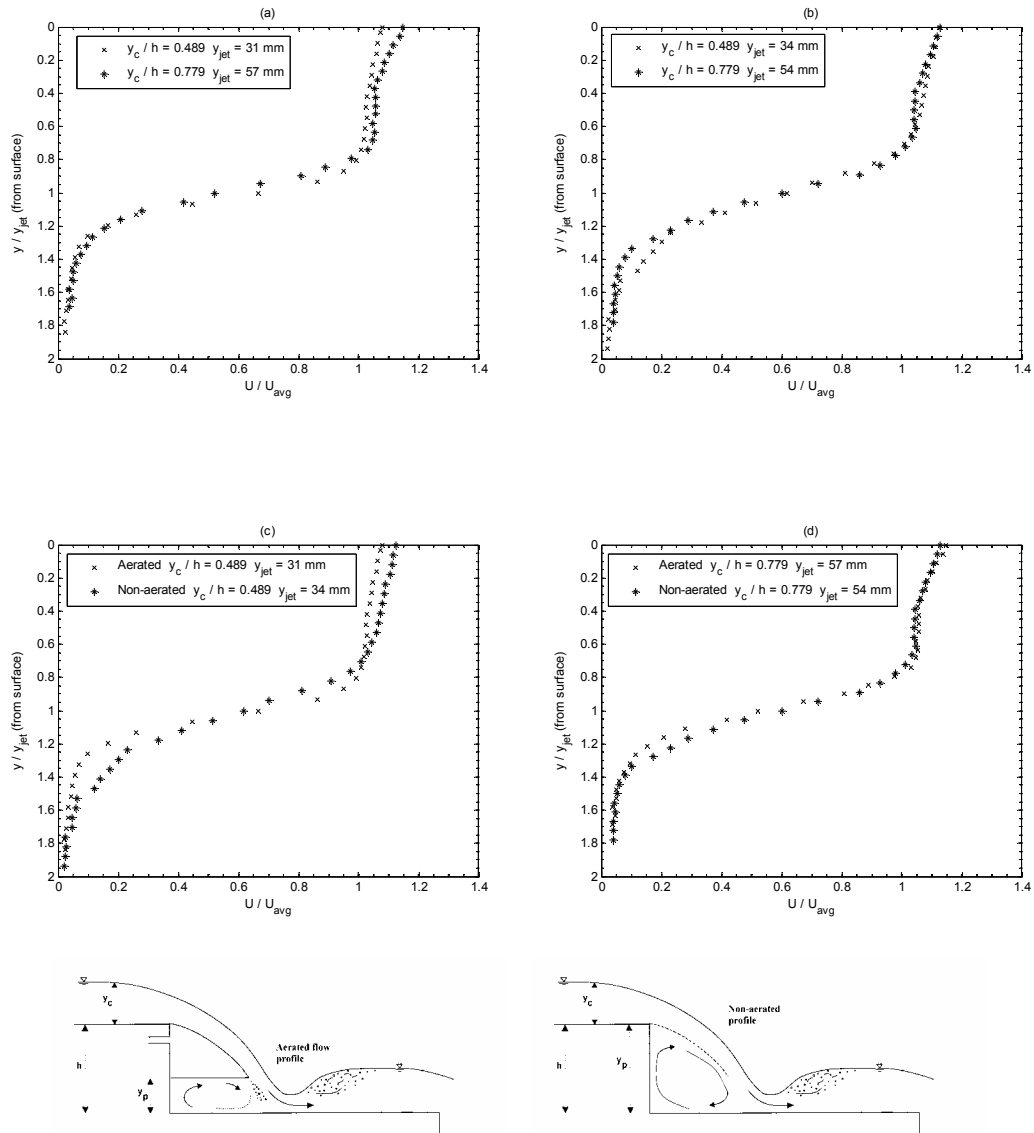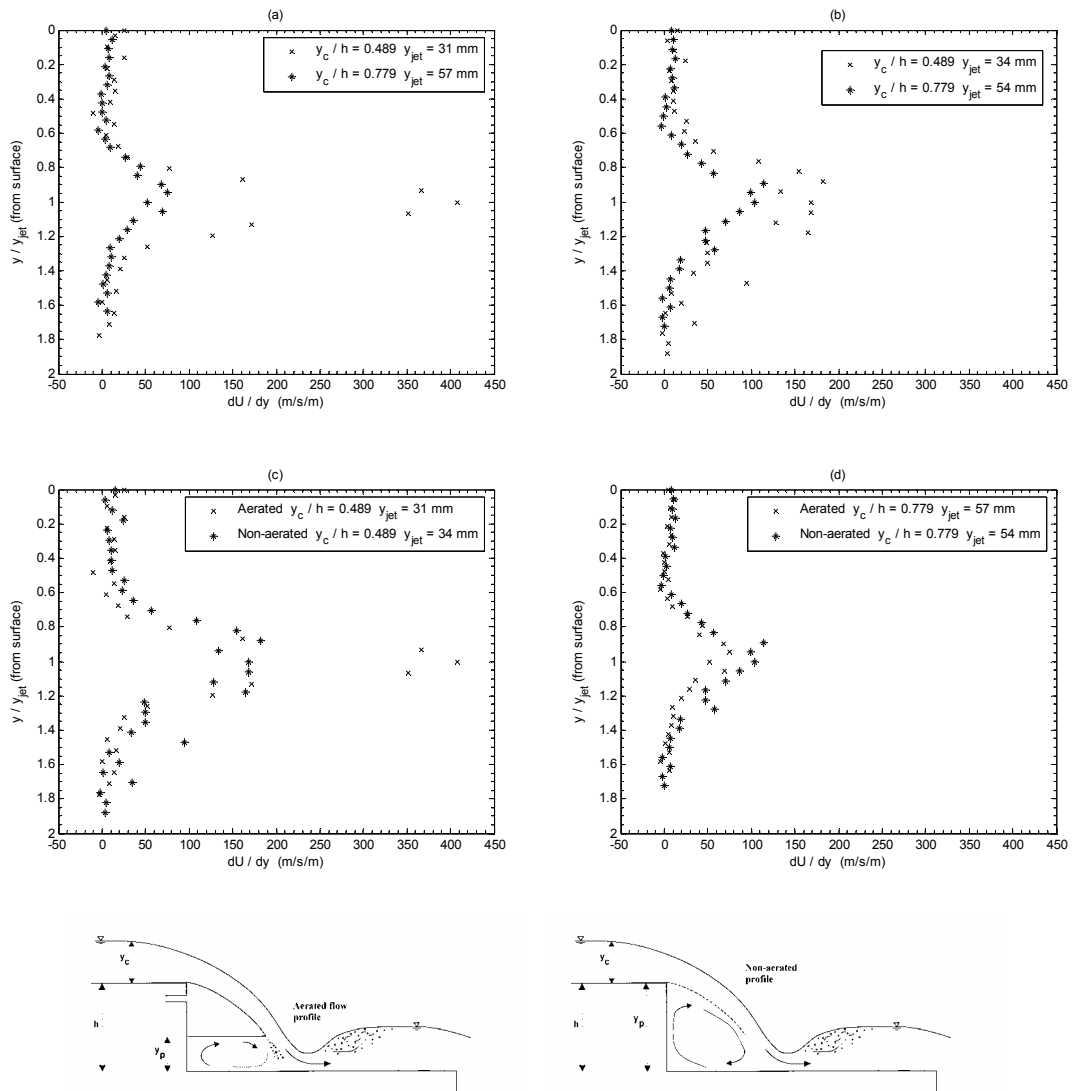
a)
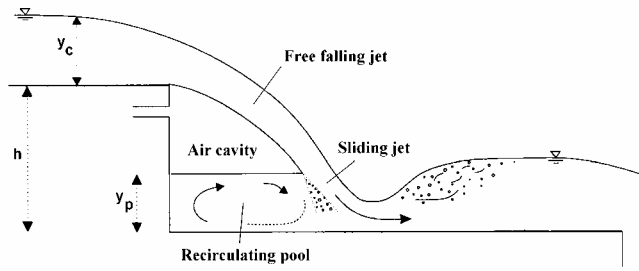
b)
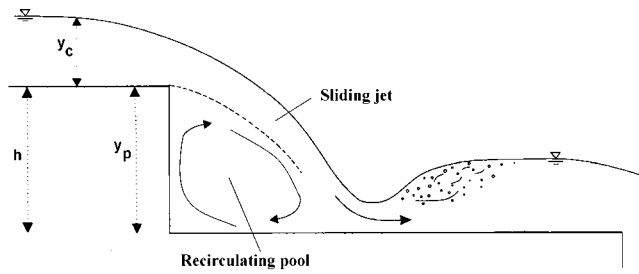
Figure 6.1 Flow geometry at a drop structure. a) aerated step cavity; b) non-aerated step cavity.
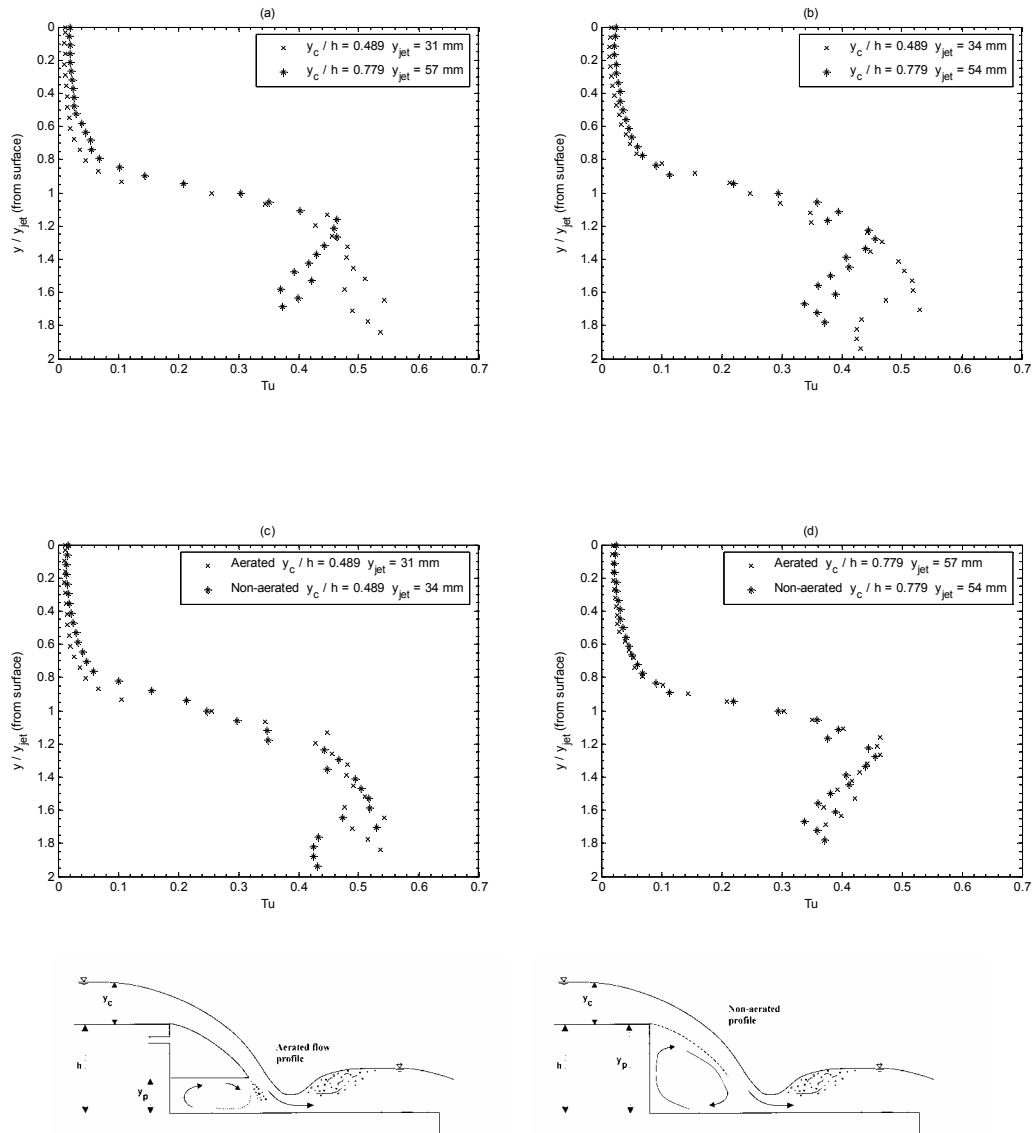
Figure 6.2 Velocity profiles on the midsection of the sliding jet. a) Aerated flow; b) fully depleted nappe; c) low discharge, d) large discharge.

Figure 6.3 Velocity gradient profiles on the midsection of the sliding jet.

a) Aerated flow; b) fully depleted nappe; c) low discharge, d) large

discharge.

Figure 6.4 Turbulence intensity profiles on the midsection of the sliding jet. a) Aerated flow; b) fully depleted nappe; c) low discharge, d) large discharge.
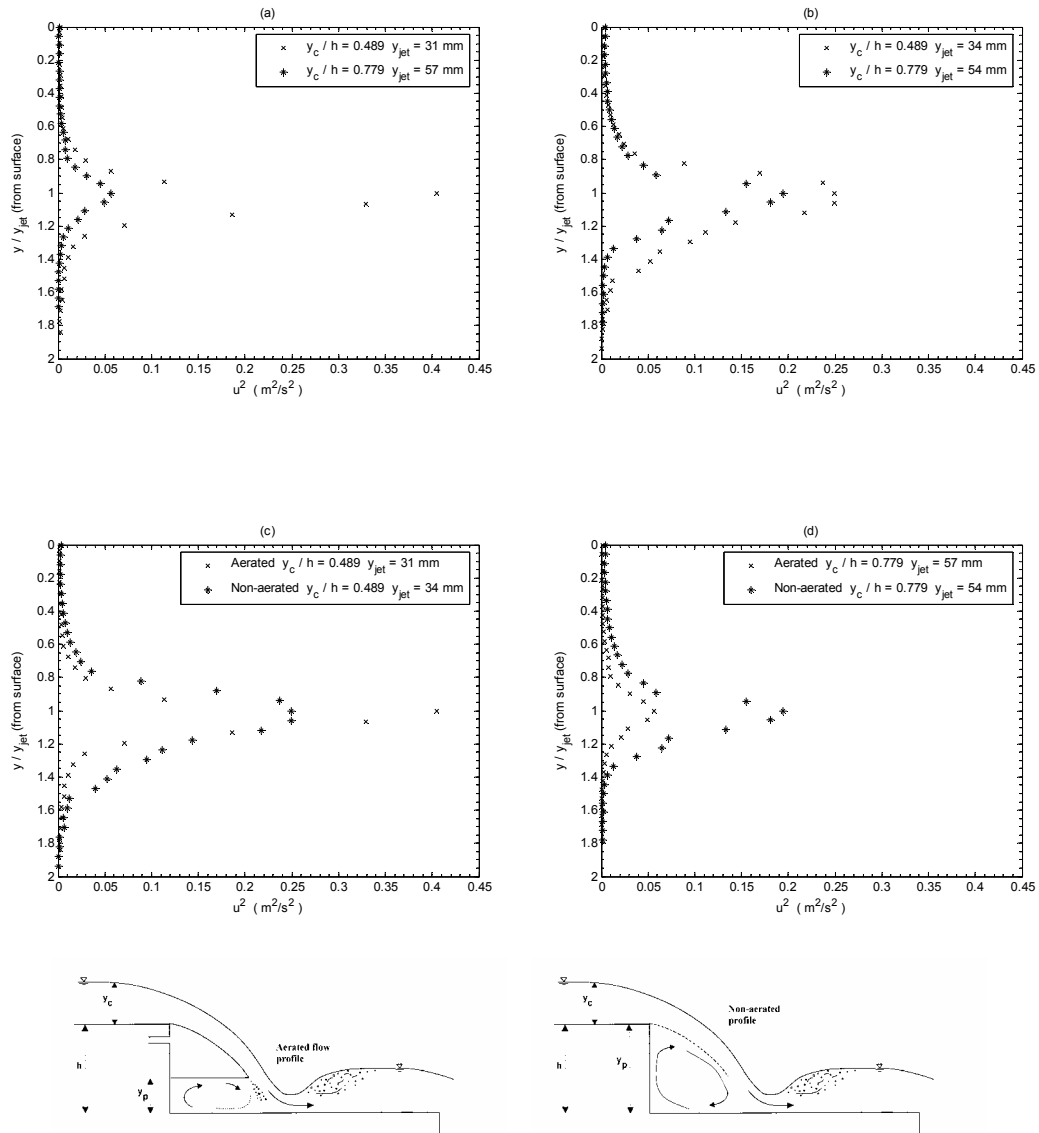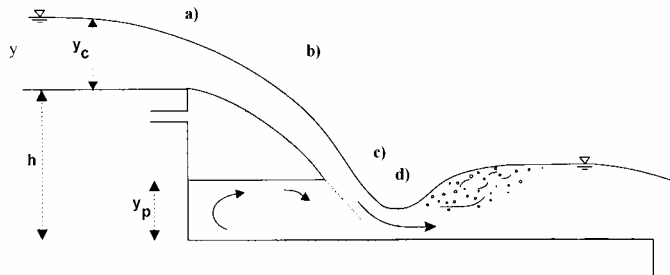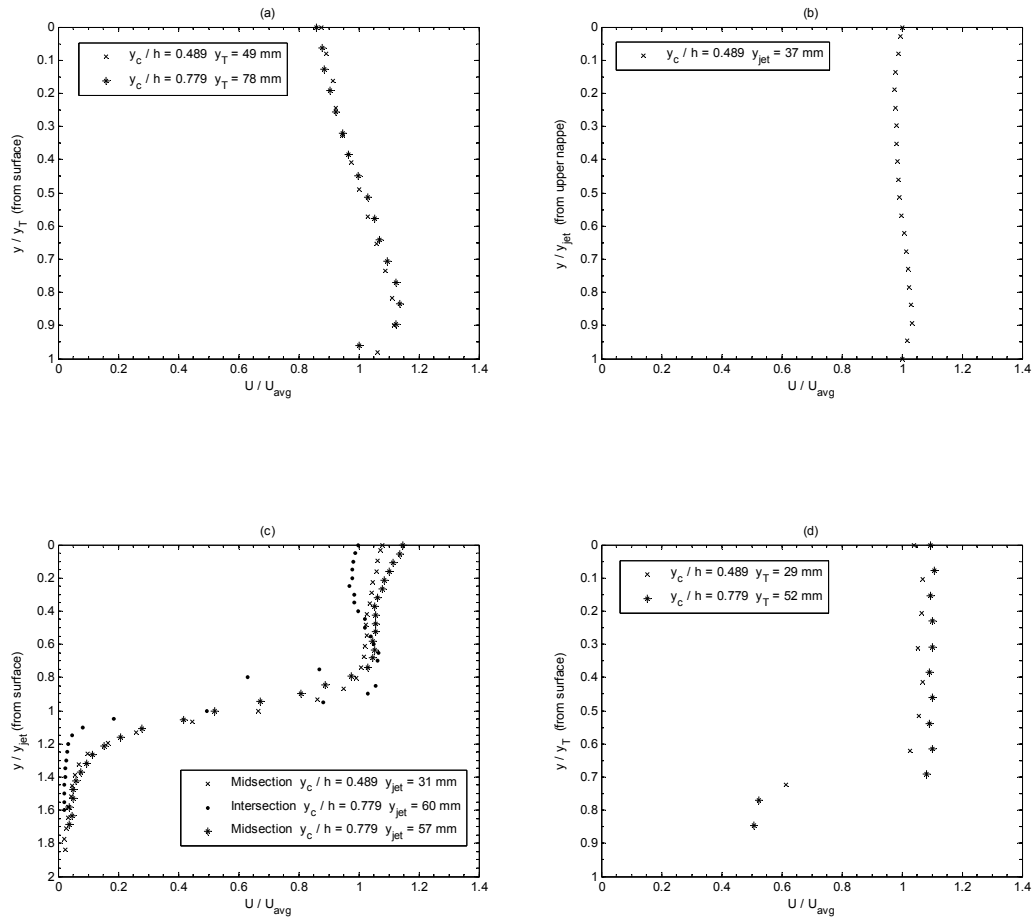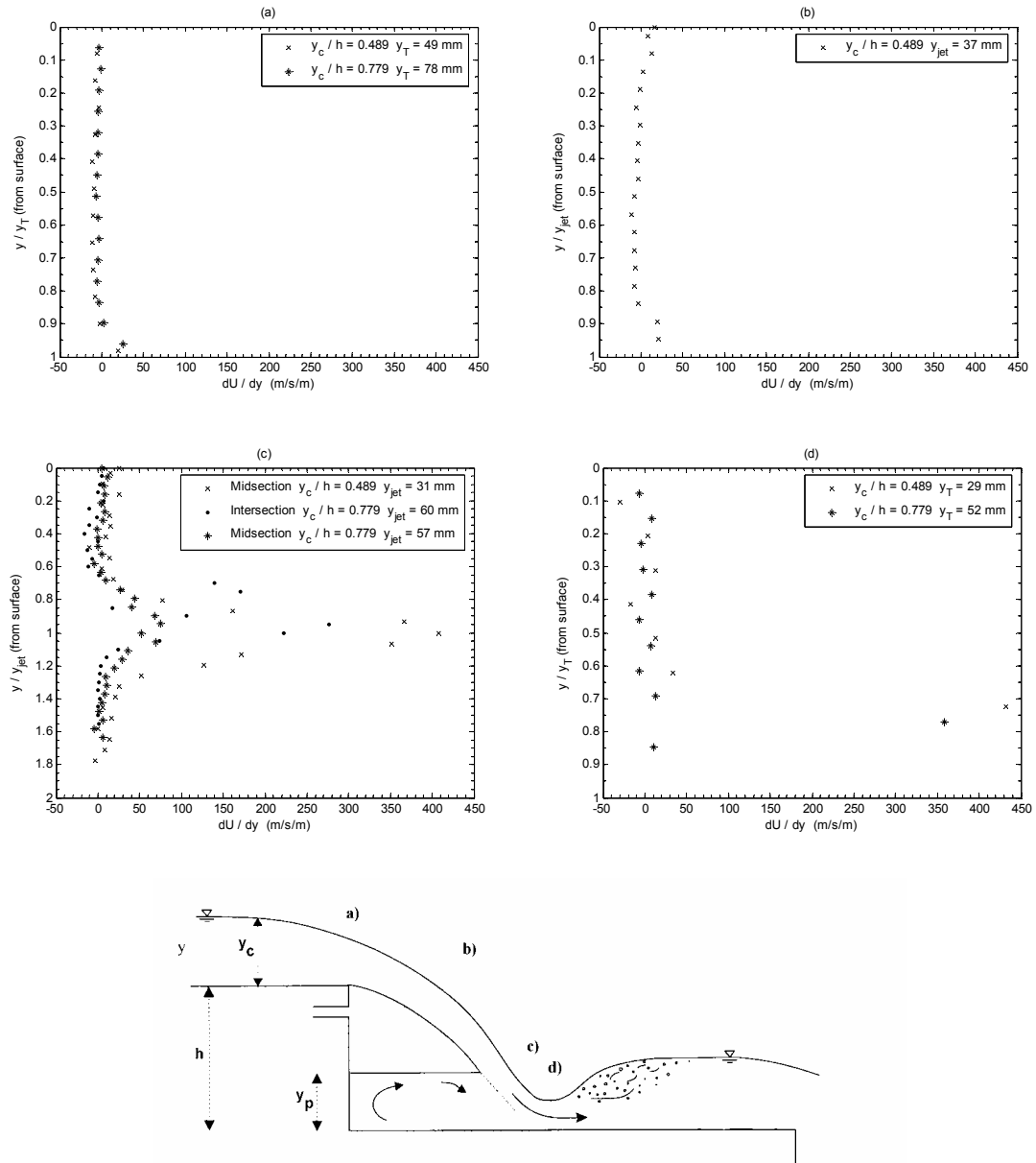
**Figure 6.5** Normal stress profiles on the midsection of sliding jet. a) Aerated flow; b) fully depleted nappe; c) low discharge, d) large discharge.

Figure 6.6 Velocity profiles along the jet trajectory. a) upstream brink;

b) free falling jet; c) sliding jet, d) toe of sliding jet.

Figure 6.7 Velocity gradient profiles along the jet trajectory. a) upstream

brink; b) free falling jet; c) sliding jet, d) toe of sliding jet.
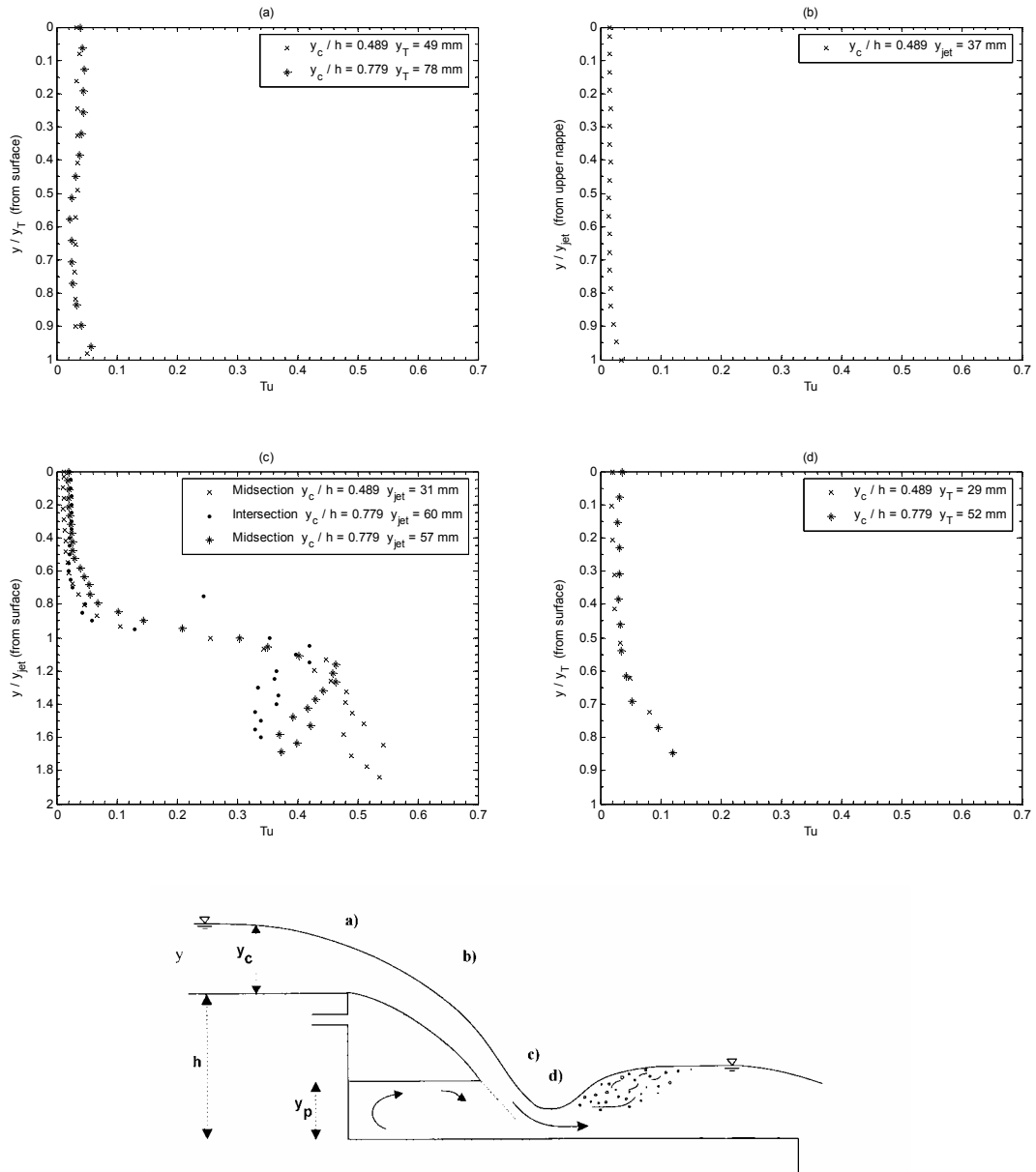
Figure 6.8 Turbulence intensity profiles along the jet trajectory. a) upstream brink; b) free falling jet; c) sliding jet, d) toe of sliding jet.
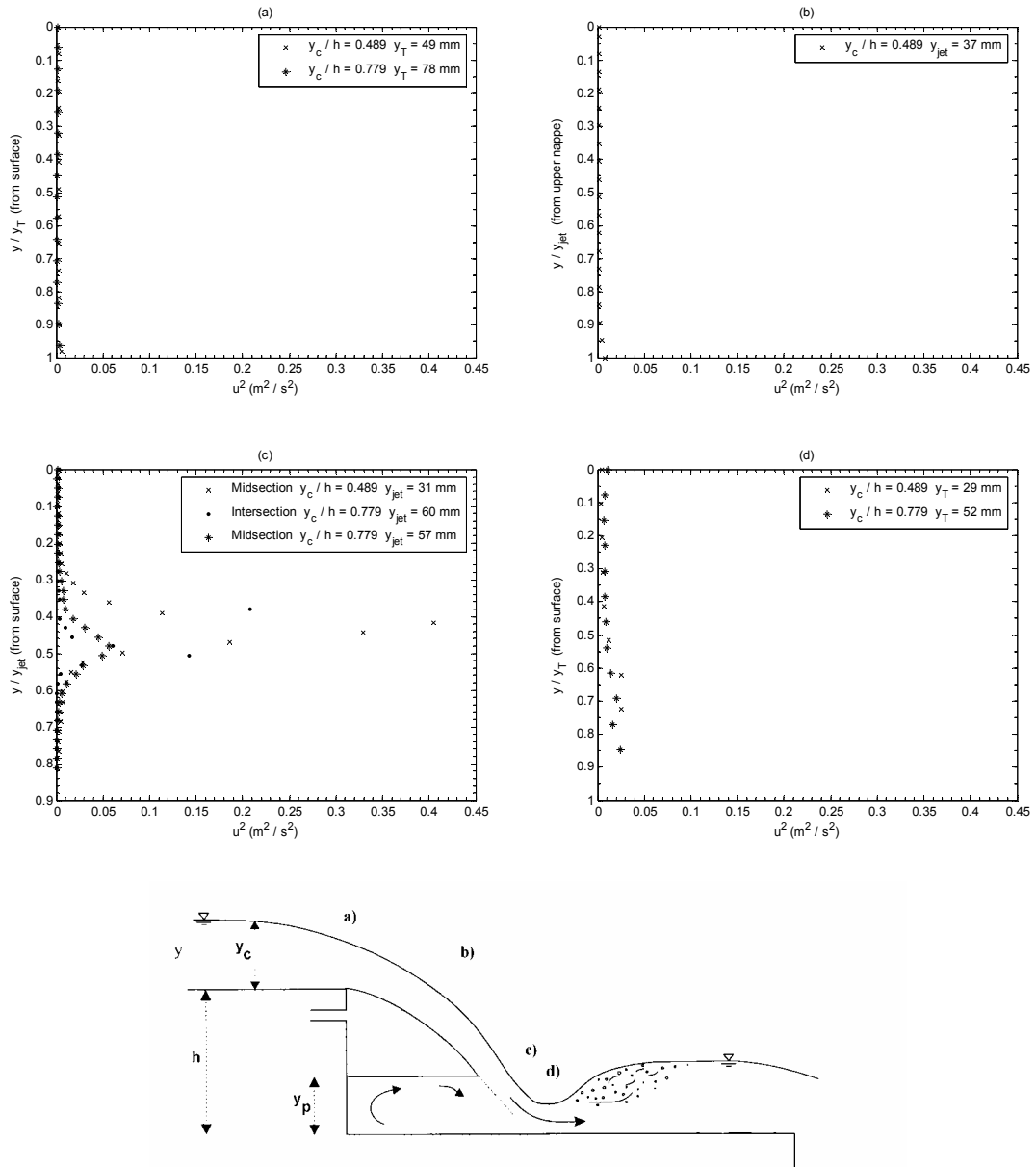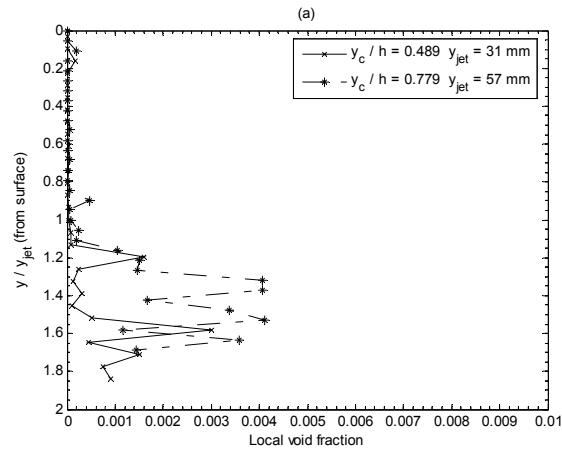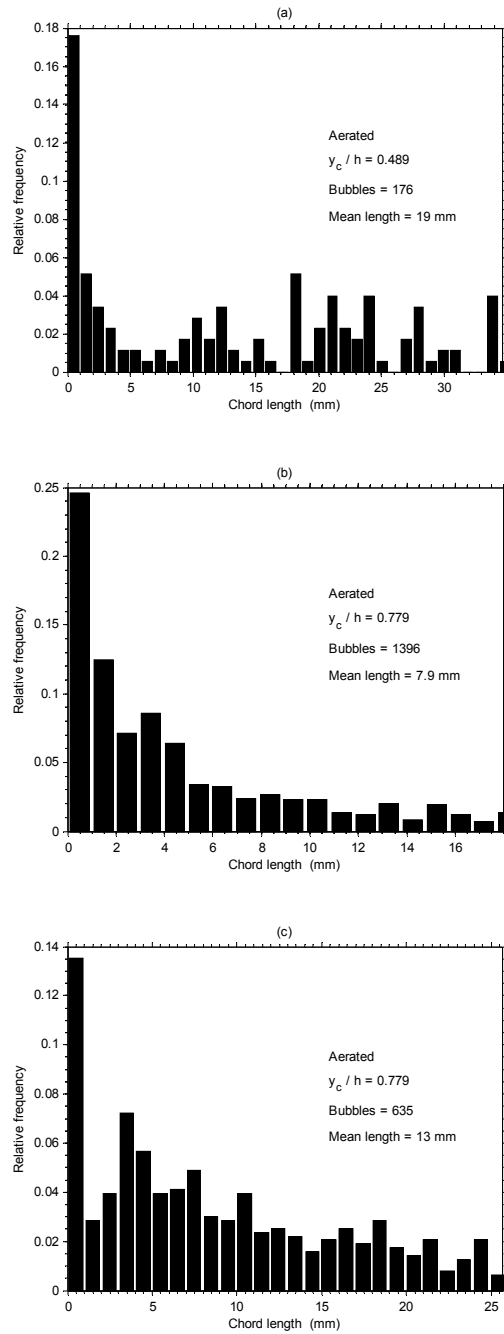
Figure 6.9 Normal stress profiles along the jet trajectory. a) upstream

brink; b) free falling jet; c) sliding jet, d) toe of sliding jet.

Figure 6.10 Local void fraction. a) midsection of sliding jet.

Figure 6.11 Chord length distribution at midsection (a and

c) and intersection line (b) of the sliding jet.

<u>   </u>

Chapter 7   *Summary and conclusions*

7.1 Introduction

In this study a constant temperature anemometer as well as pressure transducers were used to experimentally study the characteristics of the flow development region on stepped chutes. Three physical models with chute slopes of $3.5H:1V$, $5H:1V$, $10H:1V$ were used in the study; all models had five steps 15 cm in height. Several flow conditions in the range of $0.47 \leq y_c/h \leq 1.66$ were tested in conjunction with aerated and non-aerated step cavities.

7.2 Summary

Constant temperature anemometry

The constant temperature anemometry system used in this study was subject to three problems: probe contamination, bubble formation, and temperature drift. These problems, which are commonly attributed to the use of CTA in water flow measurements,

can be overcome by an appropriate selection of the overheat ratio, careful application of a suitable temperature compensation technique and frequent calibrations.

The experimental results indicated that the constant sensor temperature technique can be used to adequately compensate temperature drift as long as the water temperature variations are smaller than $0.5°C$. In using this technique, the compensation should be applied to the CTA raw data where the functional form of the compensation depends on the overheat ratio and the flow velocity. In this study, a linear correction in terms of Nu and Θ was obtained for each fixed value of flow velocity. In addition to this, heat transfer relationships for the expected water temperature range should be obtained for each CTA setup condition.

On the other hand, compensation of temperature drift by means of a constant overheat ratio technique produced good results and does not require numerous calibrations. This procedure should be preferred over a constant sensor temperature when dealing with water flows. In this study, manual compensation of the overheat ratio produced good results, but it required a post-processing analysis of the raw data in order to correct for possible under/over compensation. This correction was successfully applied in this study but an automatic compensation should be developed in order to eliminate this step. Moreover, from the analytical functions tested to represent the heat transfer relationship on the constant overheat ratio technique; the extended power law (Eq. 3.4) produced the best representation of the conical hot-film probe response. A fourth-order polynomial in terms of E as well as a cubic spline interpolation produced satisfactory results as well. Nevertheless, these two methods pose a risk of strong deviations for the lower range of flow velocities.

In dealing with air-water flows, the phase detection methodology is quite sensitive to the selection of the threshold values. In this study several approaches to select those values were attempted. The autocorrelation values of the empirical cumulative density function produced an adequate estimation of such values in terms of CTA output voltage. In the case of the slope threshold method, the change of sign of the CTA signal slope produced the best results in identifying the characteristic points of a bubble.

Constant temperature anemometry has the potential to become as valuable tool in the study of water flow problems as it is in air flows. The technique has good spatial and temporal resolution and it is capable of handling two phase flow. Its use at large hydraulic facilities should not be overlooked since current hot-film systems are capable of overcoming the issues that prevented their use in water flows previously.

Velocity and local void fraction observations

The experimental observations indicated that the conditions along the development flow region on stepped chutes are complex and change abruptly between steps. As an overall, supercritical flow was observed along the steps and provision of air into the step cavity affected the first step only. In fact, the flow geometry of this step depended on whether or not air was supplied. In this regard the first step resembled the flow behavior of a drop structure. This was not observed on the remaining steps

It was observed that the flow jet breaks up easily on steeper slopes, this is because shorter step treads do not provide enough distance for the flow to dissipate the perturbations produce by the impact onto the step. Hence, two-phase flow along the chute is obtained at smaller discharges for steep chutes than for mild ones. Furthermore,

measurements indicate that the condition of the step cavity does not affect the velocity field at the step brinks. This field presents a logarithmic distribution as found in an open channel. However, it vanishes quickly as the jet break up process develops. Before this occurred in each of the models, a similar velocity distribution was observed at the step brinks. It was also observed that on the transition flow regime an air cavity randomly formed on some of the steps. The formation process of this cavity looked like a "bursting mechanism" where air bubbles spontaneously appear and flock to form the cavity. This phenomenon will bring complications if an attempt to mathematically model the transition flow is carried out. This "bursting mechanism" would require the switch on and off of a boundary condition on the lower nappe of the jet.

In regards to the air pocket condition, it was observed that in aerated flows, the recirculating pool became shallower and elongated in the downstream direction. If the step cavity is full of water (non-aerated condition), two symmetric spiral vortices were observed in the vicinity of the step riser, these vortices had a flow direction towards the sides of the models in the area closest to the riser and an ascending flow direction. Additionally, it was observed that the length of the step cavity was about 2 to $3h$. In transition flow regime, the step cavity was usually full air bubbles and high levels of turbulence were observed. If a stepped chute with horizontal steps would be used as a fish ladder, fishes would be forced to rest in the step cavity before continuing their upstream journey. However, given the observed size of the cavity it is unlikely that mature fishes would fit into it. Furthermore, the high turbulence levels together with the observed vortices do not provide good conditions for resting while the large quantities of air bubbles might locally saturate the water with oxygen or nitrogen, a harmful condition

for fish. On the other hand, the mixing of chemical with the water could be carried out on this location since the vortices will produce enough agitation for their dispersion and possible reaction with air.

According to the measurements, the local void fraction along the chute is not affected by the condition of the step cavity. In fact, the air concentration distribution throughout the flow development region seems to have a "C" shape. Larger values were observed at the bottom and top of the flow while minimum values in the middle of the water column. The observations suggest that the local void fraction remains below 0.6. Moreover, larger chord sizes were measured immediately downstream of the jet impact than on the step brinks. In addition, larger chord sizes were measured on the steeper slopes. Knowledge of these parameters is of vital importance for the proper design of stepped chutes as water treatment systems since they allow the quantification of the air-water interface area. Moreover, they also facilitate the assessment of the gas transfer between air and water. Consequently, the environmental effects of the induced two phase flow on the downstream ecosystem can be effectively assessed.

Finally, the water surface profile was observed to be in phase with the chute geometry within the clear water region. Additionally, a significant amount of spray was observed on the transition flow regime and drops were observed to reach 4 to $5h$ above the chute invert on average. Nevertheless, some drops were observed up to 7 to $8h$. This is of considerable importance when designing side wall heights, especially in cold climates where icy conditions in the vicinity of the structure are potentially dangerous. It is also important to mention that surface shock waves were observed in Model III during the skimming flow regime, and in some degree, they were also present on Model II

Shock waves were not observed on Model I probably because the relatively step slope prevented their formation. The shock waves produce considerable disturbance on the water surface, especially after the second step, they also entrain air into the upper layers of the water stream. The observed shock waves reached heights of about 1 to $2h$ over the pseudo bottom, factor that should be considered during the dimensioning of the side walls.

Pressure observations

Pressure observations carried out in this study indicate that the value of y_c/h at which step cavities become filled with water seems to have a dependency on the chute slope. In fact, the cavity condition (aerated or non-aerated) plays a role on the first step only. In addition, on the three slopes studied, the fourth steps did not become filled with water at the same discharge, but rather in a progressive order, which is an indication that the preceding upstream flow condition significantly affects the behavior of each step. The pressure observations also indicated that the step cavity pressure behaves differently on each step.

As observed, the occurrence of minimum pressure values agrees with the regime boundaries of a long stepped spillway, however, the value of y_c/h at which the minimum value occurs increases in the downstream direction, from the first sub-regime of the transition regime to the second sub-regime. Measurements indicate that pressure distribution along a tread is different on each step, although they share the presence of a peak value at the point of flow impact. Additionally, observations on the different chute slopes indicate that there is no 'typical' pressure profile on the treads, where each model

seems to behave in a characteristic way with some similarities but not sufficient to determine a unique pressure profile. Regarding the step risers, measurements within a model displayed a similar pressure profile for the aerated and non-aerated conditions. Nevertheless, the pressure profiles on each step are not similar. On the vertical face, a gradual modification of the pressure distribution was observed as air gets entrained in the flow.

Finally, no correlation was observed on the recirculation pool depth in any of the steps or between them. The expressions for pool depth of drop structures do not represent the observed depths. Moreover, the water level in the pool fluctuated intensively in a wavy pattern. This wavy level was more intense for the steeper slopes and it was also observed that on average, the water level was slightly inclined towards the point of jet impact.

Drop structure observations

Taking advantage of the geometric similarity between a drop structure and the first step of a stepped chute, several measurements were carried out on Model II in order to study such a structure. These observations indicated that in the sliding jet there is no significant difference between the aerated and non-aerated cavities. In addition, the experimental results confirmed the presence of a uniform velocity distribution in the sliding jet and a quantification of the shear layer between the jet and the pool was successfully achieved. Finally, the measurements indicated that the transfer of kinetic energy from the jet to the pool –as turbulence- and subsequent dissipation by viscous forces seems to govern the observed energy losses.

7.3 Conclusions

The following conclusions can be drawn from this study:

i.   The use of constant temperature anemometry in water flows should not be overlooked. The constant overheat ratio procedure produced good results and it is a strong technique for dealing with the non-isothermal conditions often encountered at hydraulic laboratories.

ii.   Conical hot-film probes proved to be a valuable tool in this study not only due to its great spatial and temporal resolution but also due to its capability to cope with the problem of the two-phase flow.

iii. The use of the autocorrelation of the empirical cumulative density function proof to be a good procedure to estimate the amplitude threshold allowing the separation of the two phases. In addition, the change on sign of the slope signal was the selected value to identify the bubble characteristic points.

iv.   In the development flow region of stepped chutes the conditions are complex and they change abruptly between steps. These abrupt changes are chiefly due to the disintegration of the jet.

v.   Flow conditions along the chutes do not resemble a drop structure. Furthermore, provision of air into the step cavity affects the flow geometry of the first step only.

vi.   A logarithmic velocity distribution was observed in the flow downstream of the jet impact. However, this distribution vanishes quickly as the break up of the jet takes place.

vii. Observations of the filling up process in a step cavity indicated that the preceding upstream flow condition have a significant affect on the behavior of each step.

viii. The boundary between regimes seems to coincide with local minimum pressure values in the step cavity.

ix. A "bursting mechanism" was observed on the step cavity during the transition flow regime. This mechanism allows the air cavity to form in a random fashion bringing complexity on a possible mathematical model of these structures.

x. Shock waves developed at skimming flow regime on chutes with mild slopes. This is an important phenomenon since it has considerable design implications. At the stepper slope, i.e. Model I, shock waves were not observed.

xi. In the recirculating pool, depths fluctuate intensely and the shape of the pool seems to become shallower and elongated in the downstream direction.

xii. If the step cavity was full of water, the recirculating pool was small. This fact could preclude the use of stepped chutes as fish passage since a mature fish may not fit into the possible resting area: the step cavity. Furthermore, the presence of vortices and large quantities of air bubbles are also detrimental conditions for this possible use.

xiii. The quantification of the local void fractions, chord length and turbulence levels provide environmental engineers valuable information for the design of stepped chutes as water treatment systems. Similarly, they allow the correct assessment of the gases transfer between the air and water when dealing with stepped chutes. Assessment that benefits the quantification of effects on the downstream aquatic ecosystem.

xiv.   Observations indicated that there is no 'typical' pressure profile on either the tread or the step risers.

 xv.   A qualitative and quantitative description of the shear layer between the jet and pool was successfully achieved.

7.4 Future works

The use of constant temperature anemometry has proven to be a useful tool at a large hydraulic facility. In spite of the fact that CTA has been around for more than 30 years, automatic temperature compensation for water flows is not as developed as it is for air flows. The successful implementation of such a technique in a water flow still requires the development of an adequate probe. The desirable probe should be fast enough to cope with the frequency response of current conical hot-film probes, insensitive to all flow parameters but water temperature, and small enough so that it does not affect the flow. In this way, a temperature compensator bridge could be used instead of a standard bridge.

Many aspects of stepped chutes and the flow characteristics are still unfamiliar to researchers and practitioners. The vast field of inclined and pooled steps have not been studied yet. Nevertheless, these should be studied in detail especially since they may provide suitable fish passing structures. In addition, the environmental applications of stepped chutes are quite varied and therefore, studies for specific applications will always be needed.

This study provided valuable insight to the development flow region of stepped chutes. Nevertheless, the flow in this region is complex and more analysis of the velocity

field and void fraction distribution should be carried out. Specific studies on the 3-dimensional flow observed inside the recirculating pool should be performed. It is likely that this circulation pattern and the presence of shock waves are linked and should be studied in detail. In addition, the presence of such a wave is a problem that should addressed since they may significantly affect the performance of the structure. It also important to carried out a systematic study on the effect that model width could have on the formation of shock waves. Moreover, the length of the development flow region on mild slopes remains to be determined and the mechanism of the air cavity formation on transition flow regime deserves special attention.

This study also encountered unexpected pressure profiles in the development flow region. These profiles presented a saw shape, which are not typical, and therefore they need to be studied in detail in order to be confirmed. Furthermore, this research suggested a change in the hydraulic behavior of stepped chutes when the slope changes from 5.7° to 11.3°. The occurrence of this phenomenon should also be addressed in the future.

References

Agha, M. and Ibrahim, M.T. (1984). "Algorithm AS 203: maximum likelihood estimation of mixtures of distributions". *Applied Statistics*, 33(3), 327-332.

Aigner, D. (2001). "Hydraulic design of pooled step cascades". *21st Century: The new era for hydraulic research and its applications. Proc. 29th IAHR Congress, Theme D, Vol. I.*, G. Li, ed., Beijing, China, 635-640.

Bakhmeteff, B.A. and Feodoroff, N.V. (1943). "Discussion of Moore (1943)". *Transactions,* ASCE, Vol. 108, 1364-1373.

Boes, R.M. (1999). "Physical model study on two-phase cascade flow". *Proc. 28th IAHR Congress*. Graz, Austria. CD-rom.

Boes, R.M. (2000). "Scale effects in modeling two-phase spillway flow". *Intl. Workshop on Hydraulics of stepped spillways*, H.E. Minor and W.H. Hager, eds., Balkema Publ., Netherlands, 53-60.

Boes, R.M. and Minor, H.E. (2000). "Guidelines for the hydraulic design of stepped spillways". *Intl. Workshop on Hydraulics of stepped spillways*, H.E. Minor and W.H. Hager, eds., Balkema Publ., Netherlands, 163-170.

Bruun, H.H. (1996). "Hot-film anemometry in liquid flows". *Meas. Sci. Technol.*,

7(10), 1301-1312.

Bruun, H.H.; Khan, M.A.; Al-Kayiem, H.H. and Fardad, A.A. (1988). "Velocity calibration relationships for hot-wire anemometry". *J. Phys. E: Sci. Instrum.*, the Institute of Physics, 21, 225-232.

Chamani, M.R. (1993). "Jet flow on stepped spillways and drops". M.Sc. thesis, University of Alberta, Alberta, Canada.

Chamani, M.R. (1997). "Skimming flow in a large model of a stepped spillway". Ph.D. thesis, University of Alberta, Canada.

Chamani, M.R. and Rajaratnam, N. (1999). "Onset of skimming flow on stepped spillways". *J. Hydr. Engrg.*, ASCE, 125(9), 969-971. Discussion: 127(6), 519-525.

Chanson, H. (1994). "Hydraulics of nappe flow regime above stepped chutes and spillways". *Aust. Civil Eng. Trans.*, IEAust., CE36(1), 69-76.

Chanson, H. (1995a). *Hydraulic design of stepped cascades, channels, weirs and spillways*. Pergamon. Oxford, U.K.

Chanson, H. (1995b). "History of stepped channels and spillways: a rediscovery of the "wheel"". *Can. J. of Civil Eng.*, 22(2), 247-259.

Chanson, H. (1996). "Prediction of the transition nappe/skimming flow on a stepped channel". *J. Hydr. Res.*, IAHR, 34(3), 421-429.

Chanson, H. (1998). "Le développement historique des cascades et fontaines en gradins" (Historical development of stepped cascades and fountains). *La Houille blanche*, Revue de la Société Hydrotechnique de France, No 7, 76-84. (In French).

Chanson, H. (1999). "Current expertise and experience on stepped chute flows". Seminar presented at Kyoto University, Disaster Prevention Research Institute. April, Kyoto, Japan.

Chanson, H. (2000a). "Hydraulics of Roman Aqueducts : Steep Chutes, Cascades and Dropshafts". *American J. of Archaeology*, 104(1), 47-72.

Chanson, H. (2001a). "A transition flow regime on stepped spillway? The facts". *21st Century: The new era for hydraulic research and its applications. Proc. 29th IAHR Congress, Theme D, Vol. I.*, G. Li, ed., Beijing, China, 490-498.

Chanson, H. (2001b). Caractéristiques diphasiques des ecoulements sur les coursiers en marches d'escalier.). *La Houille blanche*, Revue de la Société Hydrotechnique de France, No 8, 16-28. (In French).

Chanson, H. (2001c). *The hydraulics of stepped chutes and spillways..* Balkema. Lisse, The Netherlands.

Chanson, H. and Toombes, L. (1998a). "Air-water flow structures at an abrupt drop with supercritical flow". *Proc. 3rd Intl. Conf. Multiphase flow, ICMF'98*, Lyon, France, Session 2.2.5, Paper No. 119, 6 pages.

Chanson, H. and Toombes, L. (1998b). "Supercritical flow at an abrupt drop: flow patterns and aeration". *Can. J. of Civil Eng.*, 25(5), 956-966.

Chanson, H. and Toombes, L. (2001). "*Experimental investigation of air entrainment in transition and skimming flows down a stepped chute. Application to embankment overflow stepped spillways*", Report CE 158, University of Queensland, Australia.

Chanson, H. and Toombes, L. (2004). "Hydraulics of stepped chutes: the transition

flow". *J. Hydr. Res.*, IAHR, 42(1), 43-54.

Collins, D.C., and Williams, M.J. (1959). "Two-dimensional convection from heated wires at low Reynolds numbers". *J. Fluid Mech.*, 6(3), 357-384.

Dantec Dynamics (2003). "*Probes for Hot-wire Anemometry*". Publication No 103-105-07, Dantec Dynamics A/S, Denmark.

Dantec Dynamics (2005). "Technical data for conical film sensors". Single sensor film probes, conical film probes, <http://www.dantecmt.com> (Aug 3, 2005).

Delhaye, J.M. (1968). "Hot-film anemometry in two-phase flow". *Proc. 11th National Heat transfer conferences*, ASME/AIChE, Minneapolis, Minnesota, USA.

De Marinis, G., Fratino, U. and Piccinni, A.F. (2001). "Flow regimes on stepped spillways". *21st Century: The new era for hydraulic research and its applications. Proc. 29th IAHR Congress, Theme D, Vol. I.*, G. Li, ed., Beijing, China, 641-646.

Diez-Cascon, J., Blanco, J.L., Revilla, J. and Garcia, R. (1991). "Studies on the hydraulic behaviour of stepped spillways". *Water Power & Dam Construction*, 43(9), 22-26.

DISA. (1977). *Instruction manual, DISA 55M system with 55M10 CTA standard bridge*. Disa Elektronik A/S, Denmark.

El-Kamash, M.K., Lowen, M.R. and Rajaratnam, M. (2005). "En experimental investigation of jet flow on a stepped chute". *J. Hydr. Res.*, IAHR, 43(1), 31-43.

Essery, I.T.S., and Horner, M.W. (1978). "*The hydraulic design of stepped spillways*". Report No. 33, CIRIA, London, U.K.

Farrar, B. and Bruun, H.H. (1989). "Interaction effects between a cylindrical hot-film

anemometer probe and bubbles in air/water and oil/water flows". *J. Phys. E: Sci. Instrum.*, the Institute of Physics, 22, 114-123.

Farrar, B., Samways, A.L. Ali, J. and Bruun, H.H. (1995). "A computer-based hot-film technique for two-phase flow measurements". *Meas. Sci. Technol.*, 6(10), 1528-1537.

Hager, W. and Boes, R. (2000). "Backwater and drawdown curves in stepped spillways". *Intl Workshop on Hydraulics of stepped spillways*, H.E. Minor and W.H. Hager, eds., Balkema Publ., Netherlands, 129-136.

Horner, M.W. (1969). "An analysis of flow on cascades of steps". Ph.D. Thesis, University of Birmingham, United Kingdom.

Houston, K.L. and Richardson, A.T. (1988). "Energy dissipation characteristics of a stepped spillway for an RCC dam". *Proc. Intl. Symp. on hydraulics for high dams*, IAHR, Beijing, China, 91-98.

James, C., Comnino, M. and Palmer, M.W. (1999). "Effects of slope and step size on the hydraulics of stepped chutes". *J. South African Inst. Civil Engrg.*, 41(2), 1-6.

Jørgensen, F.E. (2002). *How to measure turbulence with hot-wire anemometers –a Practical Guide*, Dantec Dynamics A/S, Denmark.

Lekakis, I. (1996). "Calibration and signal interpretation for single and multiple hot-wire/hot-film probes". *Meas. Sci. Technol.*, 7(10), 1313-1332.

Lilliefors, H.W. (1967). "On the Kolmogorv-Smirnov test for normality with mean and variance unknown". *J. American Statistical Association*, 62(318), 399-402.

Lin, C.; Huang, W.Y.; Suen, H.F.; Hsieh, S.C. (2002). "Study on the characteristics of velocity field of free overfalls over a vertical drop". *Hydraulic Measurements and Experimental Methods 2002*, ASCE, U.S.A., 178-187.

Macaitis, B. (1990). "Sidestream elevated pool aeration station design". *Proc. 2nd Symp. On Gas transfer at water surfaces, air-water mass transfer*, S.C. Wilhelms and J.S. Gulliver, eds., ASCE, U.S.A., 670-681.

Minor, H.E., and Boes, R.M. (2001). "Hydraulic design of stepped spillways". *21st Century: The new era for hydraulic research and its applications. Proc. 29th IAHR Congress, Theme D, Vol. I.*, G. Li, ed., Beijing, China, 754-759.

Minor, H.E. and Hager, W.H. (2000). *Proceedings of the Intl. Workshop on Hydraulics of stepped spillways*. Zurich, Switzerland. Balkema Publ., Netherlands.

Ohtsu, I. and Yasuda, Y. (1997). "Characteristics of flow conditions on stepped channels". *Energy and water: sustainable development. Proc. 27th IAHR Congress*, J.S. Gulliever and P.L. Viollet, eds., San Francisco, USA, 583-588.

Ohtsu, I.; Yasuda, Y. and Takahashi, M. (2004). "Flow characteristics of skimming flows in stepped channels". *J. Hydr. Eng.*, ASCE, 130(9), 860-869.

Peyras, L.; Royet, P. and Degoutte, G. (1991). "Ecoulement et dissipation sur les déversoirs en gradins de gabions". *La Houille blanche*, Revue de la Société Hydrotechnique de France, No 1, 37-47. (In French).

Peyras, L.; Royet, P. and Degoutte, G. (1992). "Flow and energy dissipation over stepped gabion weirs". *J. Hydr. Engrg.*, ASCE, 118(5), 707-717.

Pinheiro, A.N. and Fael, C.S. (2000). "Nappe flow in stepped channels – occurrence and energy dissipation". *Intl. Workshop on Hydraulics of stepped spillways*, H.E. Minor and W.H. Hager, eds., Balkema Publ., Netherlands, 119-126.

Poggi, B. (1949). "Sopra gli scaricatori a scala di stramazzi". *L'Energia elettrica,* 26(10), 600-604. (In Italian).

Poggi, B. (1956). "Lo scaricatore a scala di stramazzi, criteri di calcolo e rilievi sperimentali". *L' Energia elettrica,* 33(1), 33-40. (In Italian).

Rajaratnam, N. (1990). "Skimming flow in stepped spillways". *J. Hydr. Engrg.*, ASCE, 116(4), 587-591. Discussion: 118(1), 111-114.

Rajaratnam, N. and Muralidhar, D. (1968). "Characteristics of the rectangular free overfall". *J. Hydr. Res.*, IAHR, 6(3), 233-258.

Rand, W. (1955). "Flow geometry at straight drop spillways". *Proceedings*, ASCE. 81(791), September, 1-13.

Rasmussen, C.G. (1967). "The air bubble problem in water flow hot-film anemometry". *Disa Information*, Disa Elektronic A/S, No. 5 (June), 21-26.

Robison, R. (1994). "Chicago's waterfalls". *Civil Engineering*, ASCE, June, 36-39.

Sorensen, R.M. (1985). "Stepped spillway hydraulic model investigation". *J. Hydr. Engrg.*, ASCE, 111(12), 1461-1472. Discussion: 113(8), 1095-1097.

Stenhouse, M.H., and Stoy, R. (1974). "The calibration and use of a conical hot film anemometer probe in recirculating water flow". *Rev. Sci. Instrum.*, 45(3), 368-370.

Stephenson, D. (1991). "Energy dissipation down stepped spillways". *Water Power & Dam Construction*, 43(9), 27-30.

United Stated Bureau of Reclamation. (1953). *"Hydraulic laboratory practice"*. Engineering monograph 18, Department of the Interior, Denver, Colorado, U.S.A..

Wegman, E. (1907). "The design of the New Croton dam". *Transactions*, ASCE. Vol. LVIII, Paper No. 1047, June, 398-457.

Wu, S., and Bose, N. (1993). "Calibration of a wedge-shaped vee hot-film probe in a Towing tank". *Meas. Sci. Technol.*, 4(1), 101-108.

Yasuda, Y. and Ohtsu, I. (1999). "Flow resistance of skimming flow in stepped channels". *Proc. 28th IAHR Congress*. Graz, Austria. CD-Rom.

Young, M.F. (1982). "Feasibility study of a stepped spillway". *Proc. Conf. Applying research to hydraulic practice,* P.E. Smith, ed., ASCE, Jackson, Mississipi, U.S.A. 96-105.

Appendix A   *Flow conditions for the runs*

Table A.1 Pressure, Model I $(3.5H : 1V)$

Run	Step	Location	Condition
A1	1	Riser	Aerated
A2	1	Riser	Non-aerated
A3	1	Tread	Aerated
A4	1	Tread	Non-aerated
A5	1 to 4	Riser, port 7	Non-aerated
A6	1 to 4	Riser	Non-aerated
A7	1 to 4	Riser	Non-aerated
A8	1 to 4	Riser	Aerated
A9	1 to 4	Riser	Non-aerated
A10	1 to 4	Riser	Aerated
A11	2	Riser & Tread	Aerated
A12	3	Riser & Tread	Aerated
A13	4	Riser & Tread	Aerated

Table A.2 Pressure, Model II $(5H:1V)$

Run	Step	Location	Condition
B1	1 to 4	Riser, port 8	Non-aerated
B2	1 to 4	Riser, port 8	Non-aerated
B3	1	Riser	Non-aerated
B4	2	Riser	Non-aerated
B5	3	Riser	Non-aerated
B6	4	Riser	Non-aerated
B7	4	Tread	Non-aerated
B8	3	Tread	Non-aerated
B9	2	Tread	Non-aerated
B10	1	Tread	Non-aerated
B11	1	Tread	Aerated
B12	2	Tread	Aerated
B13	3	Tread	Aerated
B14	4	Tread	Aerated
B15	1	Riser	Aerated
B16	2	Riser	Aerated
B17	3	Riser	Aerated
B18	4	Riser	Aerated

Table A.3 Pressure, Model III $(10H : 1V)$

Run	Step	Location	Condition
C1	1 to 4	Riser, port 8	Non-aerated
C2	1 to 4	Riser, port 8	Non-aerated
C3	1	Riser	Non-aerated
C4	2	Riser	Non-aerated
C5	3	Riser	Non-aerated
C6	4	Riser	Non-aerated
C7	1	Tread	Non-aerated
C8	2	Tread	Non-aerated
C9	3	Tread	Non-aerated
C10	4	Tread	Non-aerated
C11	1	Tread	Aerated
C12	2	Tread	Aerated
C13	3	Tread	Aerated
C14	4	Tread	Aerated
C15	1	Riser	Aerated
C16	2	Riser	Aerated
C17	3	Riser	Aerated
C18	4	Riser	Aerated
C19	1 to 4	Riser, Tap 8	Aerated

Table A.4 Hot-film, Model I $(3.5H : 1V)$

Run	Step	Condition	Discharge (l/s)	Location
D1	-	Aerated	26.2	Approach channel
D2	-	Aerated	52.2	Approach channel
D3	1	Aerated	26.8	u/s brink, 40%, 50%, d/s brink
D4	2	Aerated	26.8	u/s brink, 65%
D5	3	Aerated	26.8	u/s brink, 80%
D6	4	Aerated	26.8	u/s brink, 85%
D7	1	Aerated	37.6	u/s brink, 65%
D8	2	Aerated	37.6	u/s brink, 80%
D9	3	Aerated	37.6	u/s brink
D10	4	Aerated	37.6	u/s brink
D11	1	Aerated	50.6	u/s brink, 65%
D12	2	Aerated	50.6	d/s brink
D13	3	Aerated	50.6	d/s brink
D14	4	Aerated	50.6	d/s brink

Table A.5 Hot-film, Model II $(5H:1V)$

Run	Step	Condition	Discharge (l/s)	Location
E1	1	Non-aerated	27.2	30%, d/s brink
E2	2	Non-aerated	27.0	45%, d/s brink
E3	3	Non-aerated	27.0	55%, d/s brink
E4	4	Non-aerated	27.0	55%, d/s brink
E5	1	Non-aerated	54.1	41%, d/s brink
E6	2	Non-aerated	54.1	55%, d/s brink
E7	3	Non-aerated	54.1	55%, d/s brink
E8	4	Non-aerated	54.1	75%, d/s brink
E9	1	Non-aerated	54.1	Recirculating pool
E10	1	Aerated	26.2	u/s brink, 45%, d/s brink
E11	2	Aerated	26.2	45%, d/s brink
E12	3	Aerated	26.2	55%, d/s brink
E13	4	Aerated	26.2	60%, d/s brink
E14	1	Aerated	26.2	Recirculating pool
E15	1	Aerate	52.6	u/s brink, 45%, d/s brink
E16	2	Aerated	52.6	55%, d/s brink
E17	3	Aerated	52.6	60%, d/s brink
E18	4	Aerated	52.6	65%, d/s brink

Table A.6 Hot-film, Model II $(5H:1V)$

Run	Step	Condition	Discharge (l/s)	Location
E19	1	Non-aerated	72.5	u/s brink, d/s brink
E20	2	Non-aerated	72.5	d/s brink
E21	3	Non-aerated	72.5	d/s brink
E22	4	Non-aerated	72.5	d/s brink
E23	1	Non-aerated	160.1	u/s brink, d/s brink
E24	2	Non-aerated	160.1	d/s brink
E25	3	Non-aerated	160.1	d/s brink
E26	4	Non-aerated	160.1	d/s brink

Table A.7 Hot-film, Model III $(10H : 1V)$

Run	Step	Condition	Discharge (l/s)	Location
F1	1	Non-aerated	26.0	20%, d/s brink
F2	2	Non-aerated	26.0	25%, d/s brink
F3	3	Non-aerated	26.0	25%, d/s brink
F4	4	Non-aerated	26.0	25%, d/s brink
F5	1	Non-aerated	73.4	u/s brink, d/s brink
F6	2	Non-aerated	73.4	d/s brink
F7	3	Non-aerated	73.4	d/s brink
F8	4	Non-aerated	73.4	d/s brink
F9	1	Non-aerated	161.3	u/s brink, d/s brink
F10	2	Non-aerated	161.3	d/s brink
F11	3	Non-aerated	161.3	d/s brink
F12	4	Non-aerated	161.3	d/s brink
F13	1	Non-aerate	51.5	25%, d/s brink
F14	2	Non-aerated	51.5	25%, d/s brink
F15	3	Non-aerated	51.5	30%, d/s brink
F16	4	Non-aerated	51.5	30%, d/s brink

Table A.8 Hot-film, Model III $(10H:1V)$

Run	Step	Condition	Discharge (l/s)	Location
F17	1	Aerated	26.4	u/s brink, 20%, d/s brink
F18	2	Aerated	26.4	25%, d/s brink
F19	3	Aerated	26.4	25%, d/s brink
F20	4	Aerated	26.4	25%, d/s brink
F21	1	Aerated	54.5	u/s brink, 25%, d/s brink
F22	2	Aerated	54.5	25%, d/s brink
F23	3	Aerated	54.5	30%, d/s brink
F24	4	Aerated	54.5	30%, d/s brink

_____

Appendix B

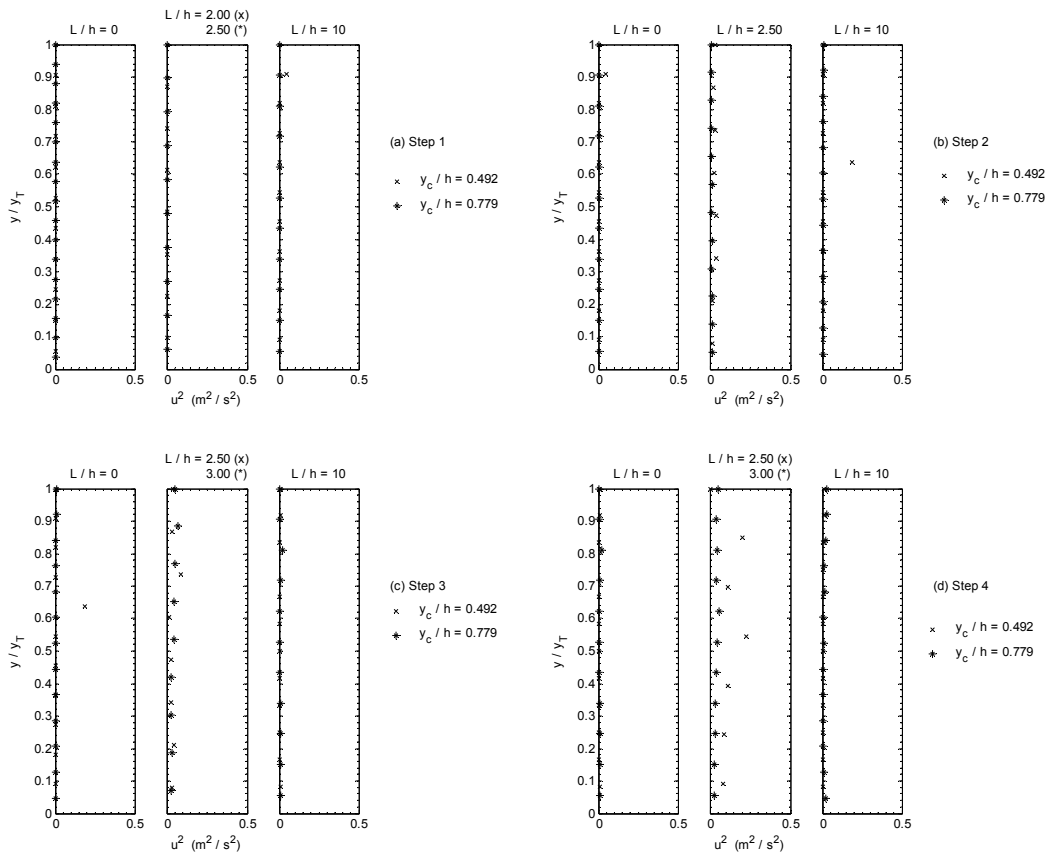*Velocity field and local void fraction*

observations. Model II
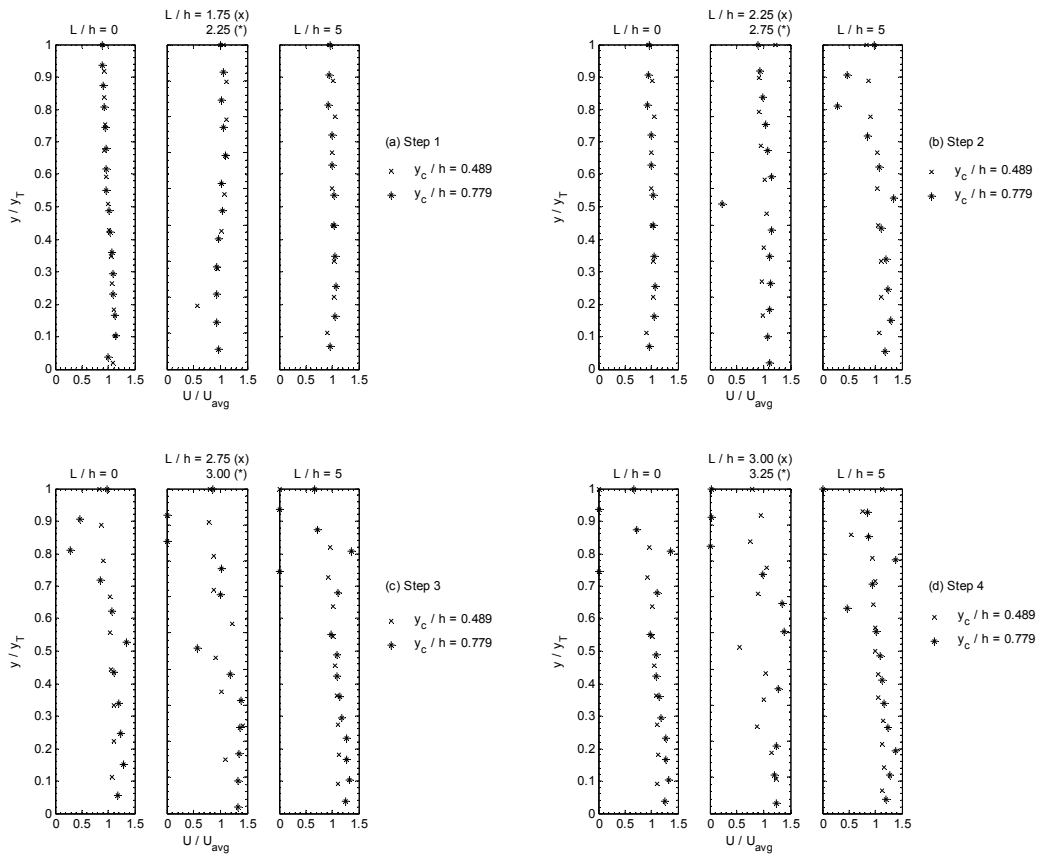
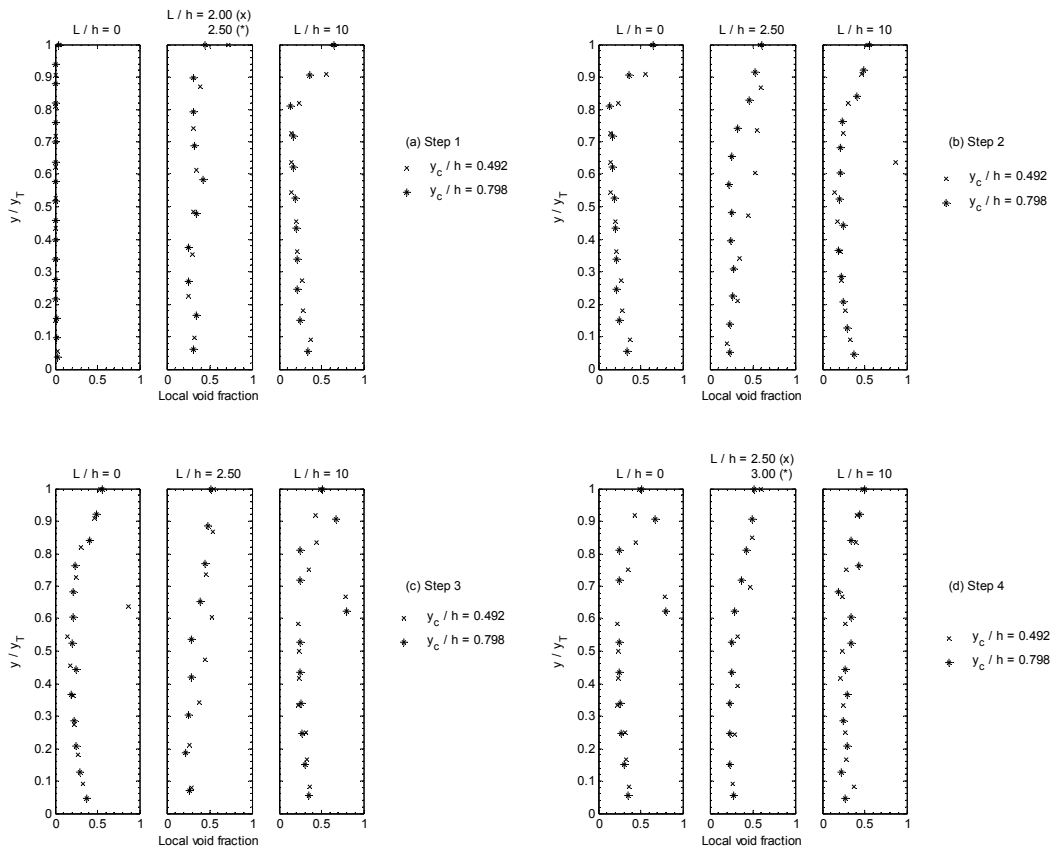**Figure B.1** Velocity profiles. Nappe flow regime, aerated condition.
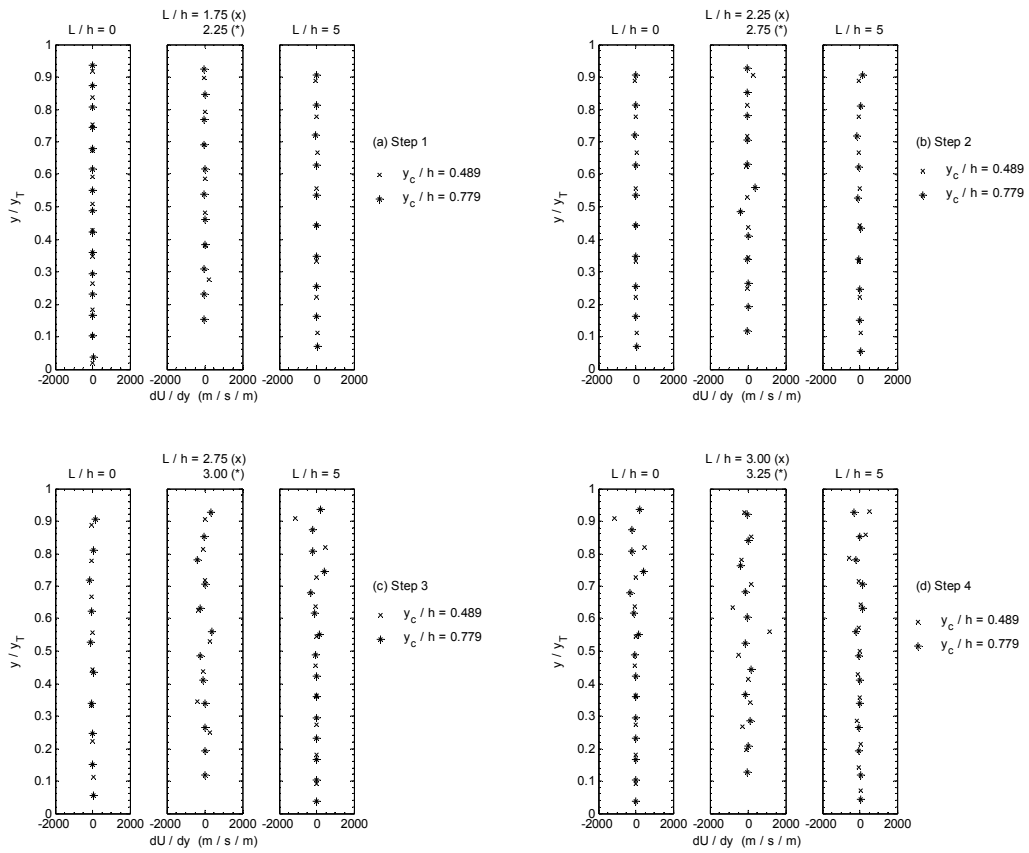
Figure B.2 Velocity gradient profiles. Nappe flow regime, aerated condition.
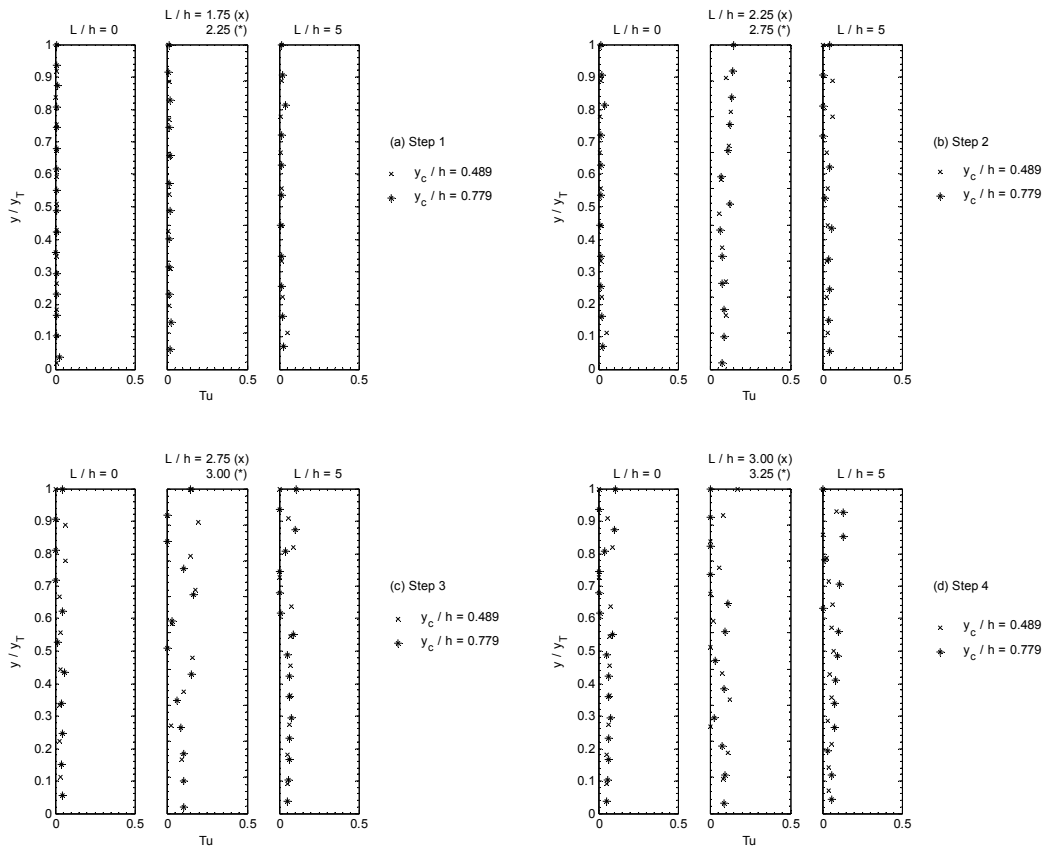
Figure B.3 Turbulence intensity profiles. Nappe flow regime, aerated condition.
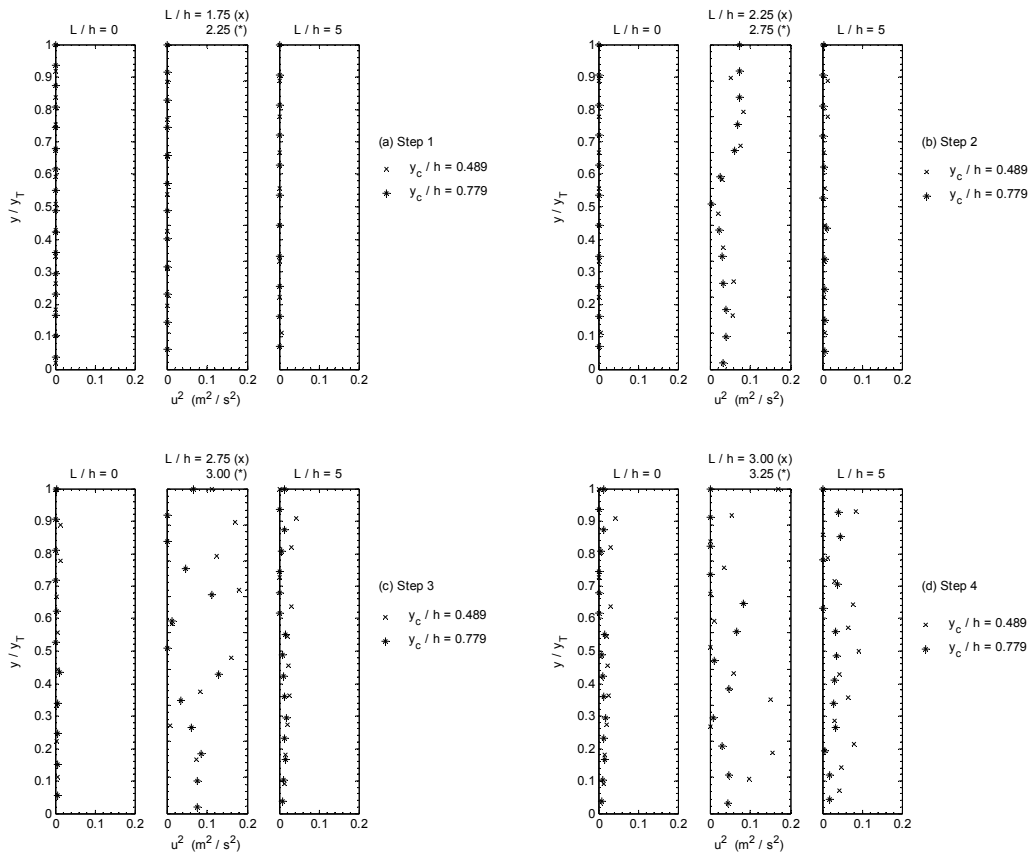
Figure B.4 Normal stress profiles. Nappe flow regime, aerated condition.
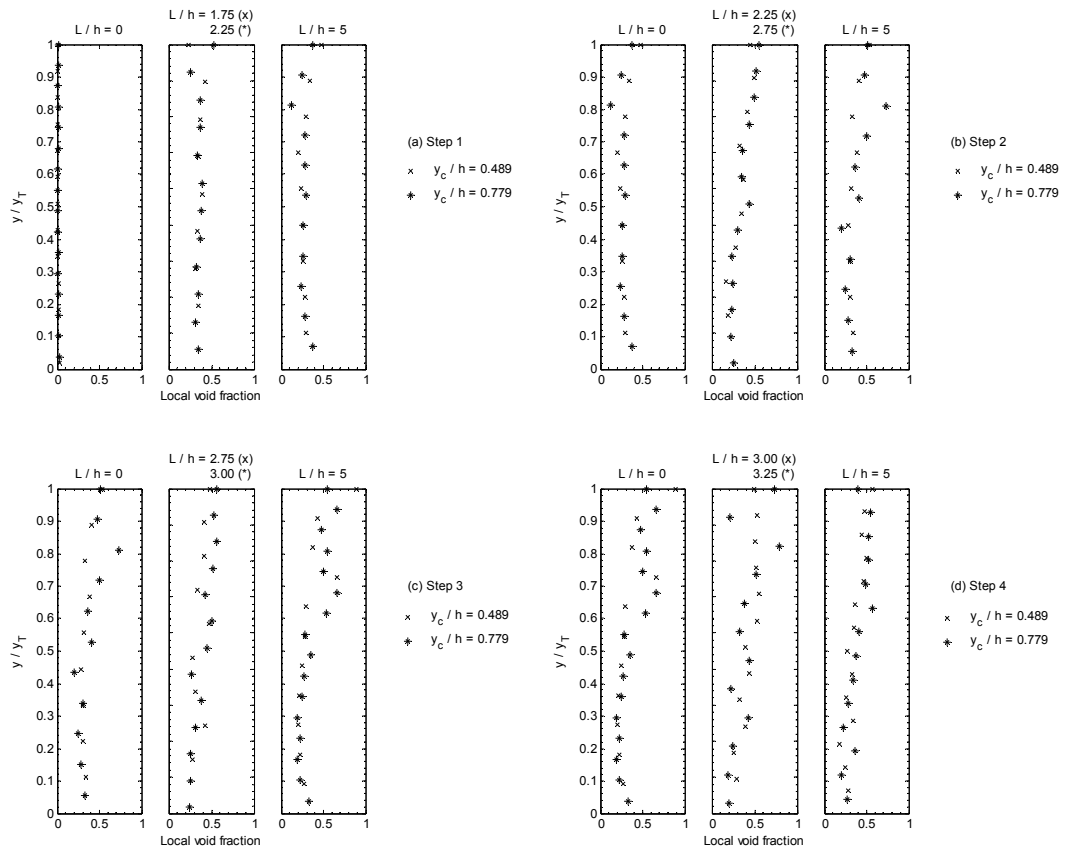
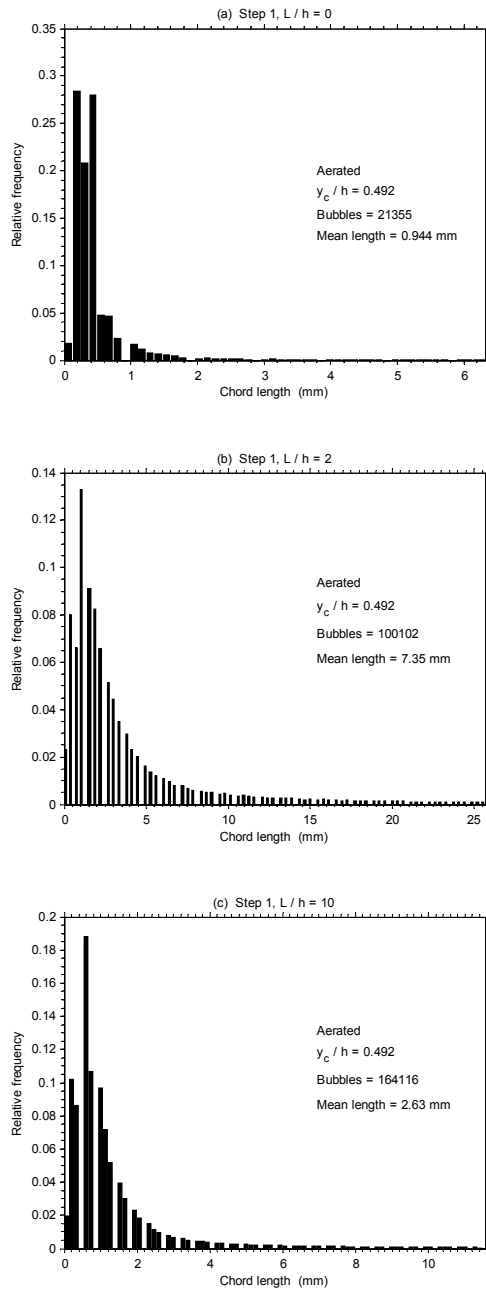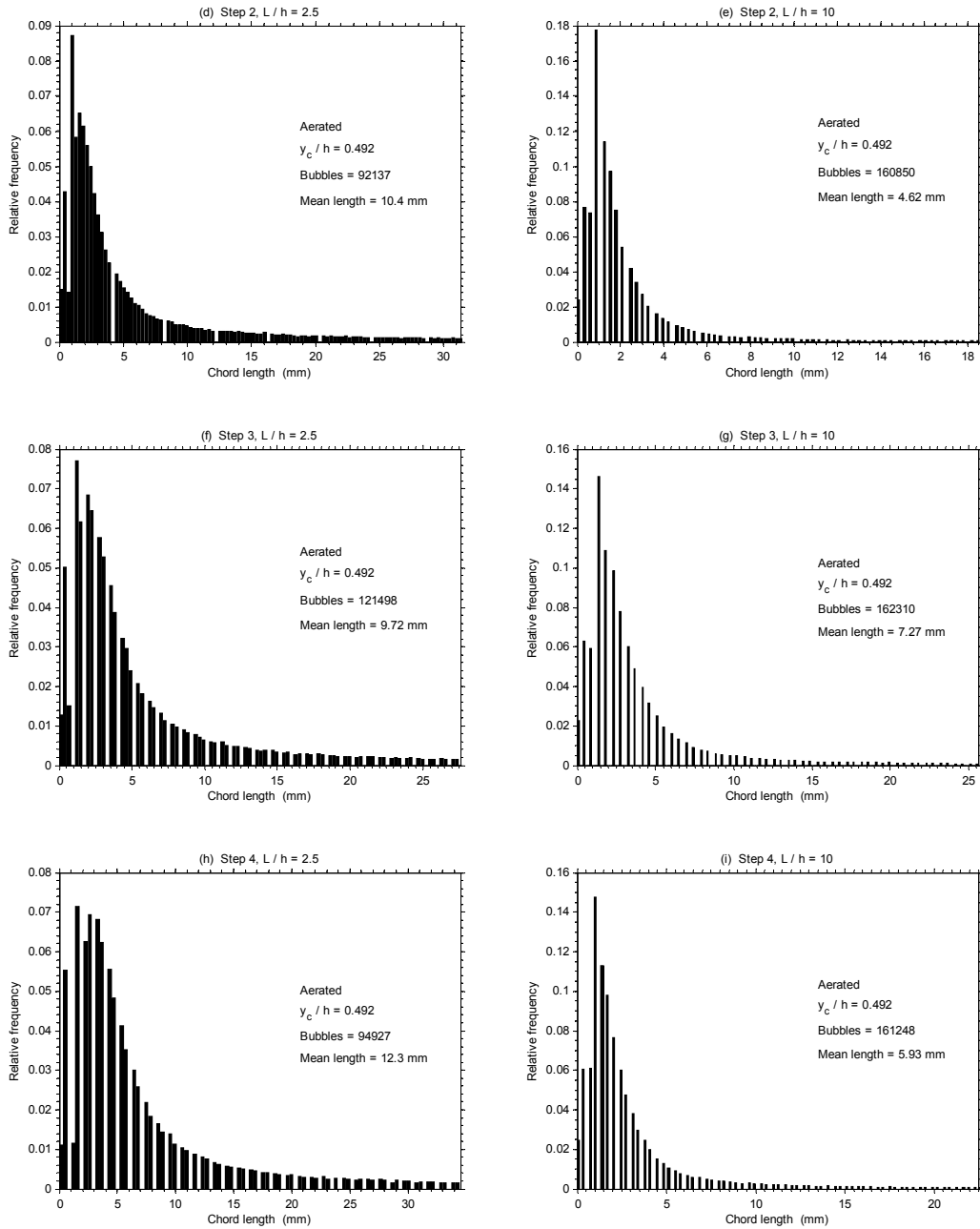**Figure B.5** Local void fraction profiles. Nappe flow regime, aerated condition.
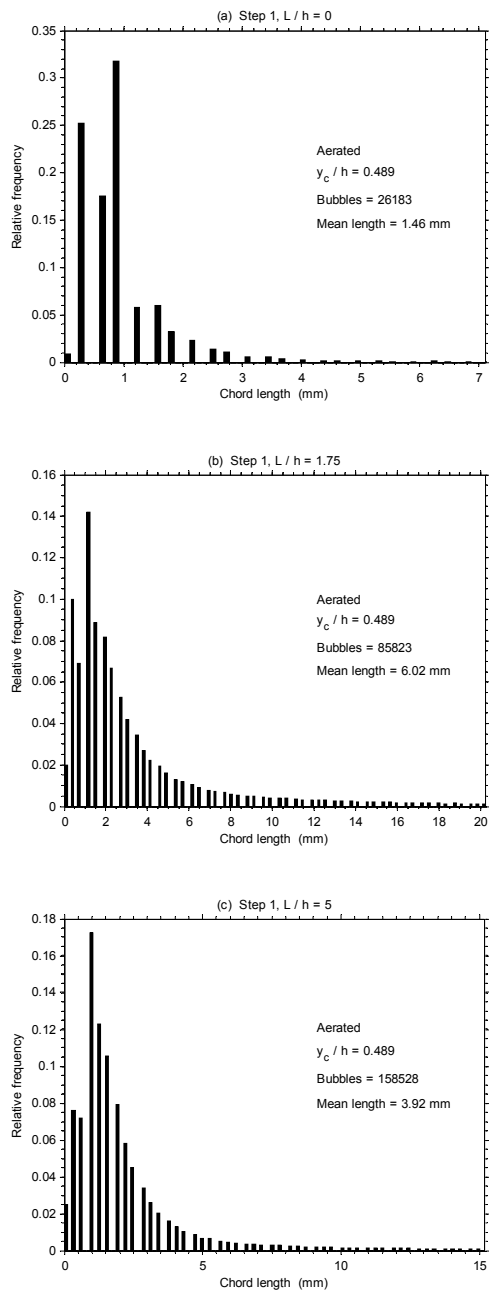
Figure B.6 Bubble chord length. Nappe flow regime, aerated condition.
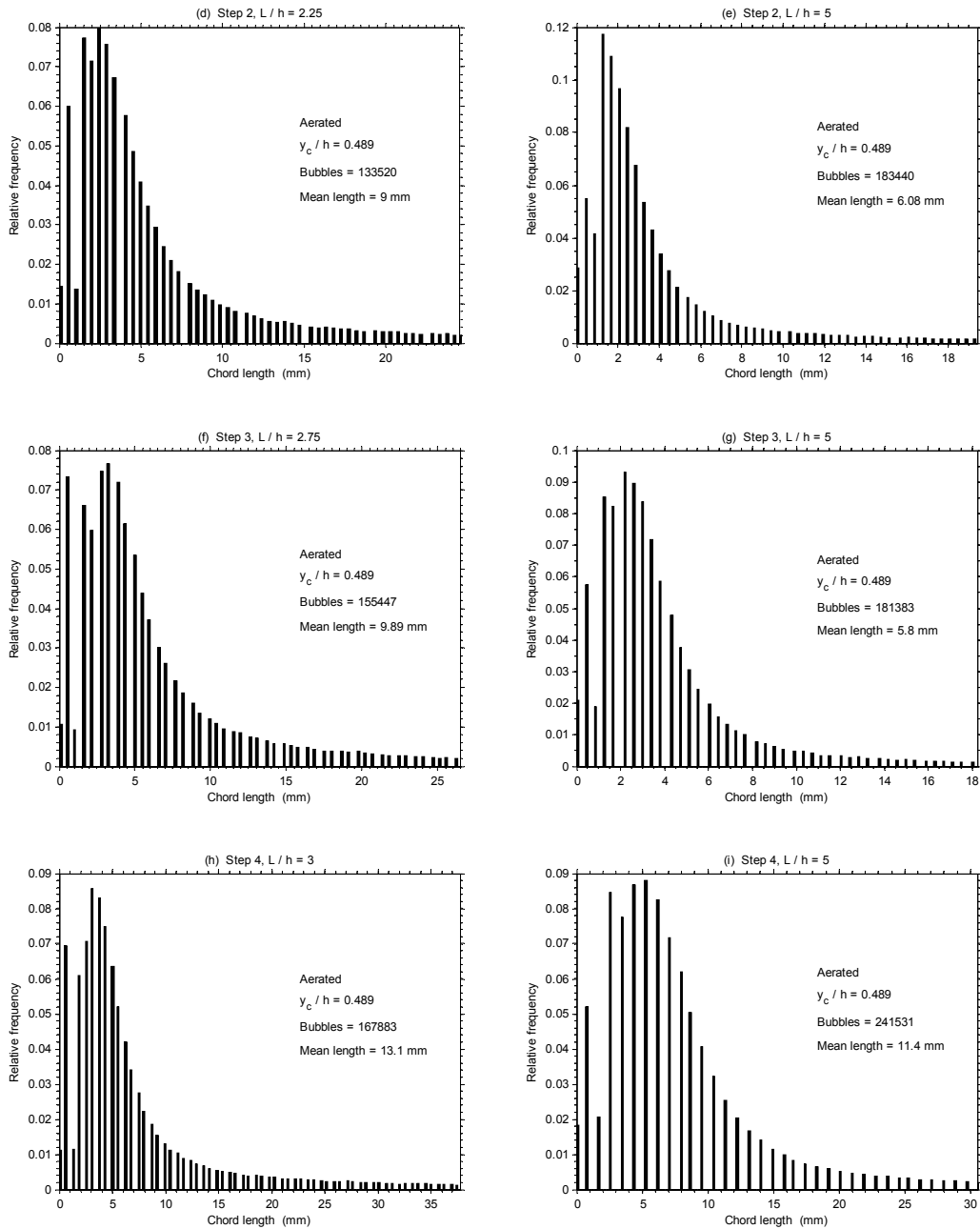
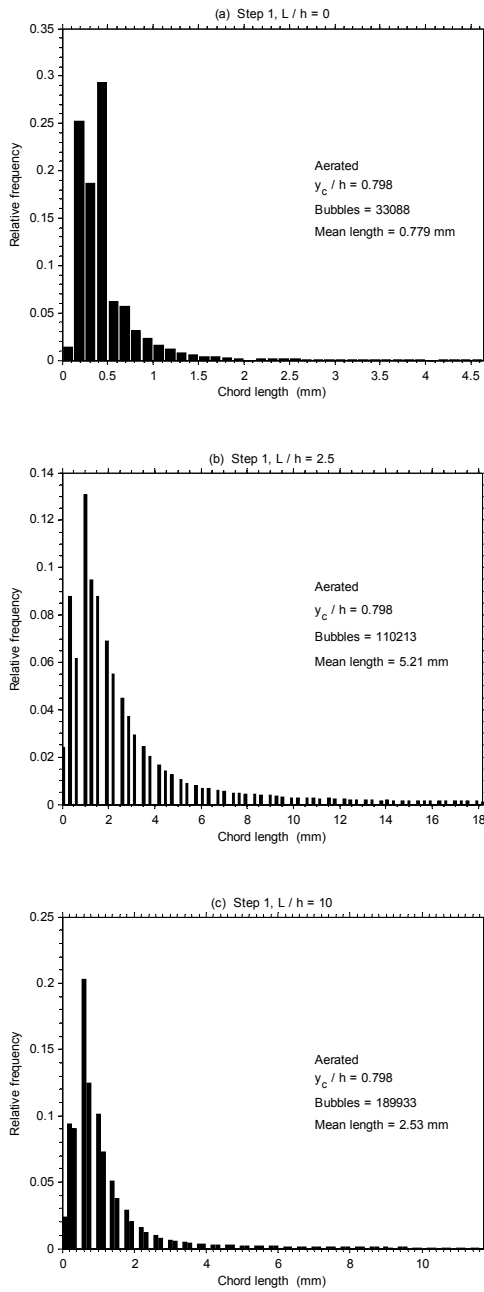**Figure B.6** (continuation) Bubble chord length. Nappe flow regime, aerated
condition.
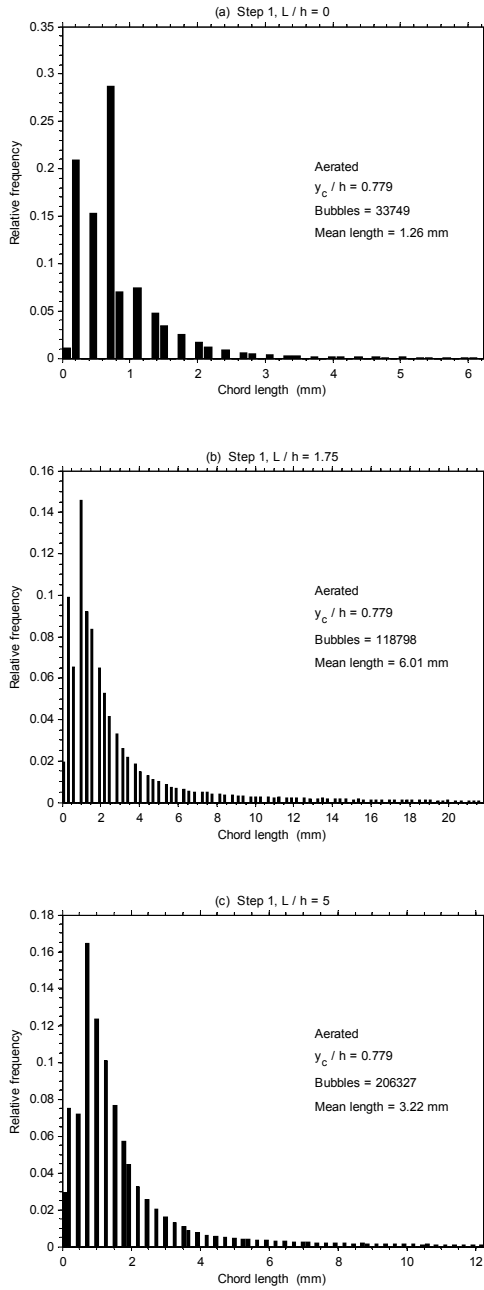
Figure B.7 Bubble chord length. Nappe flow regime, aerated condition.
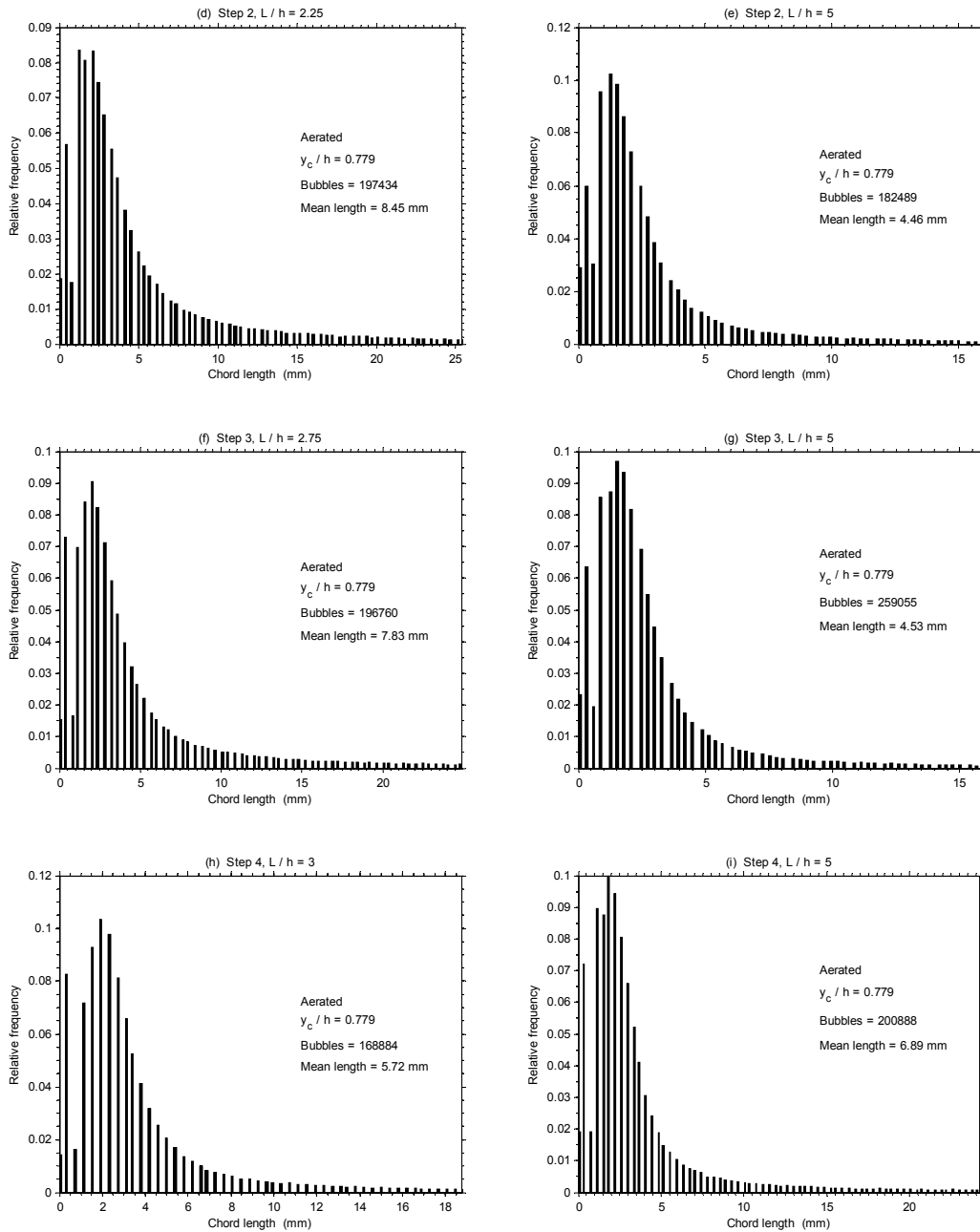
Figure B.7 (continuation) Bubble chord length. Nappe flow regime, aerated condition.
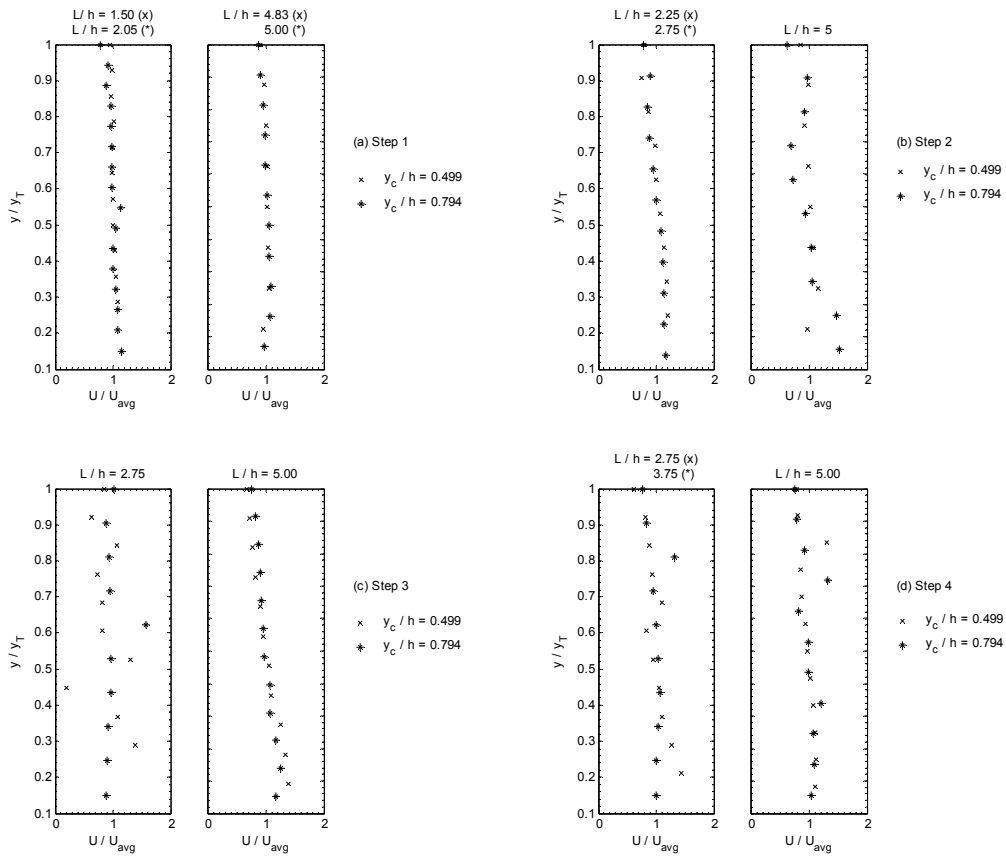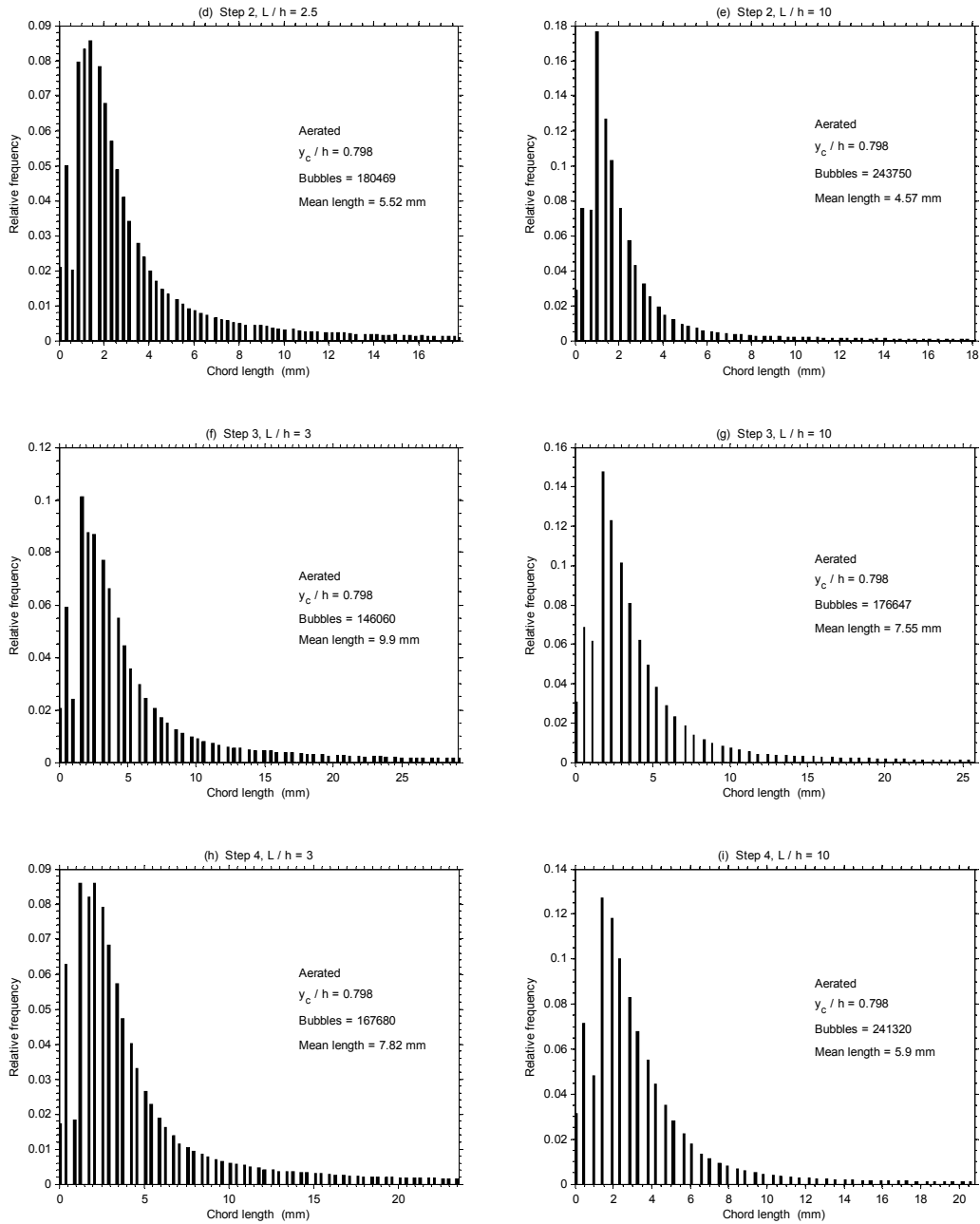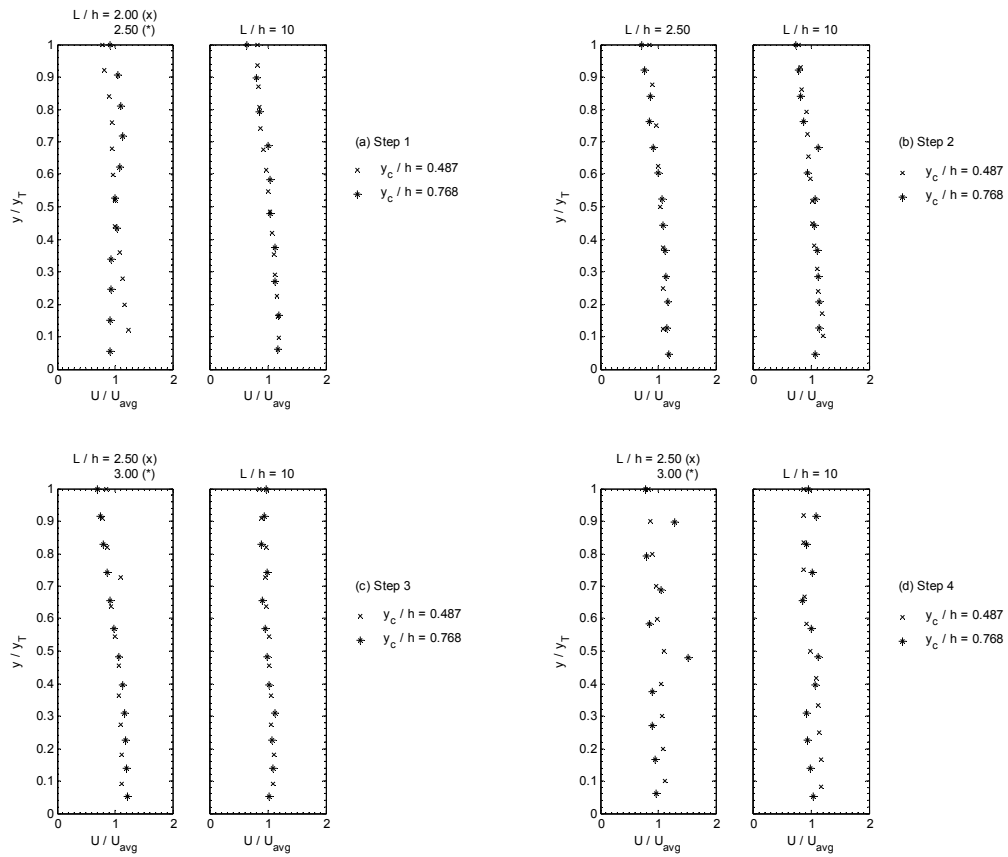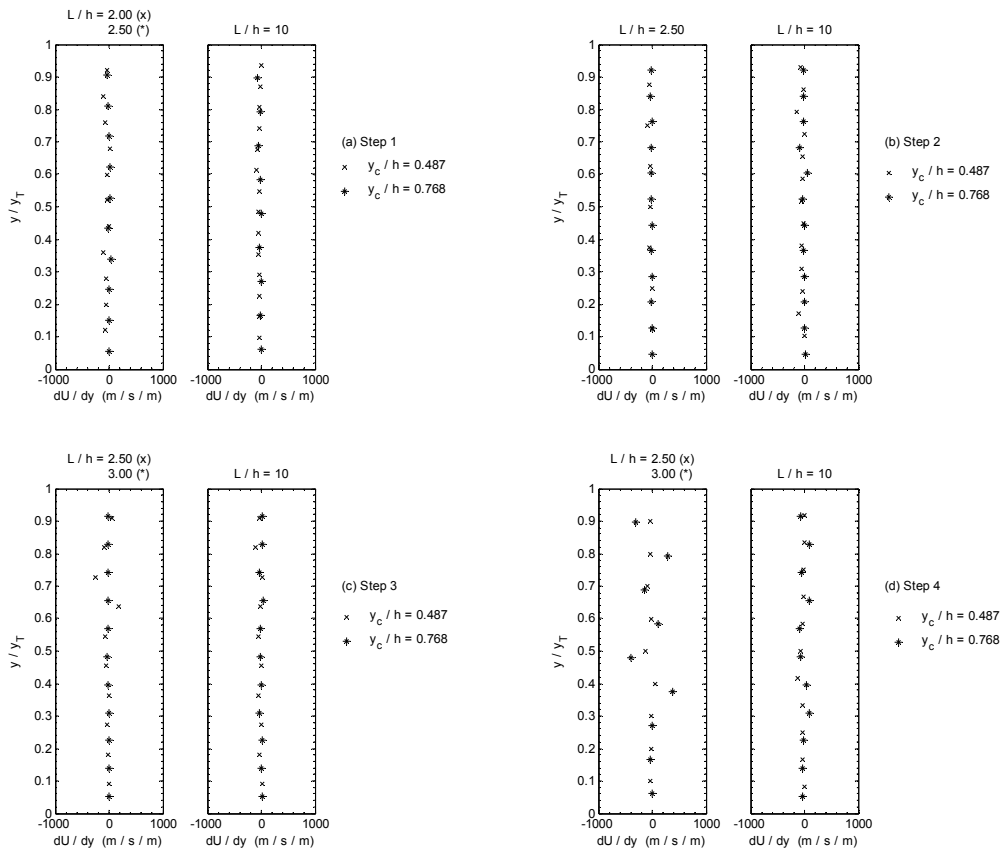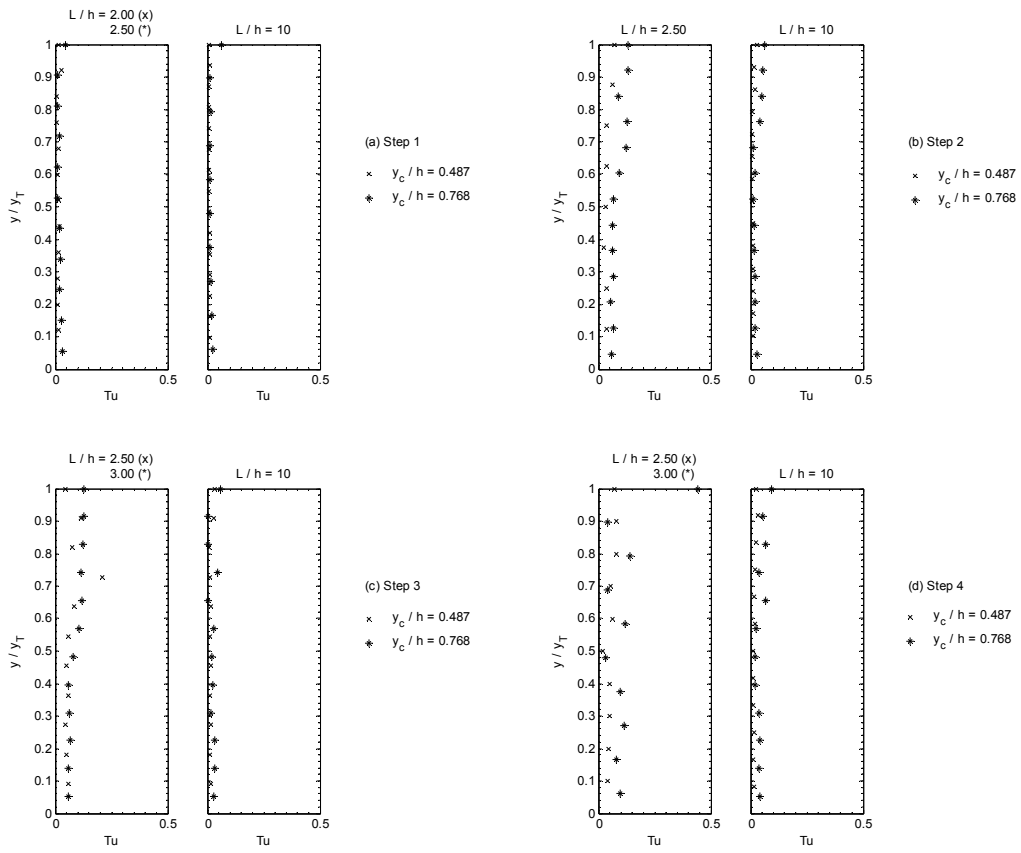
Figure B.8 Velocity profiles. Nappe flow regime, non-aerated condition.
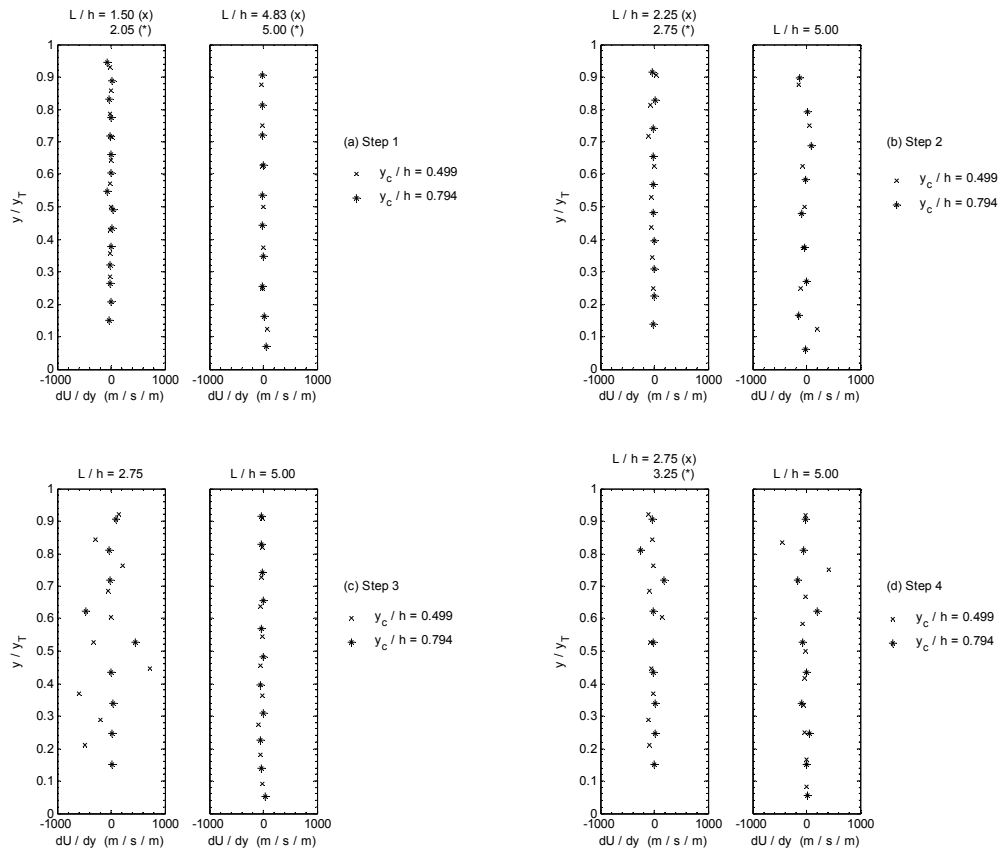
Figure B.9 Velocity gradient profiles. Nappe flow regime, non-aerated condition.
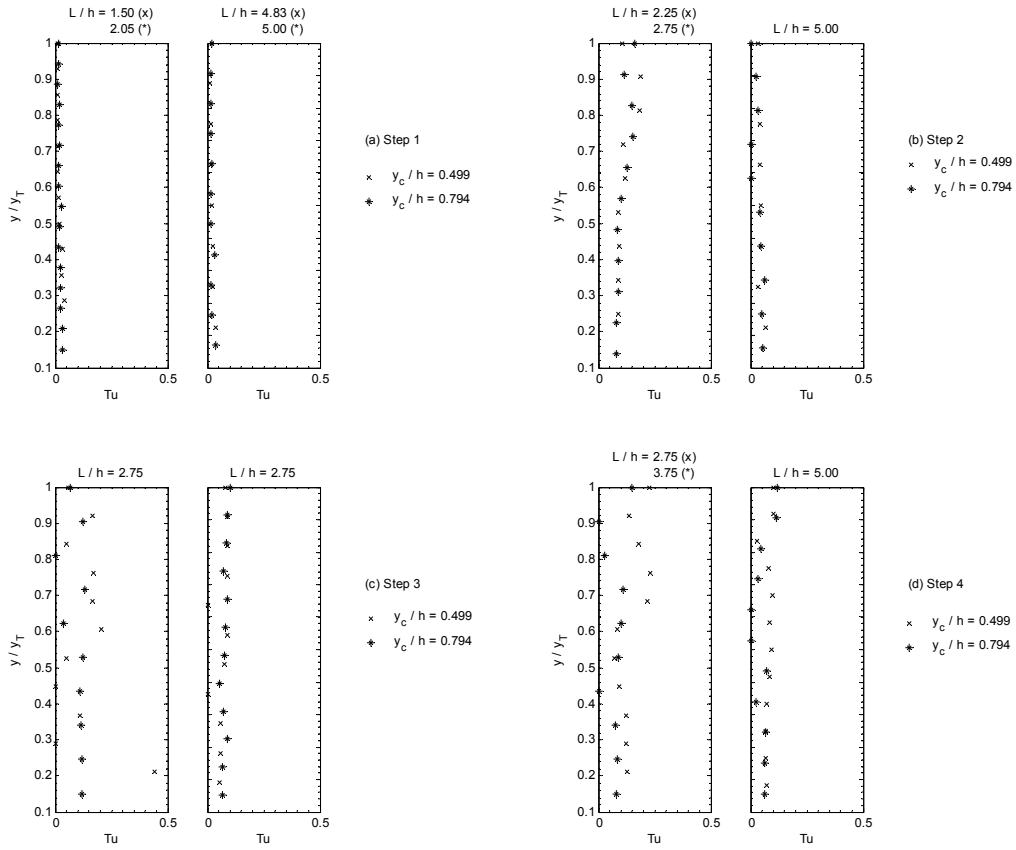
Figure B.10 Turbulence intensity profiles. Nappe flow regime, non-aerated condition.
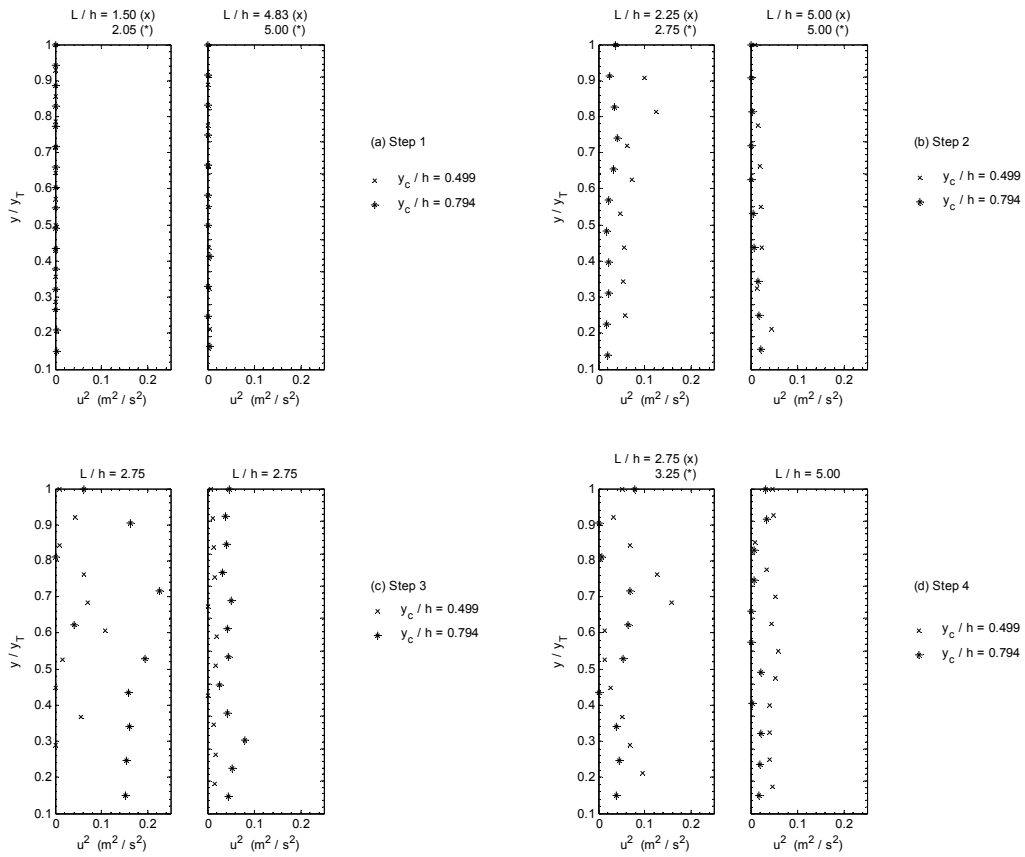
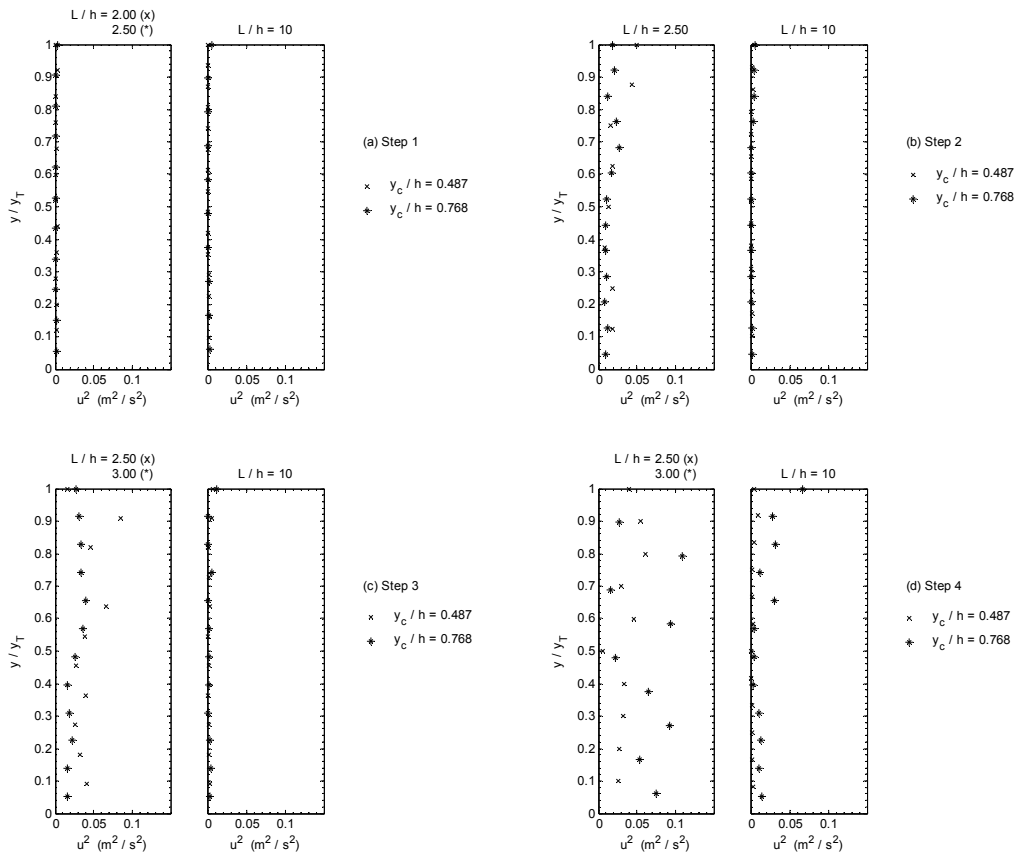**Figure B.11** Normal stress profiles. Nappe flow regime, non-aerated condition.
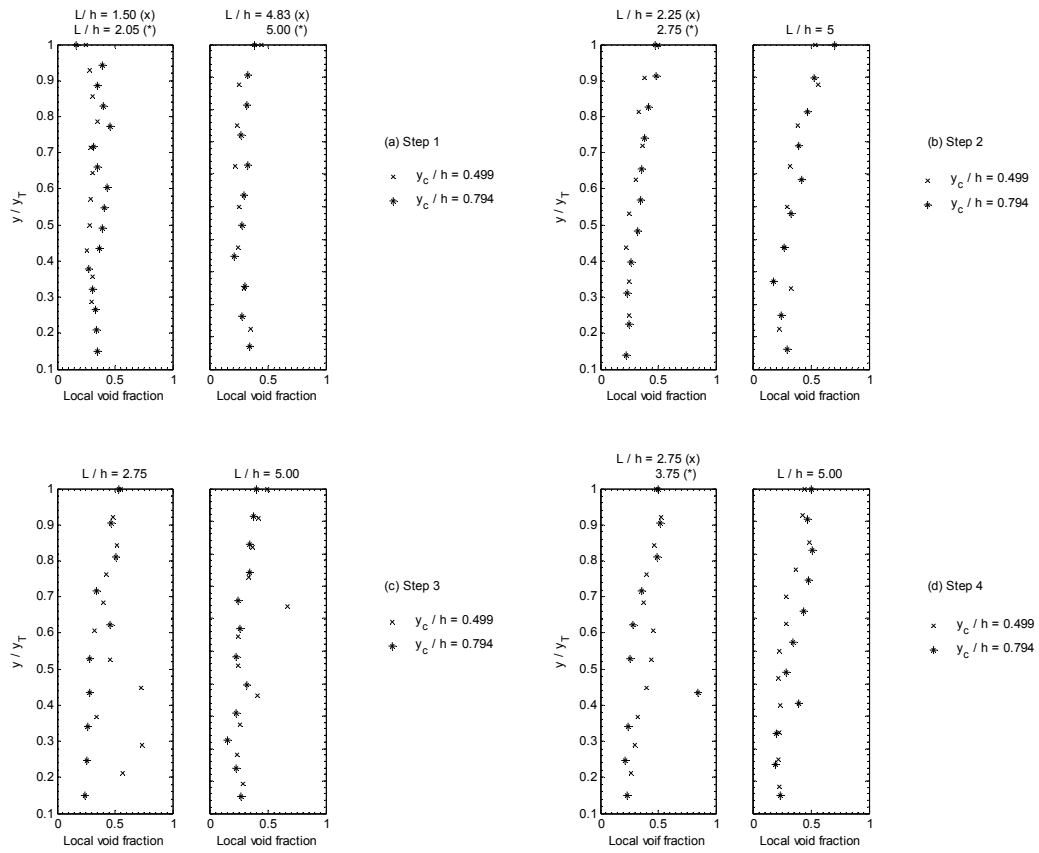
Figure B.12 Local void fraction profiles. Nappe flow regime, non-aerated condition.
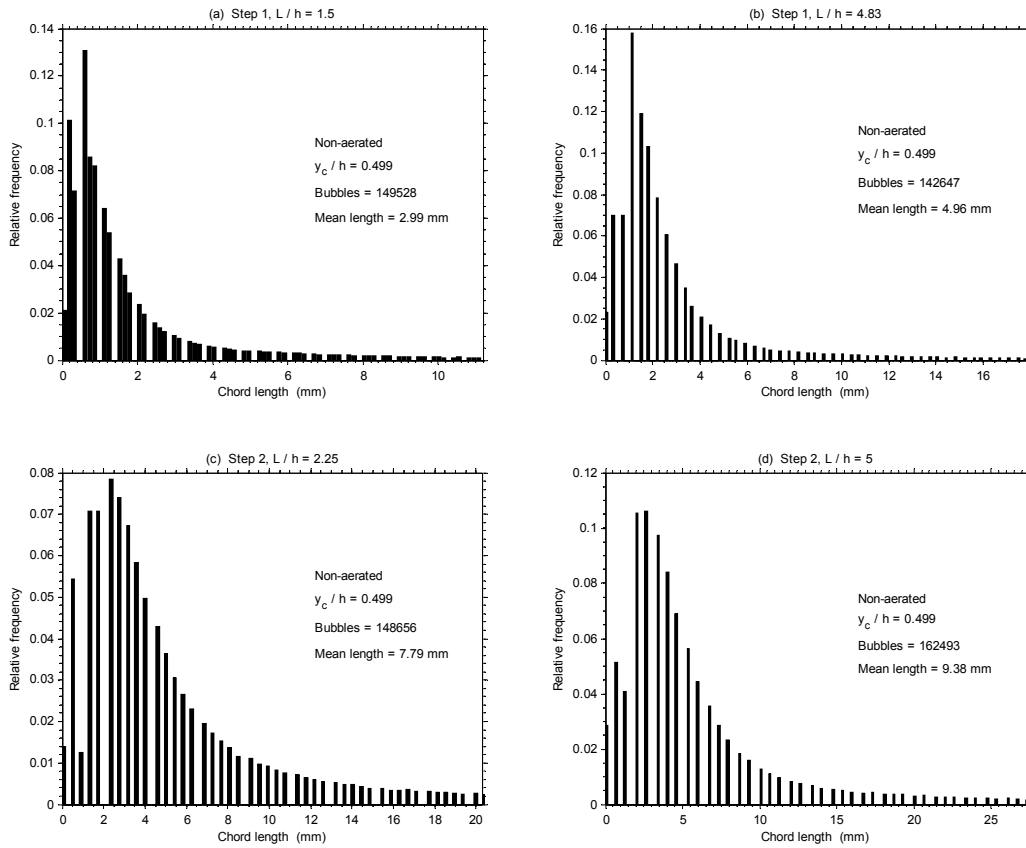
Figure B.13 Bubble chord length. Nappe flow regime, non-aerated condition.
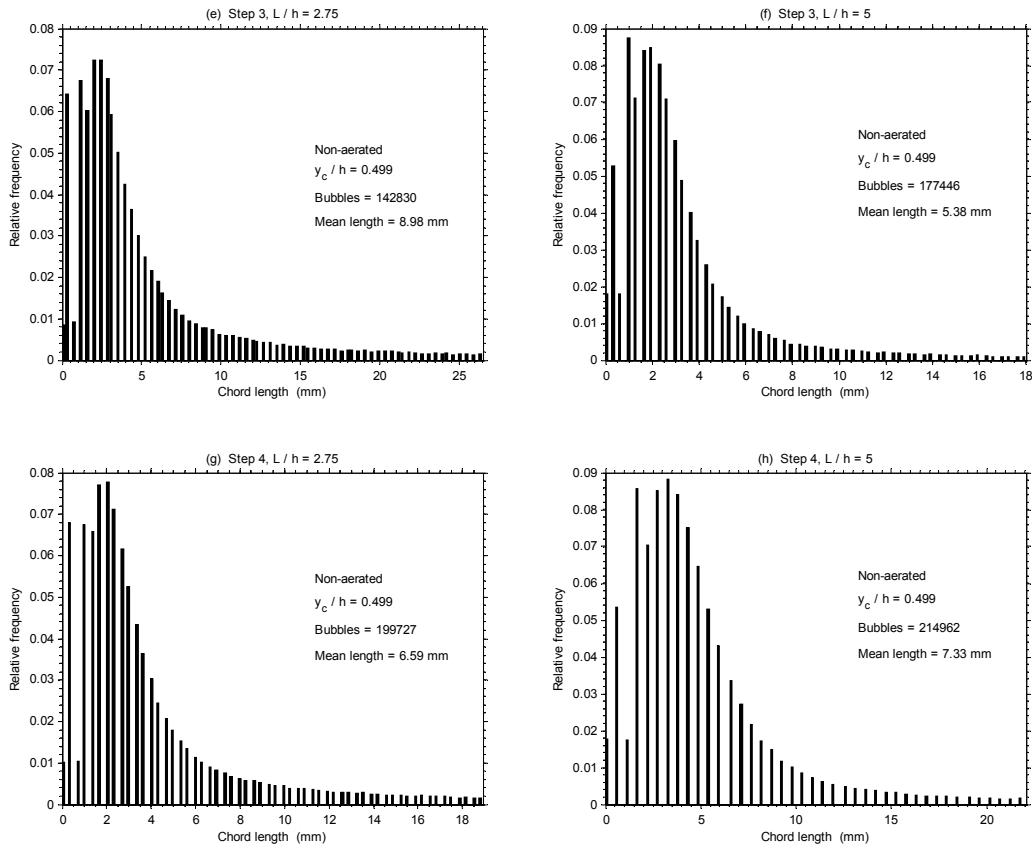
Figure B.13 (continuation) Bubble chord length. Nappe flow regime, non-

aerated condition.
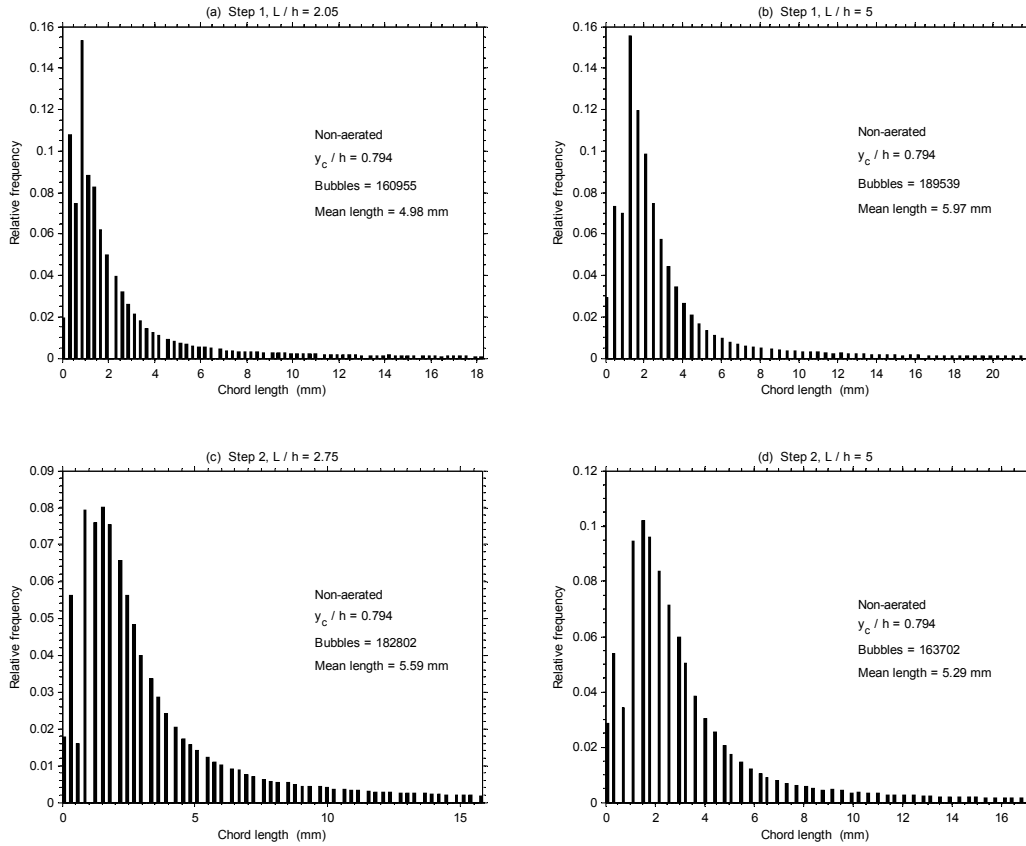
Figure B.14 Bubble chord length. Nappe flow regime, non-aerated condition.
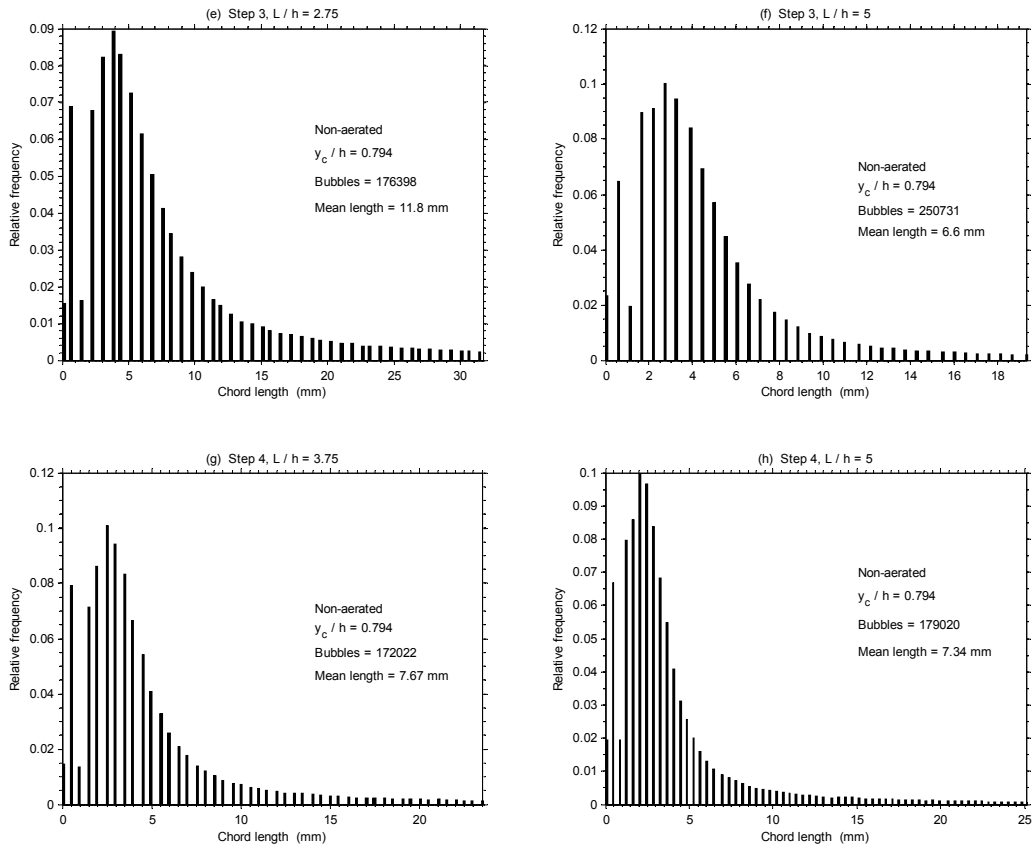
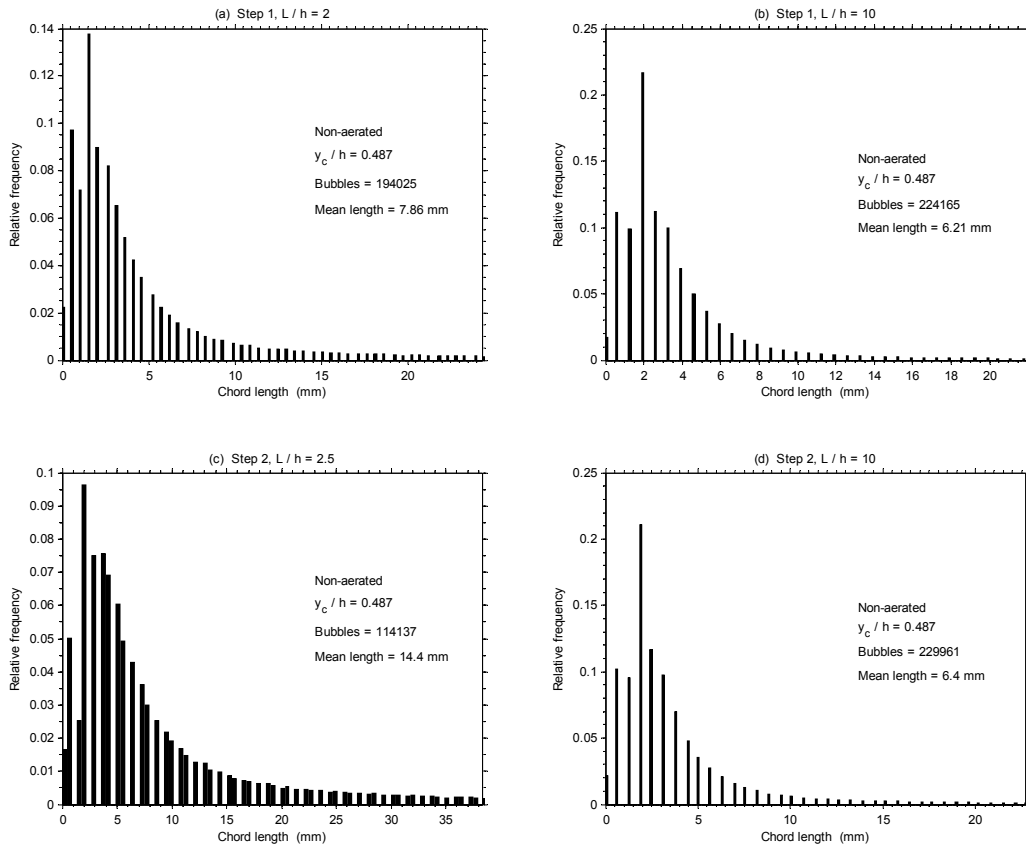**Figure B.14** (continuation) Bubble chord length. Nappe flow regime, non-

aerated condition.
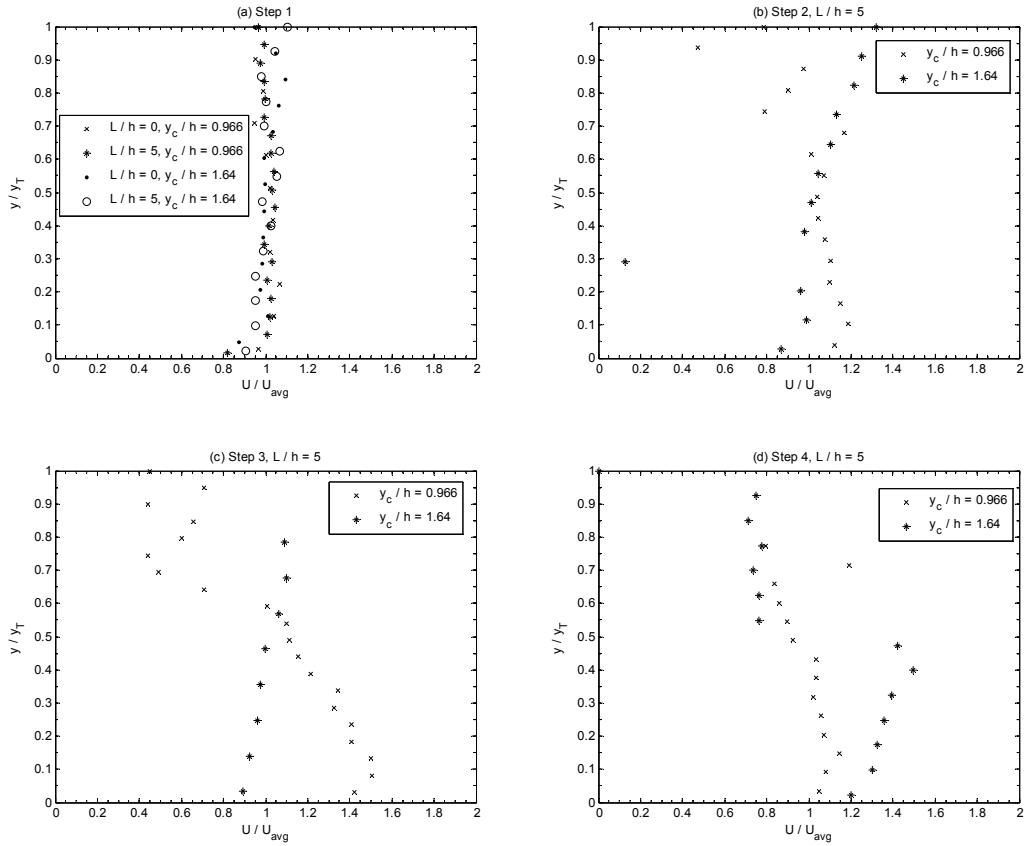
Figure B.15 Velocity profiles. Transition and skimming flow regimes.
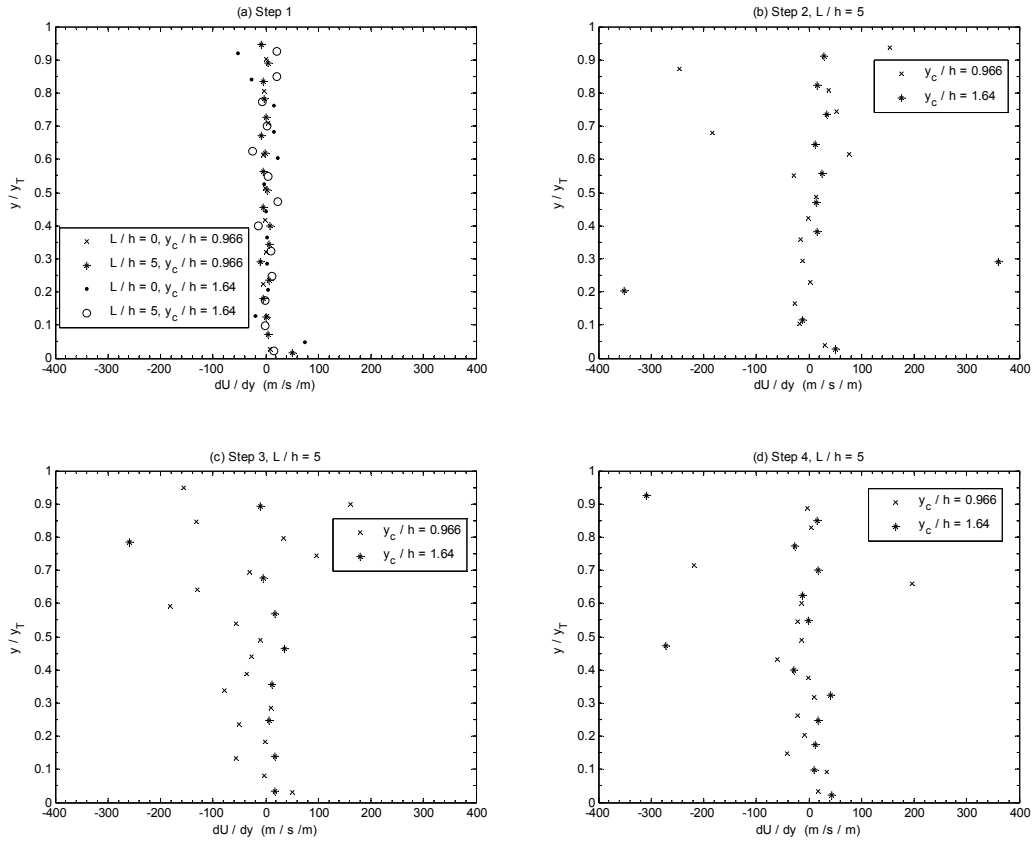
Figure B.16 Velocity gradient profiles. Transition and skimming flow regimes.
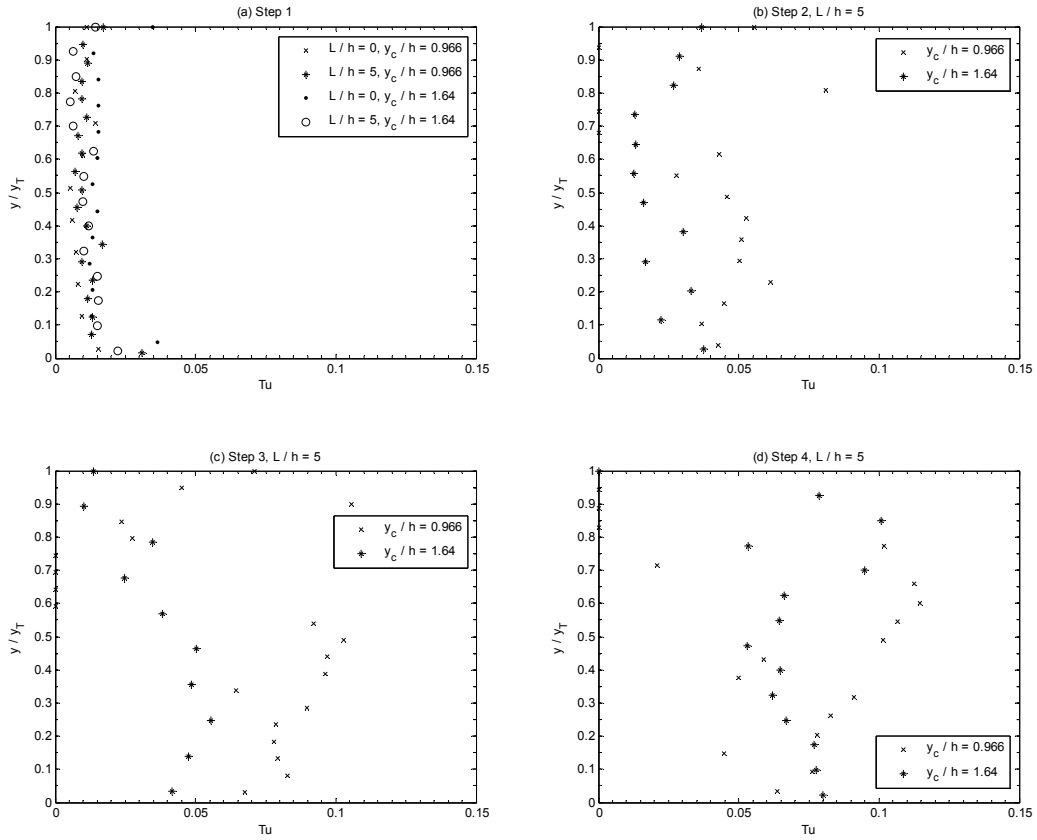
Figure B.17 Turbulence intensity profiles. Transition and skimming flow regimes.
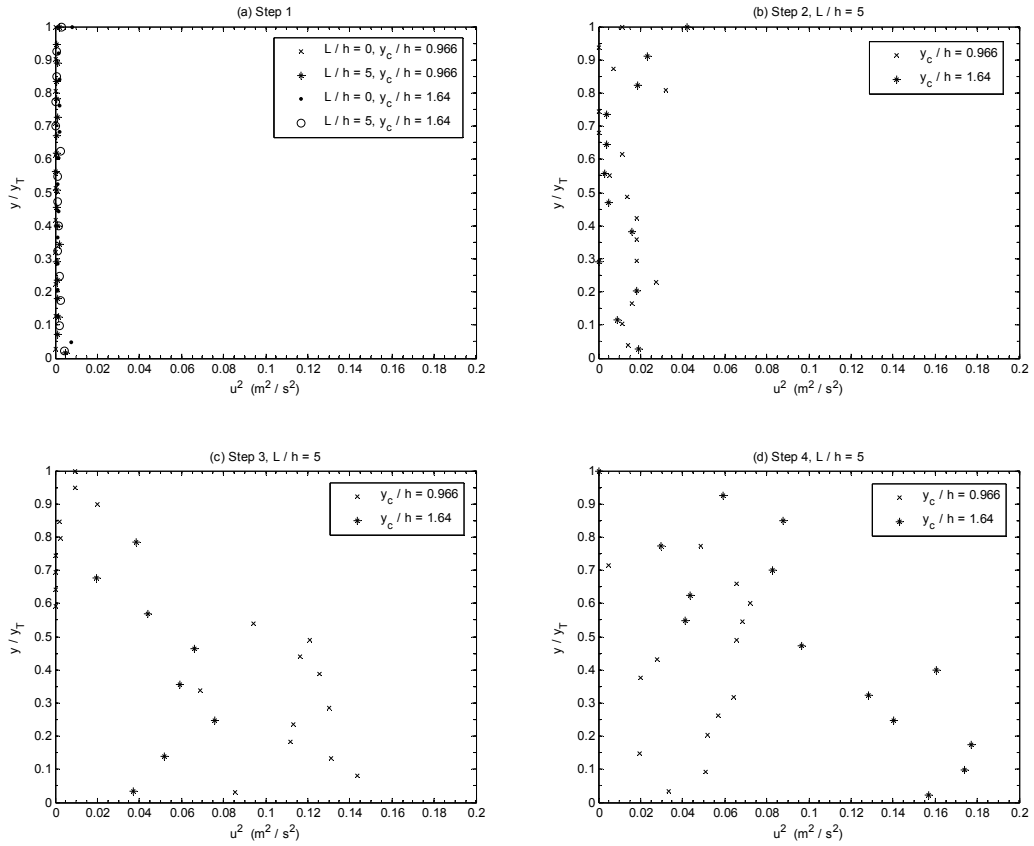
Figure B.18 Normal stress profiles. Transition and skimming flow regimes.
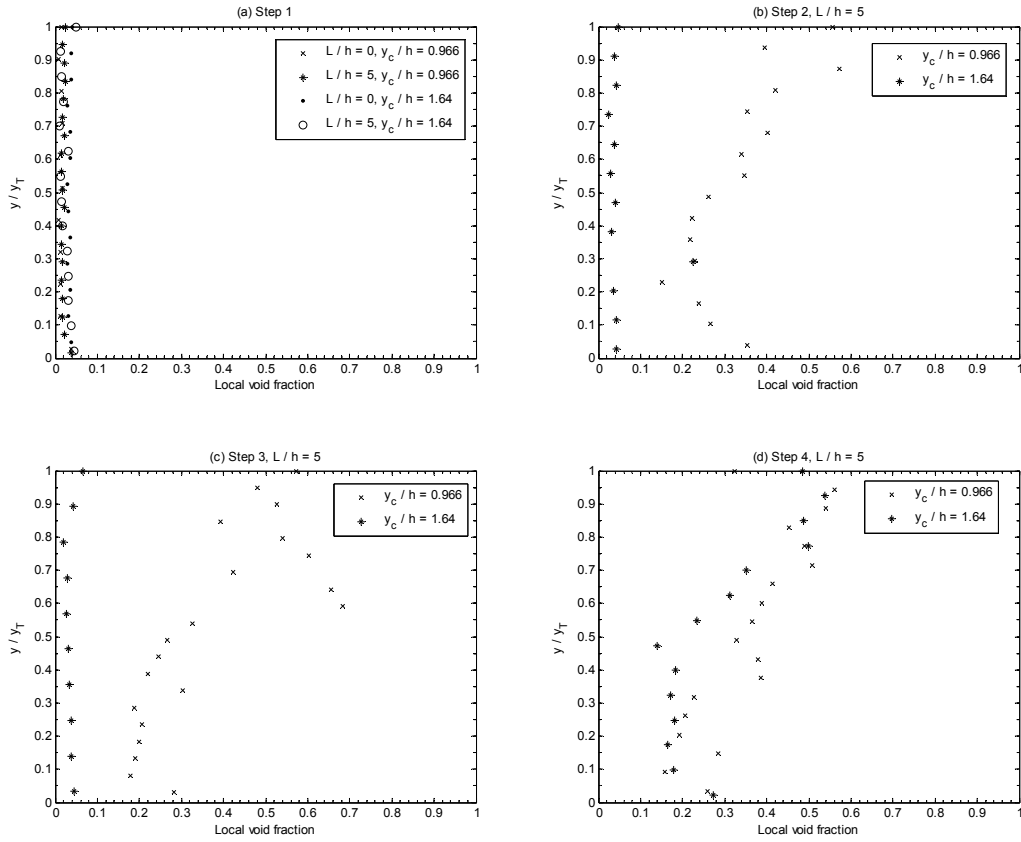
Figure B.19 Local void fraction profiles. Transition and skimming flow regimes.
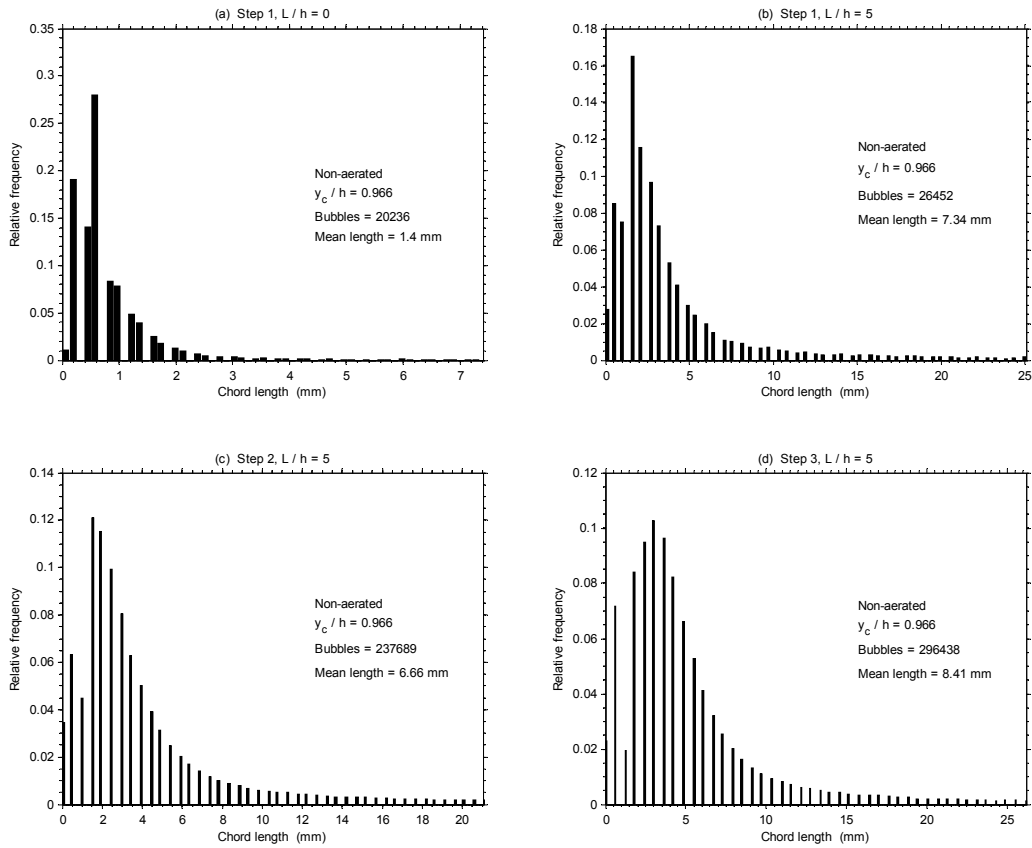
Figure B.20 Bubble chord length. Transition flow regime.
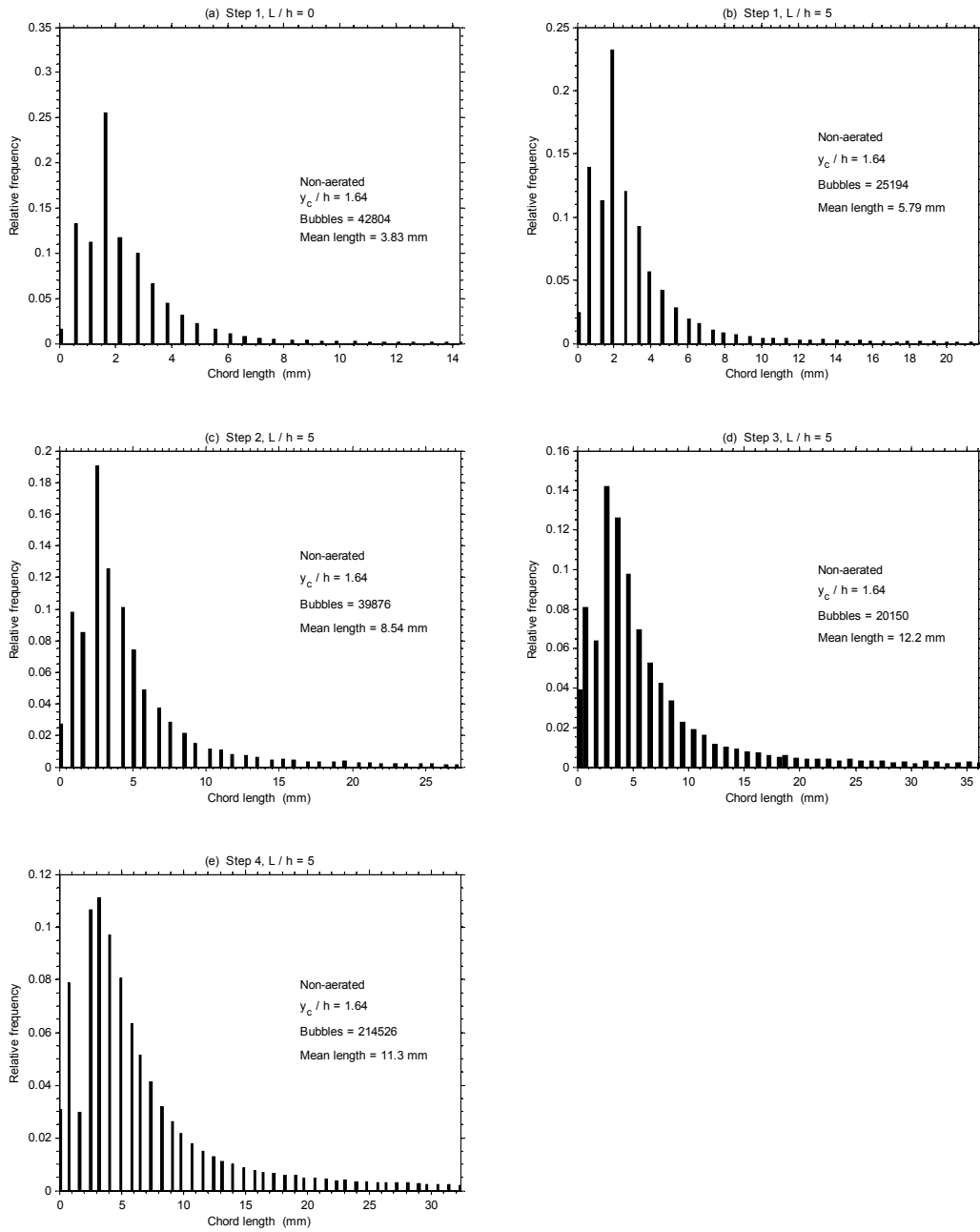
Figure B.21 Bubble chord length. Skimming flow regime.

Appendix C   Velocity *field and local void fraction*

observations. Model III
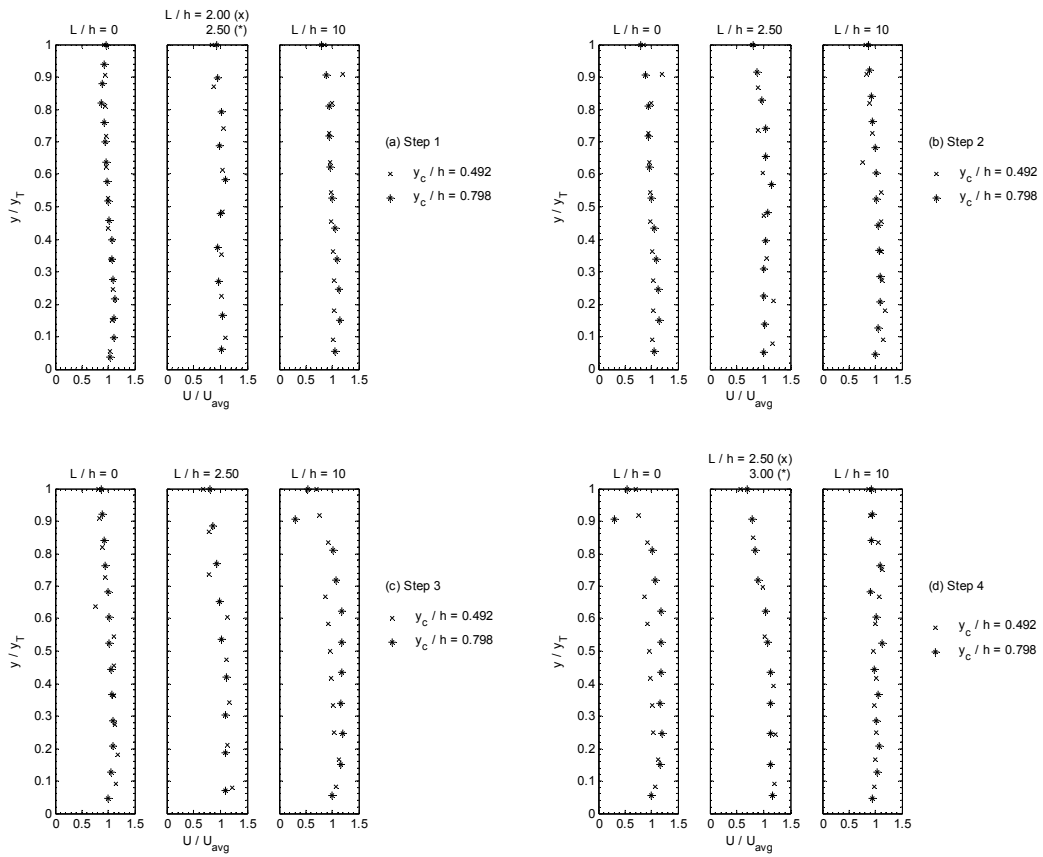
Figure C.1 Velocity profiles. Nappe flow regime, aerated condition.
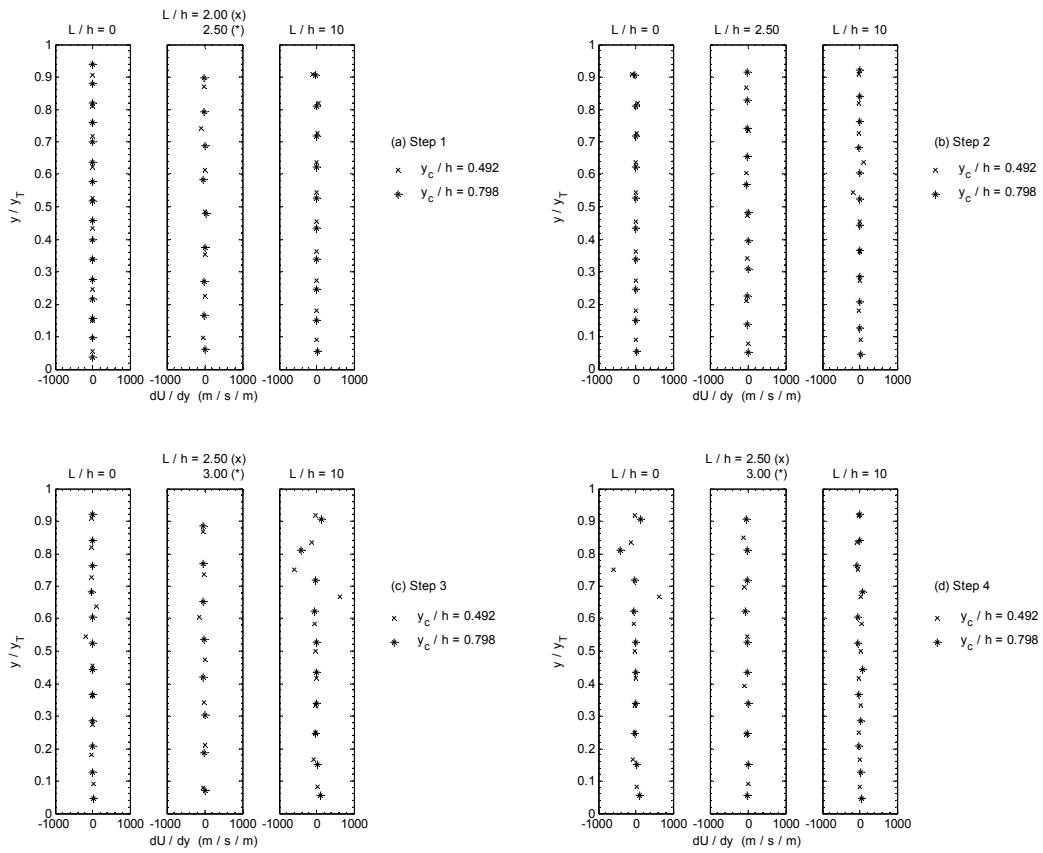
Figure C.2 Velocity gradient profiles. Nappe flow regime, aerated condition.
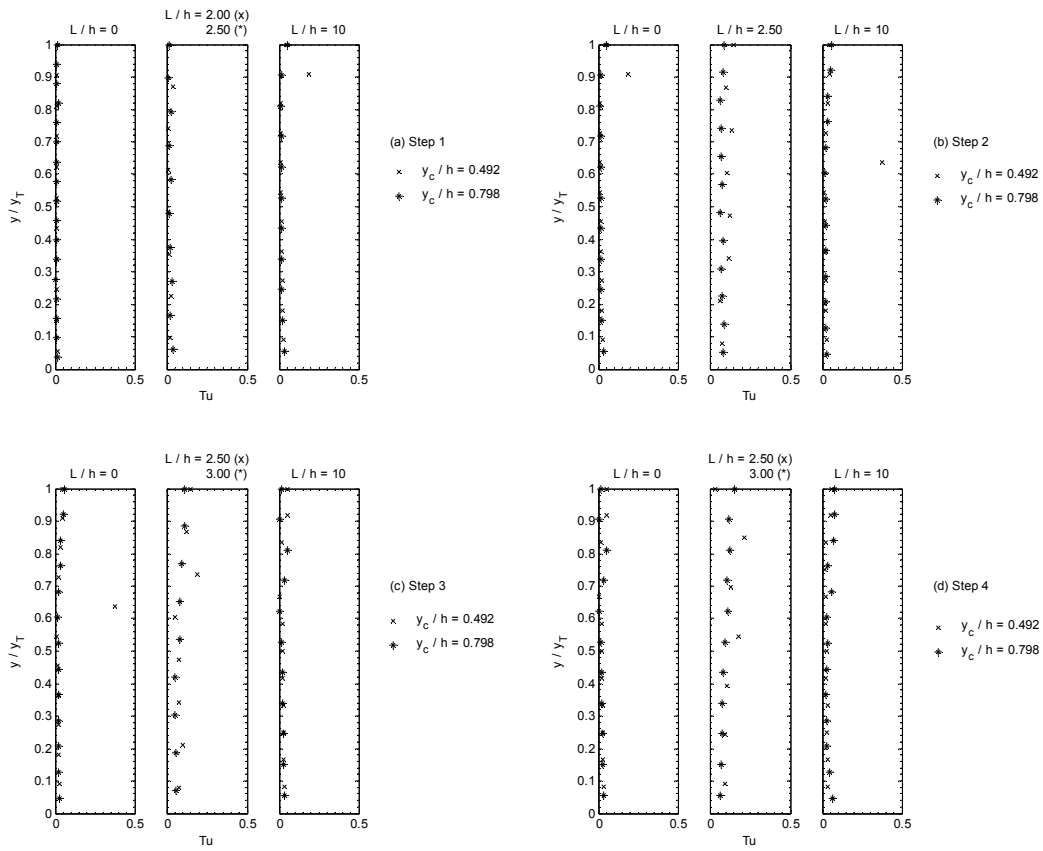
Figure C.3 Turbulence intensity profiles. Nappe flow regime, aerated condition.

Figure C.4 Normal stresss profiles. Nappe flow regime, aerated condition.

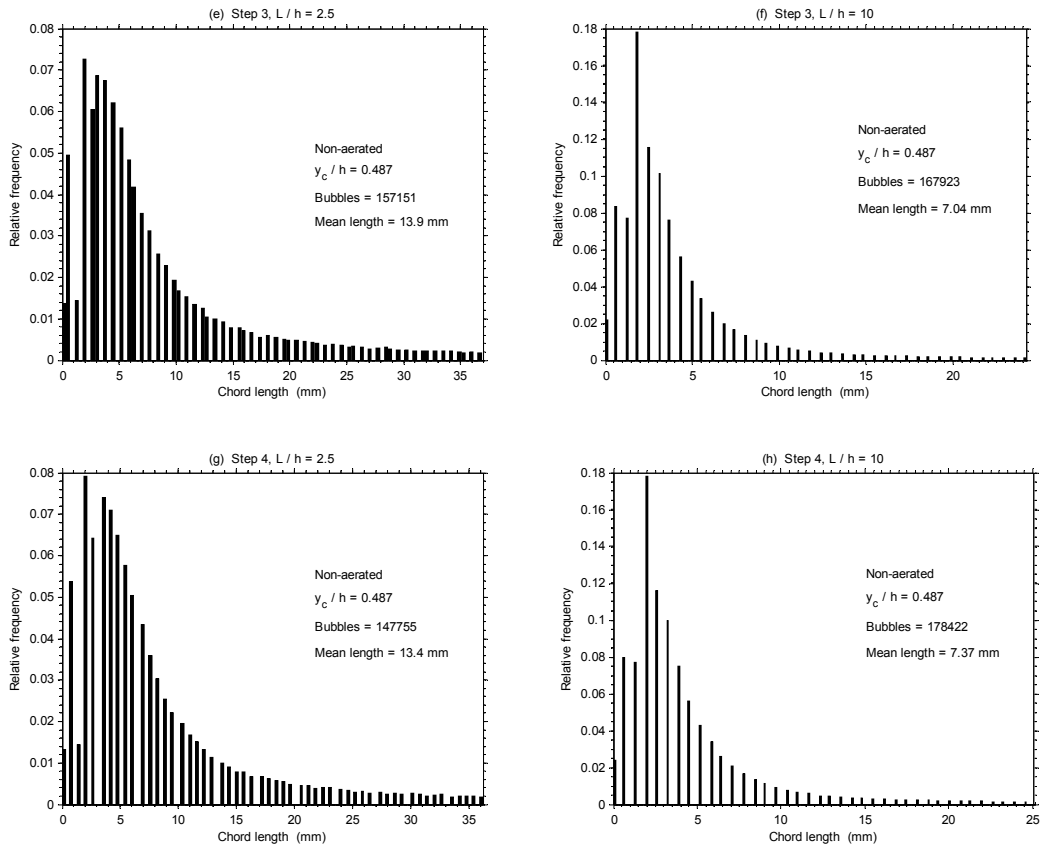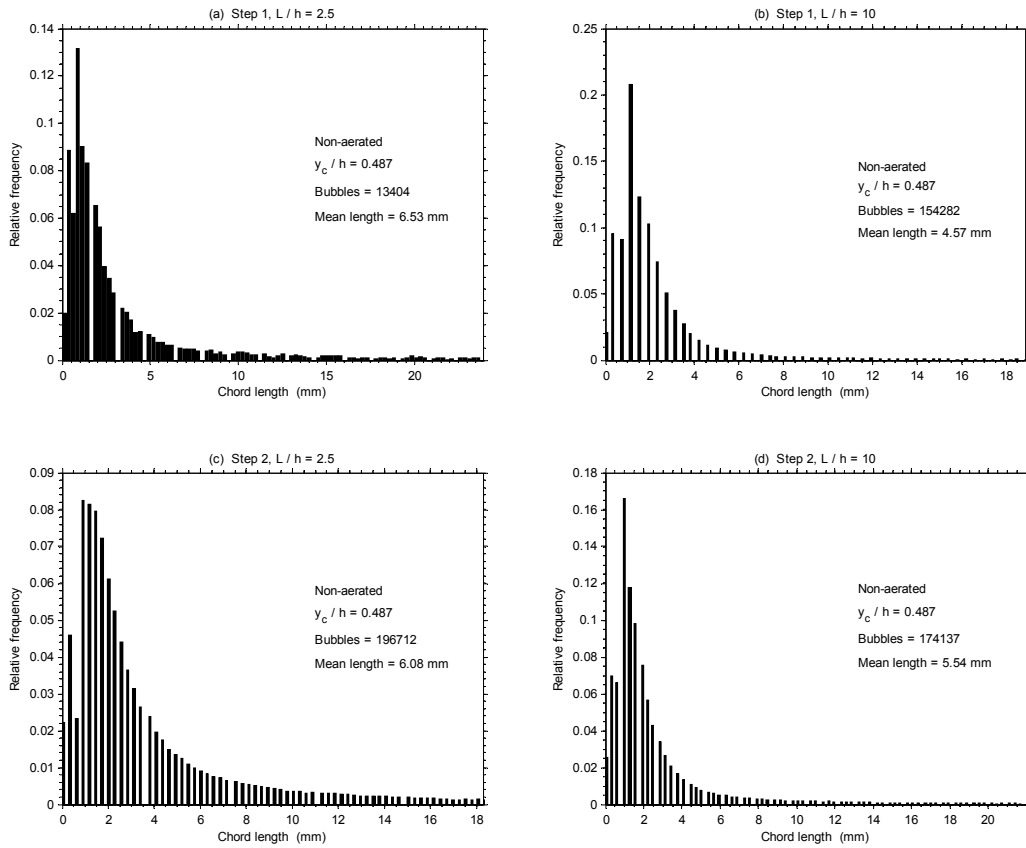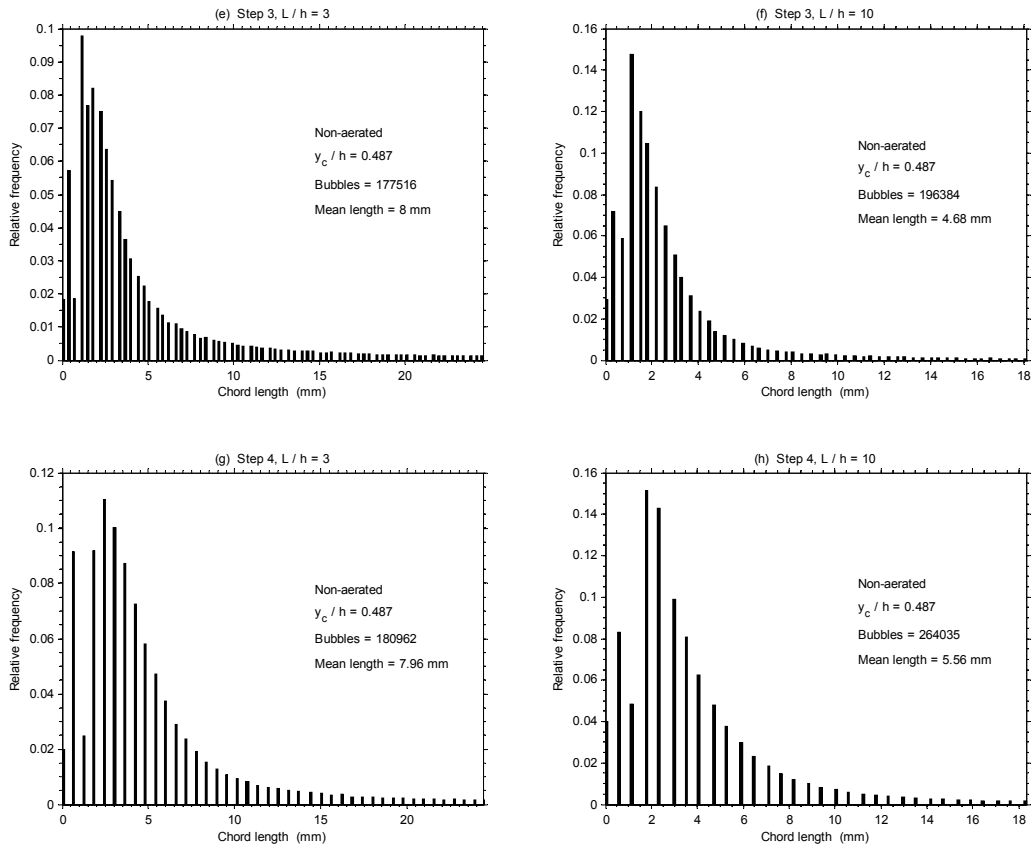**Figure C.5** Local void fraction profiles. Nappe flow regime, aerated condition.

**Figure C.6** Bubble chord length. Nappe flow regime, aerated condition.

Figure C.6 (continuation) Bubble chord length. Nappe flow regime, aerated condition.

Figure C.7 Bubble chord length. Nappe flow regime, aerated condition.

Figure C.7 (continuation) Bubble chord length. Nappe flow regime, aerated condition.

Figure C.8 Velocity profiles. Nappe flow regime, non-aerated condition.
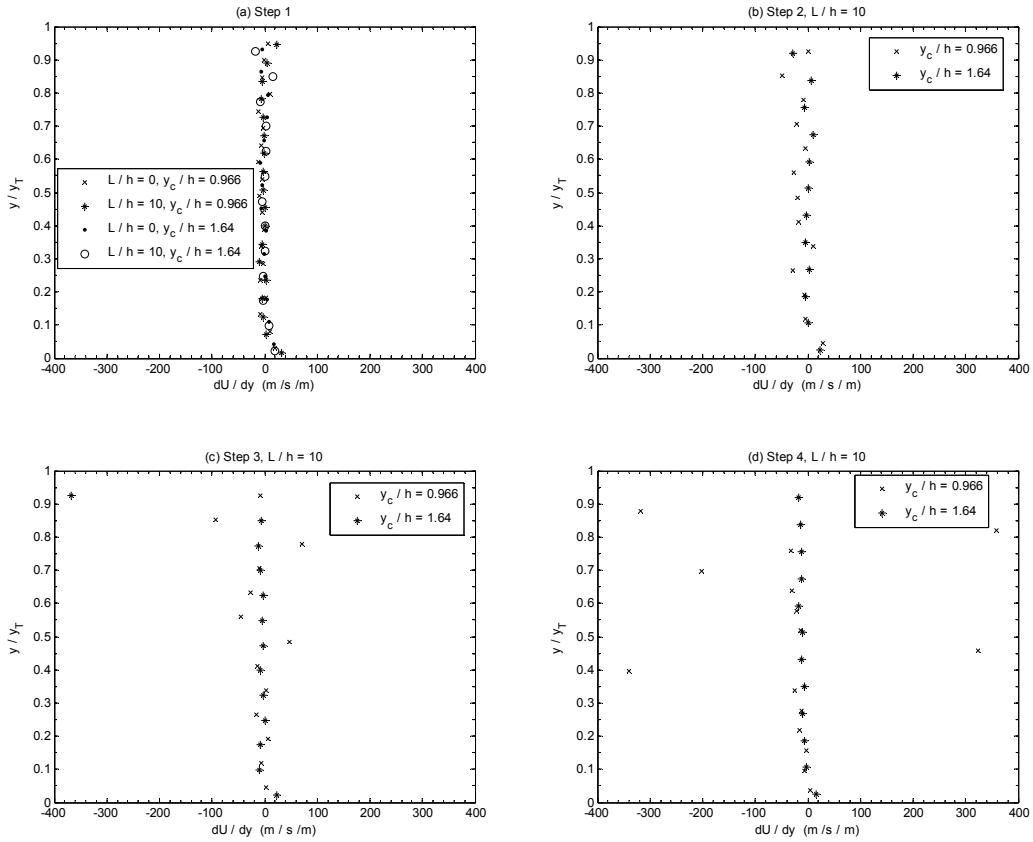
Figure C.9 Velocity gradient profiles. Nappe flow regime, non-aerated condition.

Figure C.10 Turbulence intensity profiles. Nappe flow regime, non-aerated condition.

Figure C.11 Normal stress profiles. Nappe flow regime, non-aerated condition.
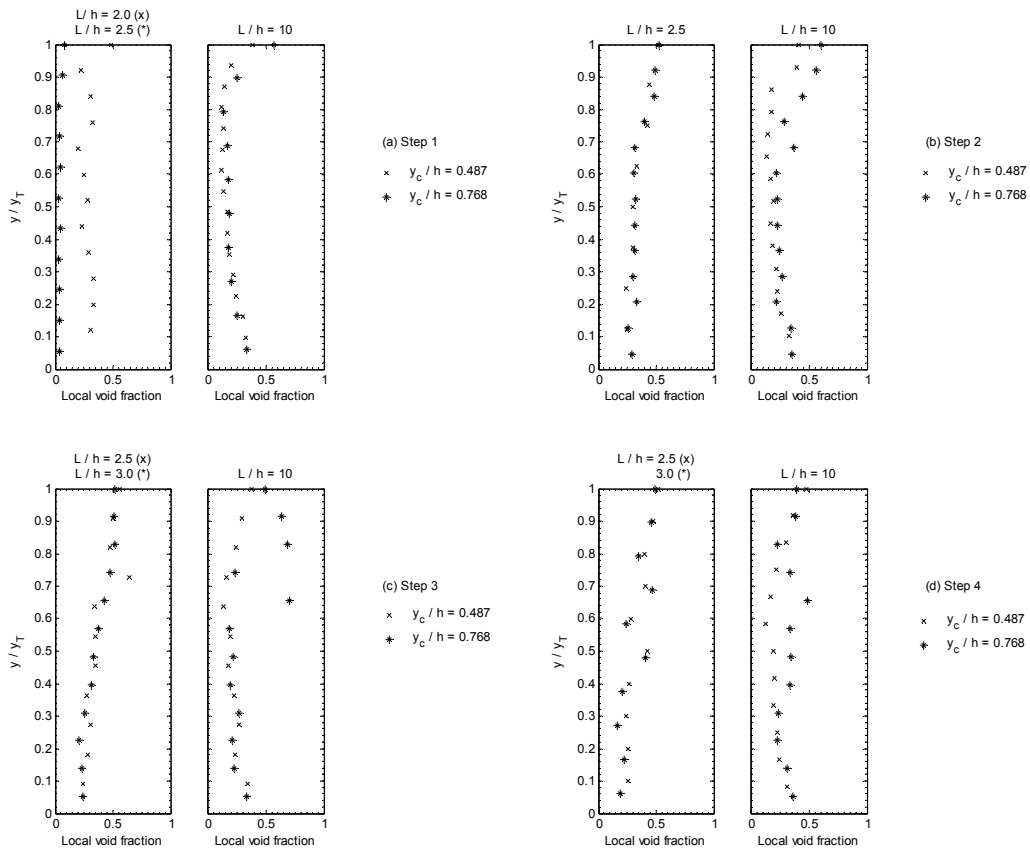
Figure C.12 Local void fraction profiles. Nappe flow regime, non-aerated condition.

Figure C.13 Bubble chord length. Nappe flow regime, non-aerated condition.

Figure C.13 (continuation) Bubble chord length. Nappe flow regime, non-

aerated condition.

Figure C.14 Bubble chord length. Nappe flow regime, non-aerated condition.

Figure C.14 (continuation) Bubble chord length. Nappe flow regime, non-

aerated condition.
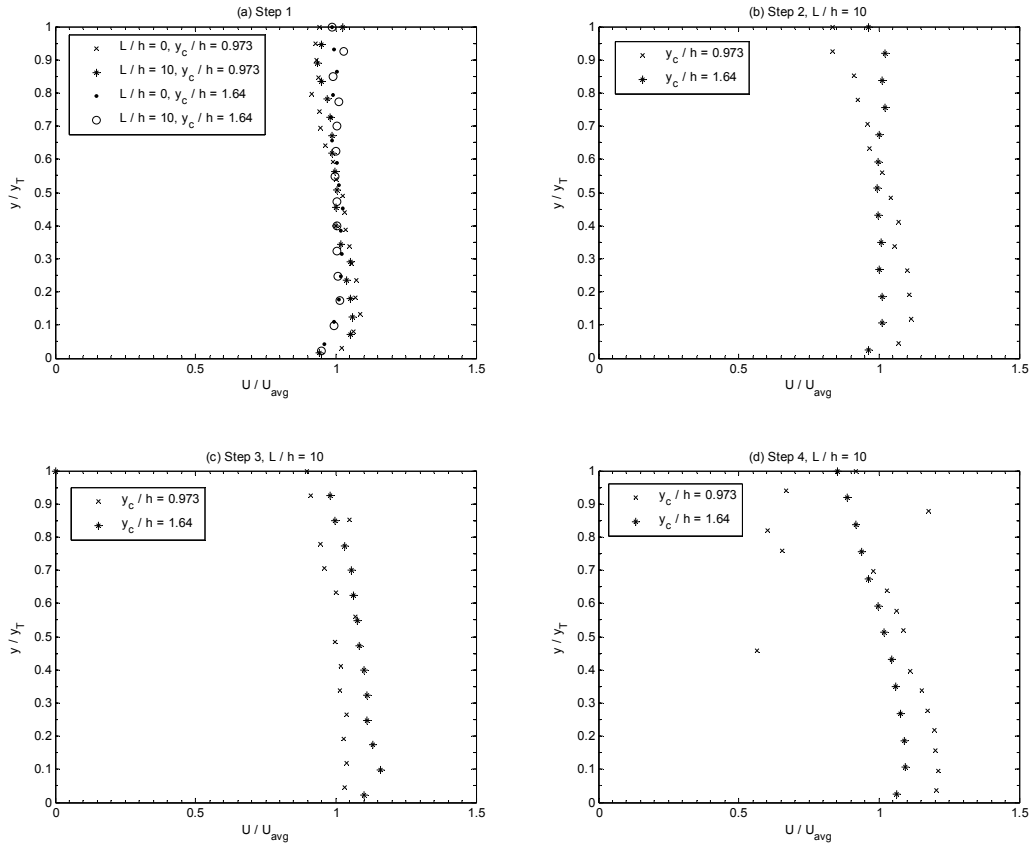
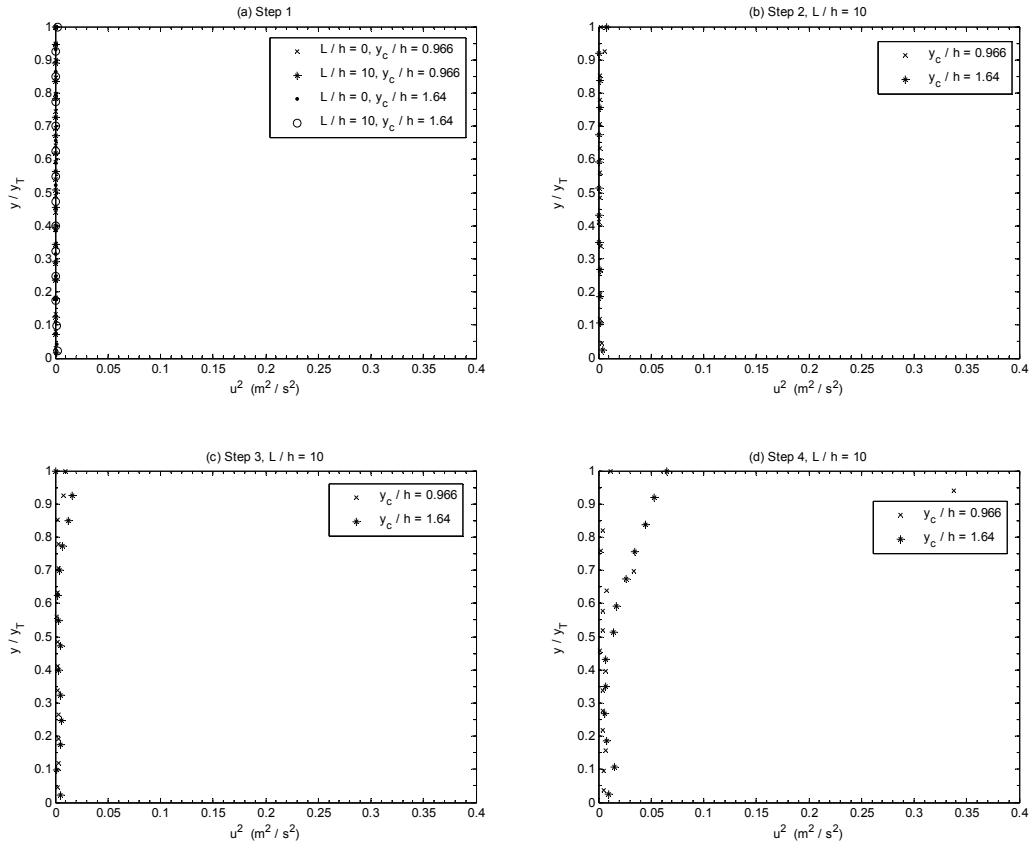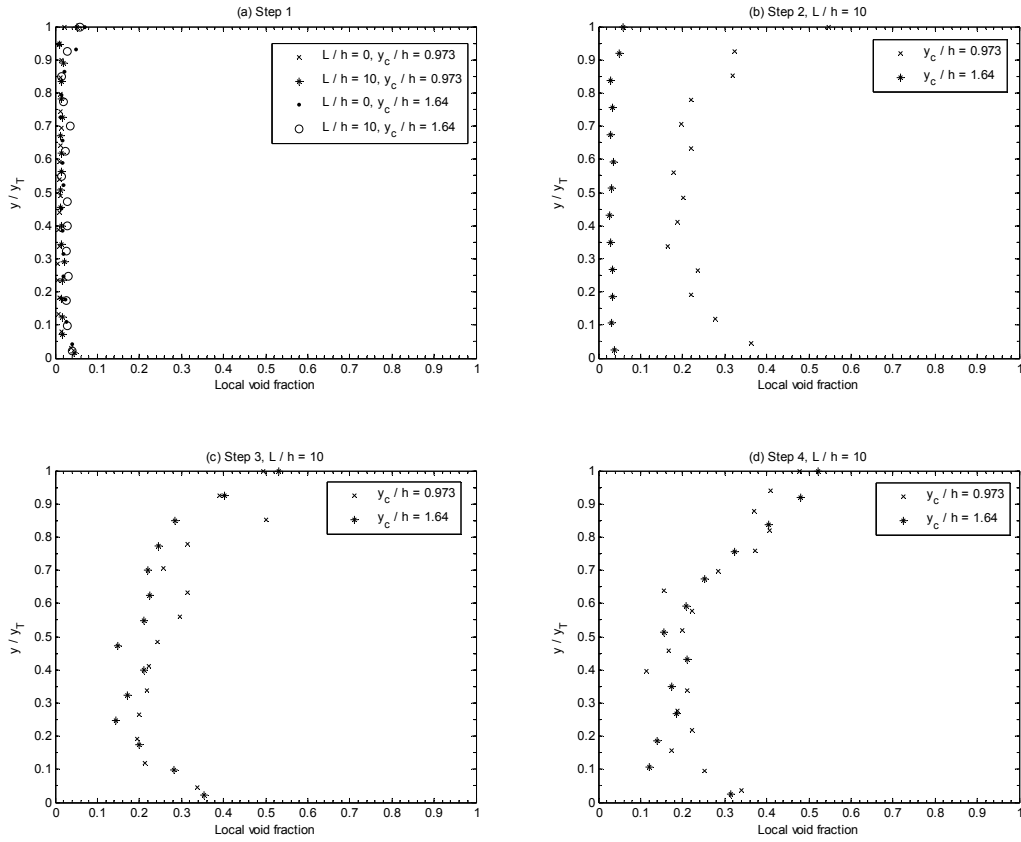**Figure C.15** Velocity profiles. Transition and skimming flow regimes.

Figure C.16 Velocity gradient profiles. Transition and skimming flow regimes.
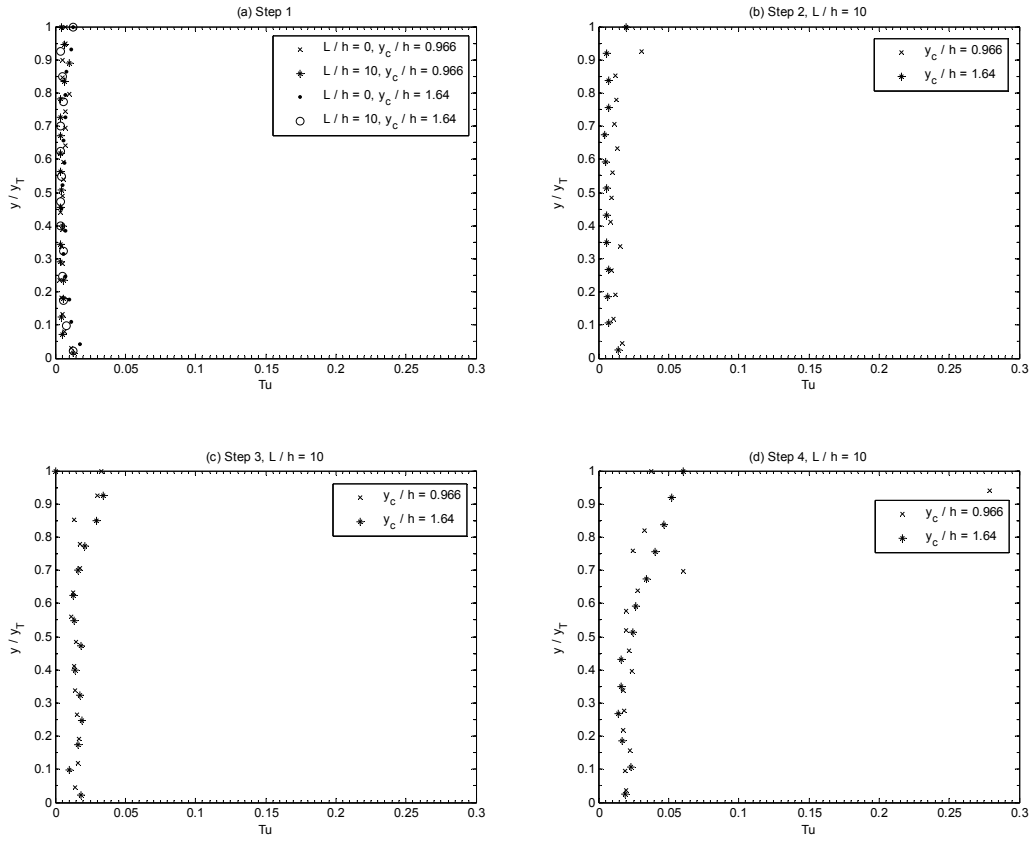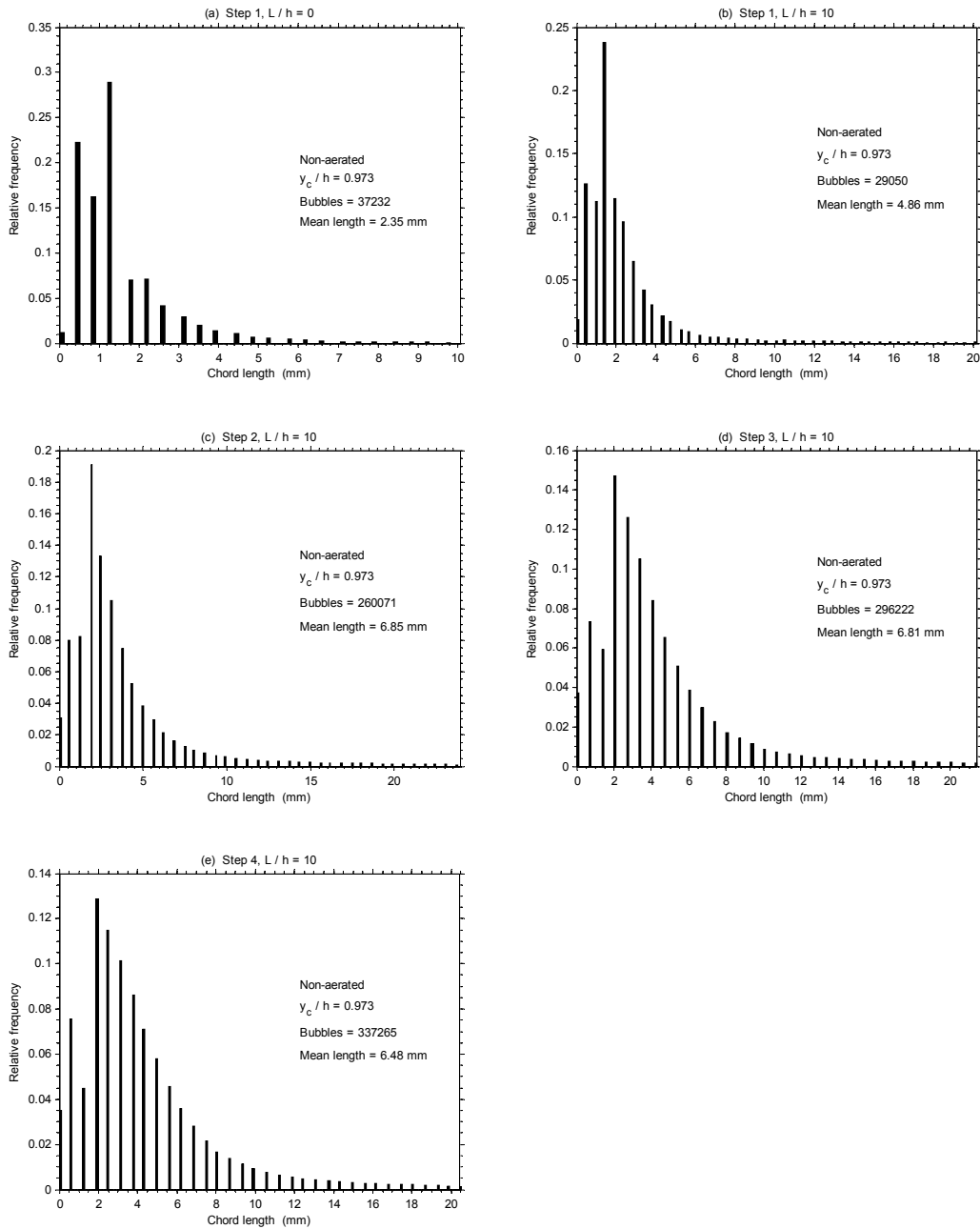
Figure C.17 Turbulence intensity profiles. Transition and skimming flow regimes.
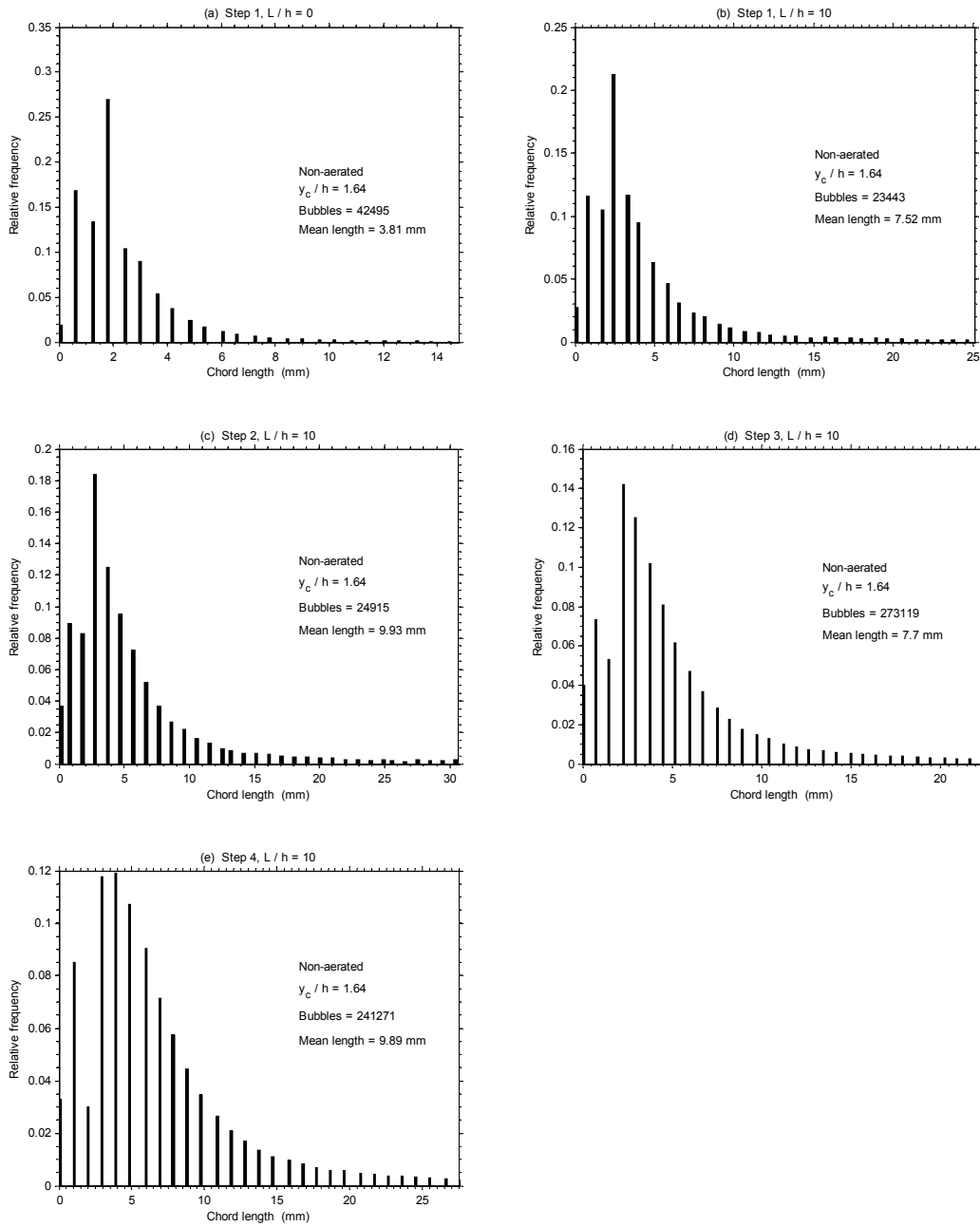
Figure C.18 Normal stress profiles. Transition and skimming flow regimes.

Figure C.19 Local void fraction profiles. Transition and skimming flow regimes.

Figure C.20 Bubble chord length. Transition flow regime.

Figure C.21 Bubble chord length. Skimming flow regime.